University of Southampton Research Repository
ePrints Soton

Copyright © and Moral Rights for this thesis are retained by the author and/or other copyright owners. A copy can be downloaded for personal non-commercial research or study, without prior permission or charge. This thesis cannot be reproduced or quoted extensively from without first obtaining permission in writing from the copyright holder/s. The content must not be changed in any way or sold commercially in any format or medium without the formal permission of the copyright holders.

When referring to this work, full bibliographic details including the author, title, awarding institution and date of the thesis must be given e.g.

AUTHOR (year of submission) "Full thesis title", University of Southampton, name of the University School or Department, PhD Thesis, pagination

http://eprints.soton.ac.uk

UNIVERSITY OF SOUTHAMPTON

FACULTY OF PHYSICAL SCIENCES & ENGINEERING

Optoelectronics Research Centre

Pulsed laser deposition of thin film magneto-optic materials and lasing waveguides

by

Alberto Sposito

Thesis for the degree of Doctor of Philosophy

January 2014

UNIVERSITY OF SOUTHAMPTON

ABSTRACT

FACULTY OF PHYSICAL SCIENCES & ENGINEERING
OPTOELECTRONICS RESEARCH CENTRE

Doctor of Philosophy

PULSED LASER DEPOSITION OF THIN FILM MAGNETO-OPTIC MATERIALS AND LASING WAVEGUIDES

by Alberto Sposito

The aim of this thesis was to study and improve the properties of optical materials deposited by the film growth technique called Pulsed Laser Deposition (PLD), a relatively fast, inexpensive and versatile deposition method using a laser to ablate a target and transfer material on top of a substrate. The materials of interest were titanium-doped sapphire (Ti:sapphire or Ti:Al_2O_3) for fabrication of compact, low-loss, high-efficiency and high-power waveguide lasers, which could be also operated in ultra-fast high-repetition-rate pulsed mode, and magneto-optic garnets, e.g. yttrium iron garnet (YIG, $Y_3Fe_5O_{12}$), for fabrication of low-loss magneto-optic and microwave devices with high performance.

Deposition conditions were optimised for Ti:sapphire and YIG film growth and a multi-laser multi-target PLD system (multi-PLD) was used to tune the composition of YIG film by co-ablation of two different targets (e.g. YIG and Y_2O_3 or Fe_2O_3 or Bi_2O_3 or CeO_2). Ti:sapphire waveguides were fabricated and their optical performances (e.g. transmission losses and lasing characteristics) measured. A study of the effect of compositional variation on structural, optical and magnetic properties of magneto-optic garnet films was carried out and it demonstrated the feasibility of the multi-PLD approach, which was shown to be capable to grow complex crystalline oxide materials, such as YIG and yttrium ferrite ($YFeO_3$), from ablation of their precursor targets (Y_2O_3 or Fe_2O_3) with different ablation rates and deposition of material on different substrates and, in particular, yttrium aluminium garnet (YAG or $Y_3Al_5O_{12}$) and sapphire (Al_2O_3). Some YIG films were also used to demonstrate Laser-Induced Forward Transfer (LIFT) of crystalline materials and the applicability of PLD-grown YIG films in novel meta-material microwave devices.

Physics is essentially an intuitive and concrete science.
Mathematics is only a means for expressing the laws that govern phenomena.
(“Lettre à Maurice Solvine”, by Albert Einstein)

CONTENTS

DECLARATION OF AUTHORSHIP

I, Alberto Sposito, declare that this thesis titled “Pulsed laser deposition of thin film magneto-optic materials and lasing waveguides” and the work presented in it are both my own and have been generated by me as the result of my own original research.

I confirm that:

1. This work was done wholly or mainly while in candidature for a research degree at this University;
2. Where any part of this thesis has previously been submitted for a degree or any other qualification at this University or any other institution, this has been clearly stated;
3. Where I have consulted the published work of others, this is always clearly attributed;
4. Where I have quoted from the work of others, the source is always given. With the exception of such quotations, this thesis is entirely my own work;
5. I have acknowledged all main sources of help;
6. Where the thesis is based on work done by myself jointly with others, I have made clear exactly what was done by others and what I have contributed myself;
7. Either none of this work has been published before submission, or parts of this work have been published as [please see list of publications (Appendix C)]:

Signed: ……………………….……………………………………….……………………….……………

Date: ……………………………….

Acknowledgements

The work presented in this thesis has been primarily funded by EPSRC grant numbers EP/F019300/1, EP/G060363/1, EP/H035745/1 and EP/J008052/1. I am also grateful for the support of an EPSRC studentship.

Various people have made direct contributions to many of the results described in this thesis. I would like to particularly highlight the help of Dr. Amol Choudary, Prof. David P. Shepherd, Dr. Sakellaris Mailis, Dr. Matthias Feinäugle, Dr. Collin Sones (ORC, University of Southampton), Simon A. Gregory, Dr. Gavin B.G. Stenning, Prof. Peter A.J. de Groot (School of Physics and Astronomy, University of Southampton).

I would like to thank Prof. Rob W. Eason for his invaluable support throughout my PhD and for being an excellent supervisor, always encouraging me. Many thanks also to Dr. Timothy May Smith for his support during the first year of my PhD and also for technical support later, in spite of being in a different research group of the ORC and his commitments. Thanks go also to Dr. Katherine A. Sloyan for her help while she was in the PLD group.

I would like to thank Neil Sessions for his patience and technical support in the clean-room, polishing and SEM labs, etc.

Many thanks to my friends and colleagues in the ORC Alex May, Zhihong Li, Feras Al-Saab and Stevan Stankovic.

I would like to thank Alessandro Tomasino and Michele Manzo for their friendship and for some useful discussions.

I would like to thank all my previous professors and, in particular, the supervisors for my BSc and MSc degrees at the University of Palermo, Prof. Alessandro C. Busacca, Prof. Claudio Calì and Dr. Mauro Mosca for introducing me to photonics and giving me an invaluable theoretical background and expertise.

Thanks also to all the people whom I have met in Southampton and who showed me their support and accompanied me in this long journey called “PhD”.

My thanks go especially to all my family for always supporting and encouraging me.

SYMBOLS AND ABBREVIATIONS

A	Total area of substrate surface
AFRL	Air Force Research Laboratory
a, b, c	Lattice constants
a_{FILM}	Lattice constant of film
a_{SUB}	Lattice constant of substrate
at. %	Atomic percent (elemental concentration)
a.u.	Arbitrary Unit
B	Magnetic induction
B_{a}	Applied magnetic field
B_{R}	Remnant magnetisation
BFO	Bismuth Ferrite: $BiFeO_3$
BIG	Bismuth Iron Garnet: $Bi_3Fe_5O_{12}$
Bi:YIG	Bismuth-doped YIG
BSE	Back-Scattered Electrons
C_{mm}	Capacitance of a meta-molecule
Ce:YIG	Cerium-doped YIG
Combi-PLD	Combinatorial Pulsed Laser Deposition
Conc.	Concentration
CPW	Coplanar Waveguide
CW	Continuous Wave
c	Speed of light in vacuum
D	Lattice spacing
DC	Direct Current
DI	De-Ionised
DRS	Diffuse Reflectance Spectroscopy

d	Target-substrate distance
E	Energy
$E\ (x, y, z, t)$	Full electric field function of a guided mode
$E\ (x, y)$	x and y dependence of the electric field function of a guided mode
E_A	Amplitude of the electric field
E_a	Activation energy
E_binding	Binding energy
E_kinetc	Kinetic energy
E_i	Input electric field
E_o	Output electric field
$E_\mathrm{x\text{-}ray}$	X-ray energy
E_x, E_y, E_z	Electric field components along x, y and z directions respectively
E_+, E_-	Right- and left-circularly polarised components of the electric field
EDX	Energy-Dispersive X-ray (spectroscopy)
e-beam	Electron beam
F	Fresnel losses
F_KrF	KrF laser fluence
F_L	Laser fluence
$F_\mathrm{L,\ th}$	Ablation threshold
$F_\mathrm{Nd:YAG}$	Nd:YAG laser fluence
FMR	Ferromagnetic Resonance
FWHM	Full Width at Half Maximum
f	Attempt frequency
f_KrF	KrF laser repetition frequency
$f_\mathrm{Nd:YAG}$	Nd:YAG laser repetition frequency
GGG	Gadolinium Gallium Garnet: $Gd_3Ga_5O_{12}$
GSGG	Gadolinium Scandium Gallium Garnet: $Gd_3(ScGa)_5O_{12}$
g	Landé factor

$H(x, y, z, t)$	Full magnetic field function of a guided mode
$H(x, y)$	x and y dependence of the magnetic field function of a guided mode
H_0	DC magnetic field
H_C	Coercivity
H_dem	Demagnetising field
H_eff	Effective magnetic field
H_RF	RF magnetic field
H_x, H_y, H_z	Magnetic field components along x, y and z directions respectively
HR	High Reflectivity
HT	High Transmission
h	Planck constant
$\hbar$	Reduced Planck constant
IR	Infra-Red
ir	Inverted target ablation ratio: $f_\mathrm{Nd:YAG}/f_\mathrm{KrF}$
J	Angular momentum
j	Characteristic jump distance
k_0	Propagation constant of light in vacuum
k_B	Boltzmann's constant
k_x	Propagation constant of light in the waveguide along the x direction
k_y	Propagation constant of light in the waveguide along the y direction
k_z	Propagation constant of light in the waveguide along the z direction
L	Launch efficiency
L_i	Internal losses
L_mm	Inductance of a meta-molecule
L_TOT	Total losses
LCP	Left-Circularly-Polarised
LIPSS	Laser Induced Periodic Surface Structures
LPE	Liquid Phase Epitaxy

l	Waveguide length
l_c	Optical cavity length
l_d	Surface diffusion length
l_F	Faraday rotator length
l_{td}	Heat diffusion length
l_α	Absorption length
M	Magnetisation field
M_0	DC magnetisation field
M_S	Saturation magnetisation
MIR	Mid Infra-Red
MSSW	Magnetostatic Surface Wave
Multi-PLD	Multi-beam, multi-target Pulsed Laser Deposition
m	Integer
m_e	Electron rest mass
N	Effective waveguide refractive index
N_i	Density of ions in a gas
N_n	Density of neutral atoms in a gas
N_{th}	Threshold value of population inversion
NA	Numerical Aperture
NIR	Near Infra-Red
Nd:GSGG	Neodymium-doped GSGG: $(NdGd)_3(ScGa)_5O_{12}$
n	Refractive index
n^*	Modified refractive index
n_+, n_-	Refractive indexes for RCP and LCP waves
n_c	Refractive index of cladding
n_e	Extraordinary refractive index
n_f	Refractive index of film
n_o	Ordinary refractive index

n_s	Refractive index of substrate
P_{in}	Input power
P_{abs}	Absorbed power
P_{GAS}	Gas pressure (in the vacuum chamber)
P_{O2}	Oxygen pressure (in the vacuum chamber)
P_{out}	Output power
P_{th}	Lasing threshold (absorbed power)
P_{VAC}	Base vacuum pressure
PCB	Printed Circuit Board
PLD	Pulsed Laser Deposition
R	Reflectivity
RCP	Right-Circularly-Polarised
RF	Radiofrequency
RMS	Root Mean Square
RT	Room temperature (~300 K)
r	Target ablation ratio: $f_{KrF}/f_{Nd:YAG}$
S_{21}	Scattering parameter (microwave transmission of CPW)
S_a	Average surface roughness
S_q	RMS surface roughness
Single-PLD	Single-beam, single-target Pulsed Laser Deposition
SE	Secondary Electrons
SEM	Scanning Electron Microscope
SRR	Split Ring Resonator
T	Temperature
T_C	Curie temperature
T_m	Melting temperature
T_N	Néel temperature
T^*	Waveguide transmission coefficient

TE	Transverse Electric
TEC	Thermal Expansion Coefficient
TIR	Total Internal Reflection
TM	Transverse Magnetic
t	Time dimension
t_C	Critical (film) thickness
t_f	Film thickness
UHV	Ultra-High Vacuum
USAF	United States Air Force
UV	Ultra-Violet
VNA	Vector Network Analyser
v	Velocity
v_g	Group velocity
W	Work function
w_0	Beam waist (in the waveguide)
X	Example elemental species
XRD	X-Ray Diffraction
YAG	Yttrium Aluminium Garnet: $Y_3Al_5O_{12}$
YFO	Yttrium Ferrite: $YFeO_3$
YIG	Yttrium Iron Garnet: $Y_3Fe_5O_{12}$
α	Absorption coefficient
β	Propagation constant
β_+, β_-	Propagation constants for RCP and LCP waves
Γ	Torque
γ	Gyromagnetic ratio
γ_F	Free energy of the film surface
γ_S	Free energy of the substrate surface
γ^*	Free energy of the interface between film and surface

δ	Ablation depth
$\mathit{\Delta}$	Phase shift
Δa	Absolute lattice mismatch
$\Delta a/a_{\mathrm{SUB}}$	Relative lattice mismatch
ΔH	FMR linewidth
$\Delta\lambda_{\mathrm{abs}}$	Absorption bandwidth
$\Delta\lambda_{\mathrm{em}}$	Emission bandwidth
$\Delta\rho$	Absolute TEC mismatch
$\Delta\rho/\rho_{\mathrm{SUB}}$	Relative TEC mismatch
ε	Emissivity
ε_0	Vacuum permittivity or electric constant
ε_+, ε_-	Permittivity for RCP and LCP waves
$\varepsilon_\perp$, $\varepsilon_{/\!/}$	Permittivity in the directions orthogonal and parallel to the *z* axis
η	Slope efficiency
ϑ	Propagation angle
ϑ_{c}	Critical angle for the interface film-cladding
ϑ_{max}	Maximum acceptance angle
$\vartheta_{\mathrm{launch}}$	Incident angle of the beam launched into the waveguide
ϑ_{s}	Critical angle for the interface film-substrate
θ	Glazing angle of x-rays
θ_{F}	Faraday rotation angle per unit length
κ_{tc}	Thermal conductivity
κ_{td}	Thermal diffusivity
$\mathit{\Lambda}$	Mean free path
λ	Wavelength
μ	Permeability
μ_0	Vacuum permeability or magnetic constant
μ_{B}	Bohr magneton

μ_{m}	Magnetic moment
ν	Radiation frequency
ν_{21}	Frequency associated to energy transition $E_2 - E_1$
ϱ	Radius of a circle
ρ	Thermal expansion coefficient
ρ_{FILM}	Thermal expansion coefficient of film
ρ_{SUB}	Thermal expansion coefficient of substrate
σ	Stefan-Boltzmann constant
σ_{em}	Emission cross-section
τ	Laser pulse duration
τ_{fl}	Fluorescence life-time
τ_{r}	Residence time before re-evaporation
Φ	Faraday rotation angle
ϕ	Faraday rotation angle per unit length
φ	Angle between two vectors
ω	Angular frequency
ω_0	Resonance frequency
ω_{L}	Larmor frequency
ω_{mm}	Resonant (angular) frequency of a single meta-molecule

1. CHAPTER 1
INTRODUCTION

1.1. MATERIAL ENGINEERING WITH PLD

Among the wide range of thin-film deposition techniques pulsed laser deposition (PLD) is one of the most versatile, whose full potential in material and device engineering has been explored only recently. Although developed in 1965 [1], quite soon after the invention of the laser in 1960, it was only in the 1980s, when it was proven a reliable technique to grow superconductive thin films [2], that PLD started to be adopted as a useful laboratory-based thin-film deposition technique. In the recent past PLD has been proven capable of growing high-quality crystalline materials for lasing devices [3] and over the last two decades the basic PLD set-up has been improved to further extend its capabilities, especially in the field of material engineering. The introduction of a target carousel inside the vacuum chamber allows the sequential deposition of different materials with a single laser, either to grow vertical multi-layered structures (e.g. superlattices, Bragg reflectors, magneto-photonic crystals) on a small (10×10 mm^2) substrate [4] or to produce a library of complex oxide materials on a large wafer (2.5 cm or more in diameter) [5]. If two or more lasers are available however, target co-ablation is possible and the possibilities for PLD growth of designer thin films increase even further. Specific capabilities that co-ablation provide include the following:

1. sequential target ablation with different lasers allows the growth of engineered multi-layer structures [6-8];
2. synchronous target ablation in a dual cross-beam configuration can be exploited:
    a. to avoid inclusion of particulates in the growing film [9],
    b. for compensation of deficiencies of volatile elements (e.g. gallium) in the film growth of complex oxides such as gadolinium gallium garnet (GGG) [10] or…
    c. for a-priori materials growth from mixing of two separate precursors [11];
3. asynchronous target ablation with controlled plume delay allows:
    a. film strain engineering [12] and…
    b. control of doping concentration within a specific target window [13].

PLD-grown films are normally deposited from targets made of the same material as the film, although more recently a few research groups have been using a dual- or multi-beam and multi-target approach, which involves a second target made of a different material to control stoichiometric transfer [10], especially when growing complex oxides such as garnets and orthoferrites, or to tune doping concentration [13]. However, for more sophisticated material engineering purposes, the use of two or more targets of precursor materials is required: thin-film compositional libraries of complex oxides have been deposited by combinatorial PLD using two or three targets and one laser ablating the targets sequentially [5].

This thesis reports the deposition of Ti:sapphire waveguides for subsequent laser operation and the optimisation of PLD growth of magneto-optic garnets, in particular YIG (Yttrium Iron Garnet: $Y_3Fe_5O_{12}$) on lattice-mismatched YAG (Yttrium Aluminium Garnet: $Y_3Al_5O_{12}$) substrates, by single-beam single-target PLD (single-PLD), but also investigates and shows the potential and capabilities of multi-target multi-beam combinatorial PLD (multi-PLD):

1. to tune the composition of complex oxide garnets (YIG) by an asynchronous dual-beam dual-target approach,
2. to grow doped thin film garnets with the same approach as above.

A novel approach to material engineering is also introduced: we demonstrate for the first time to our knowledge the capability of such a multi-PLD system to grow different crystalline complex oxides, such as YIG and YFO (Yttrium Ferrite: $YFeO_3$), from the same precursors (Y_2O_3 and Fe_2O_3) by choosing the appropriate substrate (YAG or sapphire), and to tune the material composition by adjusting the relative repetition frequency of the two lasers used. A similar approach has already been demonstrated in a sputtering system to grow Gd:YAG [14], resulting in amorphous films, which required a subsequent crystallisation step via thermal annealing; our multi-PLD system instead allows direct growth of crystalline films at high substrate temperatures, without the need of any post-growth thermal annealing step.

1.2. MOTIVATIONS

1.2.1. PLD OF TI:SAPPHIRE

PLD of Ti:sapphire competes favourably with other waveguide fabrication techniques [15]. Ti:sapphire waveguides have been made with thermal in-diffusion of Ti into un-doped sapphire substrates, however the high residual concentration of Ti near the surface reduces fluorescence because of re-absorption and causes high losses, thus lowering the device performance, although a waveguide laser with a threshold of ~0.21 W and a slope efficiency of 0.11% at λ = (775 – 820) nm has been demonstrated [16]. Planar films have been fabricated by ion beam implantation into un-doped sapphire substrates, but it causes degradation of the bombarded region, thus inducing additional undesirable losses [17]. Epitaxial re-growth of amorphous material on single-crystal substrates is restricted to <500 nm-thick films [18]. Reactive ionised cluster beam deposition produces poly-crystalline layers with very slow growth rates (~120 nm/hour) [19] when compared to PLD, which produces films of typical growth rates of ~(1 – 10) μm/hour, depending on growth conditions.

The ultimate goal of the project of PLD of Ti:sapphire was the fabrication of compact, high-quality, ultra-fast, low-loss, high-efficiency planar and channel waveguide lasers, which can be used for spectroscopic and bio-medical purposes, e.g. optical coherence tomography (OCT), which require large-bandwidth and high-brightness light sources [20, 21]. The major current limitations in continuous-wave operation of bulk Ti:sapphire lasers are the high-pump power density required for efficient lasing and the peak absorption situated in the blue-green (~500 nm), which call for expensive high-power pump sources (e.g. Ar^+ lasers) [22]. Waveguide lasers have the advantage of simultaneous pump and signal-beam confinement, which leads to average spot-sizes and lasing thresholds impossible to achieve in bulk lasers [22]; moreover the waveguide geometry offers the possibility of integrating devices with the laser for tuning or mode-locking (e.g. a high-repetition rate, compact femtosecond-laser source could be made through butting of a saturable absorber reflector) or for production of integrated optical sensors utilising the large Ti:sapphire bandwidth [23]. In order to take full advantage of these features and allow the use of cheaper, miniature solid-state lower-pump power laser sources, waveguide layers of high crystal quality, low scattering loss and the correct Ti valence state must be produced and PLD is the most promising fabrication technique for Ti:sapphire waveguide lasers, as illustrated above.

1.2.2. PLD OF MAGNETO-OPTIC GARNETS

This project focussed on the growth of magneto-optic garnets by PLD, in particular pure yttrium iron garnet and YIG doped with elements such as bismuth (Bi) and cerium (Ce), which increase the Verdet constant [24, 25]. Magneto-optic garnets are cubic crystals which can be used to make magneto-optic devices, such as Faraday rotators/isolators, magneto-optic memories and radiofrequency (RF)/microwave devices [26-29].

PLD is a very competitive growth technique, compared to other deposition methods used for magnet-optic garnets. Sol-gel and pyrolysis have problems with maintaining composition, crystalline phase and good surface morphology [30]. Liquid phase epitaxy, reactive ion beam sputtering and RF magnetron sputtering have disadvantages such as impurity admixture, low deposition rate (0.01 – 1 μm/hour) and large fluctuation in composition [27, 31-34]. On the contrary, PLD has high deposition rates (some microns per hour, depending on deposition conditions) and also the advantage over LPE of taking place in non-thermodynamic equilibrium, thus allowing the growth of fully-substituted BIG (Bismuth Iron Garnet) [26, 33], which is not possible by LPE.

Also, as already stated in Section 1.1, PLD is a very versatile growth technique, which allows tailoring of the properties of magneto-optic garnets by changing deposition conditions (e.g. it has been demonstrated that ferromagnetic resonance (FMR) linewidth and coercivity decrease with increasing substrate temperature [35, 36]) according to the final application: for instance, magneto-optic rotators/isolators require the “easy axis” to be in-plane [37], although other solutions are possible [38]; microwave devices need low coercivity, whereas magnetic recording media need high coercivity [29, 39].

Moreover, magneto-optic photonic crystals [4, 40-50] (i.e. multi-layer structures with magneto-optic materials) and magneto-optic garnets with engineered compositions can be easily fabricated by multi-PLD.

Magneto-optic devices find applications especially in the optical communication field: Faraday rotation in iron garnets is necessary to make integrated optical isolators, which are required to protect laser sources from reflected light that would cause instability or even catastrophic damage, and also integrated optical circulators, modulators, combiners, splitters and couplers [26]. Fine grain bulk YIG ceramics are already used for microwave circulators and single-crystal YIG spheres as FMR cavities in tunable network analysers

[51]; thick YIG films find applications in magneto-static wave devices: band pass/reject filter, delay lines, phase shifters, resonators, etc. [29, 51].

1.3. LAYOUT OF THE THESIS

This thesis is structured so that Chapter 2 provides some general background, placing PLD in context with other film growth techniques and waveguide fabrication methods; the theory on PLD, waveguides, Ti:sapphire and magneto-optic garnets is provided in Chapter 3. All the experimental techniques used for fabrication and characterisation of the samples described in this thesis are briefly introduced in Chapter 4. The results of the experiments are described and discussed in the following chapters:

- Chapter 5 covers single-PLD growth of Ti:sapphire films for fabrication of planar waveguide lasers and their characterization.
- Chapter 6 covers the optimisation of deposition conditions of YIG by single-PLD;
- Chapter 7 covers all multi-PLD experiments with YIG, Y_2O_3 and Fe_2O_3;
- Chapter 8 covers multi-PLD experiments with YIG and Bi_2O_3 for growth of Bi-doped YIG (Bi:YIG);
- Chapter 9 covers multi-PLD experiments with YIG and CeO_2 for growth of Ce-doped YIG (Ce:YIG);

Finally Chapter 10 summarizes the research work described in this thesis, discussing possible future actions and work.

The first two appendixes briefly describe two other project areas regarding Laser-Induced Forward Transfer of PLD-grown crystalline YIG and the use of YIG films for application in magnetic meta-materials. The third appendix is a list of publications that have resulted from the reported PhD work.

1.4. SUMMARY OF RESULTS AND ACHIEVEMENTS

The main results and achievements of this thesis are summarised as below.

- PLD growth of Ti:sapphire waveguide lasers with transmission losses lower than reported before (<1.6 dB/cm) and lasing results comparable to the best reported so far [15]: lasing at $\lambda = 750$ nm with threshold (average absorbed power) $P_{th} \approx 364$ mW, maximum output power $P_{out} \approx 7.5$ mW at $P_{abs} \approx 770$ mW and slope efficiency $\eta \approx 4\%$.
- PLD growth of crack-free µm-thick YIG films on lattice-mismatched YAG substrates is reported for the first time, to the best of our knowledge at time of writing.
- Optimisation of deposition conditions of YIG on YAG for minimisation of FMR linewidth: $\Delta H \approx 1.75$ mT as measured at $\nu = 6$ GHz from the best film deposited.
- Compositional study of YIG by multi-PLD: a systematic study of variation of YIG film properties (crystallinity, surface roughness and morphology, optical transmission and FMR linewidth) as a function of composition was carried out by co-ablation of YIG and either Y_2O_3 or Fe_2O_3.
- First demonstration to date, to the best of our knowledge at time of writing, of multi-PLD growth of different crystalline complex oxides, such as YIG and YFO (Yttrium Ferrite: $YFeO_3$), from the same precursors (Y_2O_3 and Fe_2O_3) by choosing the appropriate substrate (YAG or sapphire). Material composition tuning is also demonstrated by adjusting the relative repetition frequency of the two lasers used.
- First report to date, to the best of our knowledge at time of writing, of multi-PLD growth of Bi:YIG films by co-ablation of YIG and Bi_2O_3 targets. A study of crystalline growth of Bi:YIG as a function of substrate temperature and Bi-doping level was carried out.
- Multi-PLD of Bi_2O_3 and Fe_2O_3 in the attempt to grow pure BIG films; this is believed the first report of a-priori growth attempts of BIG by PLD.
- Multi-PLD of YIG and CeO_2 in the attempt to grow Ce:YIG films, never reported before, to the best of our knowledge.

1.5. REFERENCES

1. H. M. Smith, and A. F. Turner, "Vacuum deposited thin films using a ruby laser," Appl. Opt. **4**, 147-148 (1965).

2. D. Dijkkamp, T. Venkatesan, X. D. Wu, S. A. Shaheen, N. Jisrawi, Y. H. Minlee, W. L. McLean, and M. Croft, "Preparation of Y-Ba-Cu oxide superconductor thin-films using pulsed laser evapoartion from high-T_C bulk material," Appl. Phys. Lett. **51**, 619-621 (1987).

3. N. A. Vainos, C. Grivas, C. Fotakis, R. W. Eason, A. A. Anderson, D. S. Gill, D. P. Shepherd, M. Jelinek, J. Lancok, and J. Sonsky, "Planar laser waveguides of Ti:sapphire, Nd:GGG and Nd:YAG grown by pulsed laser deposition," Appl. Surf. Sci. **127**, 514-519 (1998).

4. S. I. Khartsev, and A. M. Grishin, "$Bi_3Fe_5O_{12}/Gd_3Ga_5O_{12}$ (m) magneto-optical photonic crystals," Appl. Phys. Lett. **87**, 122504 (2005).

5. P. K. Schenck, J. L. Klamo, N. D. Bassim, P. G. Burke, Y. B. Gerbig, and M. L. Green, "Combinatorial study of the crystallinity boundary in the HfO_2-TiO_2-Y2O_3 system using pulsed laser deposition library thin films," Thin Solid Films **517**, 691-694 (2008).

6. R. Gazia, T. C. May-Smith, and R. W. Eason, "Growth of a hybrid garnet crystal multilayer structure by combinatorial pulsed laser deposition," J. Cryst. Growth **310**, 3848-3853 (2008).

7. K. A. Sloyan, T. C. May-Smith, M. Zervas, R. W. Eason, S. Huband, D. Walker, and P. A. Thomas, "Growth of crystalline garnet mixed films, superlattices and multilayers for optical applications via shuttered Combinatorial Pulsed Laser Deposition," Opt. Express **18**, 24679-24687 (2010).

8. K. A. Sloyan, T. C. May-Smith, M. N. Zervas, and R. W. Eason, "Crystalline garnet Bragg reflectors for high power, high temperature, and integrated applications fabricated by multi-beam pulsed laser deposition," Appl. Phys. Lett. **101**, 081117 (2012).

9. L. Lambert, F. Grangeon, and M. Autric, "Crossed Beam Pulsed Laser Deposition of cryolite thin films," Appl. Surf. Sci. **138**, 574-580 (1999).

10. M. S. B. Darby, T. C. May-Smith, and R. W. Eason, "Deposition and stoichiometry control of Nd-doped gadolinium gallium garnet thin films by combinatorial pulsed laser deposition using two targets of Nd:$Gd_3Ga_5O_{12}$ and Ga_2O_3," Appl. Phys. A Mater. Sci. Process. **93**, 477-481 (2008).

11. R. Nechache, C. Harnagea, L. Gunawan, L. P. Carignan, C. Maunders, D. Menard, G. A. Botton, and A. Pignolet, "Growth, structure, and properties of $BiFeO_3$-$BiCrO_3$ films obtained by dual cross beam PLD," IEEE Trans. Ultrason. Ferroelectr. Freq. Control **54**, 2645-2652 (2007).

12. K. A. Sloyan, T. C. May-Smith, R. W. Eason, and J. G. Lunney, "The effect of relative plasma plume delay on the properties of complex oxide films grown by multi-laser, multi-target combinatorial pulsed laser deposition," Appl. Surf. Sci. **255**, 9066-9070 (2009).

13. C. Sanchez-Ake, R. Camacho, and L. Moreno, "Deposition and composition-control of Mn-doped ZnO thin films by combinatorial pulsed laser deposition using two delayed plasma plumes," J. Appl. Phys. **112**, 044904 (2012).

14. Y. Deng, J. D. Fowlkes, J. M. Fitz-Gerald, and P. D. Rack, "Combinatorial thin film synthesis of Gd-doped $Y_3Al_5O_{12}$ ultraviolet emitting materials," Appl. Phys. A-Mater. Sci. Process. **80**, 787-789 (2005).

15. A. A. Anderson, "Crystalline planar waveguide lasers fabricated by pulsed laser deposition," PhD thesis at *Optoelectronics Research Centre* (University of Southampton, Southampton, 1998).

16. L. M. B. Hickey, V. Apostolopoulos, R. W. Eason, J. S. Wilkinson, and A. A. Anderson, "Diffused Ti : sapphire channel-waveguide lasers," J. Opt. Soc. Am. B: Opt. Phys. **21**, 1452-1462 (2004).

17. P. D. Townsend, P. J. Chandler, R. A. Wood, L. Zhang, J. McCallum, and C. W. McHargue, "Chemically stabilized ion-implanted wave-guides in sapphire," Electron. Lett. **26**, 1193-1195 (1990).

18. N. Yu, and M. Nastasi, "Epitaxial-growth of Fe-doped sapphire thin-films from amorphous Al oxide layers deposited on sapphire substrates," Appl. Phys. Lett. **65**, 180-182 (1994).

19. H. Hirayama, G. H. Takaoka, H. Usui, and I. Yamada, "Low-temperature homo-epitaxy and hetero-epitaxy of sapphire films by reactive ionized cluster beam deposition," Nucl. Instrum. Methods Phys. Res. Sect. B-Beam Interact. Mater. Atoms **59**, 207-210 (1991).

20. C. Grivas, T. C. May-Smith, D. P. Shepherd, R. W. Eason, M. Pollnau, and M. Jelinek, "Broadband single-transverse-mode fluorescence sources based on ribs fabricated in pulsed laser deposited Ti:sapphire waveguides," Appl. Phys. A-Mater. Sci. Process. **79**, 1195-1198 (2004).

21. C. Grivas, D. P. Shepherd, T. C. May-Smith, R. W. Eason, and M. Pollnau, "Single-transverse-mode Ti:sapphire rib waveguide laser," Opt. Express **13**, 210-215 (2005).

22. A. A. Anderson, R. W. Eason, L. M. B. Hickey, M. Jelinek, C. Grivas, D. S. Gill, and N. A. Vainos, "Ti:sapphire planar waveguide laser grown by pulsed laser deposition," Opt. Lett. **22**, 1556-1558 (1997).

23. M. Pollnau, C. Grivas, L. Laversenne, J. S. Wilkinson, R. W. Eason, and D. P. Shepherd, "Ti:Sapphire waveguide lasers," Laser Phys. Lett. **4**, 560-571 (2007).

24. S. Higuchi, K. Ueda, F. Yahiro, Y. Nakata, H. Uetsuhara, T. Okada, and M. Maeda, "Fabrications of cerium-substituted YIG thin films for magnetic field sensor by pulsed-laser deposition," IEEE Trans. Magn. **37**, 2451-2453 (2001).

25. R. Lux, A. Heinrich, S. Leitenmeier, T. Korner, M. Herbort, and B. Stritzker, "Pulsed-laser deposition and growth studies of $Bi_3Fe_5O_{12}$ thin films," J. Appl. Phys. **100**, 113511 (2006).

26. H. Dotsch, N. Bahlmann, O. Zhuromskyy, M. Hammer, L. Wilkens, R. Gerhardt, P. Hertel, and A. F. Popkov, "Applications of magneto-optical waveguides in integrated optics: review," J. Opt. Soc. Am. B **22**, 240-253 (2005).

27. T. Boudiar, S. Capraro, T. Rouiller, M. F. Blanc-Mignon, B. Payet-Gervy, M. Le Berre, and J. J. Rousseau, *YIG thin films for magneto-optical and microwave applications* (Wiley-V C H Verlag Gmbh, Weinheim, 2004).

28. W. R. Eppler, and M. H. Kryder, "Garnets for short-wavelength magnetooptic recording," J. Phys. Chem. Solids **56**, 1479-1490 (1995).

29. S. A. Manuilov, R. Fors, S. I. Khartsev, and A. M. Grishin, "Submicron $Y_3Fe_5O_{12}$ Film Magnetostatic Wave Band Pass Filters," J. Appl. Phys. **105**, 033917 (2009).

30. P. Papakonstantinou, B. Teggart, and R. Atkinson, "Characterisation of pulsed laser deposited Bi doped Dy iron garnet thin films on GGG(111), GGG(110), YSZ(100) and Si(100)," J. Phys. IV **7**, 475-476 (1997).

31. H. Kidoh, A. Morimoto, and T. Shimizu, "Synthesis of ferromagnetic bisubstitued yttrium-iron-garnet films by laser ablation," Appl. Phys. Lett. **59**, 237-239 (1991).

32. S. Sang-Yeob, Q. Xiaoyuan, and B. J. H. Stadler, "Integrating yttrium iron garnet onto nongarnet substrates with faster deposition rates and high reliability," Appl. Phys. Lett. **87**, 121111 (2005).

33. S. H. Wee, H. S. Hong, Y. H. Kim, S. I. Yoo, and J. H. Kang, "Fabrication and characterization of Bi-substituted yttrium iron garnet films by pulsed laser deposition," Met. Mater.-Int. **9**, 507-511 (2003).

34. C. J. Yang, S. W. Kim, and Y. S. Kim, "Polycrystalline $Y_3Fe_5O_{12}$ garnet-films grown by a pulsed-laser ablation technique," IEEE Trans. Magn. **30**, 4527-4529 (1994).

35. P. C. Dorsey, S. E. Bushnell, R. G. Seed, and C. Vittoria, "Epitaxial yttrium-iron-garnet films grown by pulsed-laser deposition," J. Appl. Phys. **74**, 1242-1246 (1993).

36. N. Kumar, S. Prasad, D. S. Misra, N. Venkataramani, M. Bohra, and R. Krishnan, "The influence of substrate temperature and annealing on the properties of pulsed laser-deposited YIG films on fused quartz substrate," J. Magn. Magn. Mater. **320**, 2233-2236 (2008).

37. H. Nishihara, M. Haruna, and T. Suhara, *Optical Integrated Circuits* (McGraw-Hill Professional, 1989).

38. B. Lei, H. Juejun, J. Peng, K. Dong Hun, G. F. Dionne, L. C. Kimerling, and C. A. Ross, "On-chip optical isolation in monolithically integrated non-reciprocal optical resonators," Nat. Photonics **5**, 758-762 (2011).

39. S. Kahl, and A. M. Grishin, "Pulsed laser deposition of $Y_3Fe_5O_{12}$ and $Bi_3Fe_5O_{12}$ films on garnet substrates," J. Appl. Phys. **93**, 6945-6947 (2003).

40. A. M. Grishin, "Amplifying magneto-optical photonic crystal," Appl. Phys. Lett. **97**, 061116 (2010).

41. A. M. Grishin, and S. I. Khartsev, "Highly luminescent garnets for magneto-optical photonic crystals," Appl. Phys. Lett. **95**, 102503 (2009).

42. A. M. Grishin, S. I. Khartsev, and S. Bonetti, "Low field driven latching-type $Bi_3Fe_5O_{12}/Gd_3Ga_5O_{12}$ magneto-optical display," Appl. Phys. Lett. **88**, 242504 (2006).

43. S. M. Hamidi, M. M. Tehranchi, and M. Shasti, "Engineered one-dimensional magneto-photonic crystals for wavelength division multiplexing systems," J. Phys. D-Appl. Phys. **44**, 205107 (2011).

44. S. Kahl, and A. M. Grishin, "Enhanced Faraday rotation in all-garnet magneto-optical photonic crystal," Appl. Phys. Lett. **84**, 1438-1440 (2004).

45. S. Kahl, and A. M. Grishin, "Magneto-optical rotation of a one-dimensional all-garnet photonic crystal in transmission and reflection," Phys. Rev. B: Condens. Matter **71**, 205110 (2005).

46. S. I. Khartsev, and A. M. Grishin, "High performance $Bi_3Fe_5O_{12}/Sm_3Ga_5O_{12}$ (m) magneto-optical photonic crystals," J. Appl. Phys. **101**, 053906 (2007).

47. S. I. Khartsev, and A. M. Grishin, "Heteroepitaxial $Bi_3Fe_5O_{12}/La_3Ga_5O_{12}$ films for magneto-optical photonic crystals," Appl. Phys. Lett. **86**, 141108 (2005).

48. S. I. Khartsev, and A. M. Grishin, "High performance latching-type luminescent magneto-optical photonic crystals," Opt. Lett. **36**, 2806-2808 (2011).

49. Y. Krockenberger, J. S. Lee, D. Okuyama, H. Nakao, Y. Murakami, M. Kawasaki, and Y. Tokura, "Garnet superlattice as a transparent above-room-temperature polar magnet," Phys. Rev. B: Condens. Matter **83**, 214414 (2011).

50. Z. F. Yu, Z. Wang, and S. H. Fan, "One-way total reflection with one-dimensional magneto-optical photonic crystals," Appl. Phys. Lett. **90** (2007).

51. S. A. Manuilov, S. I. Khartsev, and A. M. Grishin, "Pulsed laser deposited $Y_3Fe_5O_{12}$ films: Nature of magnetic anisotropy I," J. Appl. Phys. **106**, 123917 (2009).

2. CHAPTER 2
BACKGROUND

2.1. INTRODUCTION

This chapter provides a general background for this thesis, placing PLD in context with other film deposition techniques and planar waveguide fabrication methods, whereas the basics of PLD and film growth are covered in the next chapter.

2.2. PULSED LASER DEPOSITION

Pulsed Laser Deposition (PLD) is a film growth technique, which can be used to deposit a wide range of materials [1]: metals, oxides, semiconductors, ceramics, glasses. Its basic setup requires just a vacuum chamber, pumps (typically a turbo-molecular as a high-vacuum pump and a rotatory vane as a roughing pump), a pulsed laser (usually emitting in the ultra-violet, such as an excimer laser or a frequency-tripled or -quadrupled Nd:YAG laser), a substrate-heating system (direct contact heaters or an indirect source such as a CO_2 laser) and a target of material to be ablated and deposited. This makes the PLD set-up a relatively simple and cheap deposition system, compared to more expensive and complex ones, such as those for liquid phase or molecular beam epitaxy. It is also a powerful technique, since it allows epitaxial growth of crystalline films of various materials at high deposition rates (several microns per hour). Finally PLD is a very versatile film growth method, as its setup (e.g. target carousel and substrate holder configuration/geometry) and deposition conditions (e.g. target material, substrate material and orientation, background gas and its pressure, substrate temperature, laser parameters, such as wavelength, energy, spot size, fluence, repetition rate) can be changed easily and over a very wide range of values. The main advantage of PLD is congruent evaporation due to energy delivery to the target via a pulsed laser. The main drawbacks of PLD are: the formation of droplets or particulates on the film surface, which can be overcome by techniques described in Section 3.2.4, the coating of the windows, which however is a disadvantage common to nearly all deposition techniques, leading to a reduction of laser energy inside the chamber, and the small deposit area, which can be overcome by resorting to different approaches (e.g. by using a tilting target to "paint" the substrate, scanning the laser spot on the target surface or simultaneously co-ablating multiple targets).

Figure 2.2.1 shows a schematic of a typical PLD setup. As the name suggests, the PLD technique uses a pulsed laser, typically emitting in the ultra-violet (UV) region of the electromagnetic spectrum, to ablate a target material for subsequent depositions. A plume consisting of electrons, ions, atoms, molecules and particles of the ablated material is formed following each laser pulse which expands away from the target surface in the vacuum chamber and is incident on the substrate, where the impinging plume material is deposited and a resultant film grows. The substrate can be heated at high temperatures (up to ~1500 K) in order to ensure crystallization of the film and a background gas can be injected inside the deposition chamber in order to control the plume dynamics and the film stoichiometry. More details of all these processes are given in Section 3.2.

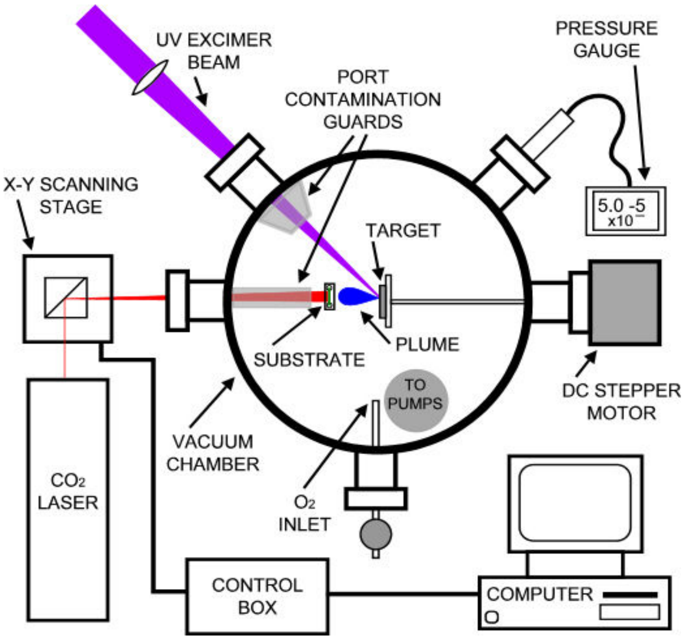

Figure 2.2.1. Typical PLD set-up [2].

2.3. ALTERNATIVE FILM GROWTH TECHNIQUES

2.3.1. THERMAL VAPOUR DEPOSITION (TVD)

Among all the film deposition methods, thermal evaporation or TVD is probably the simplest, as it consists of a vacuum chamber and a source of the material to be deposited, heated up to the melting point typically by a resistive or radiative heater or via an electron beam (e-beam), so that it evaporates and condenses again as a solid film on the substrate, placed above the source, either in a fixed position on-axis with the source or on a rotating holder, in order to improve film homogeneity and thickness uniformity [3]. Although very simple and cheap, its main drawbacks are:

- slow deposition rate, due to the high vacuum needed to minimise contamination and to the evaporation of material in all directions;
- chamber contamination, due to the same causes as above;
- film contamination from the crucible/heater, unless an electron gun is used;
- poor adhesion of the film to the substrate, although it can be improved by heating the substrate during the deposition;
- limited to simple materials (e.g. metals) with low melting points and high vapour pressures, although the e-beam deposition allows evaporation and deposition of materials with high melting points and also better control on growth rate;
- unable to grow films with complex stoichiometry (e.g. ternary or quaternary oxides such as garnets), due to different vapour pressures of constituents.

2.3.2. SPUTTERING

In a sputtering deposition system the target, i.e. the material to be deposited, is physically eroded by ionised gas species, normally Ar^+, accelerated by an electric field onto the target surface; reactive gases (e.g. O_2 and N_2) can also be introduced too into the vacuum chamber for better control of stoichiometric growth of oxides and nitrides; the sputtered material thus grows as a film on top of the substrate surface by physical and chemical deposition, if a reactive gas is used. Unlike TVD, where evaporation must be performed bottom-up, the sputtering deposition can be performed top-down, can grow films of various materials (DC sputtering is used for metals, whereas RF sputtering must be for insulators to avoid charging of the target), which is not restricted by their melting point, and produces films with better adhesion to the substrate. However, it shares some disadvantages with TVD: slow deposition rate, although this can be increased by using magnetic fields (magnetron sputtering), and chamber contamination, all due to a wide distribution of the sputtered material, which however allows deposition on large areas. Moreover, inert sputtering gases can be included in the films as unwanted impurities and in most cases the films grow amorphous or, if the substrate is heated, polycrystalline, thus requiring a subsequent annealing step to improve crystallinity. Sputtering has been reported for deposition of magneto-optic garnets [4-7] and a multi-target approach has been used for growth of Gd,Ga:YIG [8].

2.3.3. SOL-GEL

The sol-gel technique is a cheap and low-temperature film-growth method, based on the drying process of an organic precursor of the material to deposit. The precursor is made of a continuous suspension (gel), formed by partial drying of liquid particles or polymers suspended in a liquid (sol); the substrate can be coated by either dipping, spinning or spraying the sol-gel, which then needs to be dried. Although quick and inexpensive, sol-gel is limited to materials for which a solvent can be found and epitaxial growth is difficult to achieve; in fact, garnet films deposited by sol-gel are amorphous and require a subsequent thermal annealing step for crystallisation [9, 10]. The typical precursor for growth of magneto-optic garnets is an aqueous solution of citric acid ($C_6H_8O_7$) and nitrates of yttrium and iron.

2.3.4. SPRAY PYROLYSIS

This technique consists in spraying a metal salt solution onto a heated substrate: droplets of metal salts impinging on the hot substrate surface are thermally decomposed, resulting in formation of metal oxides, which then spread into a disk-shaped structure. The quality and properties of the deposited films are dependent on the deposition conditions, the most important of which is the substrate temperature, affecting crystallinity and surface morphology: if too low, the film tends to grow amorphous and cracked; if too high, the film will be rough and porous. Moreover the precursor solution affects the film morphology and properties, which can be changed also by use of additives in the solution [11]. Spray pyrolysis of YIG has been reported [12], but, like films deposited by sol-gel, film crystallisation requires a thermal annealing step.

2.3.5. LIQUID PHASE EPITAXY (LPE)

Liquid Phase Epitaxy (or LPE) consists of dipping a substrate into a hot saturated solution of precursors of the material to be deposited (e.g. a molten solution of PbO and B_2O_3, supersaturated with Y_2O_3 and Fe_2O_3 at ~1350 K, for LPE of magneto-optic iron garnets); subsequent substrate removal and slow cooling-down allows the formation of a solid film with uniform thickness and composition, a smooth surface and, above all, a high crystal quality, which is important for minimisation of FMR linewidth and thus microwave losses in magneto-optic garnets: the lowest value reported for pure YIG films grown by LPE is $\Delta H \approx 0.015$ mT [13, 14]. Growth rates can be very high: ~(6 – 60) μm/hour for LPE of YIG [15], thus making LPE the main rival deposition technique to PLD for growth of magneto-optic garnets [16, 17]; however PLD is cheaper and allows the deposition of thermodynamically unstable materials, such as Bi:YIG (at high doping levels) and BIG, which cannot be grown by LPE [18].

2.3.6. SOLID PHASE EPITAXY (SPE)

In case of SPE or epitaxial regrowth, an amorphous solid film is first deposited on top of a crystalline substrate and then re-crystallised *ex-situ* in a high-temperature oven with a subsequent thermal annealing process, which however does not allow a complete crystallisation, thus resulting in a polycrystalline film. Moreover only thin films (t << 1 μm) can be re-crystallised by thermal annealing, which hinders the production of high-quality thick films, necessary for making waveguide lasers.

2.3.7. IONISED CLUSTER BEAM (ICB) DEPOSITION

The ICB deposition consists of vaporisation into vacuum of a material source (metals or semiconductors) in a confinement crucible under conditions that promote formation of aggregates of atoms (clusters), which are subsequently ionized by electron impact and accelerated towards the substrate, normally heated at relatively low temperatures (between 400 K and 900 K) [19]. Deposition of hydrides, nitrides and oxides can be performed by injecting reactive gases into the vacuum chamber (reactive ICB deposition). Compound material films and multi-layer structure can be grown by using multiple material sources. Polycrystalline sapphire films have been grown at a deposition rate of ~120 nm/hour [20], very slow if compared to growth rates achievable by PLD (of the order of 1 μm/hour), which also allows epitaxial growth of single-crystal films.

2.3.8. CHEMICAL VAPOUR DEPOSITION (CVD)

CVD is a film growth technique that uses a mixture of precursor gases, i.e. containing components of the material to be deposited: these chemical precursors are passed across the substrate surface, where they react to form a layer of material and by-product gases, inside a vacuum chamber or tube [3]. In general, the deposition rate is slow, although modified CVD techniques, such as plasma-enhanced CVD (PECVD) and laser-assisted CVD (LACVD), allow higher growth rates. However, a major drawback is the use of often toxic precursors and also by-products can be harmful. Metalorganic CVD (MOCVD) of iron garnets has been reported [21], but it has not been developed in the recent past.

2.4. ALTERNATIVE WAVEGUIDE FABRICATION METHODS

Waveguides can be fabricated not only by physically depositing a layer of higher refractive index on top of a substrate with lower refractive index, but also by inducing a change in refractive index in a region localised close to the substrate surface, as described in the following sub-sections.

2.4.1. IN-DIFFUSION

Thermal in-diffusion consists of depositing a thin (up to a few hundreds of nanometres) layer of dopant (usually metals such as Ti, Ni, Cu and Nd) on the surface of the substrate and then diffusing it in, by placing the sample in a high temperature oven ($T \geq 1300$ K) for a long time (several hours or days), depending on the desired dopant profile depth. This allows the increase of refractive index to form a waveguide (channel waveguides can be made by appropriate prior photolithographic steps), e.g. Ti:$LiNbO_3$ waveguides [22], or even waveguide lasers, e.g. Ti:Al_2O_3 [23], although, as stated in Section 1.2.1, the high residual concentration of Ti near the surface reduces fluorescence because of re-absorption and causes high losses, thus lowering the device performance. The range of materials suitable for in-diffusion in a particular material and the long time necessary to create a µm-thick waveguide limit the applications and more general applicability of this waveguide fabrication technique.

2.4.2. ION EXCHANGE

This technique is similar to the thermal in-diffusion and has the same limitations: it consists of placing the substrate in a bath of hot molten salt, so that its alkali ions are exchanged with the ions in the glass or crystal substrate, thus causing an increase of refractive index in a region near the surface and hence the formation of waveguide; channel waveguides can be made by depositing a mask on the substrate prior to the ion exchange process and removing it afterwards. The ion exchange rate can be controlled by either adjusting the temperature or with an external electric field applied across the substrate. It is a common method for fabrication of waveguides in glass substrates, by replacing the Na^+ ions with K^+, Ag^+ or Tl^+, and also in $LiNbO_3$, by exchanging the Li^+ ions with H^+ in benzoic acid (C_6H_5COOH) [3].

2.4.3. ION IMPLANTATION

In this method high-energy (up to a few MeV) light ions, such as H^+ (protons) or He^+ are implanted in a region near the surface of the substrate, in order to induce a change in refractive index by a variation of structure, density or stoichiometry. In any case the ion implantation causes a lattice disorder, which induces changes in other properties as well (e.g. fluorescence, optical absorption, transmission losses) and can even result in amorphisation of part of the substrate, whose crystallinity can be recovered by thermal annealing, if necessary. The depth and intensity of crystal damage can be adjusted by tuning the energy of the accelerated ions, as they first lose energy by electronic interaction near the surface and then by direct interaction with the ions in the crystal lattice, causing their displacement; this means that the very first layer below the substrate surface is normally unaffected by the ion implantation. The change in refractive index can be positive or negative, depending on the substrate material and the damage mechanism. Planar waveguides can be made by flooding the whole substrate surface; otherwise channel waveguides can be created by masking the substrate where ion implantation is unwanted. Due to the high energy required for the ions, a large and expensive accelerator is needed. Planar waveguides have been fabricated by ion beam implantation of group IV elements into un-doped sapphire substrates [24], but the degradation of the bombarded region induces additional undesirable losses.

2.5. CONCLUSIONS

Film growth by PLD has been introduced and compared with other deposition techniques and planar waveguide fabrication methods, as summarised in Tables 2.5.1 and 2.5.2. It is clear that PLD has several advantages over the other techniques discussed in this chapter, namely: simplicity and ease of use; flexibility, allowing material and device engineering; lack of toxic precursors; capability of growing high-quality crystalline films at high growth rates (up to ~10 μm/hour), thus avoiding subsequent thermal annealing steps, which however could be performed *in-situ*, if necessary. In fact, PLD has already proven its potential in growing high-quality crystalline Ti:sapphire and garnet waveguide lasers [25]. Its main competitor is LPE, which – although more expensive and complex – allows the growth of higher-quality single-crystal epitaxial garnet films at even higher growth rates (up to ~60 μm/hour) and, in particular, magneto-optic YIG films with intrinsic FMR linewidth matching the value of bulk YIG spheres ($\Delta H \approx 0.015$ mT) [26]. Nevertheless, FMR linewidth in epitaxial YIG films grown on GGG by PLD has been minimised to $\Delta H \approx 0.09$ mT [26] and, unlike LPE, PLD can grow thermodynamically unstable materials, such as Bi:YIG (at high doping levels) and BIG, as already proven in [18].

TECHNIQUE	**Crystallisation**	**Typical growth rate [μm/hr]**	**Multi-element rate control**	**Vacuum requirement**
PLD	Yes	(1 – 10)	Good	HV
TVD	No	~0.1	Bad	UHV
Sputtering	No	~0.1	Moderate	HV
Sol-gel	No	N.A.	Poor	No
Spray pyrolysis	No	N.A.	Poor	No
LPE	Yes	>10	Good	No
SPE	Yes, poly	–	–	No
ICB	Yes, poly	~0.1	Good	HV
CVD	Yes	~0.1	Moderate	HV

Table 2.5.1. Summary of film growth techniques.

METHOD	**Complexity**	**Material range applicable to**
In-diffusion	Simple	Wide
Ion exchange	Moderate	Moderate
Ion implantation	Difficult	Wide

Table 2.5.2. Summary of waveguide fabrication methods.

2.6. REFERENCES

1. R. W. Eason, ed.: *Pulsed Laser Deposition of Thin Films – Applications-led Growth of Functional Materials* (Wiley Interscience, 2007).

2. R. W. Eason, T. C. May-Smith, C. Grivas, M. S. B. Darby, D. P. Shepherd, and R. Gazia, "Current state-of-the-art of pulsed laser deposition of optical waveguide structures: Existing capabilities and future trends," Appl. Surf. Sci. **255**, 5199-5205 (2009).

3. H. Nishihara, M. Haruna, and T. Suhara, *Optical Integrated Circuits* (McGraw-Hill Professional, 1989).

4. T. Boudiar, B. Payet-Gervy, M. F. Blanc-Mignon, J. Rousseau, M. Le Berre, and H. Joisten, "Magneto-optical properties of yttrium iron garnet (YIG) thin films elaborated by radio frequency sputtering," J. Magn. Magn. Mater. **284**, 77-85 (2004).

5. S. Yamamoto, H. Kuniki, H. Kurisu, M. Matsuura, and P. Jang, "Post-annealing effect of YIG ferrite thin-films epitaxially grown by reactive sputtering," Phys. Status Solidi A - Appl. Res. **201**, 1810-1814 (2004).

6. T. Goto, Y. Eto, K. Kobayashi, Y. Haga, M. Inoue, and C. A. Ross, "Vacuum annealed cerium-substituted yttrium iron garnet films on non-garnet substrates for integrated optical circuits," J. Appl. Phys. **113**, 17A939 (2013).

7. T. Boudiar, S. Capraro, T. Rouiller, M. F. Blanc-Mignon, B. Payet-Gervy, M. Le Berre, and J. J. Rousseau, *YIG thin films for magneto-optical and microwave applications* (Wiley-V C H Verlag Gmbh, Weinheim, 2004).

8. J. J. Cuomo, Sadagopa.V, Rosenber.R, Chaudhar.P, and J. Deluca, "Growth of uniaxial magnetic garnet films by RF sputtering," Appl. Phys. Lett. **21**, 581-584 (1972).

9. R. D. Sanchez, C. A. Ramos, J. Rivas, P. Vaqueiro, and M. A. Lopez-Quintela, "Ferromagnetic resonance and magnetic properties of single-domain particles of $Y_3Fe_5O_{12}$ prepared by sol-gel method," Phys. B **354**, 104-107 (2004).

10. K. Matsumoto, K. Yamaguchi, A. Ueno, and T. Fujii, "Preparation of Bi-substituted YIG garnets by sol-gel synthesis and their magnetic properties," IEEE Transl. J. Magn. Jpn. **6**, 15-22 (1991).

11. D. Perednis, and L. J. Gauckler, "Thin film deposition using spray pyrolysis," J. Electroceram. **14**, 103-111 (2005).

12. R. Todorovska, S. Groudeva-Zotova, D. Todorovsky, G. Tzvetkov, and P. Stefanov, "Highly crystalline $Y_3Fe_5O_{12}$ thin films by citric spray pyrolysis," J. Mater. Synth. Process. **10**, 283-288 (2002).

13. H. X. Wei, and W. S. Wang, "The growth of LPE YIG-films with narrow FMR linewidth," IEEE Trans. Magn. **20**, 1222-1223 (1984).

14. M. Shone, "The technology of YIG film growth," Circ. Syst. Signal Pr. **4**, 89-103 (1985).

15. D. M. Gualtieri, "Liquid-phase epitaxy of yttrium-aluminum-garnet - Reduction of growth-rate by germanium oxide," Appl. Phys. Lett. **59**, 650-652 (1991).

16. T. Aichele, A. Lorenz, R. Hergt, and P. Gornert, "Garnet layers prepared by liquid phase epitaxy for microwave and magneto-optical applications - a review," Cryst. Res. Technol. **38**, 575-587 (2003).

17. J. H. Park, J. K. Cho, K. Nishimura, H. Uchida, and M. Inoue, "Growth of epitaxial garnet film by LPE for application to integrated magneto-optic light switch arrays," Phys. Status Solidi A - Appl. Res. **201**, 1976-1979 (2004).

18. B. Vertruyen, R. Cloots, J. S. Abell, T. J. Jackson, R. C. da Silva, E. Popova, and N. Keller, "Curie temperature, exchange integrals, and magneto-optical properties in off-stoichiometric bismuth iron garnet epitaxial films," Phys. Rev. B: Condens. Matter **78**, 094429 (2008).

19. T. Takagi, "Ionized Cluster Beam (ICB) deposition and processes," Pure Appl. Chem. **60**, 781-794 (1988).

20. H. Hirayama, G. H. Takaoka, H. Usui, and I. Yamada, "Low-temperature homo-epitaxy and hetero-epitaxy of sapphire films by reactive ionized cluster beam deposition," Nucl. Instrum. Methods Phys. Res. Sect. B-Beam Interact. Mater. Atoms **59**, 207-210 (1991).

21. M. Okada, S. Katayama, and K. Tominaga, "Preparation and magneto-optic properties of Bi-substituted yttrium iron garnet thin films by metalorganic chemical vapor deposition," J. Appl. Phys. **69**, 3566-3570 (1991).

22. C. Q. Xu, H. Okayama, and M. Kawahara, "Large differences in Ti thermal diffusion caused domain inversion between undoped and MgO-doped $LiNbO_3$," Appl. Phys. Lett. **64**, 2504-2506 (1994).

23. L. M. B. Hickey, V. Apostolopoulos, R. W. Eason, J. S. Wilkinson, and A. A. Anderson, "Diffused Ti : sapphire channel-waveguide lasers," J. Opt. Soc. Am. B: Opt. Phys. **21**, 1452-1462 (2004).

24. P. D. Townsend, P. J. Chandler, R. A. Wood, L. Zhang, J. McCallum, and C. W. McHargue, "Chemically stabilized ion-implanted wave-guides in sapphire," Electron. Lett. **26**, 1193-1195 (1990).

24. N. A. Vainos, C. Grivas, C. Fotakis, R. W. Eason, A. A. Anderson, D. S. Gill, D. P. Shepherd, M. Jelinek, J. Lancok, and J. Sonsky, "Planar laser waveguides of Ti:sapphire, Nd:GGG and Nd:YAG grown by pulsed laser deposition," Appl. Surf. Sci. **127**, 514-519 (1998).

25. H. L. Glass, and M. T. Elliott, "Attainment of the intrinsic FMR linewidth in yttrium iron garnet films grown by liquid phase epitaxy," J. Cryst. Growth **34**, 285-288 (1976).

26. S. A. Manuilov, R. Fors, S. I. Khartsev, and A. M. Grishin, "Submicron $Y_3Fe_5O_{12}$ Film Magnetostatic Wave Band Pass Filters," J. Appl. Phys. **105**, 033917 (2009).

3. CHAPTER 3
THEORY

3.1. INTRODUCTION

The basics of PLD and the fundamentals of waveguide physics are provided in the first part of this chapter, whereas the second half provides some information on the materials of interest for this thesis, namely Ti:sapphire and magneto-optic garnets; some basic concepts of magnetism are also introduced in the second part.

3.2. PLD THEORY

The generic experimental set-up and the working principle of PLD have already been illustrated in Section 2.2. The physics of PLD is quite complicated and has not been fully modelled, due to the number of parameters and factors involved in the whole process; in this section a qualitative explanation of PLD physical processes is provided, in order to allow the reader to understand the experimental chapters; a comprehensive study of PLD can be found in [1, 2]. In order to simplify the study, the PLD process is divided mainly into three phases, to make it easier to understand the whole process:

1. laser-target interaction (target ablation phase), described in the next sub-section, with details on laser-induced target damage and consequent formation of particulates in sub-section 3.2.4; the typical time-scale ranges from ~100 fs to ~100 ns, depending on target material and laser pulse duration and wavelength;
2. plume formation and propagation, discussed in sub-section 3.2.2; the time-scale for plume propagation is in the range (1μs – 1 ms), depending on deposition conditions;
3. film growth, whose details are provided in sub-section 3.2.3; nucleation time-scale can be of the order of 1 ms, slightly shorter than the time between pulses (>10 ms).

3.2.1. LASER ABLATION

In order to grow a film with the same composition as the target, stoichiometric transfer must be ensured from the target to the ablation plume. If a high-power CW laser (e.g. a CO_2 laser) is used, the power delivered to the target would be transferred to the bulk as heat, thus causing melting and evaporation of the material; however, this process, in a similar vein to thermal evaporation or TVD (see Section 2.3.1), does not allow stoichiometric transfer, due to the different melting points and vapour pressures of the constituents of the target material, and hence this incongruent evaporation would produce films with different composition from the target [3]. To avoid this and achieve congruent evaporation, pulsed UV laser ablation has shown itself to be an excellent alternative technique. However, the situation is different and more complicated when using a pulsed laser: the interaction process of each laser pulse with the target can be sketched as outlined in Figure 3.2.1, as a first approximation [4].

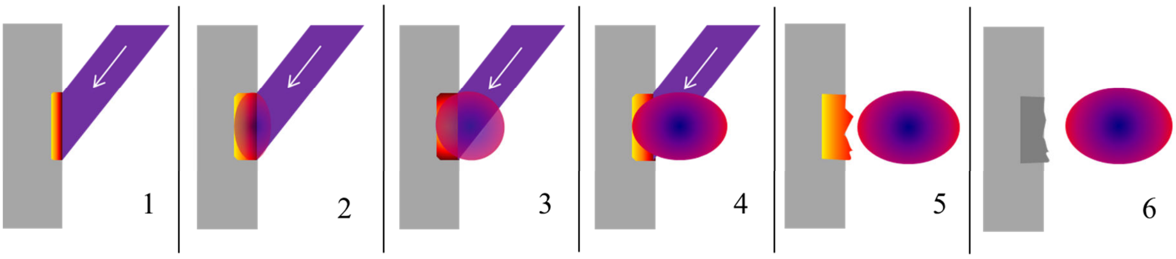

Figure 3.2.1. Stages of target ablation. Description in the text.

1. The energy of the laser pulse is absorbed by the target and the material starts melting;
2. while the melt front proceeds deeper into the target, some material starts evaporating; the ejected material is still transparent to the laser pulse, which continues heating the target, whose temperature keeps rising;
3. while the target temperature reaches a maximum value, more material evaporates, leading to the formation of a plume, which becomes denser and thus more opaque, absorbing enough energy from the laser pulse;
4. the plume expands and absorbs more energy from the laser pulse (for duration $\tau >$ 10 ps), thus increasing its temperature, reducing target surface heating and hence limiting further material ejection;
5. the laser pulse ends, thus allowing cooling down of the irradiated target area, while the plume leaves the target;
6. the target surface cools down and re-solidifies in a damaged state, featuring ripples, cones, splashes and particulates, while the plume travels towards the substrate.

The whole process is repeated for the next incident laser pulse.

Although the aforementioned process may resemble a thermal process, there are actually several mechanisms involved, which happen in non-thermodynamic equilibrium [1, 5].

A. **Thermal sputtering:** this mechanism consists of melting and vaporisation of the target area hit by the laser pulse, leading to formation of a plume of ejected material and resulting in production of wave-like structures and re-sputtered droplets on the target surface. This mechanism prevails only if the heat diffusion length (l_{td}) is shorter than the absorption length (l_{α}) of the laser pulse, $l_{\mathrm{td}} < l_{\alpha}$, meaning that the heat produced by the laser pulse in the target is not conducted away into the bulk from the ablation spot more quickly than it is absorbed. Absorption depth and the thermal diffusion depth are defined as in Equations (3.2.1) and (3.2.2) respectively [5]:

$$l_{\alpha} = \frac{1}{\alpha} \tag{3.2.1}$$

$$l_{\mathrm{td}} = 2\sqrt{\kappa_{\mathrm{td}}\tau} \tag{3.2.2}$$

where τ is the laser pulse duration, whereas α and κ_{td} are respectively the absorption coefficient (inverse of the absorption depth) and the thermal diffusivity of the target. This explains why a short ablation wavelength laser source and short laser pulses are preferred: the former means higher optical absorption α within the target and hence shorter absorption depth l_{α}, whereas the latter reduces the thermal diffusion depth l_{td}; for this reason pulsed UV lasers are commonly used for PLD, in particular excimers (such as KrF and ArF, emitting at $\lambda = 248$ nm and 193 nm respectively), with $\tau \approx 20$ ns, and frequency-tripled or -quadrupled Nd:YAG lasers, emitting at longer wavelengths ($\lambda = 355$ nm and 266 nm respectively), but with shorter pulse duration ($\tau \approx 5$ ns) than excimers.

If the condition $l_{\mathrm{td}} < l_{\alpha}$ is satisfied, then the depth of ablated material is given by [5, 6]:

$$\delta = \frac{1}{\alpha} ln \left| \frac{F_L}{F_{L,th}} \right| \tag{3.2.3}$$

where F_{L} and $F_{\mathrm{L,th}}$ are respectively the laser fluence on the target and the target ablation threshold.

B. **Electronic sputtering:** this mechanism, which actually encompasses a broad range of phenomena, prevails at the very beginning (<10 ps) of the laser ablation process and includes multi-photon absorption, which is predominant over thermal sputtering in targets ablated with ultra-short laser pulses ($\tau < 10$ ps), e.g. with fs-lasers [2]. The electric field of the laser pulse accelerates the electrons in the penetrated volume of the target, causing ionisation of the material; similarly multi-photon absorption generates free electrons, which are accelerated by interaction with bound electrons, thus causing further generation of free charge carriers and further ionisation ("avalanche ionisation") of the target material, which results in material vaporisation by "Coulomb explosion", i.e. violent ejection of highly energetic ions due to their reciprocal Coulomb repulsion induced by the electrons escaping from the target (thermo-ionic emission), if the laser fluence is over a certain threshold. Over a longer time scale (>>10 ps), the electrons will transfer their energy to the lattice (i.e. to the ions) by means of electron heat conduction and electron-phonon and electron-ion collisions, reaching thermodynamic equilibrium, thus leading to thermal sputtering [2], although other factors (e.g. laser hot spots and impurities in the target) must be taken into account to explain high ionisation fractions and temperatures, which otherwise cannot be fully explained by thermal sputtering only.

C. **Collisional sputtering:** some of the ejected species can fall back on the target surface, causing erosion of an area larger than the ablated spot.

D. **Hydrodynamic sputtering:** this is observed especially in metallic targets, where droplets of material can form on the target surface during transient melting; these droplets can be ejected and deposited on the film or re-sputtered on the target.

E. **Exfoliational sputtering:** chunks or flakes of material are detached from the target surface due to repeated thermal shock, leading to formation of particulates on the film surface. This is particularly evident in brittle materials such as garnets [5] and when ablating a freshly re-conditioned target surface: visible "spots", i.e. chunks of material, were noticed on the surface of a blank substrate in the first seconds of ablation of a non-pre-ablated target; this problem can be alleviated with target pre-ablation.

3.2.2. PLUME FORMATION AND PROPAGATION

As aforementioned, the plume starts forming before the end of the laser pulse and it starts expanding isothermally, meaning that its temperature remains constant. Also its ionisation ratio (i.e. the ratio of the number of ions in the gas over the number of neutral atoms) increases, as dictated by the following equation [1]:

$$\frac{N_i}{N_n} = 2.4 \times 10^{15} \frac{T^{\frac{3}{2}}}{N_i} e^{-\frac{U_i}{k_B T}} \qquad (3.2.4)$$

where N_i and N_n are the density of ions and neutral atoms per cm^3 in a gas in local thermodynamic equilibrium, to which the plume can be approximated, T the temperature of the plasma in Kelvin, k_B is Boltzmann's constant ($\sim 8.62 \times 10^{-5}$ ev/K) and U_i the first ionization potential in eV. The increase in ionisation ratio is due to the increase of the plasma temperature induced by the absorption of laser energy: at relatively low temperatures ($T < 3{,}000$ K), the ionisation ratio is low (~0.0001 with $U_i = 7$ eV), but it increases rapidly to ~0.8 at $T = 10{,}000$ K due to the exponential factor; however, typical values of U_i are of the order of 10 eV, requiring plasma temperatures of ~6,000 K for a significant ionisation (at least ~0.1), a value that cannot be achieved with typical laser fluences, although hot spots may seed ionisation of the whole forming plume [1, 5]. Once the plume is sufficiently ionised, it will reflect laser light and thus prevent heating.

Once the laser pulse has ended, the plume leaves the target (as there is no more material ejection from it) and expands in the vacuum chamber with a higher expansion rate in the direction with higher density and pressure gradient (the plume expands quickly away from the target because the ablation depth is much smaller than the laser spot size); at the same time the thermal energy is converted into kinetic energy, but the temperature does not drop indefinitely because of energy from recombination [4].

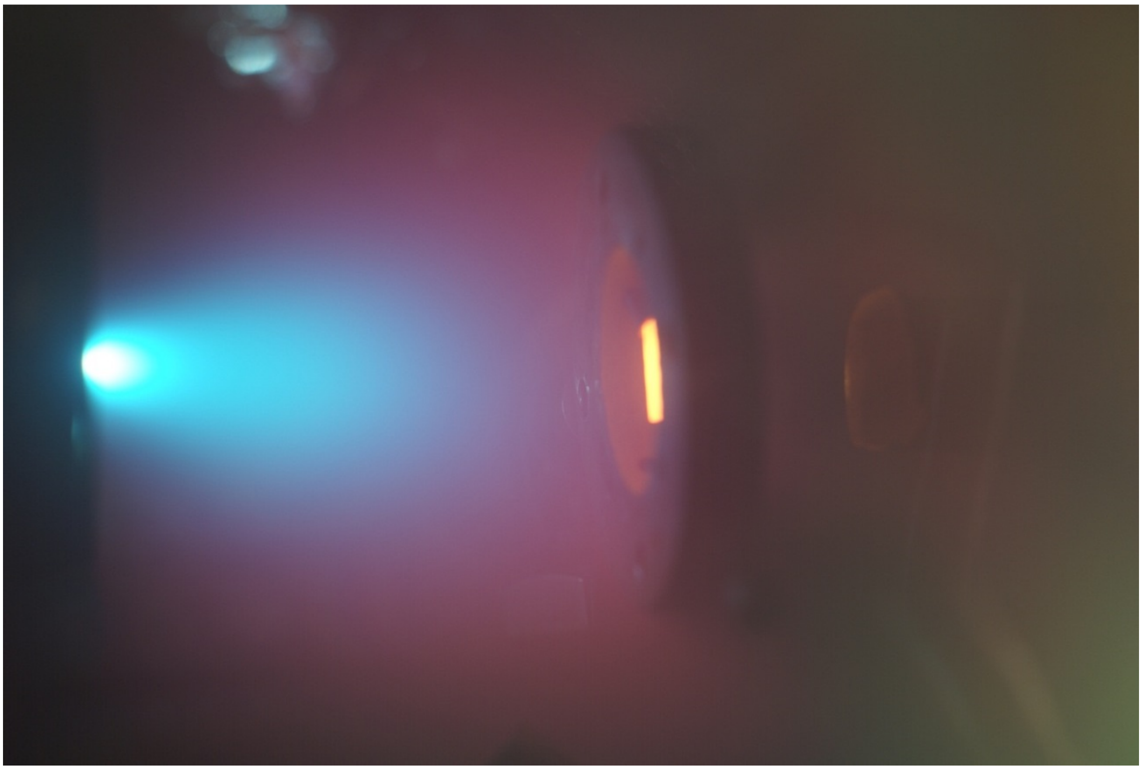

Figure 3.2.2. Plume formed by ablating a YIG target with a KrF laser at a fluence of $F_{KrF} \approx 3$ J/cm^2 in O_2.

Above the ablation threshold significant material removal and a luminous plasma plume are observed (see Figure 3.2.2, depicting a plume formed by ablating a YIG target with 248 nm radiation at a fluence $F \approx 3$ J/cm^2).

The fluence of the laser is critical to both the formation of the plume and also how it continues to develop: an increase in fluence causes a higher plasma temperature and thus a higher ionisation ratio. Also the laser spot size is critical in determining the shape and size of the plume: a large spot size will result in a plume direction that is perpendicular to the target, whereas a smaller spot size will produce a broader and more divergent plume (see Figure 3.2.3) – this is the so-called "flip over" effect, similar to diffraction (whereby a small laser beam diverges faster than a larger one) [4, 5]. Considering that excimer lasers are typically used for target ablation, their rectangular beam shape will produce plumes with elliptical cross-section, if not corrected with lenses: the plume expansion will be faster along the smaller axis than on the longer axis.

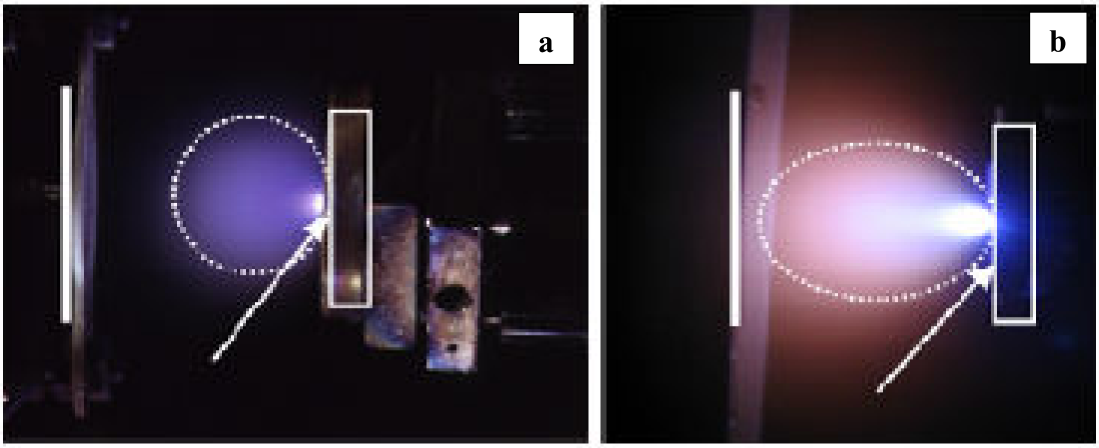

Figure 3.2.3. Plume geometry as a function of laser spot size: **(a)** tight focusing produces a spherical plume, whereas **(b)** a larger laser spot size produces a more confined and directive plume. Picture from reference [7].

The background gas and its pressure will affect plume composition and dynamics too, due to scattering, attenuation and thermalization of the plume, consequently affecting film growth. The vacuum chamber can be filled with inert gases, such as argon (Ar) and other nobles gases, or reactive gases, e.g. oxygen (O_2) and nitrogen (N_2), to control plume and film stoichiometry, in order to grow oxides and nitrides; for instance, in order to avoid oxygen deficiency in garnet films, these are typically grown in O_2. Increasing the background gas pressure will result in an increased number of collisions of the species in the plume with the background gas, thus resulting in [1]:

- an increase of plume fluorescence;
- a sharper plume boundary, due to the transfer of energy to the gas as a shock wave;

- a slower plume (compared to propagation in vacuum), resulting in…
- greater spatial confinement of the plume.

The plume directivity can therefore be tuned to some extent not only by changing the laser spot size, but also the background gas pressure. Depositions in vacuum (we normally used a base vacuum pressure of the order of $\sim 10^{-2}$ Pa) will be characterised by a slow growth rate (typically less than 1 μm/hour), due to the plume divergence, as it is not confined by background gas, which can cause severe coating of laser windows; injecting a gas into the chamber and increasing the pressure will produce a more confined plume and increase the deposition rate up to a maximum point beyond which it will slow down again, due to increased scattering (i.e. collisions of species in the plume with the background gas, diffusing the former away from their trajectory towards the substrate) or desorption from the substrate (which is discussed in more detail in the next sub-section). The target-substrate distance (d) must be chosen according to the gas pressure and should be lower than the mean free path[1], Λ, which is ~10 cm for atoms/molecules ~1 Å in diameter at a vacuum pressure of $\sim 10^{-1}$ Pa and at room temperature (~300 K); increasing the gas pressure will result in a decrease of the kinetic energy of the species arriving on the substrate, if kept at the same distance from the target; so, if growth dynamics (more in the next sub-section) must be preserved, the substrate needs to be moved closer to the target according to the rule of thumb $P_{\mathrm{GAS}} \cdot d^3 = \mathrm{const.}$ [8].

The angular distribution of the plume can be best described by a relationship of $\cos^m(\Theta)$, where m is an integer ranging from 2 to 20, depending on deposition conditions, and typically assuming a value between 10 and 12 [1, 4, 5]. When ablating multi-component targets (e.g. YIG), different elements may have different angular distributions, with the lighter ones (e.g. Fe compared to Y in YIG) more subject to scattering and thus preferentially shifted towards the edges of the plume, which likely explains the non-stoichiometric transfer from the target to the film observed in all single-PLD experiments using a stoichiometric YIG target.

The plume typically contains ions, neutral atoms, electrons, molecules, particulates and clusters. Formation of particulates and clusters has already been mentioned above and more details are given in sub-section 3.2.4. Electrons attain the highest velocities, but do not escape the plasma due to the interaction with the ions in the plume, which travel near

---

[1] $\Lambda = \frac{k_B T}{\sqrt{2}\pi D P_{GAS}}$, where D is the atom/molecule diameter.

the front of the plume, especially the lightest, thus arriving on the substrate before neutrals and particulates, which can then be filtered by exploiting this delay and thus avoid their deposition on the film (more details in the last sub-section of this paragraph).

3.2.3. FILM GROWTH

The deposition of material on the substrate and the consequent film growth is a complex process, depending on several deposition conditions such as:

- substrate crystallinity and orientation, important for epitaxial growth;
- substrate temperature, critical for crystallisation of the film, but may cause desorption of some species, if too high;
- substrate surface preparation, affecting crystalline growth and film surface roughness;
- laser fluence, affecting plume and film stoichiometry, but also deposition rate, stress and particulate size and density;
- background gas pressure, affecting growth rate and film composition;
- target-substrate distance, affecting deposition rate.

In order to simplify the treatment of this topic, we separate the effects of crystal defects, lattice mismatch and thermal expansion coefficient (TEC) mismatch on film growth, which arise in the case of hetero-epitaxial growth (growth of a material on a different substrate), and we first give an overview of nucleation and film growth for the case of homo-epitaxial growth (film and substrate are the same material) on atomically flat substrates.

3.2.3.1. GROWTH MECHANISM

Three independent phases can be identified during the film growth process [9]:

I. nucleation, i.e. condensation of atoms in the vapour on the substrate, thus forming the so-called “adatoms” (from the contraction of “adsorbed atoms”);
II. coalescence, i.e. formation of a continuous network of material;
III. growth of the final continuous film.

A schematic of various processes involved in nucleation is depicted in Figure 3.2.4: film atoms arrive on the substrate and can diffuse over bare substrate areas or pre-existing clusters, form mobile or stationary clusters with mobile or stationary film atoms, attach to pre-existing clusters, re-evaporate from a cluster or the substrate surface or detach from a cluster and remain on the substrate surface [1].

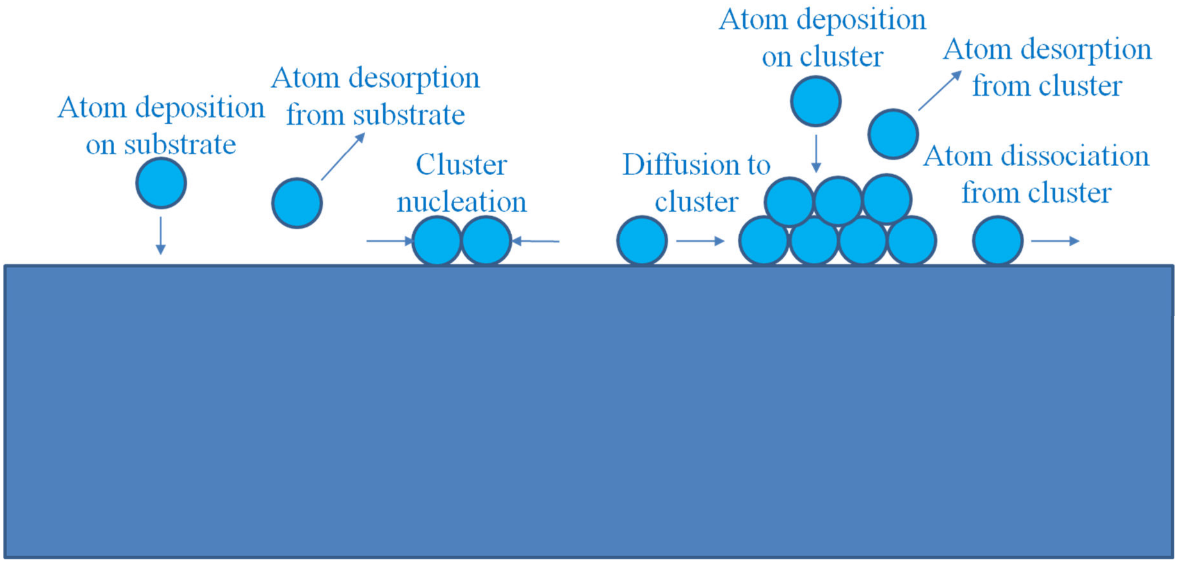

Figure 3.2.4. Summary of atomic processes involved in nucleation.

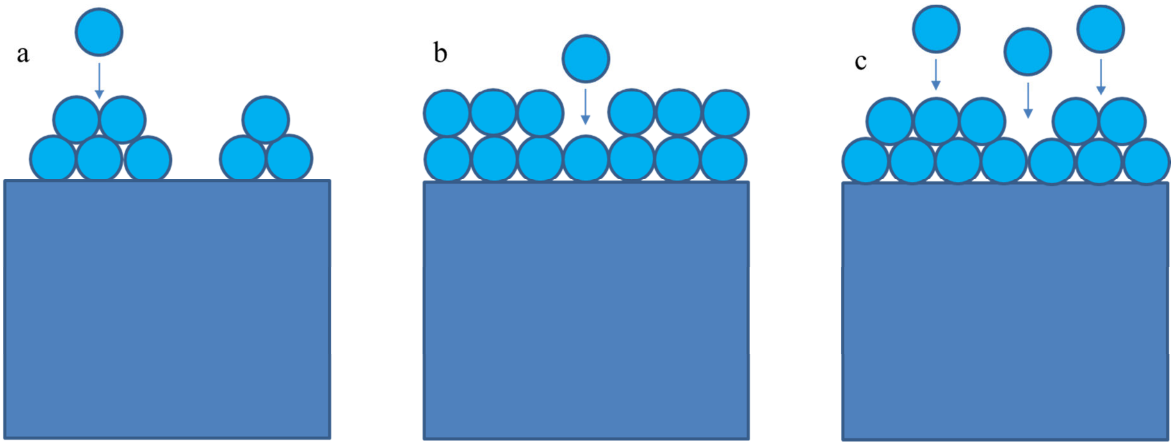

Figure 3.2.5. Summary of growth modes: **(a)** Volmer-Weber (3D) mode or island formation; **(b)** Frank-van der Merwe (2D) mode or layer by layer; **(c)** Stranski-Krastanov (2D + 3D) mode or layer + island.

Considering the case of vapour deposition at thermodynamic equilibrium, three different growth mechanisms or growth modes can take place, as depicted schematically in Figure 3.2.5, depending on the balance of the free energies of film surface (γ_F), substrate surface (γ_S) and the interface between film and substrate (γ^*) [1, 2, 4, 5, 9]:

a. *island* or Volmer–Weber mode or 3D growth mode, for $\gamma_S < \gamma_F + \gamma^*$, which means that the film components are more bound to each other than to the substrate: in this case the film atoms tends to aggregate in clusters and form separate 3D islands on the substrate surface;

b. *layer by layer* or Frank–van der Merwe mode 2D growth mode, for $\gamma_S > \gamma_F + \gamma^*$, which means that the film components are more bound to the substrate than to each other: in this case the film components nucleate forming 2D clusters, i.e. just one monolayer thick, until they coalesce forming a complete monolayer on the substrate surface, before starting depositing on top of the new monolayer;

c. *layer + island* or Stranski–Krastanov or 2D + 3D growth mode: in this case the film starts growing in monolayers (*layer by layer* or 2D) and then in islands (3D), due to an increase in interface energy with film thickness and strain/stress in the film (more in the next sub-sections); this is especially true for hetero-epitaxial growth.

The growth mode is controlled also by super-saturation: the higher its value, the more the growth tends to shift from *island* (3D) to *layer by layer* (2D) [9].

This thermodynamic approach is not entirely valid in vapour deposition techniques that do not take place in thermodynamic equilibrium, such as PLD, and kinetic effects must be considered. Due to limited surface diffusion, the deposited material tends to rearrange itself to minimise the surface energy [2]. Considering homo-epitaxial growth, a 2D growth mode is expected. The behaviour of the deposited species depends on several kinetic parameters, the most important of which is probably the surface diffusion coefficient [2]:

$$D_{\mathrm{S}} = f j^2 e^{-\frac{E_{\mathrm{a}}}{k_{\mathrm{B}}T}} \qquad (3.2.5)$$

where: f is the attempt frequency, i.e. the vibrational frequency of the adatom, j the characteristic jump distance, E_a the activation energy for diffusion and T the temperature in Kelvin. This highlights the importance of deposition temperature in controlling the diffusivity of adatoms; the surface diffusion length is defined as the average distance an atom can travel on a flat surface before being trapped [2]:

$$l_D = \sqrt{D_S \tau_r} \qquad (3.2.6)$$

where τ_r is the residence time before re-evaporation.

There are two possible 2D growth modes [2]:

1. diffusion of an atom on a terrace or intra-layer mass transport, occurring when the diffusion length is longer than the terrace width (l_T), i.e. $l_D > l_T$: nucleation on terraces is prevented, as the adatoms are mobile enough to reach the edges of the

substrate steps, acting as sinks for the deposited atoms; this is the so-called “step flow growth”, schematically pictured in Figure 3.2.6.

2. diffusion of an atom to a lower terrace or inter-layer mass transport, taking place when $l_D < l_T$: in this case the adatoms are not mobile enough to reach the edges of the substrate steps and nucleate on the terrace until a saturation density is reached, after which the atoms aggregate around existing nuclei and form islands. If there is a steady inter-layer mass transport, a *layer by layer* growth mode will take place, as the atoms on top of a growing island reach the island edge and diffuse to the lower layer; otherwise, if there is no inter-layer mass transport or it is limited, nucleation will continue on top of islands before they have coalesced (“second-layer nucleation”). In reality the growth mode in conditions far from equilibrium will be intermediate between these two modes.

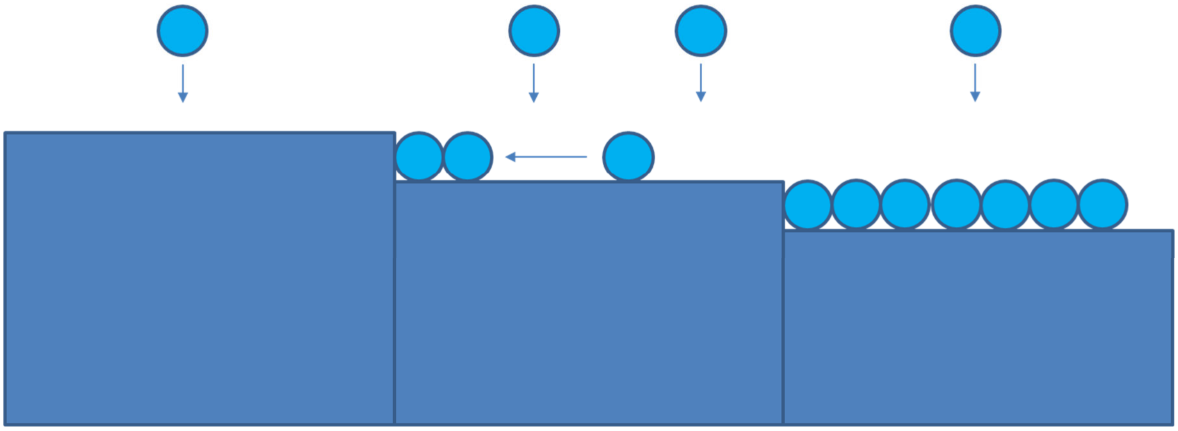

Figure 3.2.6. Schematic of 2D step flow growth mode.

3.2.3.2. CRYSTAL DEFECTS

Crystallographic defects may arise during film growth, due to defects on the substrate, lattice mismatch (more in the next sub-section) between film and substrate or contaminants in the vacuum chamber, in the target or on the substrate surface. They can be classified as:

- point defects (summarised in Figure 3.2.7), which occur only at or around a single lattice point:
    - vacancies, i.e. vacant lattice sites in a crystal;
    - interstitial defects, i.e. an atom (which can be an impurity) occupying a site in the crystal structure where there should be no atom;
    - Frenkel defects, i.e. pairs of vacancies and interstitials, due to ions moving to interstitials and thus forming vacancies;

    - substitutional defects, i.e. impurities substituting ions in the crystal lattice; the ionic radius of the impurity is generally different from that of the ion it is replacing, thus causing a distortion of the surrounding lattice;
- line defects, occurring when groups of atoms are in incorrect positions in the lattice, e.g. edge or misfit dislocations (see Figure 3.2.8), caused by termination of a plane of atoms in the middle of a crystal and causing a distortion of the adjacent planes, so that the crystal structure is ordered on either side;
- planar defects, such as grain boundaries, occurring where the crystallographic direction of the lattice changes abruptly, e.g. when two crystals start growing separately and then meet;
- bulk defects, such as voids, i.e. small regions with no atoms or "cluster of vacancies", and precipitates, i.e. small regions of impurities clustered together in a different phase.

These defects influence the film properties, such as stress/strain, which can be relieved by formation of edge dislocations for instance, magnetic properties (e.g. ferromagnetic resonance, Faraday rotation), optical properties (e.g. refractive index, optical absorption). Vacancies in ionic solids filled with one or more electrons are called "colour centres", as the electrons in the vacancies tend to absorb visible light, making a normally transparent material coloured: this has been observed in Al-deficient bulk YAG crystals, which appear brown instead of transparent, for instance [5].

In some cases substitutional defects are desired in order to improve the properties of materials: for instance replacing some Al^{3+} ions with Ti^{3+} in the crystal lattice of sapphire (α-Al_2O_3) increases the refractive index and allows lasing action, however Ti^{4+} impurities will cause re-absorption of fluorescence (more in Section 3.4); substituting Y^{3+} with Bi^{3+} or Ce^{3+} in the lattice of YIG ($Y_3Fe_5O_{12}$) improves magnetic properties and in particular allows achievement of higher values of Verdet constant or Faraday rotation (more in Section 3.6.3).

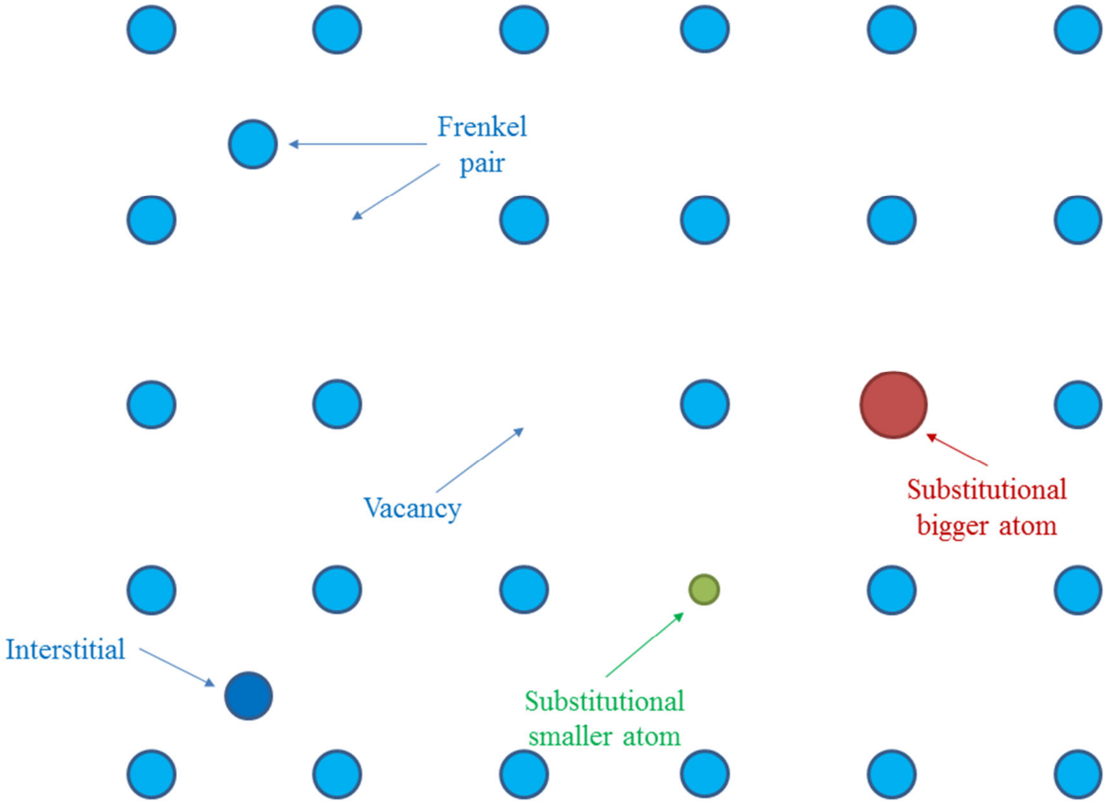

Figure 3.2.7. Summary of point defects.

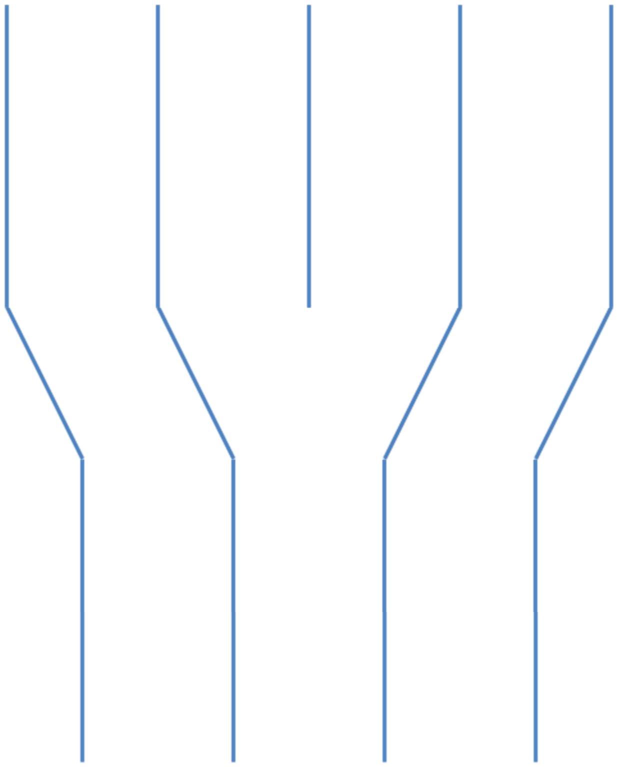

Figure 3.2.8. Schematic of edge or misfit dislocation.

3.2.3.3. LATTICE MISMATCH

If the substrate temperature is high enough to ensure crystallisation, the substrate material will generally act as a crystalline seed for the film growing on top. If the film and substrate are made of the same material, the film will grow with the same crystal structure, lattice constant and orientation as the substrate ("homo-epitaxial growth" – see Figure 3.2.9.a): this can be done to grow films with higher purity than the substrate or with controlled doping for particular applications (e.g. Ti:sapphire on sapphire for making waveguide lasers). On the contrary, if film and substrates are not the same materials ("hetero-epitaxial growth", e.g. YIG on YAG or GGG), crystal growth depends on the lattice mismatch, i.e. the difference between the lattice constants of the film (a_{FILM}) and the substrate (a_{SUB}), usually normalised to the lattice constant of the latter:

$$\frac{\Delta a}{a_{SUB}} = \frac{a_{FILM} - a_{SUB}}{a_{SUB}} \tag{3.2.7}$$

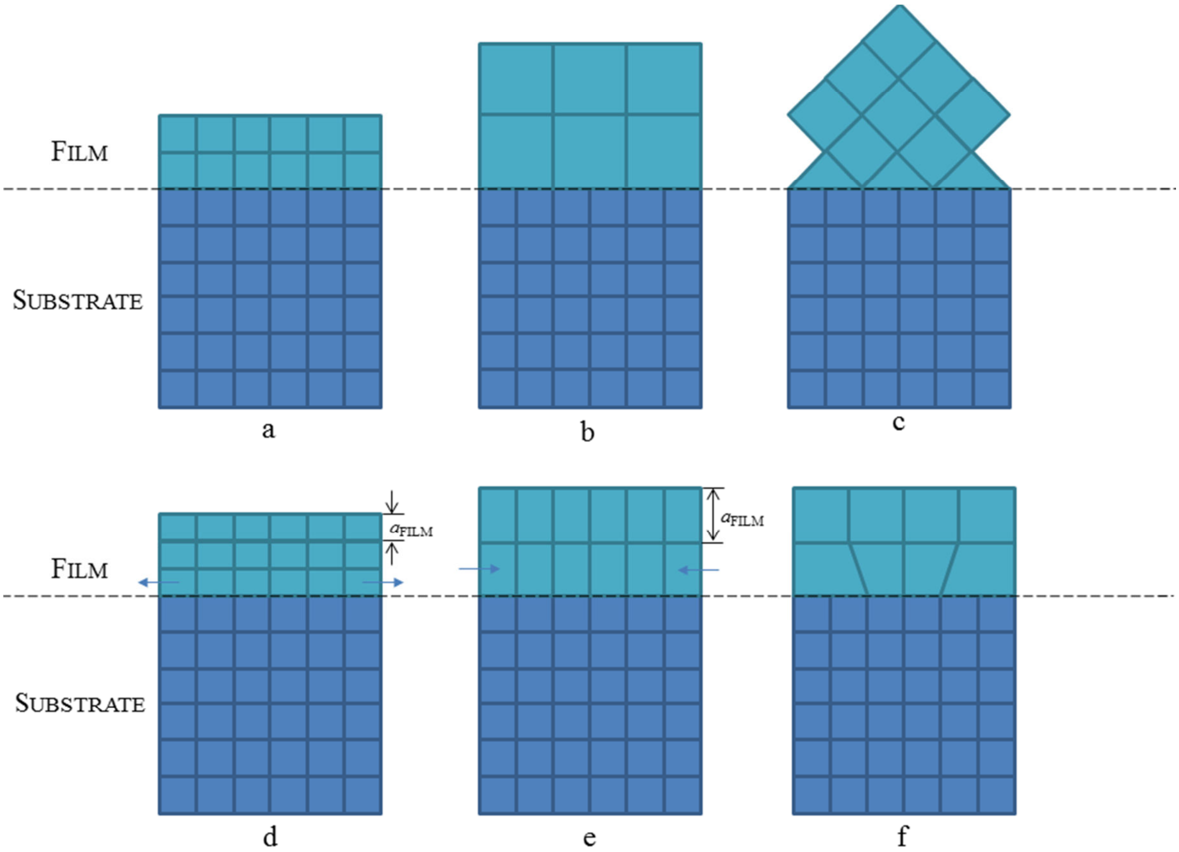

Figure 3.2.9. Schematic of growth mechanisms: **(a)** homoepitaxy ($a_{\mathrm{FILM}} = a_{\mathrm{SUB}}$); **(b)** harmonic mismatched growth (e.g. $a_{\mathrm{FILM}} = 2a_{\mathrm{SUB}}$); **(c)** lattice-matched growth with different crystal orientations; **(d)** heteroepitaxy with tensile strain ($a_{\mathrm{FILM}} < a_{\mathrm{SUB}}$); **(e)** heteroepitaxy with compressive strain ($a_{\mathrm{FILM}} > a_{\mathrm{SUB}}$); **(f)** heteroepitaxy with misfit dislocations ($a_{\mathrm{FILM}} > a_{\mathrm{SUB}}$). The blue arrows in **(d)** and **(e)** indicate the in-plane stress in the film.

If the lattice constant of the film is roughly an integer multiple of the substrate lattice constant, the film can be grown successfully ("harmonic mismatched growth" – see

Figure 3.2.9.b) with no defects. Lattice-matched crystal growth may be achieved with different crystal orientations between the film and the substrate (see Figure 3.2.9.c). Otherwise, a lattice mismatch up to ~9% can be accommodated via stress/strain or formation of defects (mainly edge dislocations) in the growing film [4, 5]: normally the film starts growing with the same lattice constant as the substrate (pseudomorphic growth), accumulating stress/strain (see Figures 3.2.9.d and e) up to a critical thickness t_c (typically of the order of some nanometres), depending on the materials and the lattice mismatch, and then relieving the accumulated stress/strain by formation of misfit dislocation (see Figure 3.2.9.f). However, if the lattice mismatch is higher than 9%, the film will grow polycrystalline or even amorphous.

As aforementioned, doping in the film (substitutional defects) will affect its properties, including the lattice constant, which will vary linearly with doping concentration according to Vegard's law, an approximate empirical rule; for instance, considering a ternary compound, such as $Ti_xAl_{2-x}O_3$, its lattice constant (a) will vary with composition according to:

$$a = \left[x a_{Ti_2O_3} + (2-x) a_{Al_2O_3}\right]/2 \qquad (3.2.8)$$

with: $0 \leq x \leq 2$, so that $x = 0$ gives the lattice constant of pure sapphire (Al_2O_3) and $x = 2$ gives the lattice constant of pure titanium oxide (Ti_2O_3).

3.2.3.4. THERMAL EXPANSION COEFFICIENT (TEC) MISMATCH

In hetero-epitaxial growth not only does the lattice-mismatch play an important role, but also the thermal expansion coefficient (TEC, ρ) mismatch, if the substrate is heated to high temperatures during the film growth. In fact, the film may grow successfully on a lattice-mismatched substrate, but it may subsequently crack upon cooling, if the TEC-mismatch ($\Delta\rho/\rho_{SUB}$) between the film and the substrate is too high, due to their different shrinking rates; this is especially true for μm-thick films [4, 5, 10]. Two cases can be distinguished, as schematically represented in Figure 3.2.10: if $\rho_{FILM} < \rho_{SUB}$ the film will be under compressive strain, whereas if $\rho_{FILM} > \rho_{SUB}$ the film will be under tensile strain. However, TEC-mismatch is difficult to predict, because TECs are normally quoted over a relatively narrow range of temperatures and may not be valid in a broader range of temperature over which the system is heated. Moreover values of TECs for materials in thin film form may not be the same as bulk materials and off-stoichiometry during the film growth may cause further changes in the TEC, which however should follow the same Vegard's law as for lattice constant; e.g. for Ti:sapphire ($Ti_xAl_{2-x}O_3$):

$$\rho = \left[x\rho_{Ti_2O_3} + (2-x)\rho_{Al_2O_3}\right]/2 \tag{3.2.9}$$

with: $0 \leq x \leq 2$, so that $x = 0$ gives the TEC of pure sapphire (Al_2O_3) and $x = 2$ gives the TEC of pure titanium oxide (Ti_2O_3).

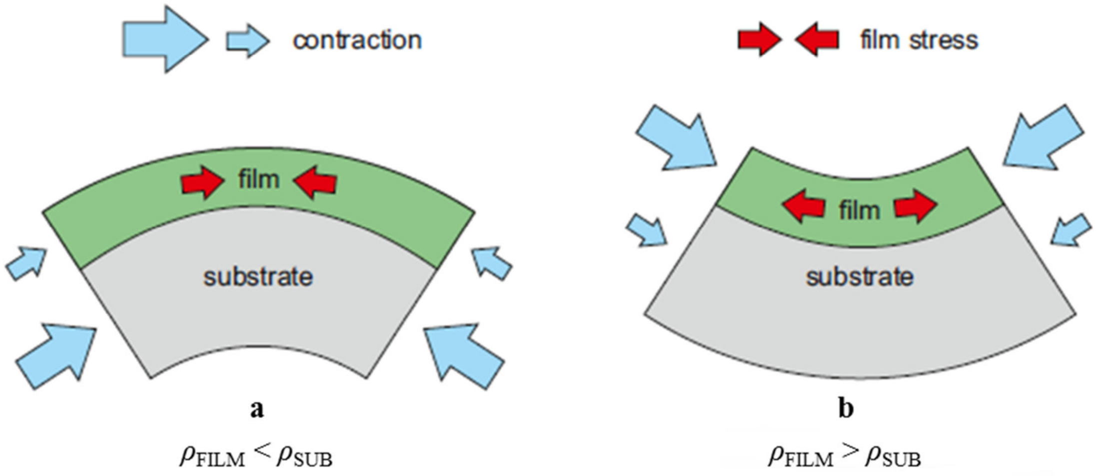

Figure 3.2.10. Effects of thermal expansion mismatch [5]:
(a) compressive strain for $\rho_{FILM} < \rho_{SUB}$; **(b)** tensile strain for $\rho_{FILM} > \rho_{SUB}$.

The film strain induced by the TEC-mismatch may (partially) compensate the film stress induced by the lattice mismatch, thus resulting in better film properties: for instance, if $a_{FILM} > a_{SUB}$ (e.g. YIG on YAG: $a_{FILM} = a_{YIG} = 1.2376$ nm $> a_{SUB} = a_{YAG} = 1.2006$ nm [11, 12]) the film can accumulate compressive strain, which however may be partially or completely relieved by the TEC-mismatch induced tensile strain, if $\rho_{FILM} > \rho_{SUB}$ (e.g. YIG on YAG: $\rho_{FILM} = \rho_{YIG} = 1\times10^{-5}$ K^{-1} $> \rho_{SUB} = \rho_{YAG} = 7.5\times10^{-6}$ K^{-1} at 300 K [13-15]).

3.2.4. TARGET DAMAGE AND PARTICULATES

3.2.4.1. TARGET MODIFICATION

As aforementioned, laser ablation modifies the target: as soon as the laser pulse ends, the surface of the ablated area cools down and re-solidifies in a damaged state with altered crystallinity and composition, featuring ripples, cones, splashes and particulates. All these features, described in this sub-section, will cause formation of particulates on the sample surface, as discussed in the next sub-section. Figure 3.2.11 shows surface modification (dark ablation trench/ring) of three targets after prolonged ablation.

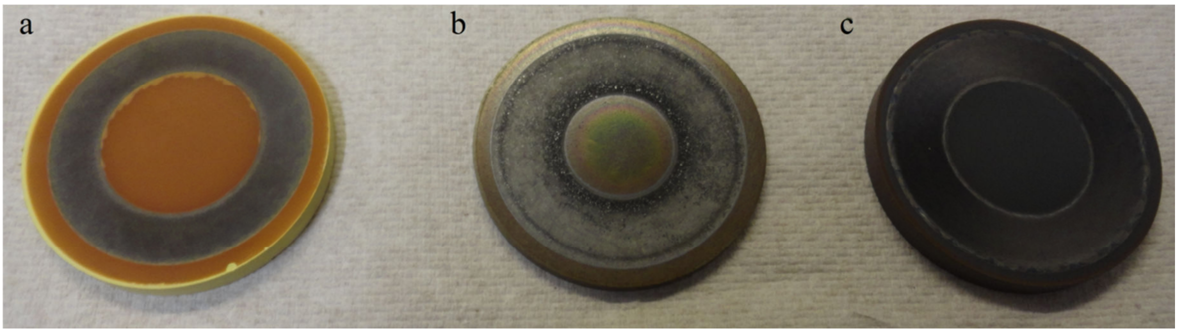

Figure 3.2.11. Ablated targets of **(a)** sintered Bi_2O_3, **(b)** polycrystalline YIG and **(c)** sintered Fe_2O_3. Re-sputtered material/dust covers the central region and the thin outer ring (visible especially in the Bi_2O_3 target, originally yellow – look at its edge).

Wave-like structures or ripples are likely due to the velocity difference between two fluids, i.e. the molten material on the target and the expanding plume, in the same fashion as the surface waves produced on water by the wind [5]; ripples on the wavelength scale, also known as LIPSS (Laser Induced Periodic Surface Structures), are observed at low fluences, typically below the ablation threshold, but their formation mechanism is not well understood yet [1, 4, 5]. Figure 3.2.12.a shows an example of wave-like structures in a poly-crystalline YIG target after around 3 hours and 45 minutes of ablation with a KrF laser: cracks and effects of exfoliation (already mentioned in Section 3.2.1 and discussed later in this section) induced by thermal shock can be noticed too. Ablation of these structures can be a source of particulates.

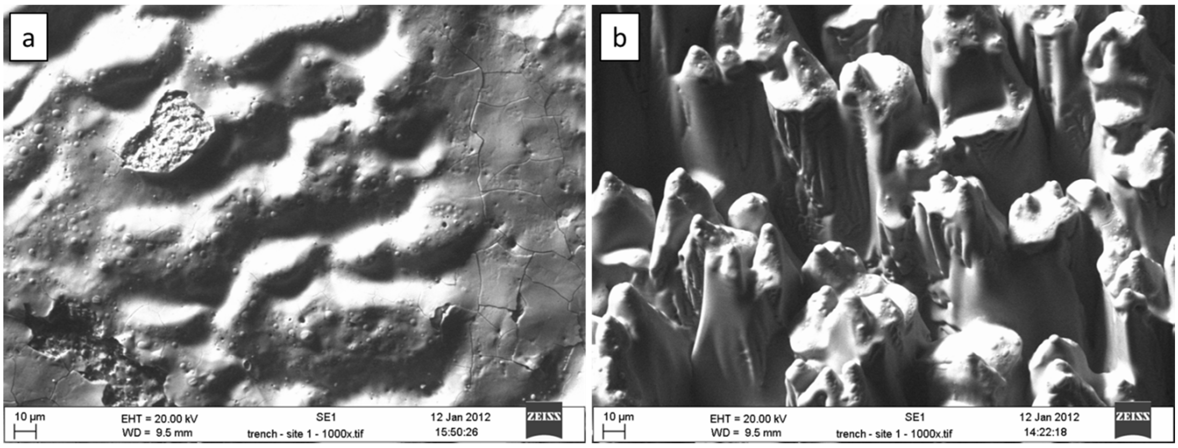

Figure 3.2.12. SEM pictures of **(a)** wave-like structures (ripples) in a poly-crystalline YIG target after ~3.75 hours of ablation and **(b)** cone-like structures in a single-crystalline YIG target after ~7.5 hours of ablation. The targets were rotated with an epitrochoidal motion during laser ablation and depositions.

Formation of cones (including cones with irregular shape, columns, clusters, etc.) on the target surface upon laser irradiation has been observed in several materials [1]. An example of cone structures in a single-crystal YIG target after ~7.5 hours of ablation with a KrF laser is shown in Figure 3.2.12.b. EDX analysis of these cones shows that they are Y-rich and Fe-deficient on the tips, which suggests that the cone formation is due to incongruent melting and phase segregation [1, 16]: as re-solidification of melt material on the target begins, high-melting point components such as Y_2O_3 ($T_{m,Y2O3} \approx 2698$ K) and $YFeO_3$ ($T_{m,YFeO3} \approx 1993$ K > $T_{m,Fe2O3} \approx 1839$ K > $T_{m,YIG} \approx 1828$ K) freeze first, leading to Y-enrichment; although this process is not significant for single pulse irradiation, in the long term, when the phenomenon is repeated over several thousands (and actually up to several hundreds of thousands) of times during target ablation, it will cause phase segregation and formation of these cone-structures with a Y-rich outer shell, causing a decrease in target ablation rate, due to UV-transparency of Y_2O_3 and an increase of surface area (leading to a lower effective laser fluence) [5, 16]; however laser channelling between the cones can increase the effective laser fluence on the target bulk, with subsequent production of particulates [4]. These can be formed also by exfoliation of cones [5]. In any case, production of particulates generally tends to increase with increasing target usage and target re-conditioning is suggested after several hours of ablation (see Section 4.3.1). Formation of cones, typically preceded by formation of shallow ripple-like structures [16], may start with poor ablation of points on the target surface (e.g. due to impurities or deposited debris) and they will always point in the direction of the incident laser beam [1, 5]. No cones have been observed in single-crystal Ti:sapphire targets, even after more than 10 hours of ablation, indicating that cone formation is material-dependent.

Splashes and particulates on the target can be formed via collisional and hydrothermal sputtering, as mentioned in Section 3.2.1: some species ejected during laser ablation may fall back on target material that is still melted, in the liquid phase, thus causing splashes and formation of particulates on the target surface; when these splashes and particulates are re-ablated, they will cause formation of particulates on the sample surface.

As aforementioned, the target composition can be altered during laser ablation, due to [4]:

- incongruent melting and phase segregation (see above);
- loss of more volatile elements;
- reactions with background gas (e.g. oxidisation of the target surface in an O_2 ambient).

The target should be re-conditioned after prolonged laser ablation (see Section 4.3.1) also for this reason, in order not only to restore a smoother surface, to avoid particulate formation on the sample in the long term, but also to ensure stoichiometric transfer. Target pre-ablation (before film growth) is important too, in order to reach a steady-state target composition and surface structuring [1, 4], which will degrade significantly only after several hours of ablation.

3.2.4.2. PARTICULATE FORMATION

Several sources of formation of particulates on the sample have been mentioned. In summary, particulates on the sample come from [1, 4, 5]:

- thermal sputtering, i.e. formation and subsequent ablation of ripples, wave-like structures, splashes and particulates on the target surface;
- collisional sputtering (target erosion);
- hydrodynamic sputtering (splashing and formation of droplets, especially in metallic targets);
- exfoliation sputtering (chunks or flakes of material detaching from the target due to thermal shock and impinging on the sample);
- cone formation and exfoliation;
- sub-surface super-heating (target material hotter than the evaporating surface above, causing micro-explosions) [1, 4];
- condensation of vapour species in the plume due to super-saturation (sub-micron particles) [1, 4, 5].

Particles coming from target surface modification are more difficult to prevent than those due to the last two factors, which can be avoided respectively by tuning the laser fluence and by adjusting the background gas pressure or the target-substrate distance. In fact, a high fluence typically causes a high density of particulate on the samples surface, due to increased sub-surface super-heating; however decreasing the fluence too much will produce poorer ablation and a slower deposition rate and may even result in formation of droplets by condensation; so a compromise value must be found. Variation of background gas pressure and/or target-substrate distance, closely related to each other via the mean free path (see Section 3.2.2), will affect plume (condensation) and film growth dynamics and thus particulate formation on the sample.

As aforementioned, particulates coming from target surface modification can be controlled by periodically re-conditioning the target by lapping/polishing or even with sandpaper (see Section 4.3.1) and pre-ablating fresh target surfaces to avoid particle deposition from the initial formation of cones and other structures. However, several techniques have been proposed to contrast this phenomenon; for instance target usage can be increased by:

- raster-scanning the laser beam on the target surface;
- moving the target with a computer-controlled XY stage;

- rotating the target, thus producing an ablation ring/trench ("race-track");
- rotating the target with an off-set cam, providing an epitrochoidal ("spirograph") motion and thus resulting in a larger ablation ring than a purely circular ablation path;
- rotating and tilting the target continuously, resulting again in a large ablation trench and allowing deposition of more uniform films, with controlled curvature, if dwell times are set at some target tilt angles; this however may result in the production of cones and splashes on the edges of the ablated tracks, which are likely to be ablated at the subsequent tilt angle with consequent formation of particulates on the sample.

The last two methods have been used for the depositions described in this thesis; some more details are given in Section 4.2.

A few other techniques to avoid formation of particulate from target surface modification use [1, 4, 5]:

- a velocity filter or a shutter synchronised with the plume, exploiting the fact that particulates, more massive than ions and neutral atoms, travel slower than either of these;
- a pulsed gas jet, synchronised with the plume, to blow particles away, exploiting the same working principle as above (see Figure 3.2.13.a) [17];
- a dual-beam approach, by heating the plume and breaking down the particles or by synchronous ablation of two targets of the same materials, thus obtaining two crossing plumes ("cross-beam PLD") [18], where the particles travel undisturbed along their axes, thus missing the substrates, whereas the other ablated species are scattered towards the substrate (see Figure 3.2.13.b);
- an off-axis geometry in the target-substrate configuration, so that particles miss the substrate, whereas the charged species in the plume can be deflected towards the substrate via a magnetic field [19].

However, all these methods complicate significantly the PLD set-up and reduce considerably the deposition rate.

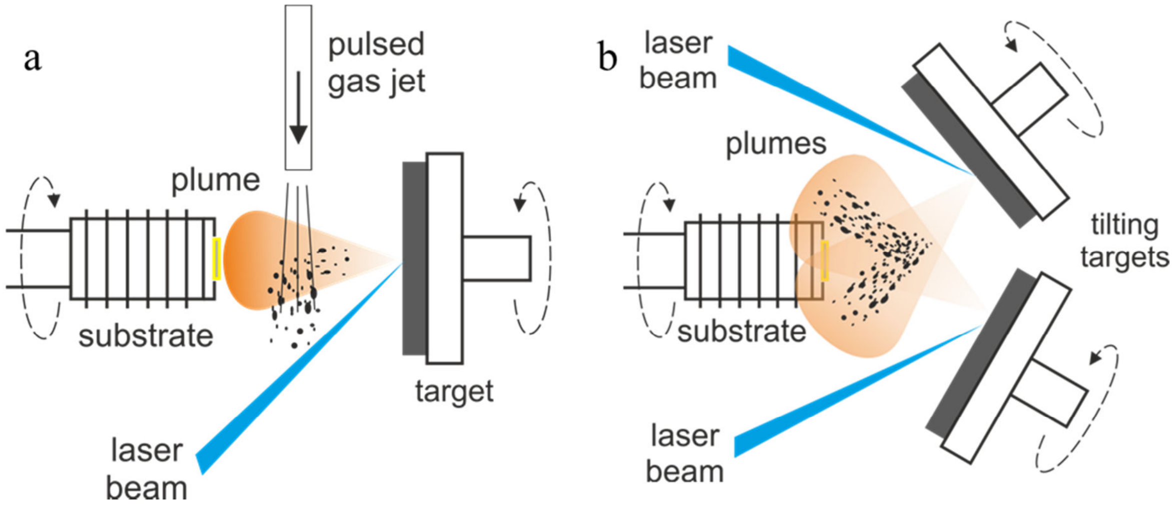

Figure 3.2.13. Two techniques to avoid or reduce the formation of particulates on the sample surface: **(a)** use of a pulsed gas jet; **(b)** use of a dual-beam approach with a "cross plume" configuration.

3.3. WAVEGUIDE THEORY

An optical waveguide is a 2D (planar) or 3D (channel) structure confining propagating light [20]. For the purposes of this thesis, only 2D or slab waveguides are considered in this section. Light confinement and waveguiding can be explained with total internal reflection (TIR) and, to a first approximation, with geometrical optics, as schematically shown in Figure 3.3.1 for an asymmetric planar waveguide. TIR requires that the refractive index of the film is higher than the refractive indexes of the surrounding regions (substrate and cladding). If n_c (≈ 1 for air), n_f and n_s are the refractive indexes of cladding, film and substrate respectively, with $n_f > n_s > n_c$, TIR is allowed only if the angle of propagation ϑ is higher than the critical angles for the cladding-film and film-substrate interfaces, which can be determined from Snell's law:

$$n_f \, sin\, \vartheta_c = n_c \;\Rightarrow\; \vartheta_c = sin^{-1}\frac{n_c}{n_f} \tag{3.3.1}$$

$$n_f \, sin\, \vartheta_s = n_s \;\Rightarrow\; \vartheta_s = sin^{-1}\frac{n_s}{n_f} \tag{3.3.2}$$

This means that waveguiding is achieved for $\vartheta_c < \vartheta_s < \vartheta < \pi/2$, condition which allows a definition of the maximum acceptance angle ϑ_{max} for the beam incident on the waveguide (ϑ_{launch}):

$$\sin \vartheta_{\max} = \sqrt{n_{\mathrm{f}}^2 - n_{\mathrm{s}}^2} = NA \tag{3.3.3}$$

with *NA* defining the numerical aperture of the waveguide.

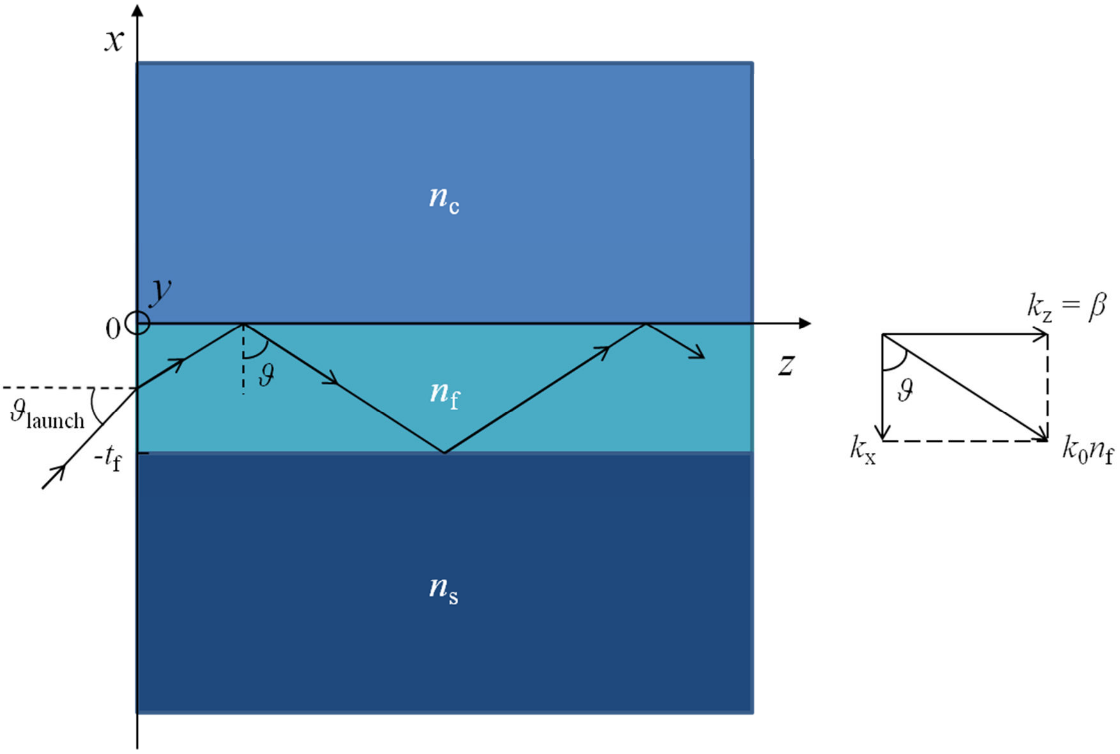

Figure 3.3.1. Waveguide schematic.

Waveguide theory however is typically formulated in terms of the propagation constant β (along the *z* direction) rather than in terms of propagation angle ϑ:

$$\beta = k_z = k_0 n_f \sin\vartheta = k_0 N \tag{3.3.4}$$

where $k_0 = 2\pi/\lambda$ is the propagation constant of light in vacuum and $N = n_f \sin\vartheta$ is the effective index of the waveguide, whose value lies in the range $n_s < N < n_f$. Similarly, the propagation constant along the *x* direction is defined as:

$$k_x = k_0 n_f \cos\vartheta \tag{3.3.5}$$

Light propagation in the waveguide can be described in more detail with electromagnetic theory, starting from Maxwell equations:

$$\nabla \times \vec{E} = -\mu_0 \frac{\partial \vec{H}}{\partial t} \tag{3.3.6}$$

$$\nabla \times \vec{H} = \varepsilon_0 n^2 \frac{\partial \vec{E}}{\partial t} \tag{3.3.7}$$

where: $\vec{E}$ and $\vec{H}$ are the electric and magnetic field vectors respectively, *n* is the refractive index of the medium, $\mu_0 = 4\pi\times10^{-7}$ V×s/(A×m) and $\varepsilon_0 \approx 8.854\times10^{-12}$ C/(V×m) the vacuum permeability and permittivity respectively, with the speed of light in vacuum defined as follows:

$$c = \frac{\omega}{k_0} = \frac{1}{\sqrt{\varepsilon_0 \mu_0}} \approx 3 \times 10^8 \text{ m/s} \tag{3.3.8}$$

Under the following assumptions:

- homogeneous, isotropic, lossless ($\alpha = 0$) and charge-less ($\nabla \cdot \vec{E} = 0$) medium,
- no field variation along the y direction: $\frac{\partial}{\partial y} = 0$,
- sinusoidal time trend: $\frac{\partial}{\partial t} = i\omega$,
- guided propagation along the z direction: $\frac{\partial}{\partial z} = -i\beta$,

Maxwell's equations can be simplified and the electric and magnetic fields can be defined as follows:

$$\vec{E}(x, y, z, t) = \vec{E}(x, y)e^{i(\omega t - \beta z)} \tag{3.3.9}$$

$$\vec{H}(x, y, z, t) = \vec{H}(x, y)e^{i(\omega t - \beta z)} \tag{3.3.10}$$

Further simplifications arise from considering propagation of either transverse electric (TE) or transverse magnetic (TM) modes: in the former case the electric field is transverse to the propagation direction z, i.e. $E_\text{y} \neq 0$, $E_\text{z} = E_\text{x} = 0$ and $H_\text{y} = 0$, whereas in the latter case the magnetic field is transverse to the propagation direction z, i.e. $H_\text{y} \neq 0$, $H_\text{z} = H_\text{x} = 0$ and $E_\text{y} = 0$.

In the case of propagation of a TE mode, Maxwell's equations are simplified as follows:

$$H_\text{x} = -\frac{\beta}{\omega \mu_0} E_\text{y} \tag{3.3.11}$$

$$H_\text{z} = \frac{i}{\omega \mu_0} \frac{\partial E_\text{y}}{\partial x} \tag{3.3.12}$$

$$-i\beta H_\text{x} - \frac{\partial H_\text{z}}{\partial x} = i\omega \varepsilon_0 n^2 E_y \tag{3.3.13}$$

Replacing H_x and H_z in (3.3.13) with the definitions in Equations (3.3.11) and in (3.3.12), the wave equation for TE modes is obtained:

$$\frac{\partial^2 E_\text{y}}{\partial x^2} + (k_0^2 n^2 - \beta^2)E_\text{y} = 0 \tag{3.3.14}$$

with $k_0^2 = \omega^2\sqrt{\varepsilon_0\mu_0}$, or:

$$\frac{\partial^2 E_\mathrm{y}}{\partial x^2} + k_0^2(n^2 - N^2)E_\mathrm{y} = 0 \tag{3.3.15}$$

In the case of propagation of a TM mode, Maxwell's equations are simplified as follows:

$$E_\mathrm{x} = \frac{\beta}{\omega\varepsilon_0 n^2}H_\mathrm{y} \tag{3.3.16}$$

$$E_\mathrm{z} = \frac{1}{i\omega\varepsilon_0 n^2}\frac{\partial H_\mathrm{y}}{\partial x} \tag{3.3.17}$$

$$i\beta E_\mathrm{x} - \frac{\partial E_\mathrm{z}}{\partial x} = -i\omega\mu_0 H_y \tag{3.3.18}$$

Replacing E_x and E_z in (3.3.18) with the definitions in Equations (3.3.16) and in (3.3.17), the wave equation for TM modes is obtained:

$$\frac{\partial^2 H_\mathrm{y}}{\partial x^2} + (k_0^2 n^2 - \beta^2)H_\mathrm{y} = 0 \tag{3.3.19}$$

The following derivations consider the case of propagation of TE mode, but are valid for the case of propagation of TM mode too, with appropriate changes where necessary.

Equation (3.3.15) can be rewritten as follows:

$$\begin{cases} \frac{\partial^2 E_\mathrm{y}}{\partial x^2} + k_0^2(n_\mathrm{c}^2 - N^2)E_\mathrm{y} = 0 & (x > 0) \\ \frac{\partial^2 E_\mathrm{y}}{\partial x^2} + k_0^2\left(n_\mathrm{f}^2 - N^2\right)E_\mathrm{y} = 0 & (-t_\mathrm{f} < x < 0) \\ \frac{\partial^2 E_\mathrm{y}}{\partial x^2} + k_0^2(n_\mathrm{s}^2 - N^2)E_\mathrm{y} = 0 & (x < -t_\mathrm{f}) \end{cases} \tag{3.3.20}$$

whose solutions are given by:

$$E_\mathrm{y}(x) = \begin{cases} E_\mathrm{c}e^{-\gamma_\mathrm{c}x} & (x > 0) \\ E_\mathrm{f}\cos(k_\mathrm{x}x + \varphi_\mathrm{c}) & (-t_\mathrm{f} < x < 0) \\ E_\mathrm{s}e^{\gamma_\mathrm{s}(x+t_\mathrm{f})} & (x < -t_\mathrm{f}) \end{cases} \tag{3.3.21}$$

where t_f is the film thickness, E_c, E_f and E_s are constants, φ_c is a phase offset, k_x has already been defined above in (3.3.5) and:

$$\gamma_\mathrm{c} = k_0\sqrt{N^2 - n_\mathrm{c}^2} \tag{3.3.22}$$

$$\gamma_\mathrm{s} = k_0\sqrt{N^2 - n_\mathrm{s}^2} \tag{3.3.23}$$

are the propagation or actually the dispersion constants in the cladding and in the substrate respectively, meaning that the electric (and magnetic) fields are evanescent in both the cladding and the substrate.

The tangential component (H_z) of the magnetic field can be found replacing E_y, as defined in (3.3.21), in Equation (3.3.12):

$$H_z(x) = \frac{i}{\mu_0\omega}\begin{cases} -\gamma_c E_c e^{-\gamma_c x} & (x > 0) \\ -k_x E_f \sin(k_x x + \varphi_c) & (-t_f < x < 0) \\ \gamma_s E_s e^{\gamma_s(x+t_f)} & (x < -t_f) \end{cases} \tag{3.3.24}$$

From the continuity of tangential components of electric and magnetic fields at the interfaces ($x = 0$ and $x = -t_f$):

$$E_y(0^+) = E_y(0^-) \Rightarrow E_c = E_f \cos\varphi_c \tag{3.3.25}$$

$$H_z(0^+) = H_z(0^-) \Rightarrow E_c = E_f \frac{k_x}{\gamma_c} \sin\varphi_c \tag{3.3.26}$$

$$E_y(-t_f^{\,+}) = E_y(-t_f^{\,-}) \Rightarrow E_s = E_f \cos(k_x t_f - \varphi_c) \tag{3.3.27}$$

$$H_z(-t_f^{\,+}) = H_z(-t_f^{\,-}) \Rightarrow E_s = E_f \frac{k_x}{\gamma_s} \sin(k_x t_f - \varphi_c) \tag{3.3.28}$$

From the ratios of the former two and of the latter two of this set of four equations:

$$\cot\varphi_c = \frac{k_x}{\gamma_c} \tag{3.3.29}$$

$$\cot(k_x t_f - \varphi_c) = \frac{k_x}{\gamma_s} \tag{3.3.30}$$

The former of these two equations can be rewritten as follows:

$$\varphi_c = \frac{\pi}{2} - \tan^{-1}\frac{k_x}{\gamma_c} \tag{3.3.31}$$

This can be used in equation (3.3.30), which can be rewritten to give the modal equation, considering that $\tan\phi = \tan(\phi + m\pi)$:

$$k_x t_f = (m+1)\pi - \tan^{-1}\frac{k_x}{\gamma_c} - \tan^{-1}\frac{k_x}{\gamma_s} \tag{3.3.32}$$

A similar modal equation can be derived for the case of propagation of TM modes:

$$k_x t_f = (m+1)\pi - \tan^{-1}\left(\frac{n_c^2}{n_f^2}\frac{k_x}{\gamma_c}\right) - \tan^{-1}\left(\frac{n_s^2}{n_f^2}\frac{k_x}{\gamma_s}\right) \qquad (3.3.33)$$

These modal equations can be solved graphically or numerically and implies that for a given film thickness t_f and refractive index n_f, there are a finite number of modes (identified by a finite number of discrete values of the TIR angles ϑ_m or effective refractive indexes N_m) which can be launched into the waveguides.

3.4. TI:SAPPHIRE

With the term "sapphire" we refer to pure corundum, i.e. the alpha phase (α-Al_2O_3) of aluminium oxide or alumina (Al_2O_3), which can exist in several other less common phases: γ-, δ-, η-, θ-, and χ-Al_2O_3 [21]. Figure 3.4.1 shows the crystallographic structure of sapphire, which can be described either as rhombohedral or hexagonal, with lattice constants $a = b = 0.4785$ nm and $c = 1.2991$ nm [22], where the O^{2-} anions form the hexagonal close-packed structure and the Al^{3+} cations occupy the octahedral interstices.

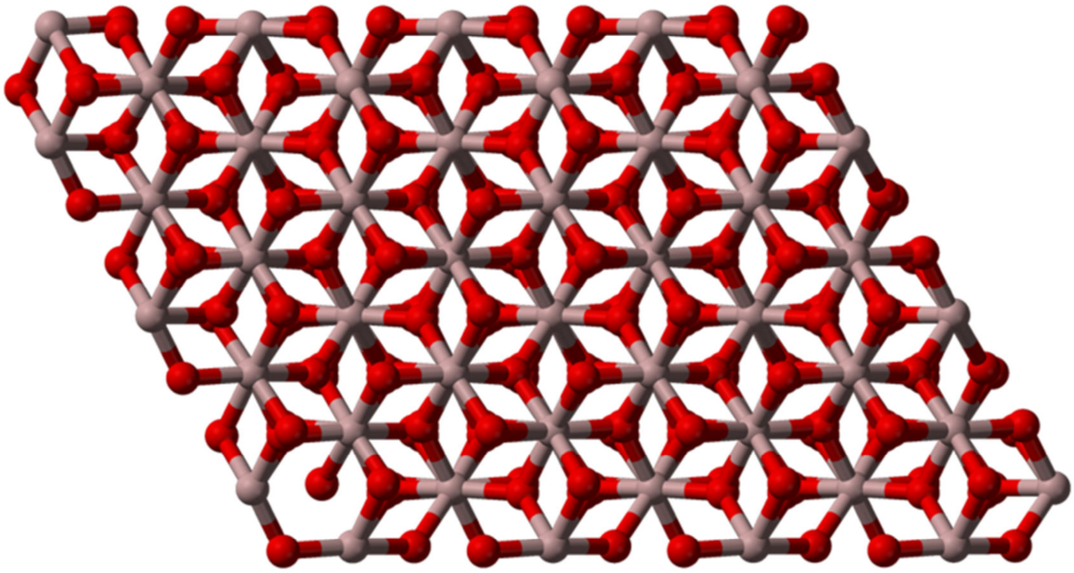

Figure 3.4.1. Crystal structure of sapphire (or corundum or α-Al_2O_3), viewed along the crystallographic c-axis [23].

The crystallographic anisotropy is reflected on the mechanical, thermal and optical properties. Optically sapphire is a uniaxial crystal, with its optical z axis parallel to the crystallographic c axis and refractive indices: $n_o \approx 1.7717$ and $n_e \approx 1.76355$ at $\lambda = 532$ nm [22]. Sapphire has several interesting and useful properties: it is transparent over a wide range of wavelengths, from ~150 nm up to ~5500 nm[2]; it has a high mechanical strength (hardness: 9 on the Mohs scale, with diamond hardness = 10), a high melting point ($T_{\mathrm{m,Al2O3}} \approx 2303$ K [22]) and good thermal conductivity ($\kappa_{\mathrm{tc},//} = 23.1$ W/(m×K) and $\kappa_{\mathrm{tc},\perp} = 25.1$ W/(m×K) respectively for parallel and perpendicular directions with respect to the optical axis at 300 K [22]), making it an excellent laser host. The anisotropic thermal properties and in particular the difference between the two TECs ($\rho_{//} = 6.6\times10^{-6}$ K^{-1} and $\rho_{\perp} = 5\times10^{-6}$ K^{-1} respectively for parallel and perpendicular directions with respect to optical axis at 323 K [22]) prevents the synthetic growth of polycrystalline samples, so that high-purity high-quality bulk sapphire is typically grown in single-crystal form [3]. Natural sapphire is not good enough for optical applications, due to impurities and defects in its crystal structure.

Doping sapphire with transition metals allows lasing action, due to the change in the electronic structure of the crystal induced by substitutional defects. In particular, the first Ti:sapphire (or Ti:Al_2O_3) laser was demonstrated in 1982 by Moulton [24]: Ti^{3+}-doping[3] creates a wide absorption band $\Delta\lambda_{\mathrm{abs}} = (400 - 650)$ nm in the visible, with peak at $\lambda \approx 490$ nm (blue-green), and an even wider emission band $\Delta\lambda_{\mathrm{em}} \approx (600 - 1200)$ nm in the visible-NIR, with peak at $\lambda \approx 790$ nm (red-NIR), although emission between $\lambda \approx 600$ nm and $\lambda \approx 630$ nm is not possible due to re-absorption (overlap of absorption and emission bands – see Figure 3.4.2) the large emission bandwidth gives Ti:sapphire lasers one of the widest wavelength-tunability ranges and allows mode-locked operation for generation of ultra-short laser pulses ($\tau \geq 5.5$ fs [15]); however the wide emission band and the large emission cross-section ($\sigma_{\mathrm{em}} = 41 \times 10^{-20}$ cm^2 at $\lambda = 790$ nm [15]) mean a short fluorescence lifetime ($\tau_{\mathrm{fl}} = 3.2$ μs [15]), which implies a high saturation power and thus high pump power density. However, as mentioned in Section 1.2.1, adoption of a waveguide geometry would have the advantage over bulk lasers of better pump and signal-beam confinement, thus leading to narrower average spot-sizes and lower lasing thresholds.

---

[2] This actually poses a problem for laser ablation. However doping causes UV absorption, thus allowing ablation with UV lasers (e.g. with KrF and ArF lasers emitting at 248 nm and 193 nm respectively).

[3] The electronic configuration of Ti is: $1s^2 2s^2 2p^6 3s^2 3p^6 3d^2 4s^2$, with the Ti^{3+} ion having the same electronic configuration as Ar with only a single $3d$ electron.

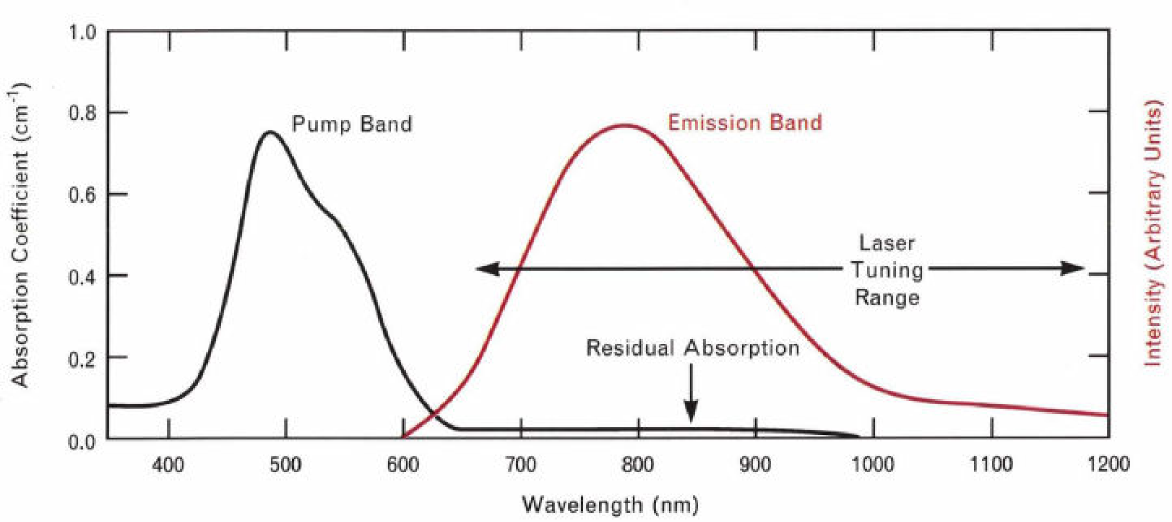

Figure 3.4.2. Absorption and emission bands of Ti:sapphire. Picture taken from reference [25].

The large bandwidth of transition-metal-doped gain media, such as Ti:sapphire, comes from the strong interaction of the electronic states of the unfilled *d* shell of the ion with the lattice vibrations or phonons of the crystal, also called vibrational-electronic or vibronic interaction, which leads to a homogeneous broadening of absorption and fluorescence bands [15]. On the contrary, the narrower bandwidth (0.6 nm [15]), smaller cross-section $\sigma_{\mathrm{em}} = 28 \times 10^{-20}\ \mathrm{cm}^2$ at $\lambda = 1064$ nm [15]) and longer fluorescence life-time ($\tau_{\mathrm{fl}} = 230\ \mu\mathrm{s}$ [15]) of rare-earth-doped gain media (e.g. Nd:YAG) is due the poor influence of the host lattice on the electronic transitions (normally occurring within the inner 4*f* shell) of trivalent rare-earth ions (e.g. Nd^{3+}), shielded by the outer electronic shell [15].

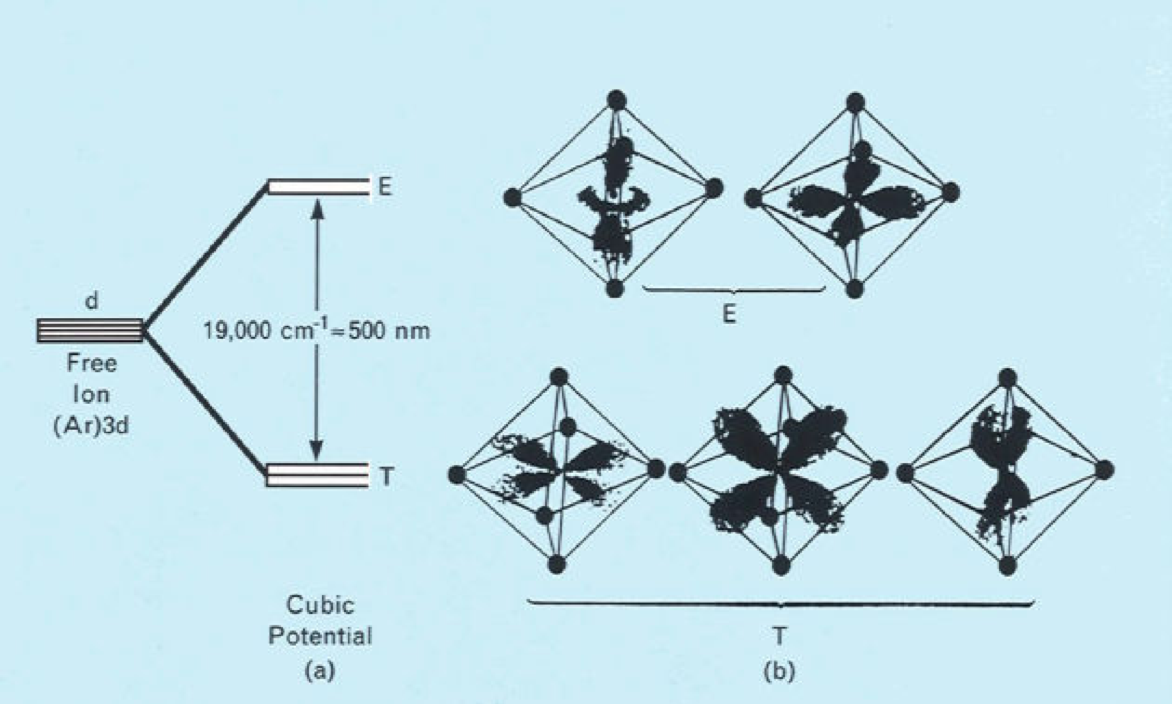

Figure 3.4.3. **(a)** Simplified energy diagram of Ti^{3+}; **(b)** orientation of the 3*d* electronic orbitals with respect to the octahedrally coordinated nearest-neighbour oxygen atoms. Picture from reference [25].

To better understand the spectroscopy of Ti:sapphire, refer to Figure 3.4.3: in the free Ti^{3+} ion, the 3*d* electron has 5 degenerate angular momentum states (orbitals), which are split by the crystal field of the Al$_2$O$_3$ lattice, thus removing the fivefold degeneracy of the ground-state level of the Ti^{3+} ion: the two orbitals pointing directly to neighbouring O atoms (doublet E, excited state) have higher energy than the other three orbitals (triplet T, ground state). This results in the energy level diagram shown in Figure 3.4.4.a: when the Ti^{3+} ion is excited, it is displaced with respect to surrounding oxygen atoms (Jahn-Teller effect), thus causing vibrations of the surrounding lattice (phonons, i.e. oscillations of energy levels around equilibrium values, represented by parabolas in the figure) and the removal of the degeneracy of the two excited angular momentum states (E), leading to a splitting of the green absorption band (there are in fact two overlapping absorption bands, actually, with peaks at $\lambda \approx 485$ nm and $\lambda \approx 550$ nm [26], resulting in a peak at $\lambda \approx 490$ nm with a shoulder – see Figure 3.4.2). The broad emission bandwidth comes from the spread in probability of the Ti^{3+} ion position at the bottom of the E potential, which can connect to a large spread of vibrational levels of the T potential via vertical transitions [25].

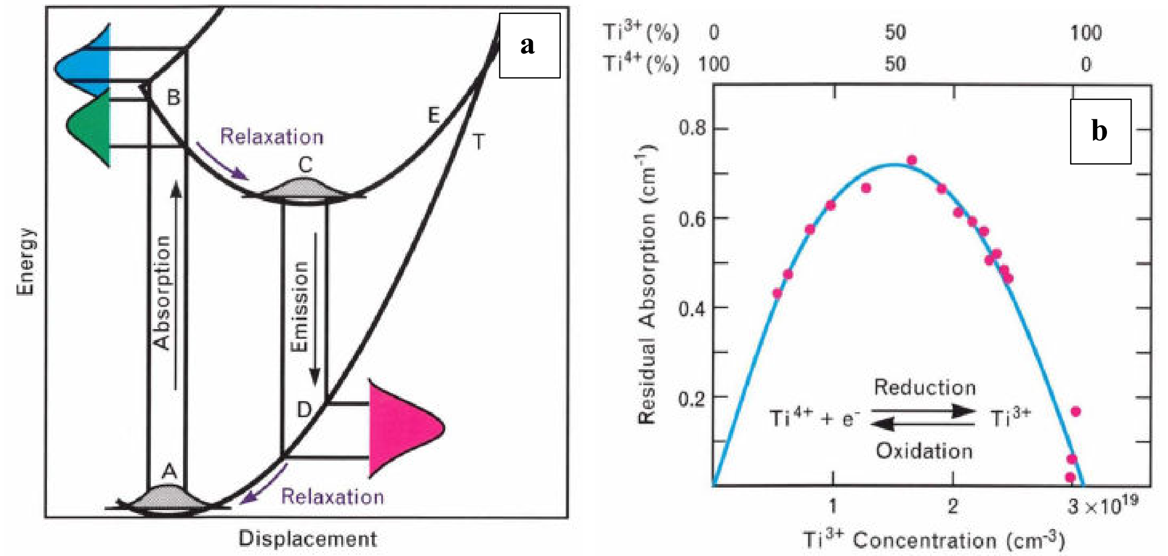

Figure 3.4.4. (a) Energy level diagram of Ti^{3+}:Al$_2$O$_3$ [25]. Parabolas (E and T) represent energy levels; optical transitions are represented by vertical lines (absorption from A to B, emission from C to D); the Gaussian-shaped curves at points A and C in the figure represent the probability of finding the Ti^{3+} ions at a particular position in the lowest vibrational states of T and E levels, respectively; the coloured curves refer to optical absorption (green and blue) and emission (red) bands; B-C and D-A are phonon-relaxation transitions. **(b)** Residual absorption versus Ti^{3+} concentration. Pictures taken from reference [25].

The aforementioned crystal and optical anisotropy of the laser host (sapphire) have effects on the spectroscopic properties of the Ti:sapphire system: absorption and fluorescence/emission spectra are polarisation-dependant and, in particular, the absorption and emission cross-sections are much larger (by a factor of ~3 [3, 24, 27]) for light polarised with the electric field parallel to the optical *z* axis than for light polarised perpendicular to the *z* axis.

Finally, two problems related to Ti-doping must be mentioned: firstly, only relatively low Ti concentrations are allowed in the sapphire crystal (<0.4 at. %, compared to typical doping concentration of the order of 1 at. % in Nd:YAG lasers, for instance), as the optical quality of Ti:sapphire will quickly degrade with Ti concentration higher than ~0.4 at. % [3, 28]; secondly, Ti dopants may be incorporated in the wrong valence state, 4+ instead of 3+, and Ti^{3+}-Ti^{4+} pairs near a vacancy will cause a broad parasitic absorption band centred between λ = 750 nm and λ = 800 nm, overlapping with fluorescence emission and thus hindering fluorescence and inhibiting lasing [3, 24, 26, 27, 29, 30]. The effect of Ti^{4+} on residual absorption in the emission band is shown in Figure 3.4.4.b, that demonstrate that residual absorption is maximised with a Ti^{4+}/Ti^{3+} ratio equal to 0.5, i.e. with formation of Ti^{3+}-Ti^{4+} pairs; residual absorption can be minimised with thermal annealing in a reducing atmosphere after crystal growth, whereas post-annealing in an oxidising atmosphere will transform Ti^{3+} ions into Ti^{4+} ions [25].

3.5. MAGNETIC MATERIALS

Prior to introduction to the magneto-optic garnets in the next paragraph, this section provides a classification of materials, according to their magnetic properties, along with some fundamentals of magnetism.

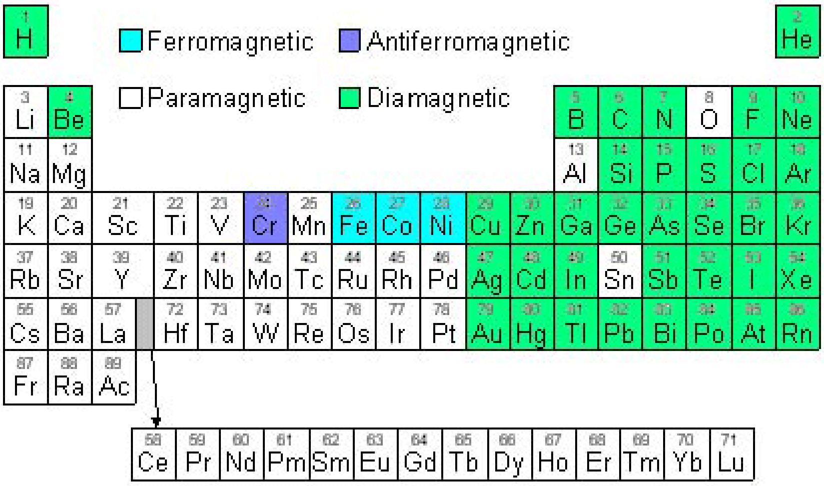

Figure 3.5.1. Periodic table showing magnetic properties at room temperature ($T \approx 300$ K) [31].

As shown in Figure 3.5.1, there are only few elements (Fe, Co and Ni) in the periodic table which show strong magnetic properties (ferromagnetism) at room temperature; however ferromagnetic properties can be found in their alloys and some compounds of rare earth metals too. To a greater or lesser extent, all materials show diamagnetism, as will be explained later.

The roots of magnetism are:

I. the electron magnetic dipole moment, arising from spin of electrons and whose unit is the Bohr magneton:

$$\mu_B = \frac{e\hbar}{2m_e} = 9.274 \times 10^{-24}\,\frac{\mathrm{J}}{\mathrm{T}} \tag{3.5.1}$$

where $\hbar = h/2\pi$ is the reduced Planck constant, a measure of angular momentum, and $m_\mathrm{e} = 9.11\times10^{-31}$ kg the electron rest mass;

II. nuclear magnetic moments of nuclei, much smaller than the electron magnetic dipole moment and thus negligible in magnetisation of materials.

The electrons in a material are typically arranged so that their magnetic moments cancel out, mainly due to the Pauli exclusion principle[4] or combination into filled sub-shells with zero net orbital motion (diamagnetism); even when the electron configuration includes unpaired electrons and/or unfilled sub-shells, the electrons in the material will contribute magnetic moments pointing in different, random directions, so that the material will not be magnetic (paramagnetism). The magnetic behaviour of materials depends on their structure and, in particular, on their electronic configuration, as explained above; moreover it depends on temperature, as random thermal motion, increasing with increasing temperature, makes it more difficult for electrons to maintain alignment.

Depending on their magnetic behaviour, materials can be classified as:

1. diamagnetic,
2. paramagnetic,
3. ferromagnetic,
4. anti-ferromagnetic,
5. ferrimagnetic.

---

[4] Fermions (particles with half integer spin), such as electrons, cannot occupy the same quantum state and thus must have opposite spin.

Further details on each type of materials are provided in the next sub-sections.

3.5.1. DIAMAGNETIC MATERIALS

Diamagnetism appears in all materials: it is the property to generate a magnetic field in opposition to an externally applied magnetic field; however, in most materials this is a weak effect and it is usually overcome by other forms of magnetism, e.g. paramagnetism and ferromagnetism. It is due to the fact that there are no unpaired electrons, so that intrinsic electron magnetic moments cannot produce any bulk effect, as explained above. Metals with many core electrons, such as Hg, Au and Bi, are examples of diamagnetic materials, with permeability $\mu = B/H < \mu_0$ (B is the magnetic induction).

3.5.2. PARAMAGNETIC MATERIALS

As opposed to diamagnetic materials, a paramagnetic material is attracted by an externally applied magnetic field; in the absence of an external magnetic field, the magnetic moments in the material are randomly oriented, so that the net magnetisation is zero. On a microscopic scale, paramagnetism is due to unpaired electrons, i.e. atomic or molecular orbitals with just one electron, whose magnetic moment tends to align along the same direction as the applied magnetic field. Most materials are paramagnetic, with permeability $\mu > \mu_0$.

3.5.3. FERROMAGNETIC MATERIALS

Macroscopically, ferromagnetism is the mechanism by which some materials (e.g. Fe, Ni, Co and their alloys) form permanent magnets and are strongly attracted by magnets. Microscopically, it is due to unpaired electrons (e.g. four 3*d* electrons in Fe[5]), which, according to Hund's rule, tend to have the same spin, i.e. parallel intrinsic magnetic moments, unlike in paramagnetic materials; this spontaneous alignment of magnetic dipoles gives rise to a spontaneous magnetisation.

---

[5] The electronic configuration of Fe is: $1s^2 2s^2 2p^6 3s^2 3p^6 3d^6 4s^2$. The *d* subshell accommodates up to 10 electrons.

3.5.3.1. EXCHANGE INTERACTION

The strong interaction between spins arises from the so-called “exchange interaction”, a quantum mechanical effect dominating over the dipole-dipole magnetic interaction (~1000 times weaker in Fe, for instance) at short distances, as it leads to a lower energy configuration; similar mechanisms, such as “super-exchange”, are responsible for anti-ferromagnetism and ferrimagnetism.

3.5.3.2. MAGNETIC ANISOTROPY

Exchange interaction keeps the spins aligned to each other, however their alignment along a particular direction comes from magnetic anisotropy, without which the material would be paramagnetic, due to thermal fluctuations. Magnetic anisotropy can have different sources:

- magneto-crystalline anisotropy, due to preferential directions of magnetisation introduced by the crystalline structure of the material;
- magneto-elastic anisotropy, due to internal stress/strain in the material;
- shape anisotropy, due to non-spherical particles in the material;
- exchange anisotropy, due to interaction of ferromagnetic and anti-ferromagnetic materials.

Magnetic anisotropy causes the formation of “easy” and “hard” axes of magnetisation: magnetising the material along the “hard axis” requires an external magnetic field with higher intensity than the case of magnetisation along the “easy axis”.

3.5.3.3. MAGNETIC DOMAINS

Due to the short range of the exchange interaction, magnetic dipoles are aligned parallel to each other only in relatively small regions, called “Weiss domains”, typically ~(1 – 100) µm in size, depending on the material, which allows also minimisation of the internal energy. Weiss domains are often randomly oriented, so that the net magnetisation of the material is zero: for this reason ferromagnetic materials are frequently found in an un-magnetised state.

3.5.3.4. MAGNETISATION

All domains can be aligned to each other by application of an external magnetic field (H_a), if intense enough, with resulting magnetisation parallel to the direction of the applied magnetic field. When the external magnetic field is removed, the domains keep their alignment, as their walls pin to crystal defects, and thus generate their own magnetic field (B), which plotted as a function of the applied field gives a hysteresis loop (see Figure 3.5.2), whose intercepts with the abscissa (H_a axis, i.e. $B = 0$) and the ordinate (B axis, i.e. $H_a = 0$) define respectively the coercivity H_C and the remanence B_R: the latter (B_R) is the value of the residual magnetisation after the external magnetic field has been removed ($H_a = 0$), whereas the former (H_C) is the intensity of the applied magnetic field necessary to demagnetise the material ($B = 0$). The maximum value of magnetisation is called "saturation magnetisation", which takes place when all domains are lined up, and is typically indicated with M_S.

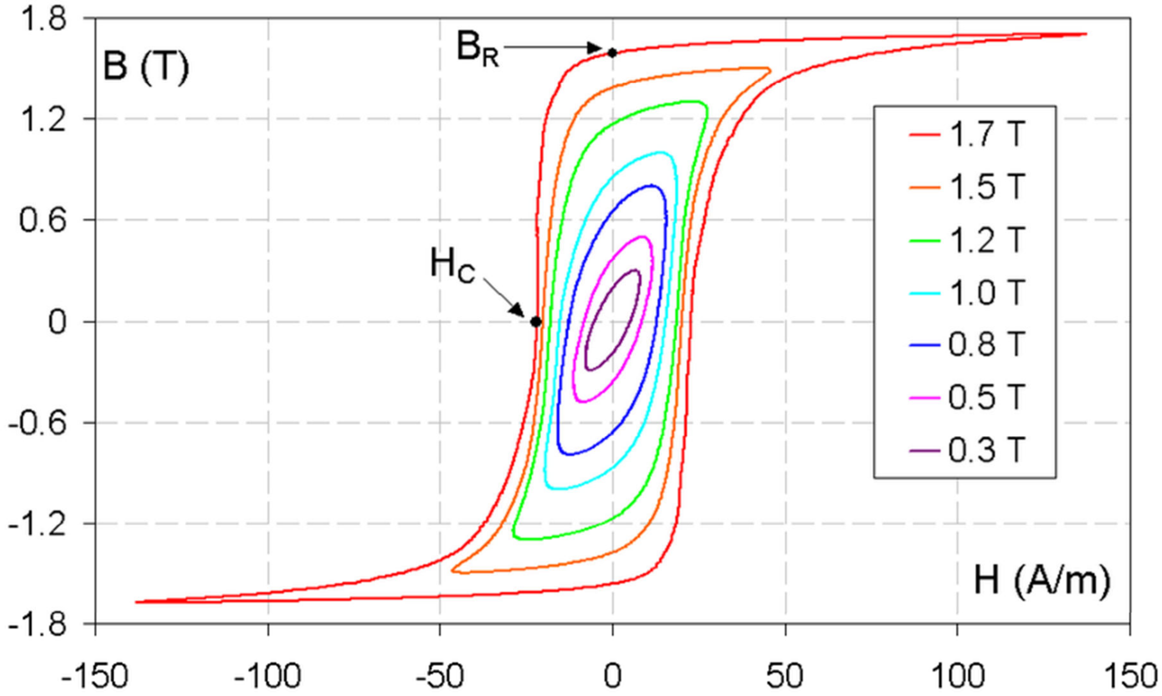

Figure 3.5.2. Examples of hysteresis loops: H_C and B_R indicate respectively coercivity and remanence. The inset shows the values of saturation magnetisation M_S for each hysteresis curve [23].

3.5.3.5. CURIE TEMPERATURE

As already mentioned, magnetic properties are temperature-dependant, due to random thermal motion. Ferromagnetic materials have a characteristic critical temperature, called the "Curie temperature" (T_C), above which spontaneous magnetisation is lost and the material becomes paramagnetic, whereby magnetic spins are randomly aligned, unless an external magnetic field is applied. Cobalt, iron and nickel have the following Curie temperatures respectively: $T_{\mathrm{C,\,Co}} = 1400$ K, $T_{\mathrm{C,\,Fe}} = 1043$ K, $T_{\mathrm{C,\,Ni}} = 631$ K.

3.5.4. ANTI-FERROMAGNETIC MATERIALS

Anti-ferromagnetism is similar to ferromagnetism, but magnetic moments align in a regular anti-parallel pattern, i.e. with neighbouring spins pointing in opposite directions, thus resulting in a vanishing net magnetisation in the absence of an externally applied magnetic field; when an external magnetic field is applied, ferrimagnetism may appear, as a result of non-zero net magnetisation. Ferrimagnetism (see next sub-section) can arise in anti-ferromagnetic materials with slightly canted structures, e.g. $YFeO_3$ (yttrium ferrite, abbreviated as YFO), a slightly canted perovskite [32].

Like ferromagnetic substances, anti-ferromagnetic materials feature a characteristic critical temperature, called the "Néel temperature" (T_{N}), above which magnetic order is lost and the material becomes paramagnetic. Examples of anti-ferromagnetic materials are Cr, NiO and CoO, whose Néel temperatures are $T_{\mathrm{N,\,Cr}} = 308$ K, $T_{\mathrm{N,\,NiO}} = 525$ K and $T_{\mathrm{N,\,CoO}} = 291$ K respectively.

3.5.5. FERRIMAGNETIC MATERIALS

Ferrimagnetism is similar to anti-ferromagnetism, but the opposing magnetic moments in the material are not equal, thus resulting in a non-zero spontaneous magnetisation: the unequal opposing magnetic moments derive from different ions (e.g. Fe^{2+} and Fe^{3+} in magnetite, Fe_3O_4). Like anti-ferromagnetic substances, ferrimagnetic materials are characterised by the "Néel temperature" (T_{N}), above which magnetic order is lost and the material becomes paramagnetic; some materials, such as magnetic garnets, feature a value of temperature $T < T_{\mathrm{N}}$, called the "magnetisation compensation point", for which the opposing magnetic moments cancel each other, so that the net magnetisation is zero.

Examples of anti-ferromagnetic materials are Cr, the aforementioned magnetite (Fe_3O_4), ferrites and magnetic garnets such as YIG. Néel temperatures of Fe_3O_4 and YIG are $T_{\mathrm{N,\,Fe3O4}} = 858$ K and $T_{\mathrm{N,\,YIG}} = 553$ K respectively; the canted anti-ferromagnetic YFO has a

Néel temperature $T_{\mathrm{N,\ YFO}} = 644.5$ K. Ferrimagnetic materials typically feature also high resistivity and anisotropic properties which can be induced by an external applied field.

A schematic summary of paramagnetic, ferromagnetic, anti-ferromagnetic and ferrimagnetic materials is depicted in Figure 3.5.3, where arrows represent magnetic dipoles.

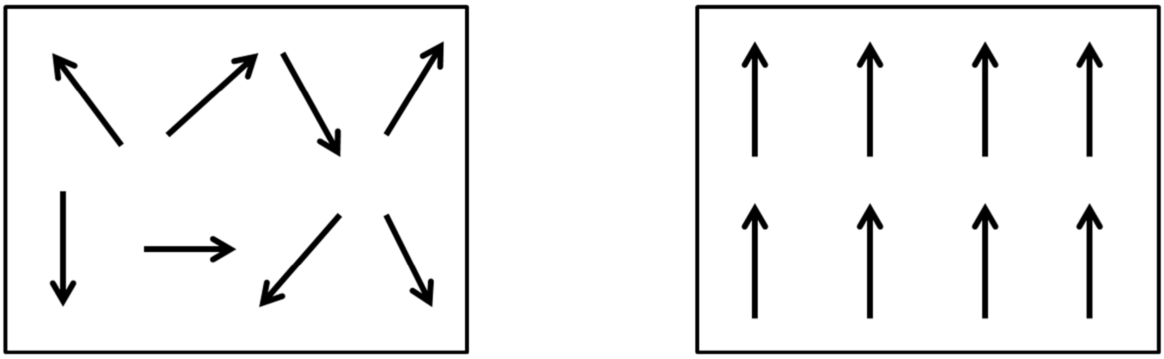

a. Paramagnetic material **b.** Ferromagnetic material

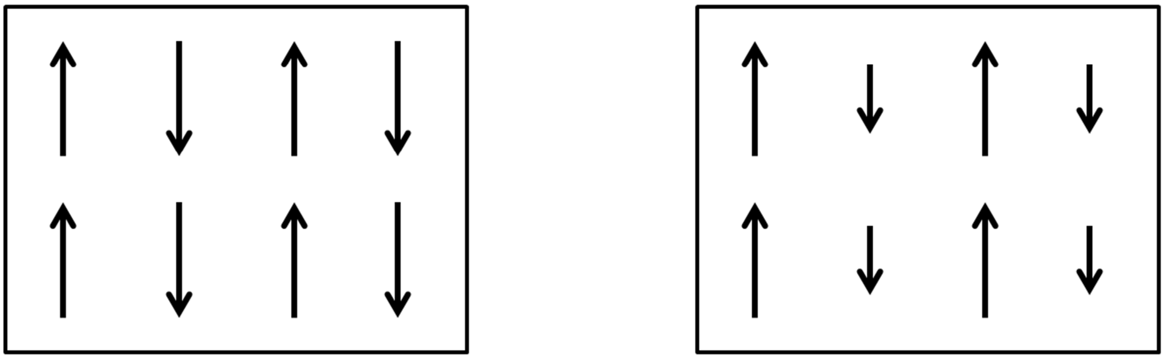

c. Anti-ferromagnetic material **d.** Ferrimagnetic material

Figure 3.5.3. Summary of magnetic materials: arrows indicate magnetic dipoles.

3.6. MAGNETO-OPTIC GARNETS

Garnets are a class of crystalline oxide compounds with a characteristic lattice structure, but whose composition can vary greatly; typical garnets are YIG (Yttrium Iron Garnet, $Y_3Fe_5O_{12}$), YAG (Yttrium Aluminium Garnet, $Y_3Al_5O_{12}$) and GGG (Gadolinium Gallium Garnet, $Gd_3Ga_5O_{12}$). For the scope of this thesis, this section will focus on a narrower group of garnets, that is the so-called magneto-optic garnets, whose name derive from their magneto-optic properties and whose most common representative is YIG, which will be used as a reference in this section.

3.6.1. STRUCTURAL PROPERTIES

The general chemical formula of garnets is the following: $\{c^{3+}\}_3[a^{3+}]_2(d^{3+})_3O_{12}$, where the different brackets indicate the different coordination of cations with respect to oxygen anions in the crystal: c^{3+} ions occupy the dodecahedral sites, indicated by { }, a^{3+} ions occupy the octahedral sites, indicated by [ ], and d^{3+} ions occupy the tetrahedral sites, indicated by ( ). The crystal structure of garnets is rhombohedral or cubic, whose unit cell is a body-centred cube, containing 160 ions, with a fairly large lattice constant: (1.2 – 1.3) nm. Such a loose structure, shown in Figure 3.6.1 for YIG as an example, can accommodate a very large variety of cations [33], which thus allows material properties to be tuned (e.g. magnetic and optical properties) by changing its composition. The dodecahedral sites are generally occupied by large trivalent ions, such as Bi^{3+}, Y^{3+} and other rare-earth ions, e.g. Ce^{3+}, Gd^{3+} and other lanthanides; octahedral and tetrahedral sites are normally occupied by medium-sized trivalent ions, such as Al^{3+}, Ga^{3+} and Fe^{3+} [34, 35].

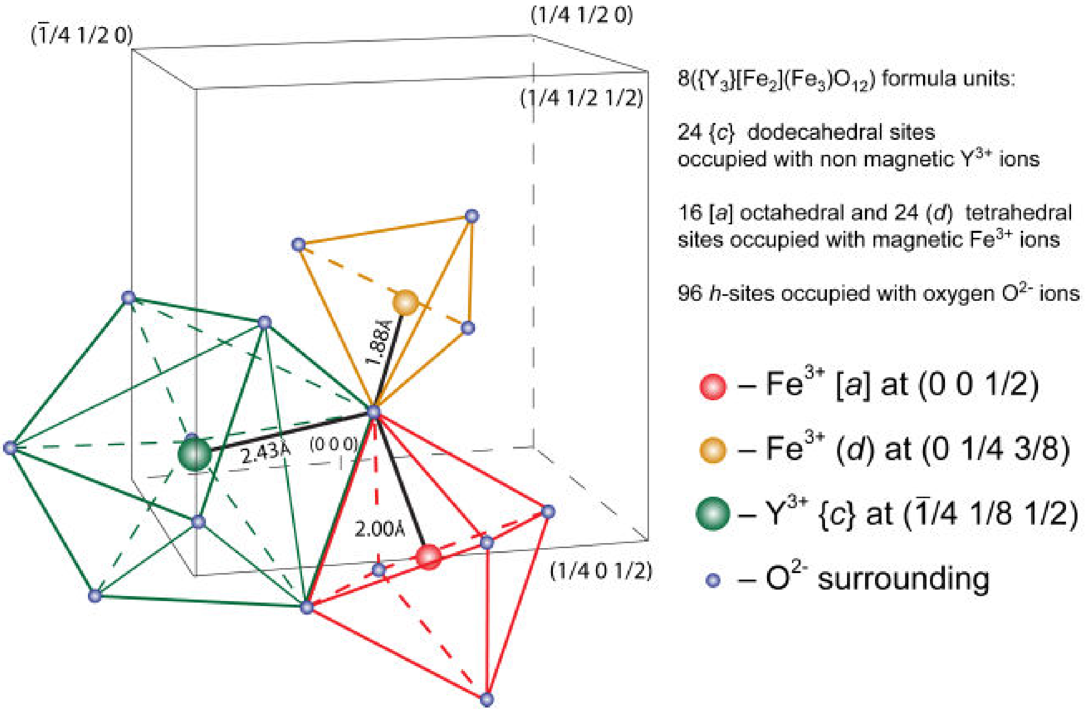

Figure 3.6.1. Crystal structure of YIG [33].

The materials studied in this thesis can be defined as iron garnets ($X_3Fe_5O_{12}$, where X can be Y, Bi, Ce or a combination of these), as they all contain iron (Fe) ions in the octahedral and tetrahedral sites. As explained in the next section, magnetic properties arise from Fe ions. Substitution of Y in YIG with a different atom (e.g. Bi or Ce) will result in a different lattice constant, according to Vegar's law – see Equation (3.2.8). The rare earth iron garnet with the smallest lattice constant is $Lu_3Fe_5O_{12}$ (a_{LIG} = 1.2283 nm), whereas the largest is found in $Sm_3Fe_5O_{12}$ (a_{SIG} = 1.2583 nm) [33]; $Bi_3Fe_5O_{12}$ has an even higher lattice constant: a_{BIG} = 1.2623 nm [36], but this prevents its growth in bulk form and as a thin film in thermodynamic equilibrium conditions. Table 3.6.1 reports and compares some properties (lattice constant a and TEC ρ) of YIG and of the garnet materials used as substrates for film growth by PLD. All garnets are isotropic due to their crystal symmetry.

MATERIAL:	a [nm]	ρ [10^{-6} K^{-1}]
YIG	1.2376 [11]	10 [13, 14]
GGG	1.2383 [11]	9.3 [13, 14]
YAG	1.2006 [12]	7.5 [15]

Table 3.6.1. Comparison of lattice constants and TECs of some garnets.

3.6.2. MAGNETIC PROPERTIES

Magnetic properties in iron garnets arise from magnetic Fe^{3+} ions in their crystal structure, where oxygen ions influence their electronic configuration, resulting in the aforementioned anti-ferromagnetic super-exchange coupling between the [Fe^{3+}] and the (Fe^{3+}) ions, each of which has a $3d^5$ electronic configuration and hence a magnetic moment of $5\mu_B$ (at $T = 0$ K); considering one formula unit of YIG and the fact that the {Y^{3+}} ion has a zero magnetic moment, the balance of the magnetic moments of the three Fe^{3+} ions in the octahedral sites with those of the two Fe^{3+} ions in the tetrahedral sites gives a total magnetic moment of $5\mu_B$ per formula unit (see Figure 3.6.2), thus resulting in ferrimagnetism in YIG. If non-magnetic {Y^{3+}} ions are replaced with magnetic ions, the super-exchange will be altered [33].

Super-exchange is a strong coupling between two next-to-nearest neighbour magnetic cations (e.g. Fe^{3+}) through a non-magnetic anion (e.g. O^{2-}), thus differing from direct exchange interaction, which couples nearest neighbour cations without involving an intermediary anion.

Ferrimagnetic materials, such as YIG, have generally high resistivity and, when an external magnetic field is applied, they also feature the magneto-optic effect and a particular phenomenon called "ferromagnetic resonance", abbreviated as FMR. Both magneto-optic effect and FMR arise from the splitting of energy levels (electronic states), which can be due to Zeeman splitting (similar to the Stark effect[6]) when an external magnetic field is applied, electron-electron interactions, crystal field splitting and exchange interaction [37].

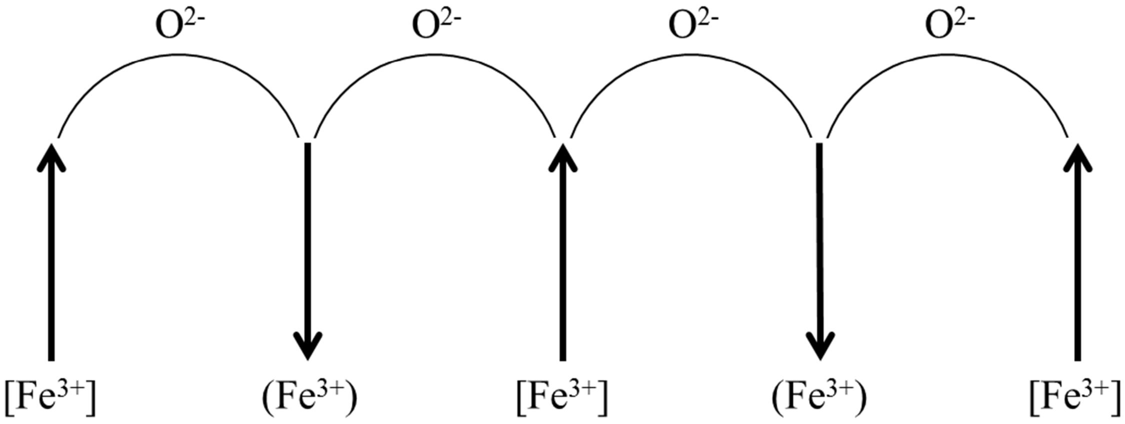

Figure 3.6.2. Anti-ferromagnetic super-exchange of magnetic moments in iron garnets.

3.6.2.1. FERROMAGNETIC RESONANCE (FMR)

FMR arises from the precessional motion of the magnetization vector $\vec{M}$ of a ferro- or ferri-magnetic material in an external magnetic field $\vec{H}$. The applied magnetic field exerts a torque on the sample magnetization $\vec{M}$ which causes the magnetic moments in the sample to precess around the direction of the externally applied magnetic field $\vec{H}$ (Larmor precession), as shown in Figure 3.6.3.

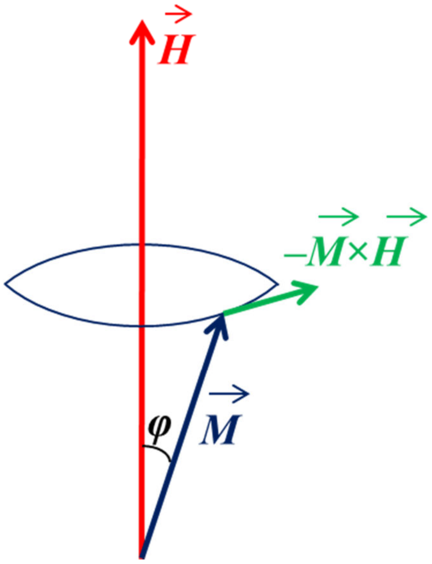

Figure 3.6.3. Schematic of ferromagnetic resonance (FMR).

---

[6] Shifting and splitting of spectral lines of atoms and molecules induced by an external electric field.

The following treatise follows references [38, 39].

The externally applied magnetic field $\vec{H}$ applies a torque to the magnetisation vector $\vec{M}$:

$$\vec{\Gamma} = \vec{M} \times \mu_0 \vec{H} \tag{3.6.1}$$

This causes the precession motion of the magnetisation vector $\vec{M}$ around $\vec{H}$ at the so-called "Larmor frequency", ω_L, giving rise to a change in the angular momentum $\vec{J}$ of the magnetic moments:

$$\frac{d\vec{M}}{dt} = -\gamma\vec{\Gamma} = -\gamma\mu_0\vec{M} \times \vec{H} \tag{3.6.2}$$

where γ is the gyromagnetic ratio, defined as:

$$\gamma = \frac{g\mu_B}{\hbar} \tag{3.6.3}$$

with g the spectroscopic splitting factor, also called "Landé factor".

The velocity at the top point of the magnetisation vector $\vec{M}$ is:

$$v = \left|\frac{d\vec{M}}{dt}\right| = \gamma\mu_0 MH \sin\varphi \tag{3.6.4}$$

with φ the angle between $\vec{M}$ and $\vec{H}$ vectors. Using $\varrho = M\sin\varphi$ as the radius of the circle and replacing it into the velocity equation above, the frequency of natural precession (Larmor frequency) of $\vec{M}$ around $\vec{H}$ is determined:

$$\omega_L = \frac{v}{\varrho} = \gamma\mu_0 H \tag{3.6.5}$$

This shows that the precession frequency of the magnetization depends on the orientation of the material, the strength of the externally applied magnetic field H, as well as the macroscopic magnetization of the sample through the Landé factor g in the gyromagnetic ratio γ.

The external magnetic field $\vec{H}$ should actually be replaced by $\vec{H}_{\text{eff}}$, i.e. the effective magnetic field, which is the vectorial sum of all the magnetic fields (e.g. demagnetising and anisotropy fields) that affect the system. Considering a RF magnetic field ($\vec{H}_{RF}e^{i\omega t}$) applied perpendicularly to the DC field ($\vec{H}_0$), which includes all DC components:

$$\vec{H}_{\text{eff}} = \vec{H}_0 + \vec{H}_{RF}e^{i\omega t} \tag{3.6.6}$$

The system will absorb energy from the RF field at all frequencies, with increasing absorption when the RF frequency approaches the Larmor frequency from either side, thus resulting in attenuation of the RF signal, which can be measured through a vector network analyzer (VNA), together with the FMR linewidth, i.e. the full-width-at-half-maximum (FWHM) of the RF signal attenuation curve versus RF frequency (more details about the experimental set-up in Section 4.10). The energy absorption from the RF field causes an increase of the radial amplitude of the precession motion of $\vec{M}$ around $\vec{H}_0$. Ferromagnetic resonances are typically in the microwave range, i.e. ~(0.1 – 100) GHz.

The theory outlined so far does not include any damping factor, so that the magnetisation vector $\vec{M}$ would precess indefinitely around $\vec{H}$; however, this is not the case in reality: relaxation occurs and $\vec{M}$ tends to return to its equilibrium position along $\vec{H}$ in a period of the order of nanoseconds, with energy transferred from the precessing dipole to the lattice via either spin-lattice relaxation, mediated by spin-orbit interaction, and/or spin wave excitations [38]. So, the equations above must be corrected by considering a precessional damping of the magnetisation, which also limits the amplitude of precession. A damping term can be introduced into Equation (3.6.2), which gives the Landau-Lifshitz equation:

$$\frac{d\vec{M}}{dt} = -\gamma\mu_0\vec{M} \times \vec{H}_{eff} + \frac{\alpha}{M_S}\left(\vec{M} \times \frac{d\vec{M}}{dt}\right) \tag{3.6.7}$$

where α is an intrinsic attenuation or damping factor, with $\alpha < 1$ for most ferromagnetic materials. The damping will result in a broader FMR linewidth.

The real FMR frequency will depend on the demagnetisation fields in the sample. Solving the Landau-Lifshitz equation for the case of thin-film geometry (i.e. in-plane magnetic anisotropy) gives the following resonance frequency:

$$\omega_0 = \gamma(B_0 - \mu_0 M_S) \tag{3.6.8}$$

with $B_0 = \mu_0 H_0$.

3.6.2.2. DEMAGNETISING FIELD

The shape of magnetic samples affects their magnetisation. Considering a thin film, if an external magnetic field is applied perpendicular to the film surface, magnetic moments or dipoles will be aligned parallel to each other and normal to the film surface too; however, this configuration is less energetically-favourable, compared to the in-plane magnetisation, i.e. the case when the external magnetic field is applied parallel to the film surface, inducing magnetic moments to align parallel to each other and to the surface too, a tail-to-head configuration which requires less energy. The demagnetising field derives from Maxwell's equation $\nabla \cdot \vec{B} = 0$, which implies $\nabla \cdot \vec{H}_{\mathrm{dem}} = -\nabla \vec{M}$, which means that the demagnetising field is opposite to the direction of the magnetisation inside the film: in the latter of the cases considered before, the demagnetising field is negligible, due to the large separation between the magnetic poles (large aspect ratio) at the small side surfaces of the film (see Figure 3.6.4) [38].

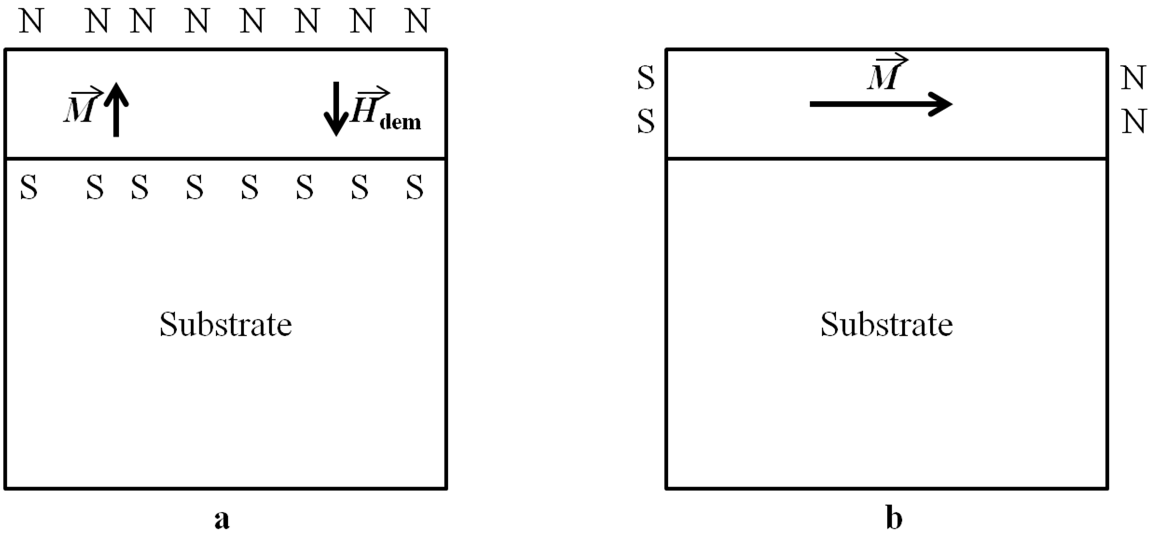

Figure 3.6.4. Schematic cross-section of magnetic samples with **(a)** out-of-plane magnetisation and **(b)** in-plane magnetisation.

3.6.3. OPTICAL AND MAGNETO-OPTICAL PROPERTIES

Due to the isotropic crystal structure of garnets, these materials exhibit isotropic optical properties too. The garnets used as substrates in this thesis, i.e. YAG and GGG, are optically transparent in a wide range of wavelengths and, in particular, in the UV-visible and visible-NIR parts of the electromagnetic spectrum (400 nm $\leq \lambda \leq$ 1500 nm), as confirmed by optical spectroscopy; magneto-optic garnets instead have different optical behaviour [35, 40, 41]. In general, absorption in the UV-visible range starts between $\lambda \approx$

300 and $\lambda \approx 350$ nm, due to the charge transfer, i.e. the raising of an electron in the *d* sub-shell from the ground state to another higher-energy level; the sensitivity of the *d*-electron to the crystal field is very high, thus affecting the width of this absorption band. The transitions which cause optical absorption in iron garnets come from the Fe^{3+} ions on the tetrahedral and octahedral sites; three main processes can be distinguished [35]:

1) inter-sub-lattice Fe^{3+}-pair transitions, resulting in strong absorption at $\lambda \leq 450$ nm,
2) crystal field transitions, resulting in a weak absorption in the band (450 – 1000) nm,
3) optical phonons (lattice vibrations and atomic transitions), leading to an increase in absorption at $\lambda \geq 10$ μm.

Substitution of Fe^{3+} ions with diamagnetic ions reduces optical absorption, but it also decreases the magnetic properties. Y^{3+}-substitution with Bi^{3+} ions causes a shift in the band edge and an increase of optical absorption in the visible [35]. The valence of substituting ions is important too: for instance, Ce^{4+} ions in Ce:YIG cause additional absorption [42].

The microscopic origins of magneto-optic properties in iron garnets are not fully understood, although it is believed that they originate from high-energy charge transfer optical transitions [33, 35]. Magneto-optic effects are non-reciprocal[7] phenomena, which are distinguished in transmission (Faraday effect) and reflection (Kerr effect): both phenomena consist of the rotation of the polarisation of a linearly-polarised optical beam incident on the magnetised materials.

Figure 3.6.5 shows the working principle of a Faraday rotator/isolator: a polarised light beam propagating through a magneto-optic material, magnetised along the same direction as the light propagation direction, undergoes a polarisation rotation Φ proportional to the length of the device l_F and to the intensity of the externally applied magnetic field H; if the light beam is reflected back, i.e. the propagation light direction is reversed (dashed red line), the light beam polarisation will undergo a further rotation Φ; if $\Phi = 45°$, the reflected light beam, whose polarisation is now rotated by $2\Phi = 90°$ with respect to the original polarisation, will be blocked by the polariser, so that the whole system acts as an optical

---

[7] Reciprocity means that (optical) properties are spatially invariant: e.g. if the light propagation direction is reversed, the light encounters the same optical properties (e.g. refractive index), as in the case of reflection and refraction in isotropic material; thus, in non-reciprocal phenomena, a light beam undergoes different changes when its propagation direction is reversed.

isolator, which can be used to protect light sources from unwanted reflections, which may for example damage or otherwise affect laser operation.

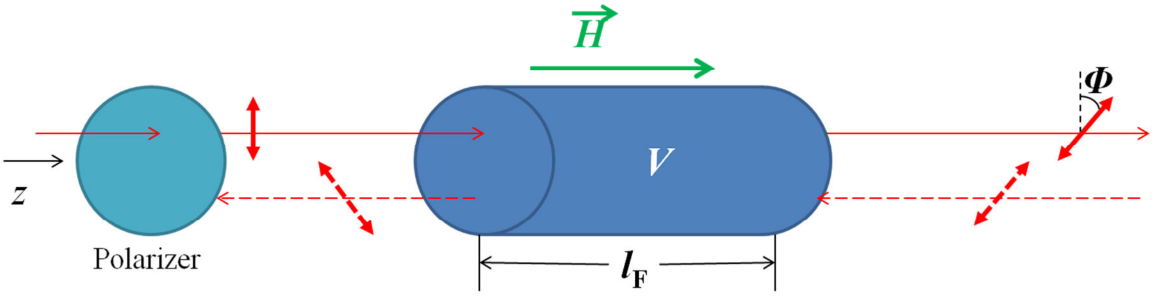

Figure 3.6.5. Working principle of Faraday rotator/isolator: H is the applied magnetic field, l_F is the length of the magneto-optic material, V its Verdet constant and Φ the Faraday rotation angle.

The polarisation rotation angle Φ, also called the Faraday rotation angle, is defined as:

$$\Phi = VHl_F \tag{3.6.9}$$

with V the Verdet constant of the magneto-optic material, expressed in deg/(T×m), which is a function of wavelength λ and temperature T: $V = V(\lambda, T)$, so that we also have: $\Phi = \Phi(\lambda, T)$. Generally the Verdet constant decreases with increasing wavelength λ, typically with high values in the visible, where iron garnets feature relatively strong optical absorption, and lower values in the NIR, where iron garnets are optically transparent.

In some cases the polarisation angle per unit length, expressed in deg/m, is provided; it is defined as:

$$\phi = \frac{\Phi}{l_F} = VH \tag{3.6.10}$$

The following treatise follows references [35, 43, 44].

Generally magneto-optic materials, including iron garnets, are isotropic in the absence of an externally applied magnetic field, thus acting as any other isotropic and reciprocal material, producing typical reflection and refraction phenomena, but no Faraday rotation. As aforementioned, an externally applied magnetic field (along the z axis) will introduce anisotropy in magneto-optic materials, making them non-reciprocal, due to the fact that the permittivity or dielectric constant (a scalar for isotropic and reciprocal materials) becomes an anti-symmetric tensor, with $\varepsilon_{yx} = -\varepsilon_{xy}$, $\varepsilon_{xx} = \varepsilon_{yy} = \varepsilon_{\perp}$ and $\varepsilon_{zz} = \varepsilon_{/\!/}$.

$$\begin{bmatrix} \varepsilon_{\perp} & \varepsilon_{xy} & 0 \\ -\varepsilon_{xy} & \varepsilon_{\perp} & 0 \\ 0 & 0 & \varepsilon_{/\!/} \end{bmatrix} \tag{3.6.11}$$

In the case of no absorption, $\varepsilon_\perp$ and $\varepsilon_{/\!/}$ are purely real, whereas ε_{xy} is purely imaginary; in case of parallel magnetisation and optical propagation along the *z* axis in Figure 3.6.5 and describing light polarisation in terms of two orthogonal circularly polarised waves, right-circularly-polarised (RCP) E_+, rotating clockwise, and left-circularly-polarised (LCP) E_-, rotating anti-clockwise:

$$E_\pm = E_\mathrm{x} \pm E_\mathrm{y} = E_\mathrm{A} e^{-i\omega t} \tag{3.6.12}$$

where $E_\mathrm{x} = E_\mathrm{A}\cos\omega t$, $E_\mathrm{y} = E_\mathrm{A}\sin\omega t$ and E_A is the amplitude of the electric field, the two polarisation components E_+ and E_- will see different refractive indexes and thus propagate with different propagation constants:

$$n_\pm = \sqrt{\varepsilon_\pm} = \sqrt{\varepsilon_\perp \pm i\varepsilon_\mathrm{xy}} \tag{3.6.13}$$

$$\beta_\pm = \omega\sqrt{\mu_0\varepsilon_0\varepsilon_\pm} = n_\pm k_0 \tag{3.6.14}$$

where $k_0 = \frac{2\pi}{\lambda} = \omega\sqrt{\varepsilon_0\mu_0}$ is the propagation constant of light in vacuum – from the definition of the speed of light in vacuum in Equation (3.3.8).

This will cause a phase change, i.e. the aforementioned rotation of polarisation, as schematically shown in Figure 3.6.6.a:

$$2\Phi = k_0 l_\mathrm{F}(n_+ - n_-) \tag{3.6.15}$$

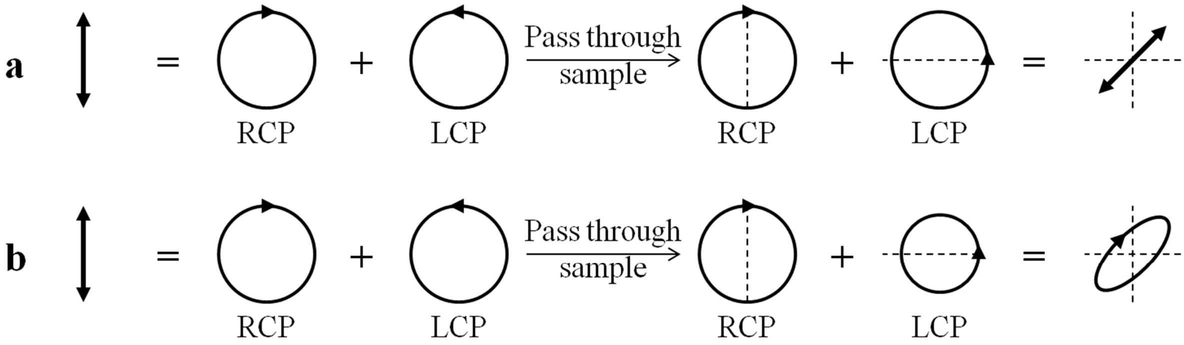

Figure 3.6.6. Faraday effect in the cases of **(a)** no absorption; **(b)** optical absorption.

In general, $\varepsilon_\perp$, $\varepsilon_{/\!/}$ and ε_{xy} are complex, so that the refractive indexes $n_\pm$ are complex too: different absorption coefficients for RCP and LCP waves derive from their imaginary parts, thus causing the so-called "Faraday ellipticity":

$$\psi = \frac{1}{2} k_0 l_\mathrm{F} \mathrm{Im}(n_+ - n_-) \tag{3.6.16}$$

so that the two polarisation components, with different amplitudes, produce an elliptical polarisation, as shown in Figure 3.6.6.b.

For small ellipticity, the complex Faraday rotation angle is thus:

$$\Phi + \psi = \frac{1}{2} k_0 l_\mathrm{F} (n_+ - n_-) \tag{3.6.17}$$

From a microscopic point of view, the magneto-optic effect can be explained with different electric-dipole transitions induced by RCP and LCP waves/photons, due to their different magnetic moments $\mu_\mathrm{m} = \pm 1$, as shown in Figure 3.6.7, where level splitting can be caused by the Zeeman effect, electron-electron interactions, crystal field splitting and exchange interaction. This means that any change in the crystal structure and composition (e.g. substitution of diamagnetic Y^{3+} with Bi^{3+} in YIG) will result in changes in the energy level system and transitions, making the understanding of magneto-optical transitions even more complicated.

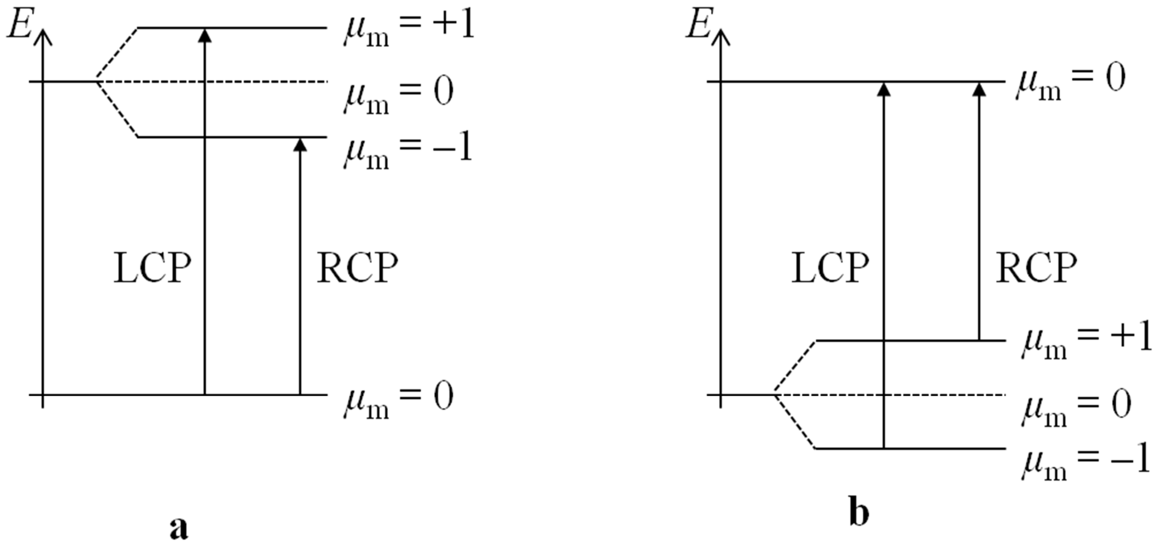

Figure 3.6.7. Schematic of **(a)** "diamagnetic" and **(b)** "paramagnetic" transitions. The names are just historical.

3.6.4. SUBSTITUTED YTTRIUM IRON GARNET

Substitution of diamagnetic $\{Y^{3+}\}$ ions with ionic species with non-zero magnetic moment (e.g. rare-earth ions and Bi^{3+}) will alter not only structural (e.g lattice constant) and optic properties (e.g. refractive index and absorption), but also magnetic and magneto-optic properties of iron garnets (e.g. Néel temperature, saturation magnetisation and Verdet constant). Substitution of Fe^{3+} ions in either the octahedral or tetrahedral sites will have effects on magnetic properties too: e.g. substituting magnetic Fe^{3+} ions with non-magnetic Ga^{3+}, which tend to occupy mainly the tetrahedral sites, will result in a reduction of magnetic contribution from this sub-lattice and thus in a decreasing net magnetisation. In general, the temperature-dependant saturation magnetisation of the crystal $M_S(T)$ is given by the sum of the sub-lattice magnetisations:

$$M_S(T) = |M_{\{c\}}(T) - M_{[a]}(T) + M_{(d)}(T)| \tag{3.6.18}$$

where $M_{\{c\}}(T)$, $M_{[a]}(T)$ and $M_{(d)}(T)$ are saturation magnetisation of dodecahedral, tetrahedral and octahedral sub-lattices respectively [33-35].

3.7. CONCLUSIONS

This chapter has provided fundamentals of all the physics involved in this thesis, necessary to understand the experiments and the results described and discussed in the next chapters: pulsed laser ablation, film growth, waveguide theory and basics of magnetism; materials of interest for the purpose of this thesis, i.e. Ti:sapphire and magneto-optic garnets, and their characteristics have been introduced too.

3.8. REFERENCES

1. D. B. Chrisey, and G. K. Hulber, ed.: *Pulsed Laser Deposition of Thin Films* (Wiley Interscience, 1994).

2. R. W. Eason, ed.: *Pulsed Laser Deposition of Thin Films – Applications-led Growth of Functional Materials* (Wiley Interscience, 2007).

3. A. A. Anderson, "Crystalline planar waveguide lasers fabricated by pulsed laser deposition," PhD thesis at *Optoelectronics Research Centre* (University of Southampton, Southampton, 1998).

4. T. C. May-Smith, "Pulsed laser deposition of thick multilayer garnet crystal films for waveguide laser devices," PhD thesis at *Optoelectronics Research Centre* (University of Southampton, Southampton, 2005).

5. K. A. Sloyan, "Multi-beam pulsed laser deposition for engineered crystal films," PhD thesis at *Optoelectronics Research Centre* (University of Southampton, Southampton, 2013).

6. S. R. Jackson, W. J. Metheringham, and P. E. Dyer, "Excimer-laser ablation of Nd:YAG and Nd:glass," Appl. Surf. Sci. **86**, 223-227 (1995).

7. R. Delmdahl, and R. Patzel, "Pulsed laser deposition - UV laser sources and applications," Appl. Phys. A-Mater. Sci. Process. **93**, 611-615 (2008).

8. R. Castro-Rodriguez, D. R. Coronado, A. Iribarren, B. E. Watts, F. Leccabue, and J. L. Pena, "Correlation between target-substrate distance and oxygen pressure in pulsed laser deposition of complex oxide thin films," Appl. Phys. A Mater. Sci. **81**, 1503-1507 (2005).

9. N. Kaiser, "Review of the fundamentals of thin-film growth," Appl. Optics **41**, 3053-3060 (2002).

10. T. C. May-Smith, K. A. Sloyan, R. Gazia, and R. W. Eason, "Stress Engineering and Optimization of Thick Garnet Crystal Films Grown by Pulsed Laser Deposition," Cryst. Growth Des. **11**, 1098-1108 (2011).

11. A. A. Serga, A. V. Chumak, and B. Hillebrands, "YIG magnonics," J. Phys. D-Appl. Phys. **43**, 16 (2010).

12. A. Nakatsuka, A. Yoshiasa, and T. Yamanaka, "Cation distribution and crystal chemistry of $Y_3Al_{5-x}Ga_xO_{12}$ ($0 \leq x \leq 5$) garnet solid solutions," Acta Crystallogr. Sect. B-Struct. Sci. **55**, 266-272 (1999).

13. T. Boudiar, B. Payet-Gervy, M. F. Blanc-Mignon, J. Rousseau, M. Le Berre, and H. Joisten, "Magneto-optical properties of yttrium iron garnet (YIG) thin films elaborated by radio frequency sputtering," J. Magn. Magn. Mater. **284**, 77-85 (2004).

14. S. M. Shahrokhvand, A. S. H. Rozatian, M. Mozaffari, S. M. Hamidi, and M. M. Tehranchi, "Preparation and investigation of Ce:YIG thin films with a high magneto-optical figure of merit," J. Phys. D-Appl. Phys. **45**, 235001 (2012).

15. R. Paschotta, "RP Photonics Encyclopedia," http://www.rp-photonics.com/, Accessed December 2013.

16. N. B. Ibrahim, C. Edwards, and S. B. Palmer, "Yttrium iron garnet surface modification during pulsed laser ablation deposition," Mater. Sci. **22**, 111-115 (2004).

17. S. J. Barrington, T. Bhutta, D. P. Shepherd, and R. W. Eason, "The effect of particulate density on performance of Nd:$Gd_3Ga_5O_{12}$ waveguide lasers grown by pulsed laser deposition," Opt. Commun. **185**, 145-152 (2000).

18. A. A. Gorbunov, W. Pompe, A. Sewing, S. V. Gaponov, A. D. Akhsakhalyan, I. G. Zabrodin, I. A. Kaskov, E. B. Klyenkov, A. P. Morozov, N. N. Salaschenko, R. Dietsch, H. Mai, and S. Vollmar, "Ultrathin film deposition by pulsed laser ablation using crossed beams," Appl. Surf. Sci. **96-8**, 649-655 (1996).

19. R. Jordan, D. Cole, and J. G. Lunney, "Pulsed laser deposition of particulate-free thin films using a curved magnetic filter," Appl. Surf. Sci. **109**, 403-407 (1997).

20. C. Grivas, "Optically pumped planar waveguide lasers, Part I: Fundamentals and fabrication techniques," Prog. Quantum Electron. **35**, 159-239 (2011).

21. P. G. Lucuta, J. D. Halliday, and B. Christian, "Phase evolution in Al_2O_3 fiber prepared from an oxychloride precursor," J. Mater. Sci. **27**, 6053-6061 (1992).

22. "MolTech GmbH sapphire datasheet," http://www.mt-berlin.com/frames_cryst/descriptions/sapphire.htm, Accessed December 2013.

23. "Wikipedia," http://www.wikipedia.org/, Accessed December 2013.

24. P. F. Moulton, "Spectroscopic and laser characteristics of Ti-Al_2O_3," J. Opt. Soc. Am. B-Opt. Phys. **3**, 125-133 (1986).

25. K. F. Wall, and A. Sanchez, "Titanium sapphire lasers," Linc. Lab. J. **3**, 447-462 (1990).

26. M. Yamaga, T. Yosida, S. Hara, N. Kodama, and B. Henderson, "Optical and electron-spin-resonance spectroscopy of Ti^{3+} and Ti^{4+} in Al_2O_3," J. Appl. Phys. **75**, 1111-1117 (1994).

27. A. Sanchez, A. J. Strauss, R. L. Aggarwal, and R. E. Fahey, "Crystal-growth, spectroscopy, and laser characteristics of Ti-Al_2O_3," IEEE J. Quantum Electron. **24**, 995-1002 (1988).

28. I. T. McKinnie, A. L. Oien, D. M. Warrington, P. N. Tonga, L. A. W. Gloster, and T. A. King, "Ti^{3+} ion concentration and Ti:sapphire laser performance," IEEE J. Quantum Electron. **33**, 1221-1230 (1997).

29. P. Lacovara, L. Esterowitz, and M. Kokta, "Growth, spectroscopy, and lasing of titanium-doped sapphire," IEEE J. Quantum Electron. **21**, 1614-1618 (1985).

30. R. L. Aggarwal, A. Sanchez, M. M. Stuppi, R. E. Fahey, A. J. Strauss, W. R. Rapoport, and C. P. Khattak, "Residual infrared-absorption in as-grown and annealed crystals of Ti-Al_2O_3," IEEE J. Quantum Electron. **24**, 1003-1008 (1988).

31. "TLP (Teaching and Learning Packages) Library at DoITPoMS (Dissemination of IT for the Promotion of Materials Science) of the University of Cambridge," http://www.doitpoms.ac.uk/tlplib/index.php, Accessed December 2013.

32. H. Shen, J. Y. Xu, A. H. Wu, J. T. Zhao, and M. L. Shi, "Magnetic and thermal properties of perovskite $YFeO_3$ single crystals," Mater. Sci. Eng. B-Adv. Funct. Solid-State Mater. **157**, 77-80 (2009).

33. F. Hansteen, "Ultrafast Optical Control of Magnetisation in Ferrimagnetic Garnets," PhD thesis at (Radboud University, Nijmegen, 2006).

34. H. Dotsch, N. Bahlmann, O. Zhuromskyy, M. Hammer, L. Wilkens, R. Gerhardt, P. Hertel, and A. F. Popkov, "Applications of magneto-optical waveguides in integrated optics: review," J. Opt. Soc. Am. B **22**, 240-253 (2005).

35. W. R. Eppler, and M. H. Kryder, "Garnets for short-wavelength magnetooptic recording," J. Phys. Chem. Solids **56**, 1479-1490 (1995).

36. M. Deb, E. Popova, A. Fouchet, and N. Keller, "Magneto-optical Faraday spectroscopy of completely bismuth-substituted $Bi_3Fe_5O_{12}$ garnet thin films," J. Phys. D-Appl. Phys. **45**, 455001 (2012).

37. S. Kahl, "Bismuth iron garnet films for magneto-optical photonic crystals," PhD thesis at *Condensed Matter Physics* (Royal Institute of Technology (KTH), Stockholm, 2004).

38. G. B. G. Stenning, "X-ray and microwave studies of strongly exchange coupled magnetic multilayers," PhD thesis at *School of Physics and Astronomy* (University of Southampton, Southampton, 2013).

39. J. Zhang, "Growth and characterization of in-plane magnetization garnet thin-films," MSc thesis at *Department of Electrical Engineering and Computer Engineering* (University of Maryland, 2004).

40. V. R. Sobol, T. V. Volchik, S. M. Arabei, B. V. Korzun, and N. A. Kalanda, "Optical constants of yttrium-iron garnet single-crystal film structures," J. Appl. Spectrosc. **76**, 203-208 (2009).

41. S. H. Wemple, S. L. Blank, J. A. Seman, and W. A. Biolsi, "Optical properties of epitaxial iron garnet thin films," Phys. Rev. B **9**, 2134-2144 (1974).

42. M. Huang, and S. Y. Zhang, "Growth and characterization of cerium-substituted yttrium iron garnet single crystals for magneto-optical applications," Appl. Phys. A-Mater. Sci. Process. **74**, 177-180 (2002).

43. S. Kahl, V. Popov, and A. M. Grishin, "Optical transmission and Faraday rotation spectra of a bismuth iron garnet film," J. Appl. Phys. **94**, 5688-5694 (2003).

44. H. Nishihara, M. Haruna, and T. Suhara, *Optical Integrated Circuits* (McGraw-Hill Professional, 1989).

4. CHAPTER 4
EXPERIMENTAL AND ANALYTICAL TECHNIQUES

4.1. INTRODUCTION

This chapter describes all the experimental and analytical techniques used to fabricate and characterise the Ti:sapphire and magneto-optic samples. Section 4.2 provides a detailed description of the PLD systems used to grow the films of Ti:sapphire and magneto-optic garnets. In Section 4.3 the procedures for target re-conditioning and target/substrate cleaning are presented. Analytical techniques are introduced in subsequent sections, starting from those for surface analysis (Section 4.4), compositional evaluation (Section 4.5) and crystal and structural examination (Section 4.6). The process of end-polishing for Ti:sapphire waveguiding films is briefly discussed in Section 4.7, whereas all the techniques for Ti:sapphire waveguide characterisation are described in Section 4.8. Spectrophotometry is presented in Section 4.9 and finally the rig for ferromagnetic characterisation described in Section 4.10. A recap is provided in Section 4.11.

4.2. PULSED LASER DEPOSITION

The PLD laboratory at the Optoelectronics Research Centre (ORC) of the University of Southampton comprises two home-built PLD systems: one for single-beam single-target PLD (single-PLD) and another one for multi-beam multi-target PLD (multi-PLD). An overview of the lab is shown in the photo in Figure 4.2.1: the vacuum chamber for single-PLD is in the foreground, with the CO_2 laser and its relative optical set-up used for heating the substrate on the left and the excimer laser on the right; the multi-PLD chamber in the background, as indicated by the red arrow. The excimer laser beam can be steered into either of the chambers by flipping a UV mirror on the optical bench between the two chambers (not clearly visible in the photo, as hidden by the single-PLD system), whereas two frequency-quadrupled Nd:YAG lasers on the optical bench are imaged onto two different target holders inside the multi-PLD chamber only, for combinatorial growth experimental purposes. The two different PLD systems are described in more detail in the next two sub-sections. They use two separate CO_2 lasers, with two different optical set-ups for substrate heating, and two separate pumping systems, comprising a turbo-molecular high-vacuum pump and a rotatory vane pump.

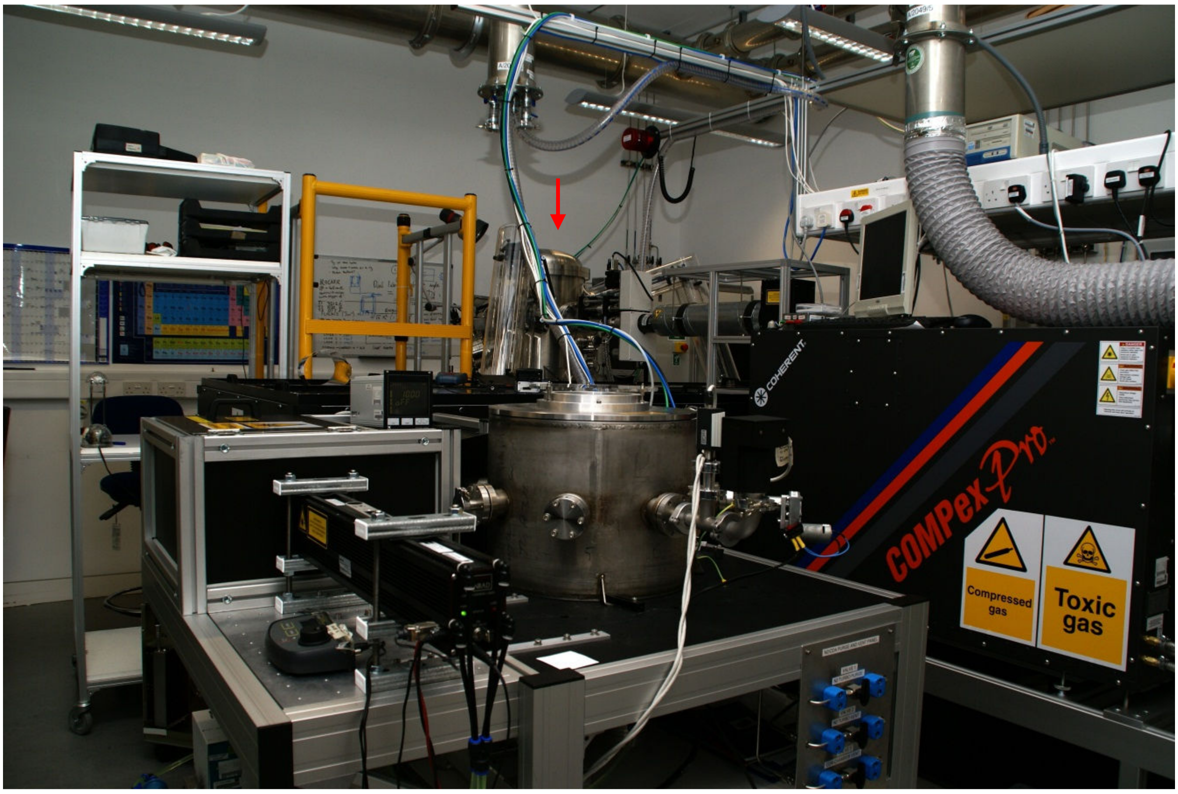

Figure 4.2.1. Overview of the PLD lab. The red arrow indicates the multi-PLD chamber.

4.2.1. SINGLE-PLD

Figure 4.2.2 shows an overview of the inside of the single-PLD chamber. The whole system comprises:

- a metal substrate holder in the centre, whose position can be adjusted relative to the target; the substrate is actually held in position from opposite corners by two notched cylindrical ceramic posts to minimise heat-sinking (see inset in Figure 4.2.2);
- a target rotator on the right; an off-set cam assembly provides an epitrochoidal ("spirograph") motion and hence a more efficient use of a larger target surface than if a purely circular ('race-track') ablation path is followed;
- a manual gas supply system (not visible in the photos), allowing injection of N_2, O_2 and Ar into the deposition chamber to control plume dynamics and film composition;
- pressure gauges for control of vacuum/gas pressure;

- a CO_2 laser (visible in Figure 4.2.1) for heating the substrate; the laser beam is homogenized to yield a square 'top-hat' profile through an optical set-up described in Section 4.2.4.1 and is enclosed in the black box visible on the left of Figure 4.2.1;
- an excimer laser, steered into the deposition chamber through an optical set-up, comprising UV mirrors and a final lens for focusing the laser beam onto the target – the laser spot size and fluence can be varied by either changing the focal length of the final lens or its position (distance from the target) to tune the magnification factor;
- aluminium cones (on the left of Figure 4.2.2), to prevent UV and IR windows from coating by unwanted stray material deposition and to lengthen their effective lifetime.

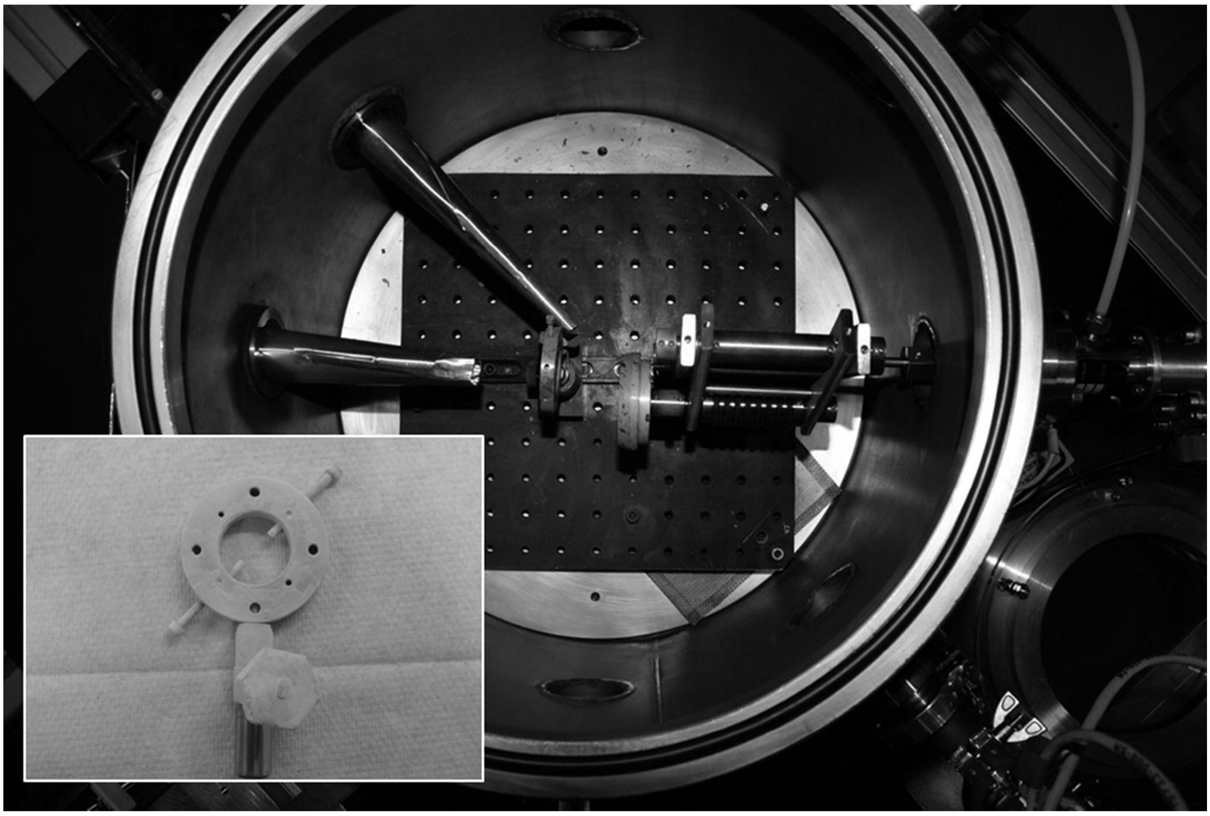

Figure 4.2.2. Overview of the single-PLD chamber. The inset shows the sample holder.

4.2.2. MULTI-PLD

Figure 4.2.3 shows an overview of the inside of the multi-PLD chamber, which allows the ablation of up to three targets with three different lasers (excimer + two frequency-quadrupled Nd:YAG).

Figure 4.2.3. Overview of the multi-PLD chamber.

The whole multi-PLD system shares some features with the single-PLD chamber, but with the following differences:

- the metal substrate holder (on the right in Figure 4.2.3) can be rotated, for better film uniformity; its distance from the targets can be adjusted via a computer;
- a computer-controlled multiple target rotator (on the left in Figure 4.2.3) allows ablation of up to three different targets with the excimer and two frequency-quadrupled Nd:YAG lasers; laser-target angle of incidence was varied over a range of 8° for the target configuration used for the experiments in this thesis – this angle may be kept constant or alternatively targets can be tilted continuously to scan the plume across the substrate, which can result in an increase in the density of particulates (a consequence of ablating ridges or splashed areas), but allows better film thickness uniformity (e.g. to obtain flat film growth) and more efficient usage of the target surface;
- computer-controlled mass flow controllers allow injection of N_2, O_2 and Ar into the deposition chamber and precise control of relative gas pressures;
- computer-controlled pressure gauges for monitoring vacuum/gas pressure;
- a computer-controlled mechanical shutter can be used to prevent unwanted material deposition on the substrate during target pre-ablation;

- laser pulses from excimer and Nd:YAG lasers may be gated with shutters, driven by digital delay controllers or automated via computer, in order to adjust relative laser repetition rates (as in the experiments described in Section 7.2.2), control plume synchronicity/delay or for programmed sequential ablation [1];
- the CO_2 laser beam used for heating the substrate is raster-scanned on its back side, in order to ensure uniform heating (more details in in Section 4.2.4.1).

All components, except for the roughing pump and substrate heating, are automated and controlled via a computer rig.

4.2.3. LASERS

As aforementioned, there are three pulsed UV lasers in the PLD lab, which can be used for target ablation:

- a Coherent COMPex PRO 102F excimer laser, always filled with KrF, thus emitting at λ = 248 nm, with a pulse duration of ~20 ns, maximum pulse repetition frequency of 20 Hz and a maximum output energy of ~480 mJ/pulse at maximum voltage (30 kV) after a fresh gas refill; operation at λ = 193 nm may be obtained at lower energy (nominal max. energy: ~200 mJ/pulse), if the laser chamber is filled with ArF;
- two Continuum Surelite II flash-pumped Nd:YAG lasers, operating at a fixed pulse repetition frequency of 10 Hz and emitting at a fundamental of λ = 1064 nm (IR), but frequency-quadrupled via non-linear crystals to generate emission at λ = 266 nm (UV), with a pulse duration of ~5 ns and maximum output energy of ~100 mJ/pulse.

Excimer lasers have the following advantages over Nd:YAG lasers for target ablation [2]:

- ✓ higher photon energy or shorter emission wavelength, better absorbed by several materials than 266 nm radiation (e.g. Y_2O_3 can be ablated with 248 nm radiation produced by KrF laser, but not with 266 nm);
- ✓ higher energy, thus allowing ablation of materials with high ablation thresholds and easy adjustment of laser fluence on the target;

- ✓ tunable pulse repetition frequency, which gives better control on film growth rate and more versatility in controlling the target ablation ratio in multi-PLD experiments without having to use external shutters;
- ✓ uniform rectangular beam shape with nearly flat-top beam profile, better than the circular beam with Gaussian profile of Nd:YAG lasers, whose thermal effects and defects in the Nd:YAG crystals can produce hot spots in the beam, causing non-uniform ablation of the target and thus formation of higher kinetic components in the plume and particulates on the deposited film and also a stronger variation in composition across the film surface;
- ✓ better energy stability, both short-term (pulse to pulse) and long-term; in fact, UV emission from frequency-tripled or -quadrupled Nd:YAG lasers requires precise tuning of non-linear crystals, whose performance tends to degrade with time due to changes in temperature and/or humidity, thus adversely affecting output laser energy and beam profile and requiring adjustments in the tuning to keep a “constant” performance.

However, Nd:YAG lasers are cheaper and safer than excimer lasers, as they do not require the use of toxic halogen gases.

For substrate heating, two continuous wave (CW) Synrad J48-2W CO_2 lasers (one for each PLD system), emitting at λ = 10.6 μm, with nominal maximum output power of 40 W, were used. Substrate heating is discussed in detail in the next section.

4.2.4. SUBSTRATE HEATING

Several techniques can be used for heating the substrate, necessary to ensure the crystallisation of the film. These methods can be separated under the two broad headings: direct and indirect.

In the former case, heat conduction is exploited by placing the substrate in contact with the heater, which can be resistive filaments or hot metal plates; however this approach has several drawbacks:

- ✗ temperature is limited to ~1000 K;

- high temperatures in an oxygen ambient can oxidise or even burn out wires;
- inefficient heating of the intended substrate (only), causing warming up of the whole chamber;
- outgassing from the heater and heated chamber walls, causing film contamination;
- slow ramp-up and ramp-down rates, due to the thermal capacity of the heater (especially true for large and bulky hot metal plates).

In the latter case, radiative elements, such as filament bulbs (e.g. quartz lamps) and IR lasers (e.g. Nd:YAG and CO_2 lasers), are used. However, filament bulbs are very inefficient, as most of radiation misses the substrate and heats the whole chamber, thus causing outgassing and film contamination. Substrate heating with IR lasers is probably the most efficient method for substrate heating, as their power can be easily directed towards the substrate only, thus avoiding the aforementioned problems and allowing shorter ramp-up and ramp-down times; moreover substrate temperatures up to the melting point of sapphire (~2317 K) can be reached with a 100 W CO_2 laser [3]; finally several materials (e.g. silicon, silica, quartz, sapphire and garnets) strongly absorb in the mid infrared (MIR), where CO_2 lasers emit (typical wavelengths: ~9.6 μm and ~10.6 μm). However, substrate heating with an IR laser still presents some issues, namely:

- minimisation of heat-sinking, achieved with the substrate holder described earlier, in Section 4.2.1 (see inset in Figure 4.2.2);
- homogenisation of the beam profile to match the substrate shape and size (a 10×10 mm^2 square for the substrates used in this thesis), addressed in the next two sub-sections of this paragraph, due to the Gaussian beam profile of IR lasers;
- temperature measurement/calibration, addressed in the third sub-section of this paragraph, which is perhaps the major problem of such a technique.

Regarding the second issue, several approaches can be adopted: aspheric or cylindrical lenses for a homogenised circular flat-top beam profile, which can be transformed into a square profile by using an aperture, although wasting power; reflective square-tapered beam-pipes or beam-folding tetra-prisms for a homogenised square flat-top beam profile; or raster-scanning the back surface of substrate via a programmable computer-controlled two-axis mirror system, which allows great flexibility, as it can match any arbitrary shape of the substrate, within a wide range of sizes, limited only by the substrate holder size. A brief review of these techniques can be found in [4], whereas a wider discussion of the problems associated with substrate heating can be found in [3, 5]. The next two sub-sections briefly describe the two approaches to beam-homogenisation used in our PLD systems.

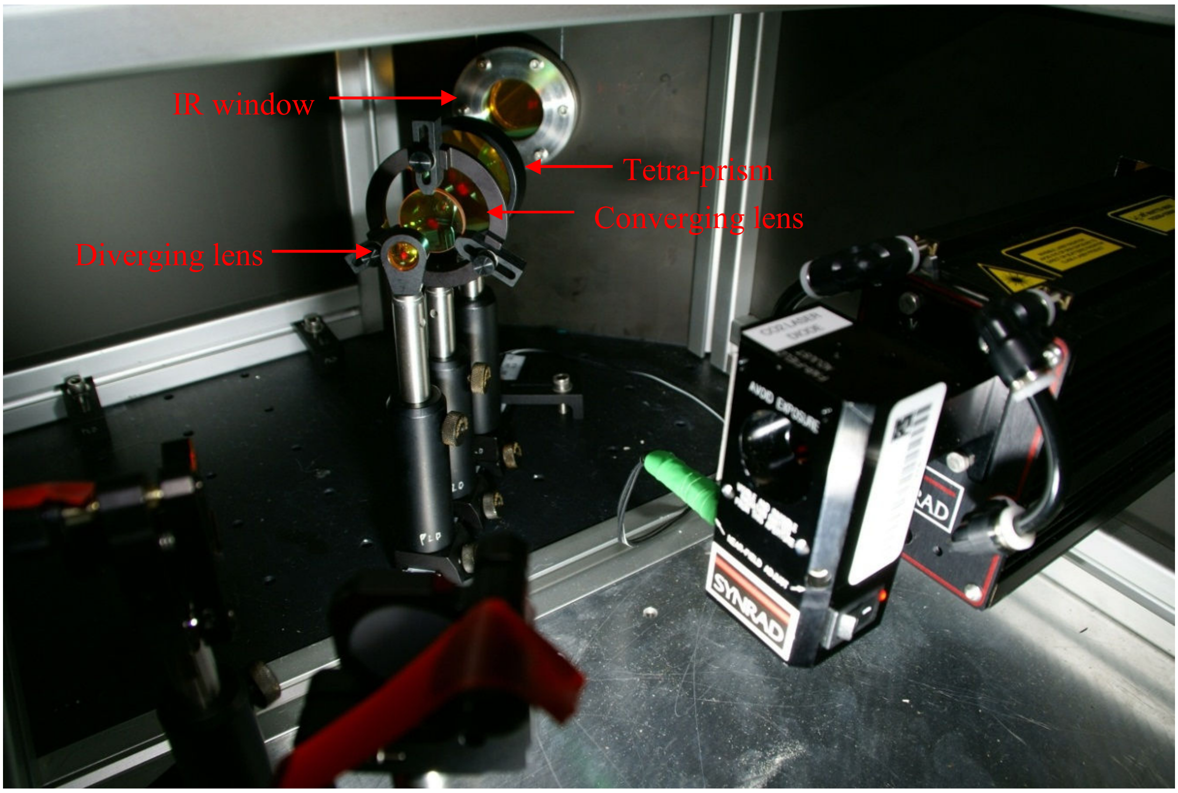

Figure 4.2.4. Overview of the IR optical set-up for homogenisation of the CO_2 laser beam for the single-PLD system. The red light visible on the ZnSe optical elements comes from the red laser diode mounted on the CO_2 laser head for its optical alignment.

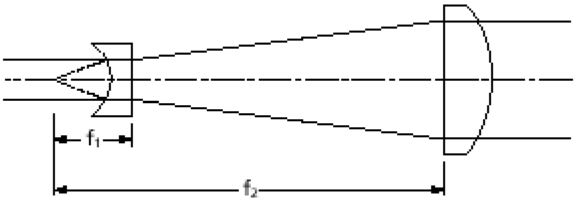

Figure 4.2.5. Diagram of a Galilean beam expander/collimator. f_1 and f_2 are the focal lengths of the diverging and converging lens respectively.

4.2.4.1. TETRA-PRISM

In order to match the shape and size of the substrates used (a 10×10 mm^2 square), the CO_2 laser beam must be:

- first expanded (to a beam waist[8] of 9 mm) and collimated for optimum performance of the ZnSe[9] prism via the optical set-up shown in Figure 4.2.4, comprising a diverging and a converging lens in ZnSe (Galilean beam expander/collimator – schematic in Figure 4.2.5),
- then converted from a Gaussian profile to a flat-top profile via the tetra-prism, whose working principle is schematically explained in Figure 4.2.6.

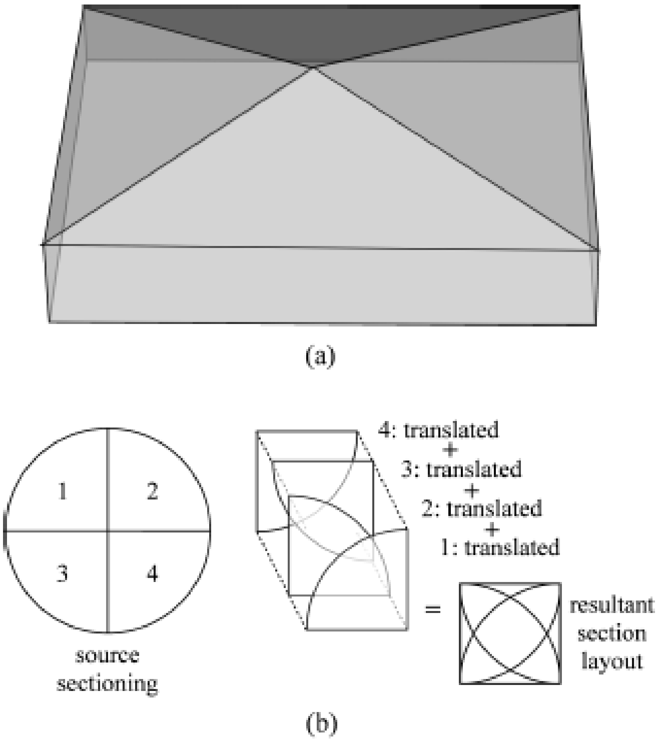
(a)

(b)

Figure 4.2.6. Schematics of **(a)** tetra-prism and **(b)** transformation of a circular Gaussian beam profile to a square flat-top profile [4].

As the beam goes through the tetra-prism, the four quadrants of the circular Gaussian beam are separated and translated on top of each other, whose overlap gives a square flat-top beam profile, which is thus matched to the substrate, placed at the correct working distance of the tetra-prism. However, as explained in [4], square substrates with different sizes may be matched by changing the distance of the tetra-prism from the substrate, although its optimum performance will be obtained at the working distance for which it is designed. Also, the interference pattern, due to the overlap of the beam sections, does not degrade significantly the performance of the tetra-prism [4] and actually it can be used to check the correct optical alignment and tune it, if necessary: in fact, the tetra-prism was placed on a

---

[8] Beam radius at $1/e^2$ intensity.

[9] Transparent at $\lambda = 10.6$ μm (MIR).

rail (to adjust its distance from the substrate) and two micrometre stages for accurate alignment (both horizontal and vertical) and optimum and repeatable performance.

The tetra-prism is relatively inexpensive and gives a minimum theoretical standard deviation in temperature over the surface of 2.2 K, comparing favourably with minimum values obtained for an untransformed Gaussian beam and square-tapered beam-pipe (43 K and 7.2 K respectively). More details can be found in [4].

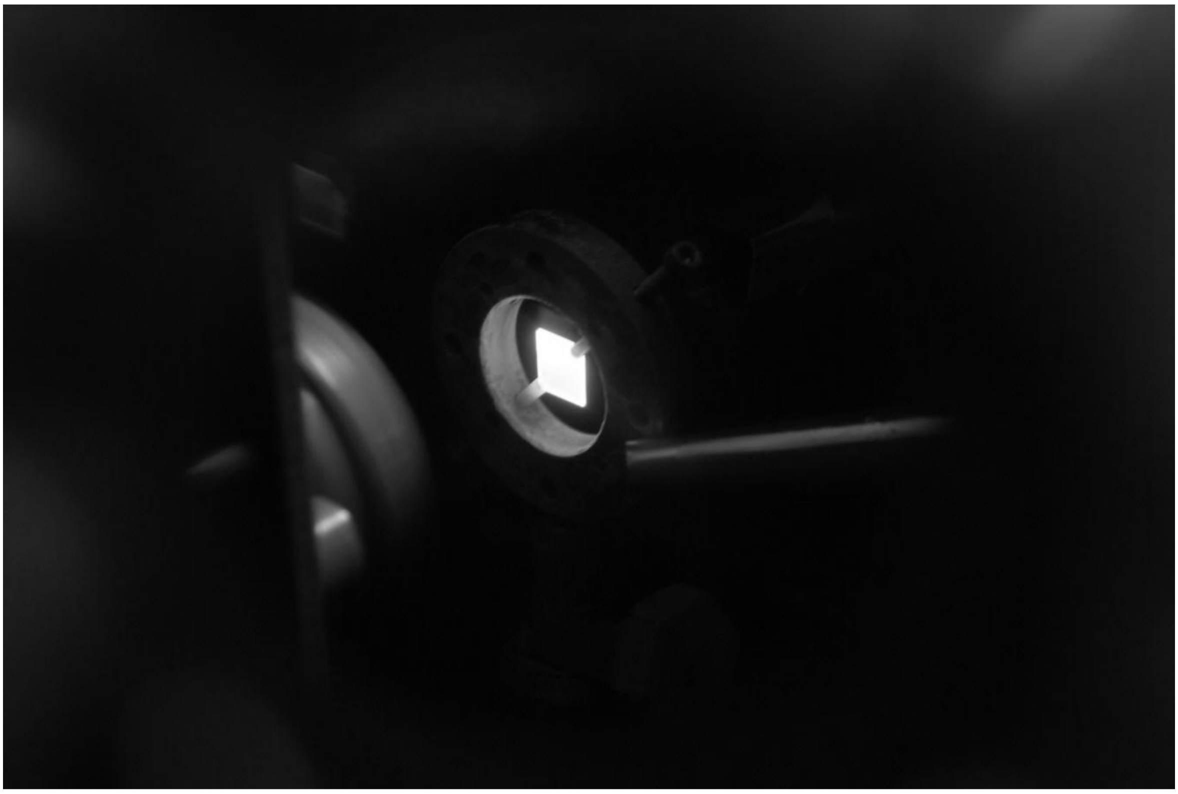

Figure 4.2.7. Photo of a blank sapphire substrate heated up to high temperature ($T > 1300$ K) with the CO_2 laser at full power.

4.2.4.2. RASTER SCANNING

Although more complicated and expensive than the tetra-prism, a two-axis mirror raster-scanner (see Figure 4.2.8) allows more flexibility: in fact, it is possible to program it via a computer in order to raster scan the back side of substrates of arbitrary shape in a wide range of sizes, limited only by the size of the substrate holder. Moreover it is possible to compensate any temperature differences across the substrate area, e.g. by increasing the dwell time of the CO_2 laser along the edges of the substrate, which tend to be cooler than the centre, due to the higher radiative emission caused by the higher surface/volume ratio [4].

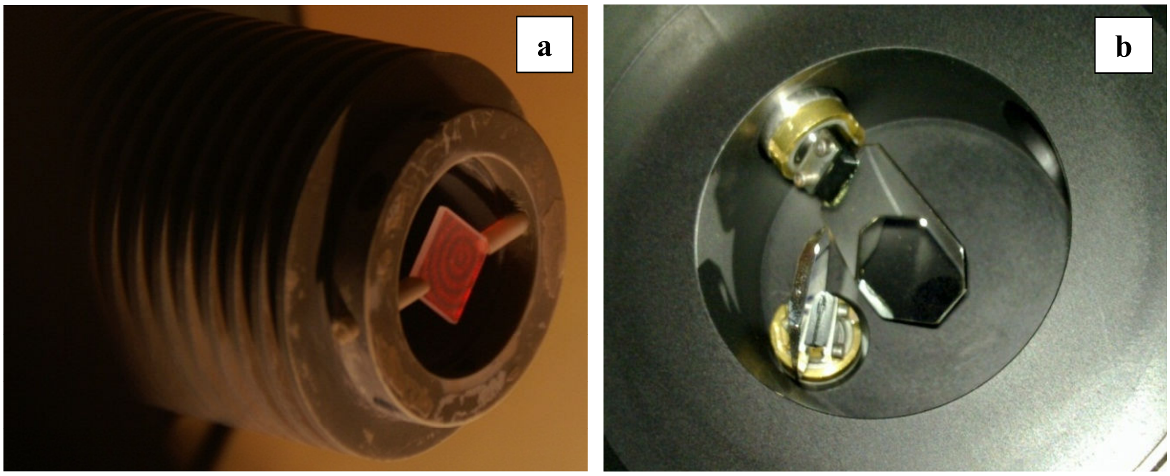

Figure 4.2.8. (a) Photo of the circular pattern created by the raster-scanned red diode laser beam (mounted on the CO_2 laser head for its optical alignment) on a substrate in the multi-PLD chamber. **(b)** Photo of raster-scanning mirrors.

4.2.4.3. TEMPERATURE CALIBRATION

One of the aforementioned issues with indirect (radiative) substrate heating is temperature measurement/calibration. Minimisation of heat-sinking does not allow *in-situ* direct measurement of substrate temperature with a thermocouple, which would cause undesirable heat-sinking, a consequent inhomogeneity in the temperature across the substrate surface and thus non-uniform crystallinity, surface morphology and composition in the film.

Substrate temperature measurements may be performed remotely, e.g. by pyrometry or diffuse reflectance spectroscopy (DRS), but they would complicate PLD systems without providing the levels of accuracy expected. In particular, two-colour pyrometry requires the usage of two pyrometers at two different wavelengths, which must not fall in the transparency range of the substrate, but this does not work with substrates with low emissivity (ε) and requires *a priori* knowledge of the variation of emissivity with temperature and wavelength; DRS, based on measurement of diffusely reflected light from the substrate, determines its temperature from the variation of absorbance spectrum with temperature and also allows *in situ* measurement of film thickness. However both techniques are affected by gradual coating of port windows, making absolute intensity measurements impractical, if not impossible [5].

Nevertheless, it is still possible to estimate the substrate temperature from measurements of CO_2 laser power incident on and absorbed by the substrate and calculations using the

Stefan-Boltzmann law, where some assumptions and approximations must be taken into account:

$$P = \sigma \varepsilon A T^4 \tag{4.2.1}$$

where $\sigma = 5.67\times10^{-8}$ W/(m^{2}K^4) is the Stefan-Boltzmann constant, A is the total area of the substrate surface and T is the substrate temperature in Kelvin). Although emissivity varies with temperature, a grey-body approximation (ε = 0.5, constant with temperature) can be used. The values of substrate temperature reported in this thesis were estimated using this method (see Figure 4.2.9 and Figure 4.2.10), which provides similar results in the low range of temperature (T < 1100 K) to those obtained by CO_2 laser calibration via metal balancing experiments, consisting of balancing thin and short metal strips on the edge of the substrate and melting them by slowly increasing the CO_2 laser power; at high temperatures ($T \geq$ 1100 K) the linear approximation of Stefan-Boltzmann law from CO_2 laser calibration (as derived from previous metal balancing experiments carried out by Dr. Timothy May-Smith [5]) is not valid anymore, as its extrapolation would over-estimate the substrate temperature from the absorbed CO_2 laser power. For the purpose of this thesis, the CO_2 laser power was calibrated with a few metal balancing experiments with gold (Au) and aluminium (Al) strips on 0.5 mm-thick sapphire and GGG substrates respectively, in order to double-check the validity of our approximations and assumptions, as the melting points of Au ($T_{\mathrm{m,\ Au}}$ = 1337 K) and Al ($T_{\mathrm{m,\ Al}}$ = 933 K) are close to the optimum temperatures reported in literature for epitaxial growth of Ti:sapphire ($T \approx$ 1350 K) [6] and YIG ($T \approx$ 1050 K) [7] respectively. The CO_2 laser power was measured regularly both outside and inside the chamber before each deposition, in order to ensure that the transmission of the IR window was not degraded by unwanted material coating.

The data-points in Figures 4.2.9 and 4.2.10 refer to values of power absorbed by the substrate, calculated from the difference of the measured CO2 laser power incident on the substrate and the power measured behind the heated substrate.

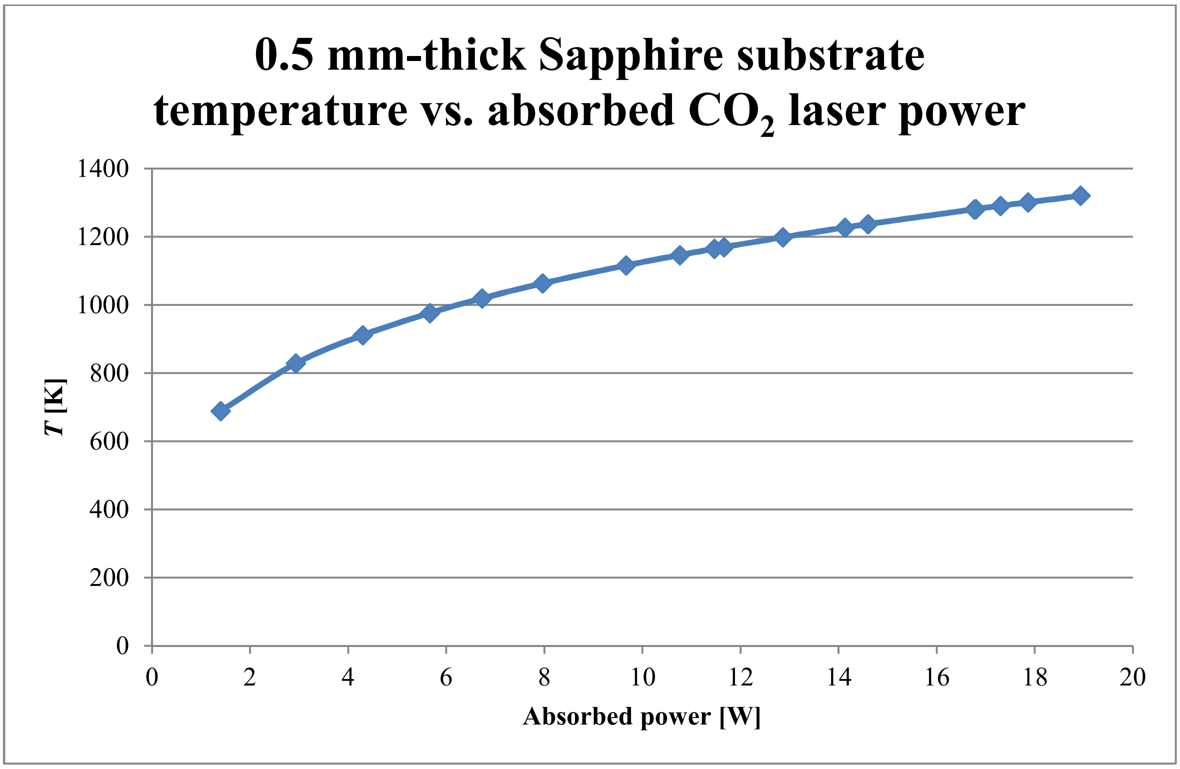

Figure 4.2.9. Substrate temperature vs. absorbed power for 0.5 mm-thick sapphire substrate, according to grey body approximation (theoretical curve from Stefan-Boltzmann law with $\varepsilon = 0.5$).

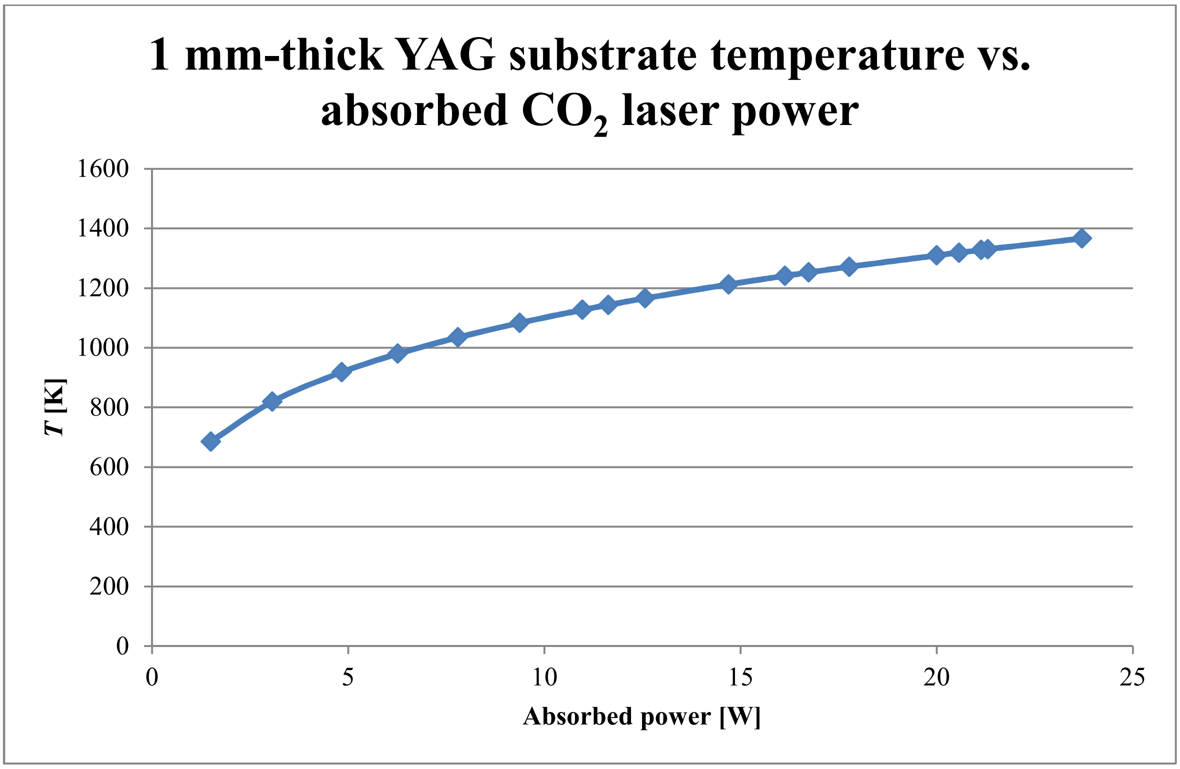

Figure 4.2.10. Substrate temperature vs. absorbed power for 1 mm-thick YAG substrate, according to grey body approximation (theoretical curve from Stefan-Boltzmann law with $\varepsilon = 0.5$).

4.3. TARGET RE-CONDITIONING AND TARGET/SUBSTRATE CLEANING PROCEDURES

4.3.1. TARGET RE-CONDITIONING

As mentioned in Sections 2.2 and 3.2, one of the main drawbacks of PLD is the formation of particulates on the film surface, due to prolonged use of the target, which results in formation of an ablated ring or trench, featuring a rippled surface morphology and whose composition can change significantly from the original value (see Section 3.2.4). Cone-like structures, richer in Y in the tips, have been observed in the single-crystal YIG target after several hours of ablation (see Figure 4.3.1), i.e. after several hundreds of thousands of ablation laser shots, as reported also in [8]. For this reason, in order to minimise production of particulates on PLD-grown films from the ablation of such structures, the ablation of all targets was limited to ~10 hours on the same surface. After such a prolonged ablation time and usage of both target surfaces, the targets were re-conditioned according to the following procedures.

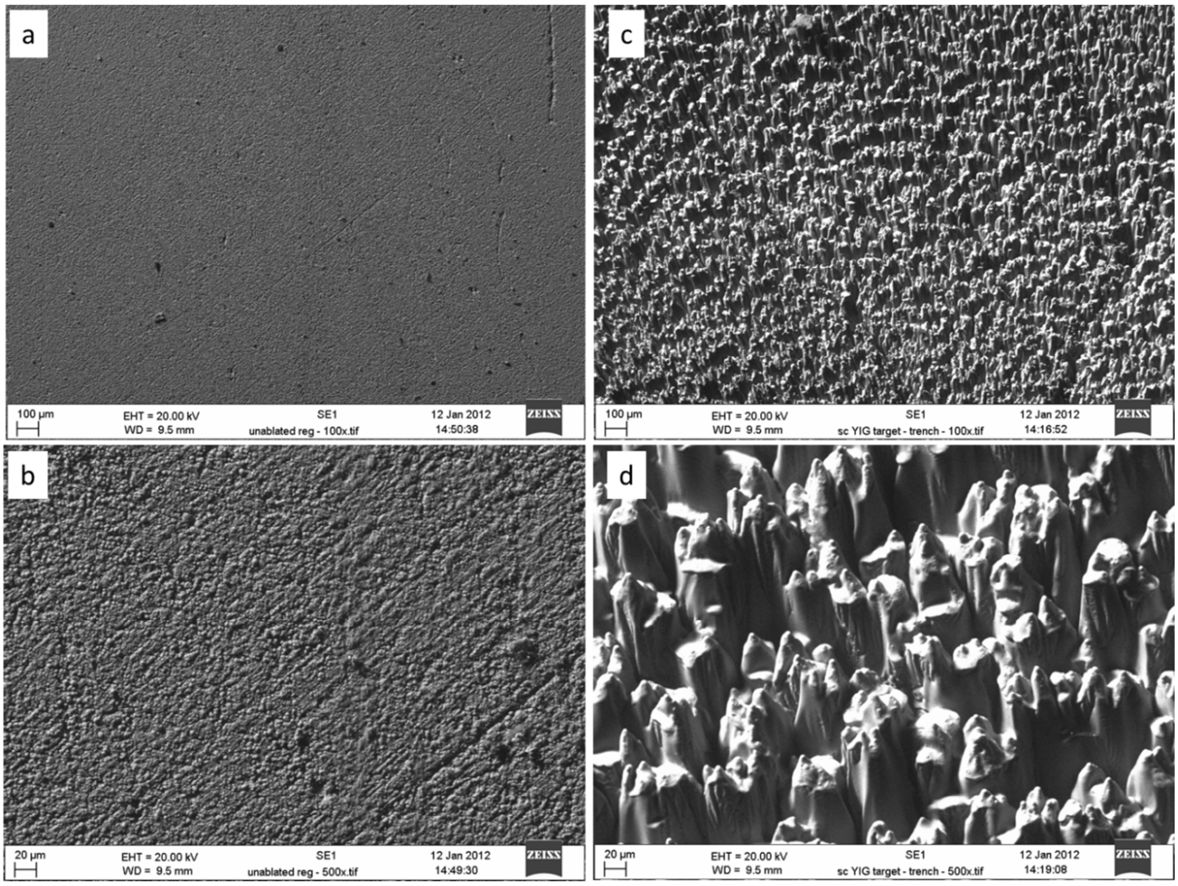

Figure 4.3.1. SEM pictures of an un-ablated region of the YIG target at a magnification factor of **(a)** 100× and **(b)** 500×; SEM pictures of part of the ablated trench of the YIG target, after ~7.5 hours of ablation, at a magnification factor of **(c)** 100× and **(d)** 500×. Cone-like structures are clearly visible in **(d)**.

Targets of hard materials, such as Ti:sapphire (Mohs hardness: 9 – diamond is 10 on the same scale), must be re-conditioned by lapping, although lapping powder can get stuck on the surface and cause formation of particulates on the film surface in the first hour or so of ablation, as observed during PLD experiments of YIG and briefly discussed in Section 6.2.5. Softer materials, such as YIG (Mohs hardness: 6.5-7), Fe_2O_3 (Mohs hardness: 5.5-7.5) and Bi_2O_3 (Mohs hardness: 2-3) can be re-conditioned either by lapping or with sandpaper, which avoids inclusion of lapping particles, which are difficult to remove even by ultra-sonic cleaning; for this reason, freshly re-conditioned targets are firstly pre-ablated for at least ~30-60 minutes with the shutter placed in front of the substrate before starting a deposition run.

When lapping a used target, this is waxed on a metal disc, which is then mounted on a jig; the latter is then held on a rotating flat iron plate, with a solution of DI water and lapping grit (B_4C for sapphire and SiC or calcined Al_2O_3 for YIG and other softer materials) constantly dripping on the plate, providing abrasive action and thus removing material from the target surface, until it is fully re-conditioned. Once the target is re-conditioned on both sides, it can be cleaned as described in the next section.

4.3.2. TARGET/SUBSTRATE CLEANING

In order to minimise contamination and ensure epitaxial film growth, both substrates and targets need to be cleaned prior to their first usage, especially after re-conditioning the targets. The following procedure was used for cleaning the targets after lapping:

1) scrub and rinse targets with non-solvent cleaning fluid (**Eco-Clear**) to get rid of most of the wax;
2) leave targets overnight or at least for ~1 hour in hot (~50°C) **Eco-Clear** to get rid of remainders of wax;
3) place targets in a basket in a beaker with **Eco-Clear** in *ultrasonic bath* heated up to ~40°C and leave for 30 min. to remove particles of wax stuck into the target surfaces;
4) rinse the basket with **acetone** (to get rid of Eco-Clear);
5) transfer the basket in a beaker with **acetone** in *ultrasonic bath* at ~40°C and leave for 30 min. (to dissolve any leftover of Eco-Clear);
6) rinse the basket with **fresh acetone**;

7) rinse the basket with **fresh isopropanol** (to get rid of acetone);
8) transfer the basket in a beaker with **hot isopropanol** in *ultrasonic bath* at ~40°C and leave for 30 min. (to dissolve any leftover of acetone);
9) rinse the basket with **fresh isopropanol**;
10) rinse the basket with **fresh de-ionised water** (to get rid of isopropanol);
11) transfer the basket in a beaker with **hot de-ionised water** in *ultrasonic bath* at ~40°C and leave for 30 min. (to dissolve any leftover of isopropanol);
12) rinse the basket with **fresh de-ionised water**;
13) dry the targets with **compressed N_2** (to wipe out water);
14) transfer the targets into hot oven at 120°C and leave them overnight (for evaporation of any leftover of water and solvents).

The procedure for cleaning of blank substrates is the same as above, but the first 4 steps are replaced with the following three:

1) rinse substrates with **acetone**;
2) thoroughly scrub the surfaces of each substrate with a swab wet with **acetone**;
3) place substrates in a basket;

the cleaning procedure continues as above from point 5), skipping the last step (14), as the substrate are normally heated up to high temperatures, thus ensuring evaporation of any residual contaminants from its surfaces.

The procedure for cleaning of polished samples, before their optical characterisation, is the same as that for targets, but the last step (14) is skipped.

4.4. VISUAL AND SURFACE ANALYSIS

4.4.1. VISUAL INSPECTION

As soon as the deposition is finished, the sample is inspected, looking for cracks and particulates visible by naked eye and recording the film uniformity, transparency/opacity and colour/tint. This first simple method of analysis can be very effective: in fact, YIG films with good crystal quality feature a yellow colour, which tends to become darker with degrading crystal quality, as the substrate temperature is decreased (more details in Section 6.2.3); amorphous YIG films grown at room temperature are instead completely black. The film colour provides qualitative information not only on crystallinity, but also on composition, as explained in Chapter 7: YIG films grown by multi-PLD become redder and also more opaque with increasing Fe concentration. The presence of cracks, lines or flaking may be due to poor temperature homogeneity or stress in the film, induced by high lattice- or TEC-mismatch with the substrate. Film inhomogeneity can be due to the abovementioned causes and also to variation of stoichiometry across the film surface.

4.4.2. MICROSCOPY

Microscopy allows a closer look at both the film surface and morphology: micro-cracks and particulates smaller than ~0.1 mm, not visible by naked eye, can be distinguished and analysed in terms of size and surface density; sometimes what appears as one big particulate by naked eye is actually an agglomerate of smaller particles. However, magnification factors are limited to 100× (for the final objective) and optical microscopy cannot resolve features less than ~300 nm in size, due to the diffraction limit in the visible:

$$res = \frac{\lambda}{2NA} \tag{4.4.1}$$

where *res* refers to "resolution" and *NA* to the numerical aperture of the objective lens (max. $NA = 0.95$ for conventional lenses in air); using $\lambda = 550$ nm (green): $res \approx 290$ nm.

Scanning Electron Microscope (SEM) overcomes this limitation due to the shorter wavelength associated with electrons (12.2 pm for electrons accelerated at 10 keV), featuring magnification factors up to 500,000× and also a high depth of field. However, in practice the resolution is limited by both the size of the final focussed electron beam spot and the interaction volume; typical resolution of the order of ~1 nm is achievable in high vacuum mode. The SEM used for surface analysis was a Zeiss Evo 50.

The SEM consists mainly of a vacuum chamber, an electron gun and detectors. An electron beam (e-beam) is emitted by a cathode, usually a tungsten filament, then focused down to ~(0.4 – 5) nm spot size by condenser lenses and finally raster-scanned on the sample surface by deflecting plates. The electrons, usually with energy between 0.2 keV and 40 keV, depending on the accelerating voltage, penetrate the sample and interact with the atoms of the material in a teardrop-shaped volume, whose depth ("e-beam penetration depth", typically between 100 nm and 5 μm) depends mainly on the e-beam energy and on the density of the material; for instance the e-beam penetration depth for

YIG (bulk density: 5.17 g/cm^3) is ~2 μm and ~1 μm for electrons accelerated at 20 keV and 15 keV respectively. The interactions of incident and scattered electrons with the atoms of the materials cause different phenomena:

- reflection of high-energy electrons by elastic scattering (back-scattered electrons – BSE);
- emission of secondary electrons (SE) by inelastic scattering;
- emission of electromagnetic radiation (x-ray and optical radiation).

Different specialised detectors can measure intensity and energy of these reflections and emissions: from their analysis, images of the surface of the sample can be reconstructed and more data relative to the interaction volume calculated. The SE detector (a scintillator-photomultiplier system collecting electrons with energy lower than 50 eV) allows imaging of the sample surface; the BSE sensor, positioned at the bottom of the e-beam column around its edge, does the same as the SE detector, but can distinguish areas with different chemical compositions (heavy elements back-scatter electrons more strongly than elements with low atomic number). X-ray radiation and cathodoluminescence can be measured with different detectors, e.g. compositional analysis can be performed by energy-dispersive x-ray spectroscopy (EDX).

In order to avoid charge accumulation on the surface of non-conductive samples (such as garnets and sapphire), which would hamper its analysis and characterisation, two approaches can be adopted:

1. coating the film surface with ~nm-thick gold or carbon films, normally deposited by sputtering; however this method may hide small features on the surface and hinder compositional analysis by the EDX module (more in Section 4.5.1), especially if Au-coating is used; finally, this technique is partially destructive, as it is not necessarily easy to remove the coating layer without damaging the film;
2. using a relatively low vacuum (~40 Pa) in the SEM chamber (“environmental SEM” used in “variable pressure” or “VP” mode), while maintaining a high vacuum (of the order of 10^{-3} Pa or lower) in the e-beam column; in this way the air, ionised by the e-gun, allows charge removal from the sample surface; however, the e-beam scattering with air and the larger aperture (100 μm) used in VP mode reduce the resolution.

4.4.3. PROFILOMETRY

4.4.3.1. STYLUS PROFILER

A KLA Tencor P-16 stylus profiler was used to measure film thickness and curvature profiles of Ti:sapphire and YIG samples.

A diamond stylus, whose width ranges from 20 nm to 50 µm (2 µm for the instrument used), is dropped down and brought in contact with the sample and scans its surface along a horizontal direction, revealing any height variation, which is converted into an electrical signal, decoded and recorded. Horizontal resolution depends on scan speed and data acquisition rate and is limited by the size of the stylus and its sloping sides. Vertical resolution is limited by mechanical vibrations and electrical noise and theoretically it can be of the order of Angstroms; in practice, if the system is not vibration-free and mechanically-isolated, vertical resolution is typically of the order of nanometres or tens of nanometres.

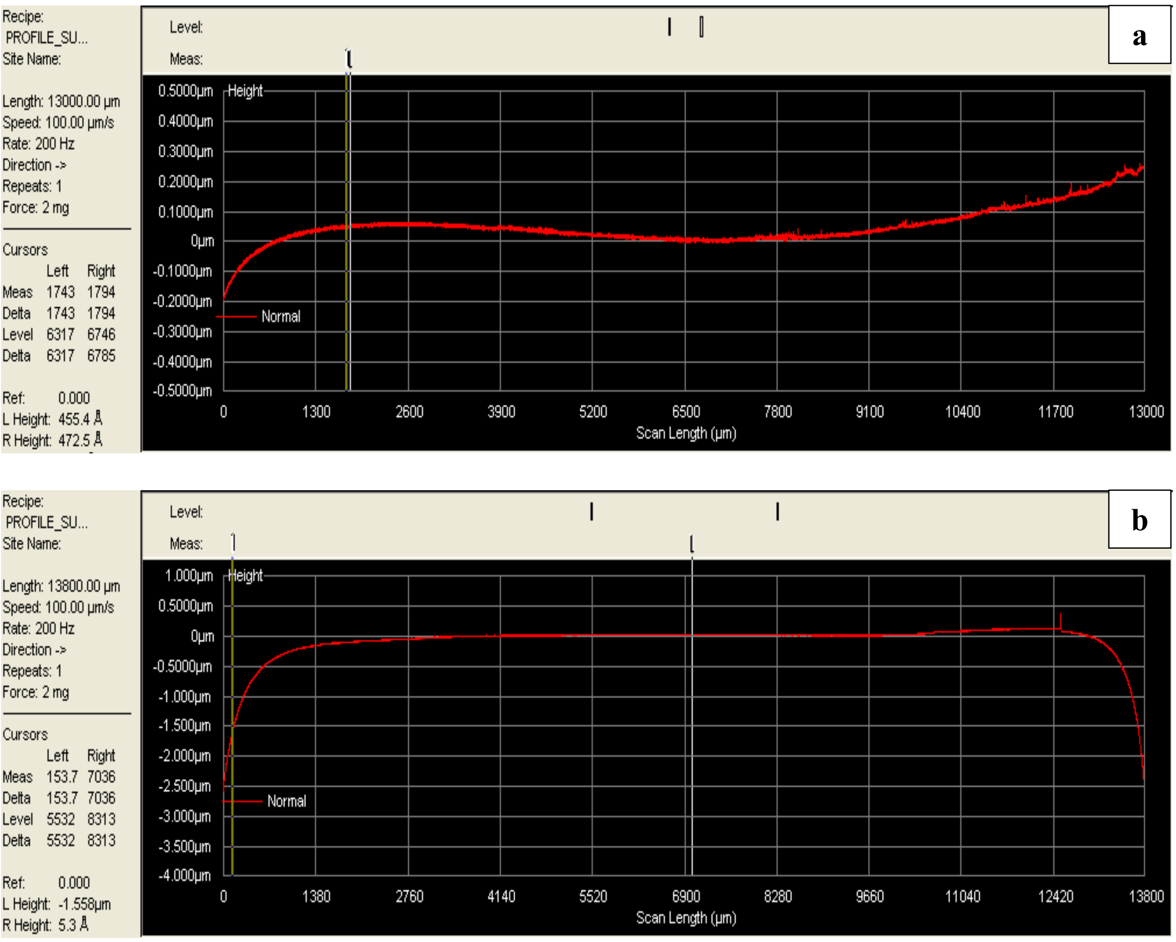

Recipe:
PROFILE_SU...
Site Name:

Length: 13000.00 µm
Speed: 100.00 µm/s
Rate: 200 Hz
Direction ->
Repeats: 1
Force: 2 mg

Cursors

	Left	Right
Meas	1743	1794
Delta	1743	1794
Level	6317	6746
Delta	6317	6785

Ref: 0.000
L Height: 455.4 Å
R Height: 472.5 Å

Recipe:
PROFILE_SU...
Site Name:

Length: 13800.00 µm
Speed: 100.00 µm/s
Rate: 200 Hz
Direction ->
Repeats: 1
Force: 2 mg

Cursors

	Left	Right
Meas	153.7	7036
Delta	153.7	7036
Level	5532	8313
Delta	5532	8313

Ref: 0.000
L Height: -1.558µm
R Height: 5.3 Å

Figure 4.4.1. Examples of surface profiles of blank YAG substrates with **(a)** “flat” surface and **(b)** high surface curvature (near the corners). In the latter case the high surface curvature near the corners will make film thickness measurements impossible, if the substrate has not been pre-measured.

A 2D surface profile can be traced by scanning the whole surface from corner to corner or from edge to edge. 3D surface profiles can be traced as well with multiple 2D scans and surface roughness can be measured too. Film thickness can be measured by scanning the sample surface on the corners shadowed by the ceramic posts in the substrate holder, if the substrate is flat enough (e.g. variation of curvature much smaller than 1 μm across ~1 mm – see Figure 4.4.1.a); otherwise, the substrate curvature will not allow the correct measurement of film thickness (see Figure 4.4.1.b), if the substrate curvature has not been measured before the deposition.

4.4.3.2. OPTICAL PROFILER

A Zemetrics ZeScope optical surface profiler was used to study surface morphology and measure the surface roughness of Ti:sapphire and YIG samples. SPIP (Scanning Probe Image Processor) software was used to analyse the data acquired from the ZeScope.

The working principle of such a 3D optical profiler is based on comparison of reflected images of the samples and of a flat reference mirror, using a white light source and an interferometric setup. It has the following advantages over stylus profiler:

- ✓ higher acquisition speed, limited by the speed of the acquisition electronics;
- ✓ higher reliability, as it does not touch the surface (stylus can be damaged in contact profilers);
- ✓ non-destructive, as soft samples can be scratched/damaged by the stylus in contact profilers.

The horizontal resolution is sub-micrometre, whereas the vertical resolution is of the order of Angstroms and is less sensitive to mechanical vibrations than for the stylus profiler; however, in practice, vertical resolution is reduced to a few nanometres due to vibrations and air currents.

4.5. COMPOSITIONAL ANALYSIS

4.5.1. ENERGY-DISPERSIVE X-RAY SPECTROSCOPY (EDX)

Compositional analysis was routinely performed by EDX (Energy-Dispersive X-ray spectroscopy) with an INCA PentaFETx3 module mounted on the Zeiss Evo 50 SEM.

Such a system, consisting of a scintillator, detects x-rays emitted by atoms in the interaction volume of the sample analysed by SEM. Primary electrons excite electrons bound in the inner energy shells of the atoms; when the vacancy so-formed is re-filled by an electron from a higher energy shell, x-ray radiation, whose energy is equal to the energy difference between the shells, is emitted. Detection of the intensity and energy of such x-rays allows the compositional analysis of the sample within the interaction volume: energies of x-rays indicate the elements present in the sample and their intensity the abundance of each element.

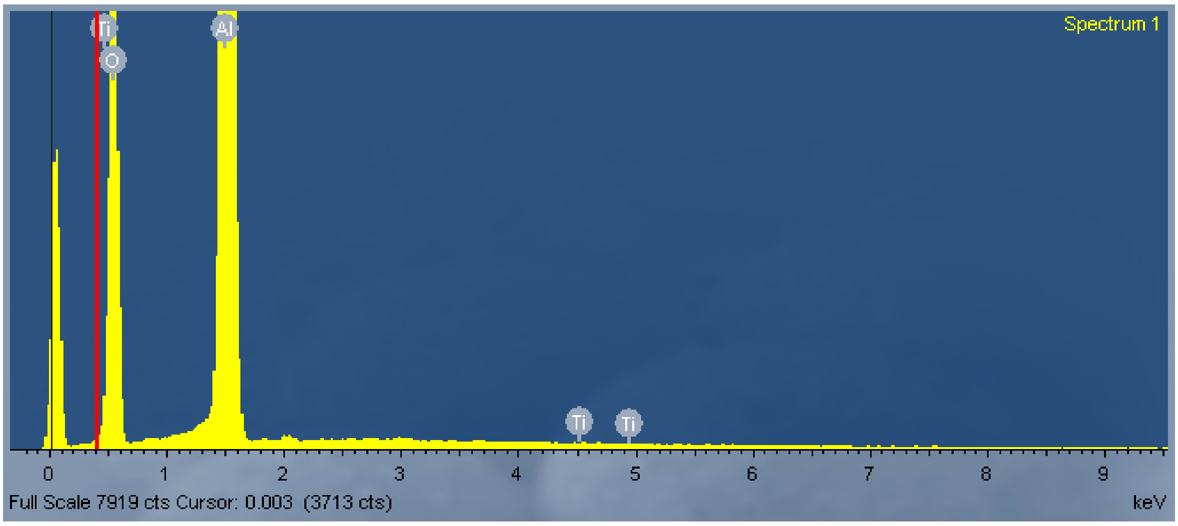

Figure 4.5.1. Example of EDX spectrum of a Ti:sapphire sample (AS20). The Ti and O peaks are very close to each other and overlapping, thus making measurements of Ti concentration inaccurate.

However, EDX is not very accurate, because of the following issues:

- x-rays are released isotropically and hence many will not escape the sample, especially if the surface is rough;
- broad energy peaks can be formed by the overlap of different energy peaks, making it difficult to discern those due to different elements – for instance, the energy peak due to Ti is very close to that due to O (see Figure 4.5.1) and this can introduce error in assessing the Ti concentration in Ti:sapphire films;
- the detector window (Be) can absorb low-energy x-rays emitted by light elements (e.g. O);

- if the film is thinner than the e-beam penetration depth, the substrate will be analysed too; if the film is much thicker than the e-beam penetration depth, then the analysis may not be representative of the whole film. In order to avoid this, the e-beam penetration depth was tuned by changing the electron acceleration voltage.

Due to the inaccuracy of EDX in measuring oxygen concentration, this has been always assumed constant, fixed at the stoichiometric value (i.e. 60 at. % in Ti:sapphire and garnets, equal to 3 formula units for Ti:Al_2O_3 and 12 formula units for YIG, $Y_3Fe_5O_{12}$). EDX analysis was performed by measuring the composition in three or more different regions around the centre of the sample and then taking the average value. Accuracy of EDX analysis is of the order of 0.1 at. % (atomic percent).

In order to know the Ti concentration in Ti:sapphire films, some samples were sent to external collaborators with different facilities. The techniques used are described in the following sub-sections.

4.5.2. X-RAY PHOTOELECTRON SPECTROSCOPY (XPS)

XPS analysis was performed on a few Ti:sapphire samples by our collaborators in the AFRL (Air Force Research Laboratory) of the USAF (United States Air Force) at the Wright-Patterson Air Force Base in Ohio (USA). Unlike EDX, XPS can distinguish valence state of ions (useful for Ti:sapphire samples); however, due to its poor accuracy (detection limit is ~0.1 at.%), no Ti was detected in any of the Ti:sapphire films.

XPS consists of irradiating the sample with x-rays in an ultra-high vacuum (UHV: $<10^{-7}$ Pa) chamber and measuring the number and kinetic energy of the electrons emitted from the interaction region (typically up to 12 nm-thick) of the material. The electron binding energy of the emitted electrons (E_{binding}) can be calculated from the measurement of the kinetic energy (E_{kinetic}) and the following equation of conservation of energy:

$$E_{\text{binding}} = E_{\text{x-ray}} - (E_{\text{kinetic}} - W) \tag{4.5.1}$$

where $E_{\text{x-ray}}$ is the energy of the incident x-ray and W is the work function (i.e. the energy need to remove an electron from a solid) of the material used for the electron detector (spectrometer). This can therefore distinguish between the different atoms inside the film, whereas the intensity of each energy peak is proportional to the number of electrons, thus allowing calculation of the film composition near its surface from the measured spectrum.

4.5.3. PROTON-INDUCED X-RAY EMISSION (PIXE)

This non-destructive compositional analysis technique requires the use of an accelerator, as ions must be accelerated to energies of the order of MeV: the bombardment of the sample will cause inner shell ionization of the atoms; the inner shell vacancy will be occupied by an outer electron, whose transition causes the emission of x-ray at wavelengths depending on the energy difference of the electronic transition. So, similarly to EDX, compositional analysis of the sample can be performed by measuring the energy and intensity of the x-ray emitted from the sample under analysis, with better resolution than EDX: the detection limit is of the order of ~(1 – 10) ppm[10] = (0.0001 – 0.001) at.%. Although normally performed in vacuum, PIXE analysis can be performed at ambient pressure, although air will attenuate the x-rays emitted by light elements. Some Ti:sapphire samples were analysed by PIXE by our collaborators at the University of Surrey, giving an average Ti concentration of ~0.0118 at.%.

4.5.4. SECONDARY ION MASS SPECTROMETRY (SIMS)

SIMS is a destructive compositional analysis technique that consists of sputtering the sample under analysis in high vacuum (~10^{-4} Pa) with a focussed ion beam and collecting and analysing the ejected secondary ions, which are distinguished from each other in terms of charge/mass ratio via a mass spectrometer. Due to the large variation in ionization probabilities among different materials, SIMS is generally considered a qualitative technique. However, SIMS is the most sensitive surface analysis technique, with elemental detection limits ranging from parts per million to parts per billion. SIMS analysis of a few Ti:sapphire samples was performed by our collaborators in the AFRL of the USAF at the Wright-Patterson Air Force Base in Ohio (USA), giving an average Ti concentration of ~0.073 at. %.

---

[10] part per million.

4.5.5. CONCLUSIONS

Table 4.5.1 reports and compares the results of compositional analysis (in at. %) performed by EDX, PIXE and SIMS on five Ti:sapphire samples. Unfortunately the data collected by different techniques do not agree with each other, as shown and explained below.

[at. %]	**AS18**	**AS19**	**AS20**	**AS22**	**AS32**	**Average**
EDX	0.03	0.02	0.02	0.02	0.02	0.02
PIXE	0.0123	0.0153	0.0109	0.0106	0.0101	0.0118
SIMS	0.115	0.041	0.064	0.086	0.059	0.073

Table 4.5.1. Results of compositional analysis on 5 Ti:sapphire samples.

A significantly large variation can be found among the results obtained with the three different compositional analysis techniques: the average Ti concentration measured by EDX (~0.02 at. %) is twice the value measured by PIXE (~0.012 at. %), but more than three times smaller than the value measured by SIMS (~0.073 at. %), where however there is a larger variance of composition among the five Ti:sapphire samples (0.074 at.%), compared to EDX (giving almost the same Ti concentration in all samples) and PIXE (0.0052 at. %), thus making optimisation of Ti:sapphire growth conditions via compositional analysis impractical.

However, we consider EDX analysis of our magneto-optic garnet films reliable, as the elemental concentrations are generally higher than that of Ti in Ti:sapphire films and there is no significant overlap between the energy peaks of different elements of iron garnets.

4.6. CRYSTALLINITY AND STRUCTURAL ANALYSIS

In order to check epitaxial crystal growth of Ti:sapphire and magneto-optic garnet films, x-ray diffraction (XRD) analysis was performed, using the diffractometers (Siemens D5000, Bruker D8 and D2 Phaser) at the School of Chemistry of the University of Southampton.

An x-ray diffractometer (schematic in Figure 4.6.1) consists of a static sample holder and a goniometer around it, where an x-ray source and an x-ray detector rotate in opposite directions at the same speed; the position of the former with respect to the film surface is indicated by the angle θ, whereas the x-ray detector is always placed at an angle 2θ with respect to the direction of the x-ray radiation incident on the sample surface, so that an x-ray spectrum or intensity pattern can be plotted versus 2θ.

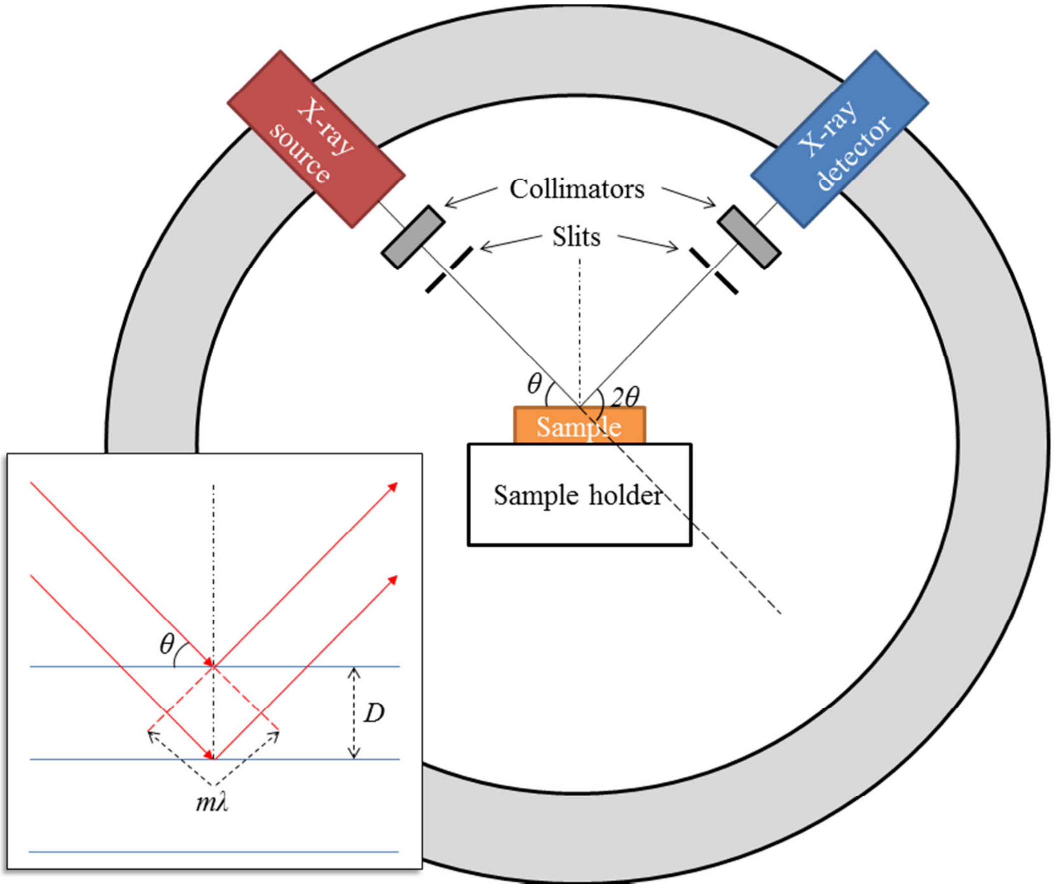

Figure 4.6.1. Schematic of an x-ray diffractometer. The inset shows a representation of Bragg's diffraction law.

In general, for single- or poly-crystalline samples, the x-rays diffracted by the crystal planes (atoms act as scattering points) will be out of phase; however, at a certain angle, dictated by Bragg's law (*D* is the spacing[11] between crystal planes and *m* an integer – see also the inset in Figure 4.6.1):

$$2D \sin\theta = m\lambda \tag{4.6.1}$$

the x-rays will be diffracted in phase, thus resulting in a high sharp peak in the diffraction pattern. On the contrary, an amorphous sample will generate a noisy pattern with low intensity, due to the random (non-periodic) arrangement of the atoms. Generally, due to the high intensity of the incident x-rays, these will penetrate into the substrate and the XRD pattern will feature also peaks due to x-ray diffraction from the substrate lattice; this normally is not an issue and is actually quite convenient, as it allows normalisation of XRD patterns, as explained below.

---

[11] $D = a/\sqrt{(h^2 + k^2 + l^2)}$, where *h*, *k* and *l* are Miller's indexes, e.g. *D* = *a*/4 for YIG (400).

The measured XRD pattern can then be compared against database values [9], in order to identify the crystal phases and orientations in the sample. When placing the samples on the stage of the diffractometer, they may not be perfectly flat, but slightly tilted, thus resulting in diffraction patterns which may be shifted by different amounts; however the patterns can be normalised and compared to each other by shifting all of them so that all the XRD peaks due to the substrate are aligned to each other at the database value. This allows a correct evaluation of the positions of XRD peaks due to the film with composition, for instance. In fact, a variation in stoichiometry can induce a larger (smaller) lattice constant a, i.e. a larger (smaller) D spacing, for instance by increasing (decreasing) the concentration of elements with high ionic radii (e.g. Y in YIG).

4.7. END-POLISHING OF WAVEGUIDES

Waveguiding films must be polished on two opposite end-faces before optical characterisation and lasing experiments, which require the end-facets to be perpendicular to the plane of the film and parallel to each other, in order to reduce losses and maximise launch efficiency. To do this, the samples to be polished are waxed together on a metallic support, which is then mounted on a jig and this is placed on a lapping/polishing machine, as described in Section 4.3.1. Firstly the samples are lapped with coarse B_4C grits to remove material to shorten the sample length; further lapping stages are performed with finer lapping powders (3 μm- and 1 μm-sized calcined Al_2O_3 particles) to remove any scratches from previous steps. The final high-quality optical finish is achieved by using SF1 alkaline colloidal silica polishing fluid, which provides both abrasive and chemical actions. Once the first end-facet has been lapped and polished, it is used as a reference in an autocollimator and the second end-face lapped and polished to high quality optical finish. Finally the samples are taken apart and cleaned as illustrated in Section 4.3.2.

4.8. WAVEGUIDE ANALYSIS AND LASING TECHNIQUES

This chapter describes the methods used for optical characterisation of Ti:sapphire waveguiding films (Sections 4.8.1 and 4.8.2) and to make them lase (Section 4.8.3).

4.8.1. FLUORESCENCE MEASUREMENTS

Measurements of fluorescence from Ti:sapphire samples were performed in collaboration with Dr. Amol Choudhary, a PhD student in the Ultrafast Optical Parametric Oscillators group of the ORC at the University of Southampton. The setup used was the same reported in [6] and is shown in Figure 4.8.1. It consisted of an a CW diode-pumped frequency-doubled Nd:YAG laser (λ = 532 nm), a beam splitter, used to transmit part of the pump beam to a reference detector and reflect the rest to the sample.

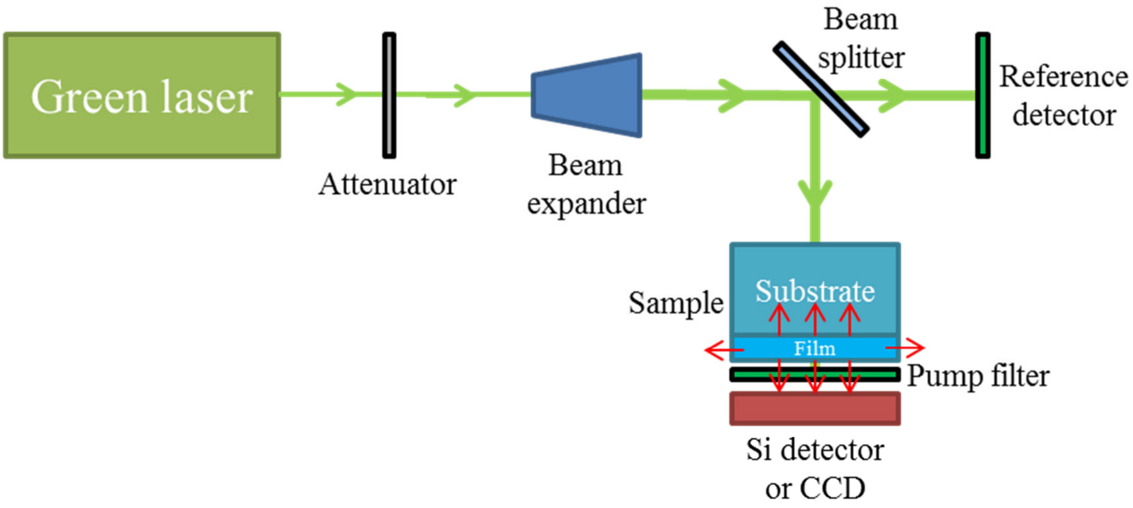

Figure 4.8.1. Schematic of setup used for fluorescence measurements of Ti:sapphire samples [6].

The net fluorescence was measured by using a photodiode and measuring the resulting voltage on the oscilloscope. Filters to block the 532 nm pump were put in between the sample and the detector. The pump was incident perpendicular to the waveguide direction and went through the film and substrate.

It was assumed that fluorescence due to Cr^{3+} ions present in both the substrate and the samples is at a constant level, so that its contribution can be subtracted; similarly the fluorescence due to Ti^{3+} impurities in the nominally un-doped substrates was assumed constant, so that its contribution can be subtracted too. Another important assumption is that the fluorescence level scales directly with film thickness, so that results can be normalised. Also the area pumped by the laser and the distance between the samples and the detector must remain constant.

From Figure 4.8.1 it is clear that this characterisation technique does not require the films to be end-polished; however, if the Ti:sapphire layers are thick enough to waveguide light, this could be diverted away from the detector, thus explaining the lower fluorescence measured from some thick samples, compared to other thin films.

For measurement of the fluorescence spectrum, the setup was kept the same, except for the fact that the silicon detector is replaced with a CCD spectrometer. The spectra recorded from samples AS6-AS12 cannot be compared with those measured from AS12-AS14, as the latter were performed with more filters to improve the signal-to-noise ratio.

4.8.2. PROPAGATION LOSS MEASUREMENTS

Waveguide losses were measured by launching a Ti:sapphire laser (pumped with an Ar^+ laser) beam into the waveguide by end-coupling technique and then measuring input power P_{in} and output powers from the whole sample P_{out} (waveguide and substrate), the waveguide only P_{out}^{W} (using a spatial filter) and from the substrate only P_{out}^{S} (to take losses from Fresnel reflections into account). The laser beam polarisation was parallel to the waveguide plane, i.e. perpendicular to the *c*-axis of the sample, but it can be polarised parallel to the *c*-axis via a half-wave plate. A schematic of the basic optical set-up used is shown in Figure 4.8.2.

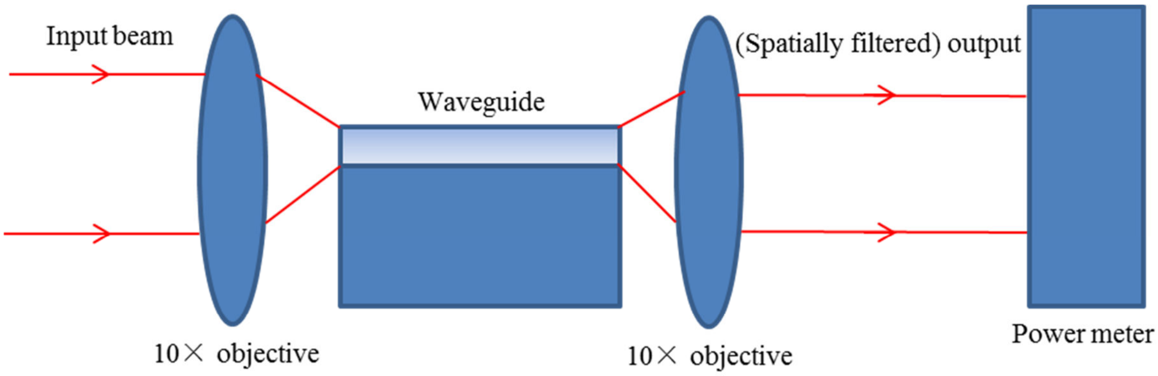

Figure 4.8.2. Schematic of the basic optical set-up for propagation loss measurements in Ti:sapphire samples.

We define: $T_{\times 10}$ as the transmission coefficient of the objective lenses, F as the transmission coefficient relative to Fresnel losses, L as the launch efficiency into the waveguide and *loss* the transmission losses in the waveguide.

The overall transmission from substrate and objectives, obtained by letting the focussed input laser beam pass through the substrate only, is:

$$T_S = \frac{P_{out}^{S}}{P_{in}} = T_{\times 10}^{2} \cdot F^{2} \qquad (4.8.1)$$

The overall transmission from sample (waveguide and substrate) and objectives, obtained by focussing the input laser beam onto the waveguide, without spatially filtering the output laser beam, is:

$$T_{W+S} = \frac{P_{out}}{P_{in}} = T_{\times 10} \cdot L \cdot F \cdot (1 - loss) \cdot F \cdot T_{\times 10} + T_{\times 10} \cdot F \cdot (1 - L) \cdot F \cdot T_{\times 10} =$$

$$= T_{\times 10}^2 \cdot F^2 \cdot (1 - L \cdot loss) = T_S \cdot (1 - L \cdot loss) \tag{4.8.2}$$

The overall transmission from waveguide only and objectives, obtained with the spatial filter on the output, is:

$$T_W = \frac{P_{out}^W}{P_{in}} = T_{\times 10} \cdot L \cdot F \cdot (1 - loss) \cdot F \cdot T_{\times 10} = T_{\times 10}^2 \cdot F^2 \cdot L \cdot (1 - loss) =$$

$$= T_S \cdot L \cdot (1 - loss) \tag{4.8.3}$$

Launch efficiency *L* and waveguide losses (*loss*) can be calculated by measuringP_{in}, P_{out}^S, P_{out} and P_{out}^W , then calculating transmission values T_S, T_{W+S} and T_W:

$$L \cdot loss = 1 - \frac{T_{W+S}}{T_S} \tag{4.8.4}$$

This allows calculation of launch efficiency *L* from Equation 4.8.3:

$$L = \frac{T_W + T_S \cdot (L \cdot loss)}{T_S} \tag{4.8.5}$$

The transmission coefficient from the waveguide only can then be calculated as $(1 - loss)$, from Equation 4.8.4, and then as:

$$T^* = \frac{10 \log_{10}(1 - loss)}{l} \left[\frac{dB}{cm}\right] \tag{4.8.6}$$

where: *l* = waveguide length in centimetres.

When referring to transmission losses, the absolute value of T^* is used. By measuring the transmission coefficient of the objectives, $T_{\times 10}$, Fresnel losses can be estimated too from the formula of T_S – Equation (4.8.1). Three measurements were taken for each sample at different transverse positions, featuring the best output profiles (with possibly no defect or ripple on the edges), and then averaged.

4.8.3. LASING EXPERIMENTS

Lasing experiments on waveguiding Ti:sapphire films were conducted in collaboration with Dr. Amol Choudhary with an optical set-up (shown in Figure 4.8.3) similar to the one used for propagation loss measurements, except for the following changes:

- the pump laser is a green laser (either an Ar^+ laser or a CW diode-pumped frequency-doubled Nd:YAG laser), which is attenuated and polarised parallel to the *c* axis of the Ti:sapphire samples via a half-wave plate and a Glan-Thompson prism;
- the pump laser beam is chopped to reduce laser-induced damage to the mirrors;
- the input lens can be changed for different ones with lower magnification factor (4× or 6.3×) to achieve better launch efficiency, depending on the film thickness;
- a high reflective (HR) mirror for the lasing wavelength ($\lambda \approx 750$ nm) and high transmission (HT) for the pump ($\lambda \approx 532$ nm) is attached on the input end-facet of the waveguide with fluorinated oil (Fluorinert), to ensure good contact and parallelism with the end-facet;
- an output coupler is attached on the output end-facet of the waveguide with Fluorinert.

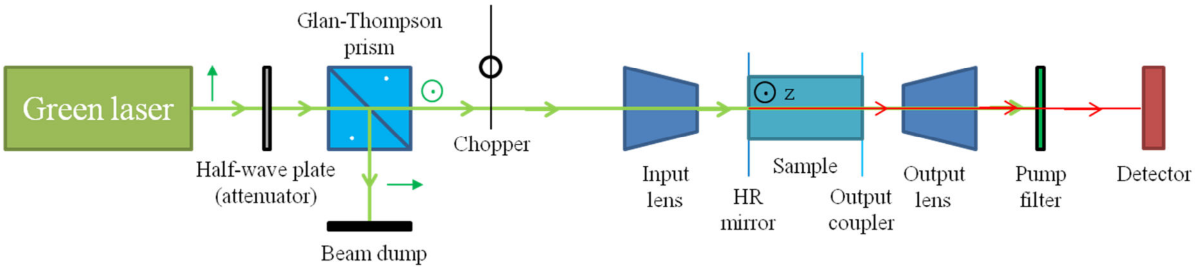

Figure 4.8.3. Schematic of the optical set-up for lasing experiments. The green symbols near the beam represent its polarization, whereas the white dots in the Glan-Thompson prism refer to its extraordinary axis.

4.9. SPECTROSCOPY

Absorption and transmission spectra of YIG samples were measured using a Varian Cary 500 Scan spectrophotometer, where a white light source is used to generate two beams with the same optical length and wavelength that is changed in the selected range (normally between 400 nm and 1400 nm) through the use of gratings: one beam is used as a reference with a blank substrate and the other is incident on the sample under test. The detector beyond the sample and a slit measures the transmitted intensity, which is then normalised to the intensity measured from the reference beam in order to take into account

Fresnel losses from the substrate and potential power variations and thus calculate the optical transmission of the film.

4.10. FERROMAGNETIC CHARACTERISATION

Ferromagnetic characterization of magneto-optic garnets was performed by Dr. Gavin Stenning and Simon Gregory of the School of Physics and Astronomy of the University of Southampton. For FMR spectroscopy a DC magnetic field was applied via an electromagnet controlled by a bipolar power supply, whereas a Vector Network Analyser (VNA) was used both to drive and monitor the properties of a loaded coplanar waveguide (CPW) as a function of frequency and magnetic field. The DC magnetic field strength (up to $B_a = 0.6$ T) was recorded using a Lakeshore 425 Gaussmeter. The RF magnetic field was achieved by excitation of microwaves from a 20 GHz VNA (HP E5071C) through low loss broadband cables passing through the centre of the electromagnetic pole pieces. These were connected to end-launch connectors which allowed for the transition from coaxial cable to a printed circuit board (PCB). The transition from coaxial to PCB allowed for the connection to the CPW, which provided the RF field to the magnetic sample. The RF field and DC field were therefore mutually perpendicular, as required for FMR (see Section 3.6.2.1). The magnetic sample was then placed in a “flip chip” configuration, i.e. with the film side towards the CPW, which ensured that there was a good coupling between the microwave excitation and the magnetic film (see Figure 4.10.1). The microwave circuit can be described as a two-port transmission system, characterised in terms of a scattering matrix S, whose elements (“S parameters”) can be measured by the VNA, including the transmission coefficient of the CPW (S_{21}).

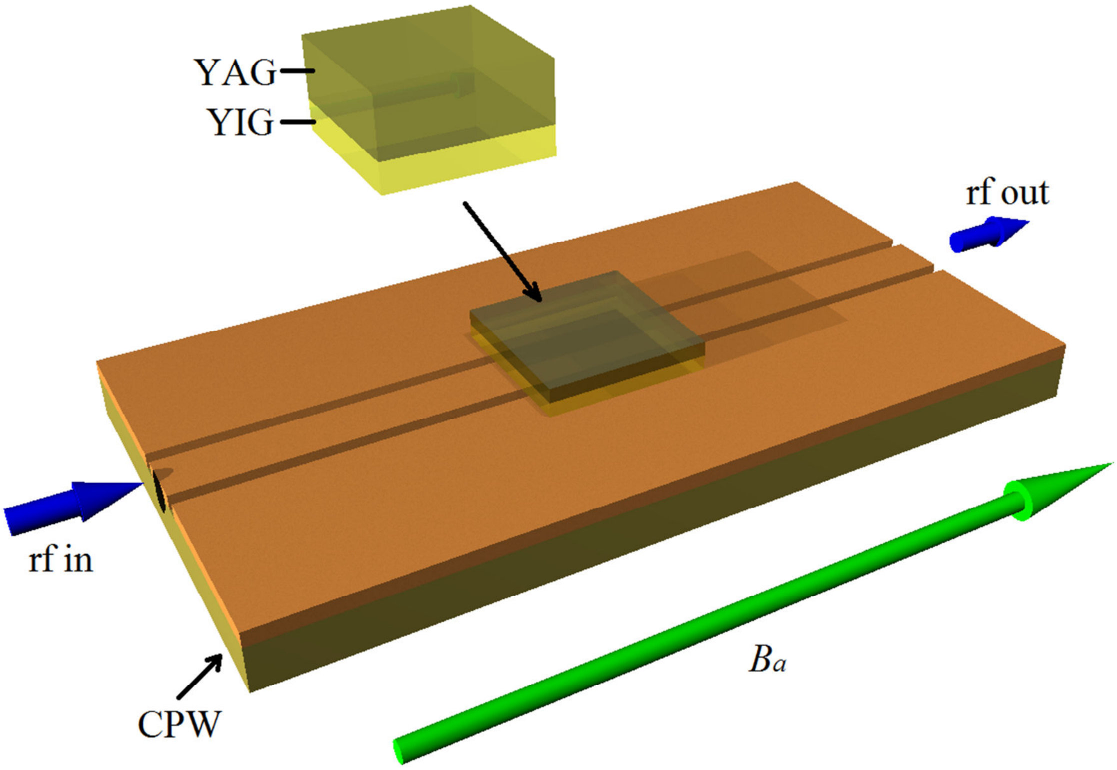

Figure 4.10.1. Schematic of the FMR set-up. B_a is the applied magnetic field.

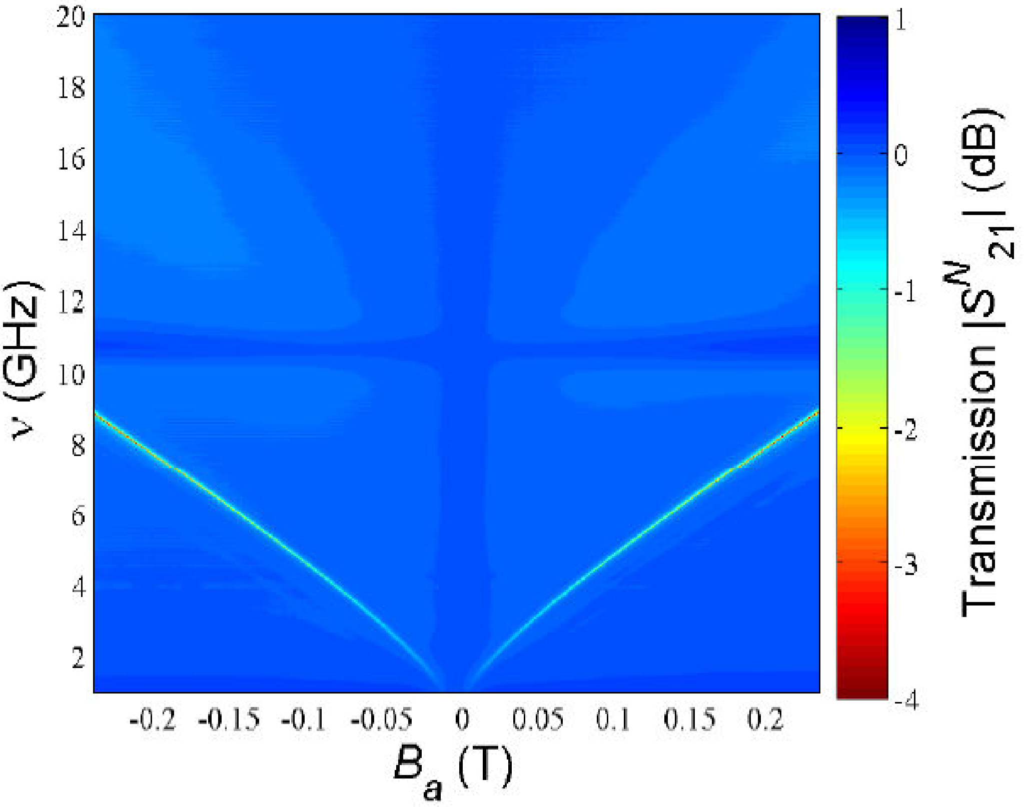

Figure 4.10.2. Normalized S^N_{21} (ν-B_a) map of YIG sample Y20.

The results from these VNA-FMR experiments are usually presented in a 2D map of frequency vs. field map (v-B_a) – see Figure 4.10.2 for an example. This measurement is obtained by sweeping the RF frequency v at different values of the applied magnetic field B_a: the single measurements are collated together into a 2D plot. The colour at a given point in the 2D-map represents the magnitude of S_{21}. Normalized values can be obtained by subtracting the S_{21} transmission obtained in very small magnetic fields (B_a = 0.001 T) from every subsequent frequency sweep: this gives $S^N{}_{21}$, leaving only the field dependent features in the resultant 2D-plot. All values of FMR linewidth (ΔH) reported in this thesis were measured as the FWHM[12] of the FMR absorption at a RF frequency v = 6 GHz (see Figure 4.10.3 for an example). FMR linewidth measurement accuracy is of the order of 0.01 mT.

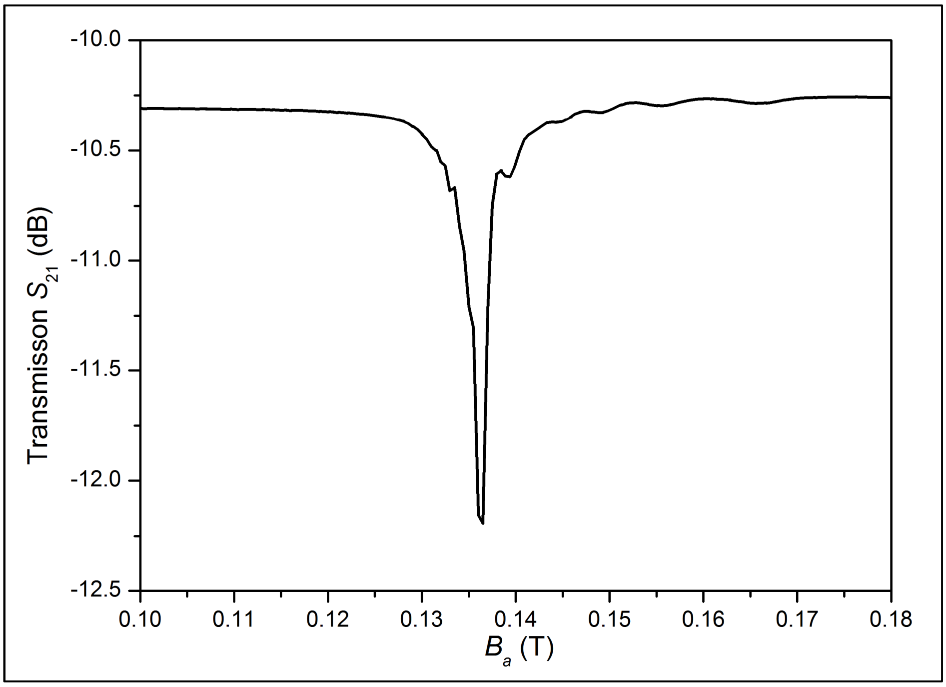

Figure 4.10.3. FMR absorption plot of YIG sample Y20 at v = 6 GHz: $\Delta H \approx$ 1.75 mT.

The relatively broad FMR linewidth measured in all YIG samples ($\Delta H >$ 1 mT), compared to the intrinsic value of bulk YIG spheres ($\Delta H \approx$ 0.015 mT), may be due to several factors:

- demagnetising effects based on the film shape and geometry;
- inhomogeneous RF field laterally across the CPW;
- excitation of magneto-static modes (satellite peaks around the main FMR peak – some are visible in Figure 4.10.3) [10-12], caused by the orientation of the RF excitation field relative to the DC applied field.

---

[12] Full Width at Half Maximum.

All these factors may hinder the measurement of the intrinsic FMR linewidth of our YIG samples. In order to investigate this, some of the YIG samples were cut in smaller 5×5 mm^2 pieces (the centre from original 10×10 mm^2 samples), but no improvement was noticed in terms of FMR linewidth; a few YIG films were also deposited on a localised circular region of the substrate through a shadow mask (a circular hole in an aluminium foil hanging from the substrate holder), but again no significant improvement was achieved. Finally a 2D frequency vs. field map (ν-B_a) was measured from a bulk 5×5×0.5 mm^3 YIG slab (see Figure 4.10.4), purchased from Ferrisphere Inc., to use as a reference for our films, but it showed quite a different behaviour, compared to FMR plots of our YIG films (compare with the right quadrant of Figure 4.10.2): an FMR absorption with a much narrower linewidth was expected (the supplier gave us a ΔH of the order of (0.05 – 0.1) mT in the GHz range); instead, several satellites of the main YIG resonance peak were observed. These are due to magneto-static modes [10-12], which can be caused by the higher aspect ratio (thickness to width) of the bulk YIG piece (1:10), compared to PLD-grown YIG films (of the order of 1:10^3), and by the aforementioned factors. Finally, the narrower FMR linewidth values reported in literature from PLD-grown YIG films were obtained with a different set-up (a microwave cavity) [7, 13], thus suggesting limitations of our rig in measuring narrow FMR linewidths ($\Delta H < 1$ mT).

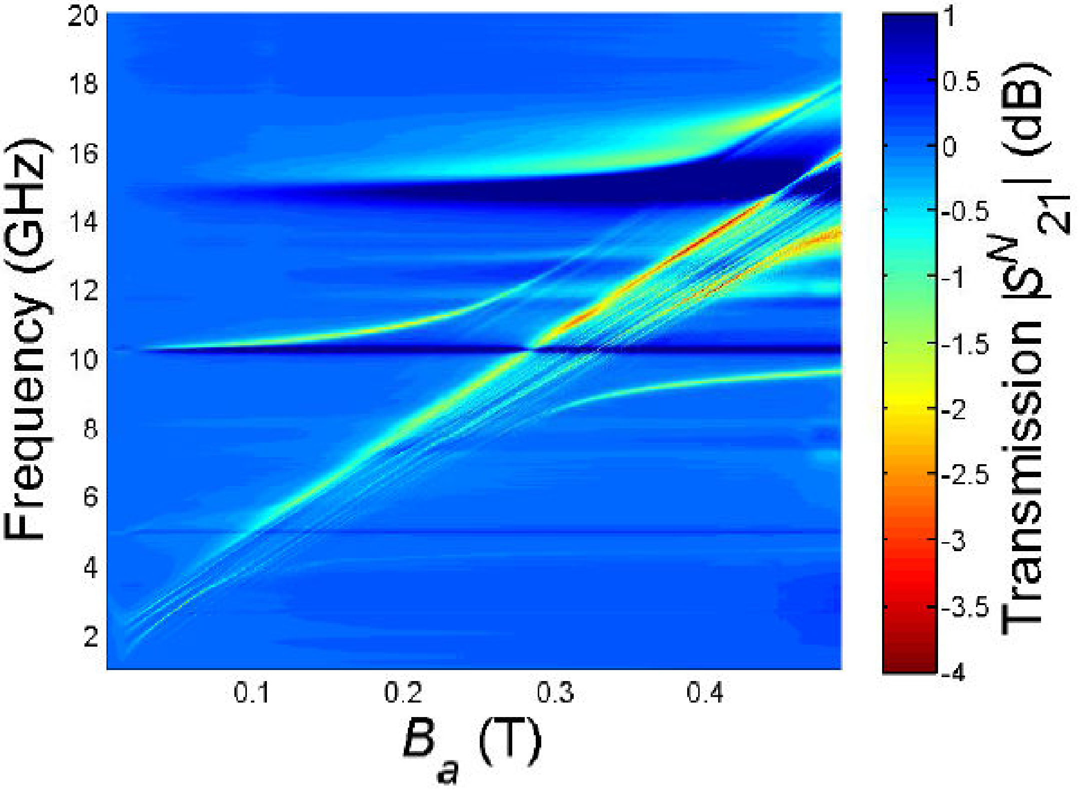

Figure 4.10.4. Normalized S^N_{21} (ν-B_a) map of a 5×5×0.5 mm^3 bulk YIG slab, obtained by VNA-FMR ($B_a \geq 0$).

4.11. CONCLUSIONS

All the experimental and analytical techniques used for the fabrication and characterisation of the samples discussed in this thesis have been presented in this Chapter. The PLD systems have been described in Section 4.2, providing details of the substrate heating systems and discussing the issues with substrate temperature measurements and calibration in Sub-section 4.2.4. Procedures for target re-conditioning and target/substrate cleaning have been described in Section 4.3. All analytical techniques have been described in the second part of this chapter: visual and surface analysis methods have been introduced in Section 4.4; compositional evaluation techniques have been compared and their issues discussed in Section 4.5; the basics of XRD analysis has been covered in Section 4.6; end-polishing of optical waveguides has been illustrated in Section 4.7, with description of optical set-ups for characterisation of Ti:sapphire waveguides in Section 4.8; optical spectroscopy has been presented in Section 4.9 and finally Section 4.10 has provided details on FMR characterisation of YIG films, presenting some issues and limitations of the rig used.

4.12. REFERENCES

1. K. A. Sloyan, "Multi-beam pulsed laser deposition for engineered crystal films," PhD thesis at *Optoelectronics Research Centre* (University of Southampton, Southampton, 2013).

2. R. Delmdahl, and R. Patzel, "Pulsed laser deposition - UV laser sources and applications," Appl. Phys. A-Mater. Sci. Process. **93**, 611-615 (2008).

3. R. W. Eason, T. C. May-Smith, C. Grivas, M. S. B. Darby, D. P. Shepherd, and R. Gazia, "Current state-of-the-art of pulsed laser deposition of optical waveguide structures: Existing capabilities and future trends," Appl. Surf. Sci. **255**, 5199-5205 (2009).

4. T. C. May-Smith, A. C. Muir, M. S. B. Darby, and R. W. Eason, "Design and performance of a ZnSe tetra-prism for homogeneous substrate heating using a CO_2 laser for pulsed laser deposition experiments," Appl. Optics **47**, 1767-1780 (2008).

5. T. C. May-Smith, "Pulsed laser deposition of thick multilayer garnet crystal films for waveguide laser devices," PhD thesis at *Optoelectronics Research Centre* (University of Southampton, Southampton, 2005).

6. A. A. Anderson, "Crystalline planar waveguide lasers fabricated by pulsed laser deposition," PhD thesis at *Optoelectronics Research Centre* (University of Southampton, Southampton, 1998).

7. S. A. Manuilov, R. Fors, S. I. Khartsev, and A. M. Grishin, "Submicron $Y_3Fe_5O_{12}$ Film Magnetostatic Wave Band Pass Filters," J. Appl. Phys. **105**, 033917 (2009).

8. N. B. Ibrahim, C. Edwards, and S. B. Palmer, "Yttrium iron garnet surface modification during pulsed laser ablation deposition," Mater. Sci. **22**, 111-115 (2004).

9. "Inorganic Crystal Structure Database (ICSD), part of the Chemical Database Service," http://icsd.cds.rsc.org/, Accessed December 2013.

10. R. W. Damon, and J. R. Eshbach, "Magnetostatic modes of a ferromagnet slab," J. Phys. Chem. Solids. **19**, 2 (1960).

11. J. F. Dillon, "Magnetostatic modes in disks and rods," J. Appl. Phys. **31**, 10 (1960).

12. L. R. Walker, "Resonant modes of ferromagnetic spheroids," J. Appl. Phys. **29**, 318–323 (1958).

13. V. P. Denysenkov, and A. M. Grishin, "Broadband ferromagnetic resonance spectrometer," Rev. Sci. Instrum. **74**, 3400-3405 (2003).

5. CHAPTER 5
SINGLE-PLD OF TI:SAPPHIRE

5.1. INTRODUCTION

The theory of Ti:sapphire, waveguiding and lasing has been covered in Chapter 3. This chapter provides the results of PLD of Ti:sapphire.

There are several reports of PLD growth of Ti:Al_2O_3 [1-15], most of which are on sapphire substrates [1-11], but only a few of these report lasing action [1-6]; typical deposition conditions of Ti:sapphire, as found from literature review, are summarised in Table 5.1.1.

Substrate	Single-crystal *c*-cut sapphire
Laser (λ [nm])	KrF ($\lambda = 248$)
Repetition frequency [Hz]	(20 – 25)
Fluence [J/cm^2]	~4
Target – substrate distance [cm]	~4
O_2 or Ar pressure [Pa]	~(0.03 – 2)
Substrate temperature [K]	~(1220 – 1370)

Table 5.1.1. Optimum deposition conditions for PLD of Ti:sapphire films.

As outlined in Section 1.2.1, the aim of this project was to replicate and try improving the performances of Ti:sapphire waveguide lasers grown on un-doped sapphire substrates by PLD. Simulations performed by Dr. Amol Choudhary suggested a Ti:sapphire film thickness of ~10 μm for waveguiding films with a ~0.04 at. % Ti doping, which induces a refractive index change of the order of 10^{-4} compared to undoped sapphire ($n_e \approx 1.7620$ and $n_e \approx 1.7540$ at $\lambda = 800$ nm) [16].

5.2. PRELIMINARY EXPERIMENTS

The first depositions (samples AS1-AS5) are not discussed here, because the PLD setup was not optimized; however some conclusions were drawn from those samples for the optimisation of the PLD setup and for subsequent depositions. For instance, CO_2 laser power and substrate temperature were calibrated at the melting point of gold ($T \approx 1337$ K), close to the optimum value reported in literature, by metal balancing experiments; the UV optical setup was re-optimised after these depositions, in order to reduce the excimer laser spot size and increase the laser fluence on the target. Further improvements were made while doing experiments: for this reason depositions of samples AS6-AS15, although useful for optimisation of deposition conditions of Ti:sapphire, are covered in this paragraph but cannot be compared with subsequent depositions because of changes in procedures and PLD setup.

After the first deposition trials (AS1-AS5), proper depositions were started in order to investigate optimum conditions for the PLD of Ti:sapphire. The typical growth conditions found in the literature were tried in the depositions of samples AS6-AS9: the parameters common to these depositions are reported in Table 5.2.1.

Target (doping [at. %])	Single-crystal Ti:sapphire (0.08 – 0.17)
Substrate	*c*-cut sapphire
Laser (λ [nm])	KrF ($\lambda = 248$)
Repetition frequency [Hz]	20
Fluence [J/cm^2]	~(3 – 4)
Target – substrate distance [cm]	4.0
Substrate temperature [K]	~1350

Table 5.2.1. Deposition conditions for PLD of Ti:sapphire samples AS6-AS9.

In all cases, the deposition time was 1 hour, i.e. 72,000 laser pulses, which produced Ti:sapphire films with thickness between 1 μm and 4 μm. The parameters varied in the deposition of samples AS6-AS9 are shown in Table 5.2.2 with the main experimental results. Reliability of EDX results has been discussed in Section 4.5: as explained there, they should not be trusted, due to their inaccuracy, although used as a guide for optimisation.

ID	Gas	P_{GAS} [Pa]	S_q [nm]	Ti conc. [at. %]	Fluorescence/t_f [μm^{-1}]
AS9	Ar	0.1	18.2	0.04	0.2083
AS8	O_2	0.1	18.5	0.03	0.0731
AS6	O_2	0.3	45.0	0.01	0.0696
AS7	O_2	2	227.5	0.01	0.1535

Table 5.2.2. Background gas, gas pressure (P_{GAS}), RMS surface roughness (S_q), Ti concentration and intensity of fluorescence normalised to film thickness (t_f) of samples AS6-AS9.

Relying on EDX measurements, the highest Ti concentration is observed in AS9, grown in an Ar ambient, which also features the highest fluorescence value. From Table 5.2.2 an increase in RMS surface roughness is observed with increasing oxygen pressure. The higher fluorescence of AS7, compared to AS6 and AS8, may be due to the scattering induced by the higher surface roughness.

Sample AS10 was deposited in vacuum (~0.01 Pa) and at lower fluence (~2.5 J/cm^2) than the other samples: although a low Ti concentration (~0.01 at. %) was measured by EDX, it features higher fluorescence (~0.3438) than samples AS6-AS9, but also high surface roughness ($S_q \approx 225.4$ nm). Samples AS11-AS14 were deposited over 5 hours, i.e. 360,000 pulses, which produced Ti:sapphire films with thickness between 12 μm and 24 μm: in particular, samples AS11 and AS12 were deposited under the same conditions (see Table 5.2.1) except for gas and its relative pressure, as shown in Table 5.2.3.

ID	Gas	P_{GAS} [Pa]	S_q [nm]	Ti conc. [at. %]	Fluorescence/t_f [μm^{-1}]
AS11	O_2	0.3	982.4	0.03	0.2964
AS12	none	0.01	802.1	0.04	0.4201

Table 5.2.3. Background gas, gas pressure (P_{GAS}), RMS surface roughness (S_q), Ti concentration and intensity of fluorescence normalised to film thickness (t_f) of samples AS11 and AS12.

The roughness of AS12 was expected to be even lower than that of samples AS8 and AS9, according to previous observation. Also AS11 is rougher than AS12 and AS6-AS10. These results may be due to a modified UV optical setup, which caused a slight change in laser spot size and fluence on the target, or alternatively to higher thickness.

According to EDX measurements, the Ti concentration is slightly higher in AS12 than in AS11 and very close to the values found in samples AS8 and AS9.

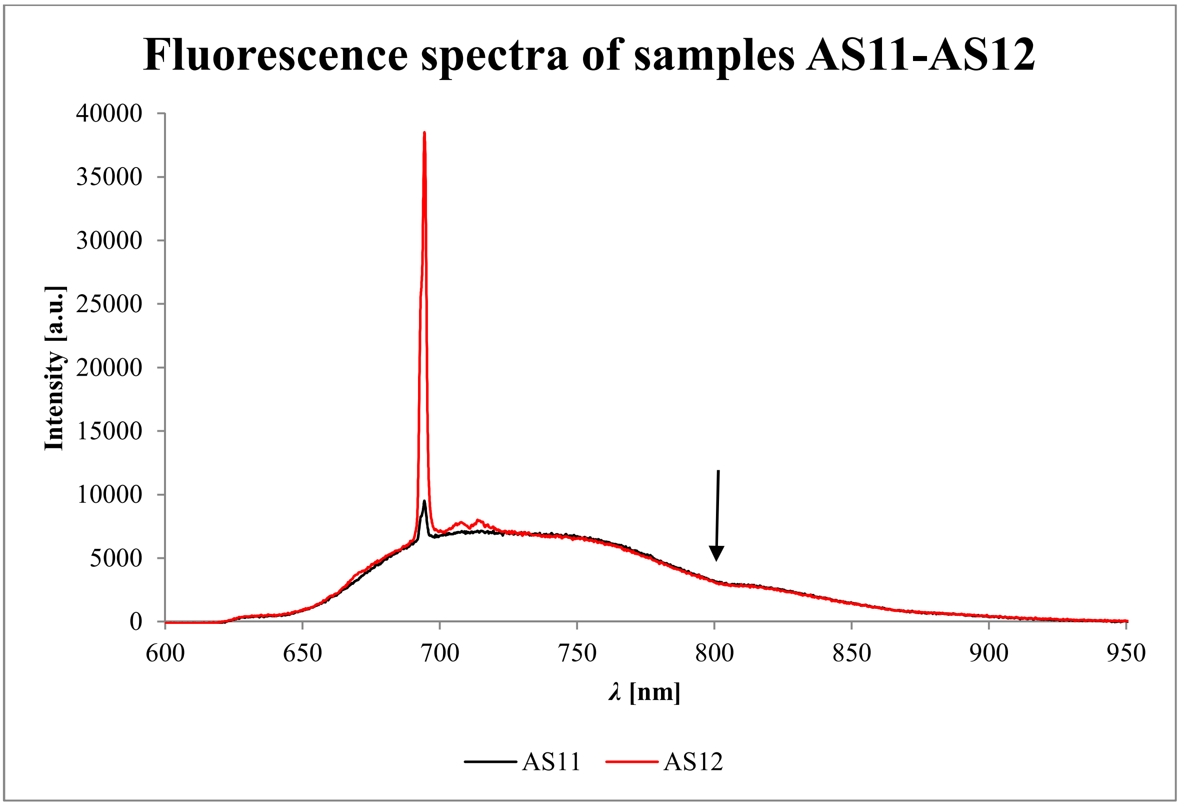

Figure 5.2.1. Fluorescence spectra of samples AS11 and AS12 – λ = (600 - 950) nm. The arrow indicates a dip. The peaks at ~694 nm are due to Cr^{3+} impurities [17].

Fluorescence is almost the same in both samples, except for the high and sharp peak at ~694 nm due to Cr^{3+} impurities [17] (see Figure 5.2.1); a shallow dip (indicated by arrow) is observed at ~800 nm and could be due to re-absorption from Ti^{4+} ions [18], as explained in Section 3.4. For this reason the subsequent samples were deposited in vacuum, i.e. without any background gas in the chamber, to verify if any improvement was possible.

In order to prevent formation of droplets and particles on the film surface, pre-ablation of the target was used for the next depositions. The results from samples AS13-AS14, illustrated below, confirmed the importance of target pre-ablation, which appears to affect surface roughness of Ti:sapphire films.

Samples AS12-AS14 were deposited in vacuum (0.01 Pa) at different substrate temperatures, in order to investigate its effect on Ti:sapphire film properties. Table 5.2.4 summarizes the main data collected from these samples.

ID	***T*** **[K]**	**S_q [nm]**	**Ti conc. [at. %]**	**Fluorescence/t_f [µm^{-1}]**
AS12	1350	802.1	0.04	0.4201
AS13	1375	55.7	0.03	0.2785
AS14	1400	73.2	0.02	0.2396

Table 5.2.4. Substrate temperature (T), RMS surface roughness (S_q), Ti concentration and intensity of fluorescence normalised to film thickness (t_f) of samples AS12-AS14.

According to the literature, the substrate temperature is one of the most critical deposition conditions of $Ti:Al_2O_3$ films grown by PLD [3, 11, 19]. Temperatures lower than ~1220 K cause the formation of polycrystalline or even amorphous films [20], whereas in Ti:sapphire films deposited at temperatures higher than ~1370 K the Ti concentration tends to decrease with increasing temperature [19]. XRD analysis showed that all samples are crystalline with the same orientation as the *c*-cut substrate.

Analysis with ZeScope showed that AS12 features the highest roughness of these samples; however the target was not pre-ablated before the deposition of this film, as was done before AS13 and AS14. Ti concentration and fluorescence are highest in AS12 and decrease with increasing substrate temperature, as expected.

From Figure 5.2.2 (not comparable with the previous fluorescence spectra because of different settings in the measurement system – see Section 4.8.1) it is clear that fluorescence is highest in sample AS12 and decreases with increasing substrate temperature, thus confirming the decreasing trend of Ti concentration with increasing temperature and previous findings in the literature [11, 20].

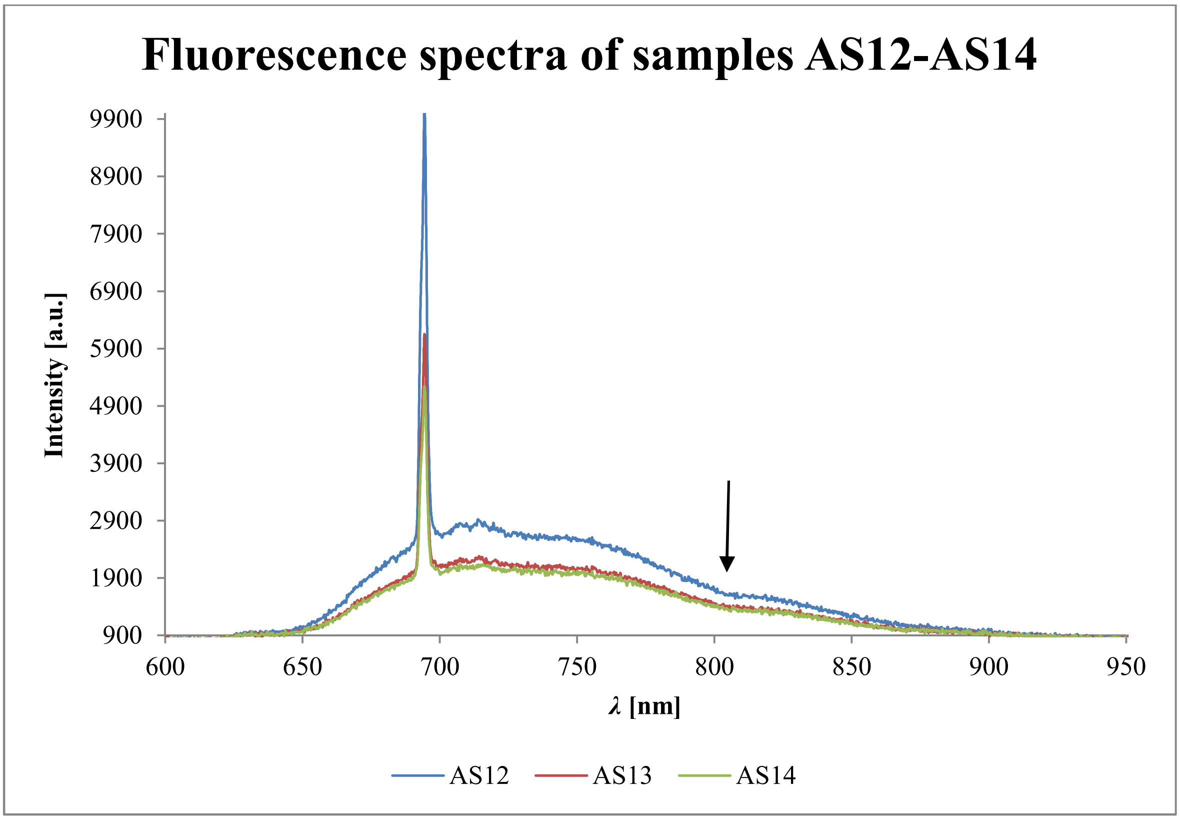

Figure 5.2.2. Fluorescence spectra of samples AS12-AS14 – λ = (600 - 950) nm.
The peaks at ~694 nm are due to Cr^{3+} impurities [17].

The thick Ti:sapphire films (AS11-AS14) were end-polished by Dr. Amol Choudhary in order to measure waveguide losses. Measurements were performed using a 1.5 mW He-Ne laser ($\lambda \approx 633$ nm) – see Section 4.8.2 for more details.

AS12 did not show waveguiding, probably because of its bad quality (the film appears rough, grainy and frosty). AS11 has losses as high as (7.1 ± 0.4) dB/cm, probably because of its high roughness and particle density. AS13 and AS14 have lower losses than AS11, (2.6 ± 0.4) dB/cm and (2.5 ± 0.4) dB/cm respectively, but higher than those reported in [5] (~1.6 dB/cm). No lasing was observed from any of these samples, though a strong fluorescence signal was measured from the output of the waveguides, probably because samples are too long and such high losses prevent lasing: in fact, samples were 2.5 times longer than the absorption length (3.4 mm) [20] and this unnecessarily increases the propagation losses and suppresses lasing.

Because all samples presented so far had non-uniform thickness, the PLD setup was re-optimised in order to deposit a thick uniform Ti:sapphire film (sample AS15) under the best conditions found so far (those of sample AS12) and reported in Table 5.2.5.

Substrate	*c*-cut sapphire
Repetition frequency [Hz]	20
Fluence [J/cm^2]	~3.3
Target – substrate distance [cm]	4.0
Substrate temperature [K]	~1350
Gas	none
Vacuum pressure [Pa]	0.01

Table 5.2.5. Deposition conditions of samples AS15.

This sample, ~12 μm thick near the edges, has a relatively low RMS surface roughness compared to samples AS11-12 ($S_q \approx 68.8$ nm), which is probably near the limit for such a thick film due to intrinsic roughness of Ti:sapphire – in fact, pyramids with an hexagonal base can be clearly observed on the film surface under optical microscopy, SEM (see Figure 5.2.3) or ZeScope (see Figure 5.2.4 and compare it with Figure 5.2.5 from sample AS12, much rougher than AS15).

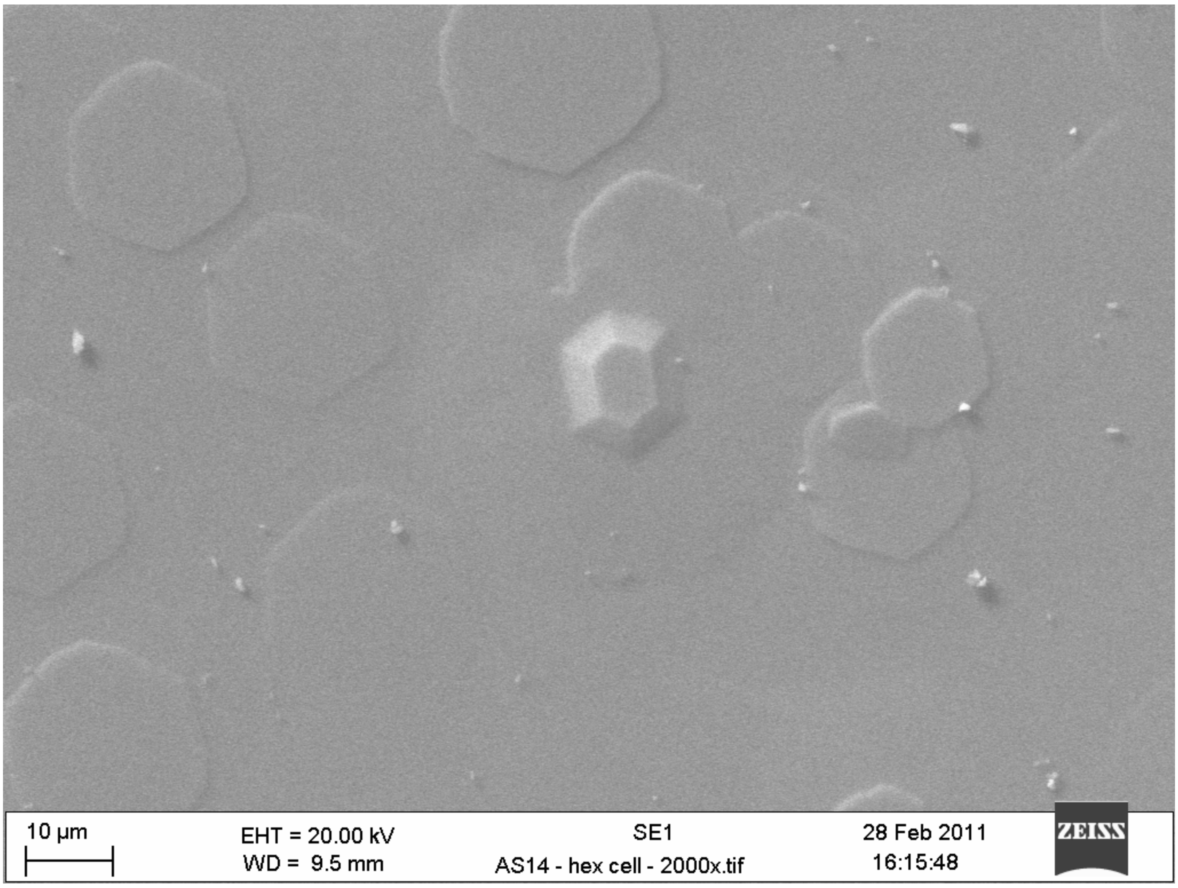

Figure 5.2.3. SEM picture of the hexagonal crystallites (sample AS14).

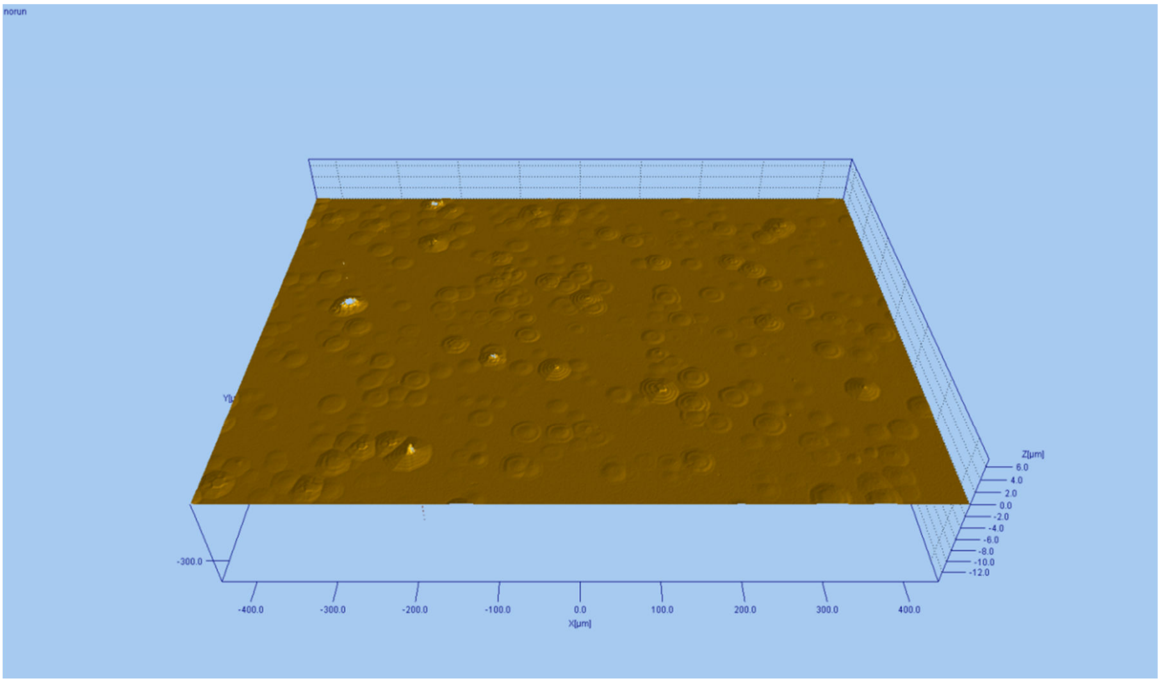

Figure 5.2.4. 3D image (flattened) of the centre of sample AS15, smooth thick Ti:sapphire film (ZeScope – 10× objective).

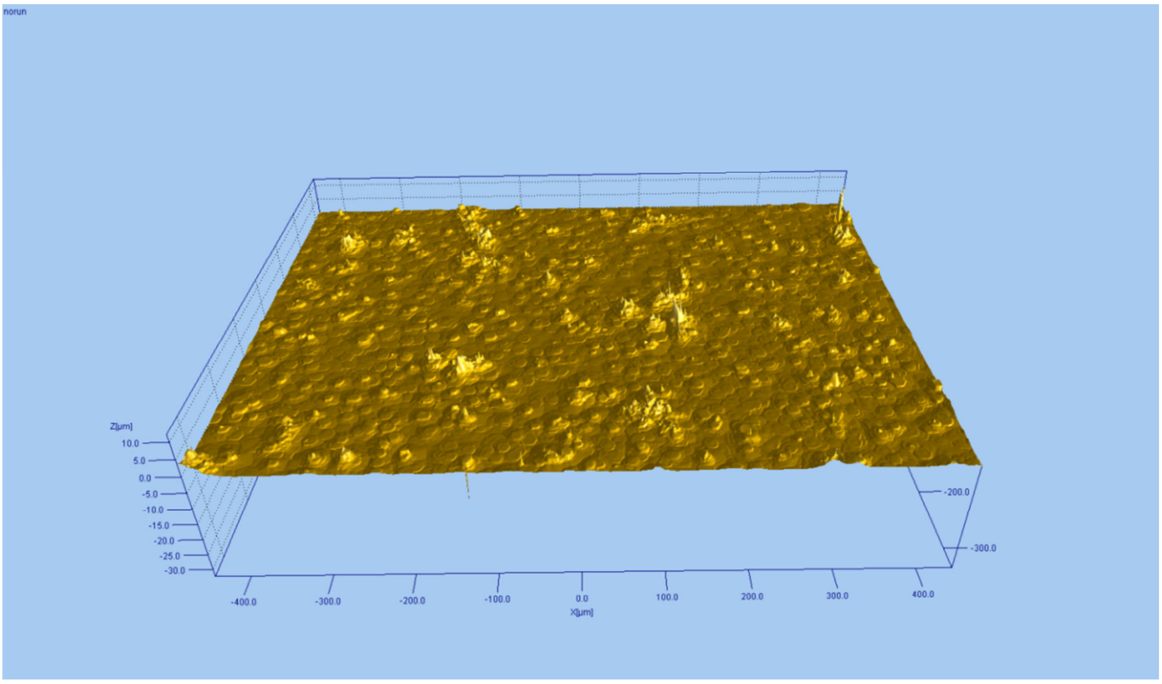

Figure 5.2.5. 3D image (flattened) of the centre of sample AS12, rough thick Ti:sapphire film (ZeScope – 10× objective).

Sample AS15 was lapped and end-polished by Dr. Amol Choudhary and then characterised in terms of waveguide losses, which were measured to be as low as ~(2.2 ± 0.4) dB/cm, ~10% lower than the value measured from AS14. This improvement may be due to the lower surface roughness and better uniformity of the Ti:sapphire film across the substrate surface. Better results are expected with a further reduction of surface roughness and particles, which could be removed by polishing.

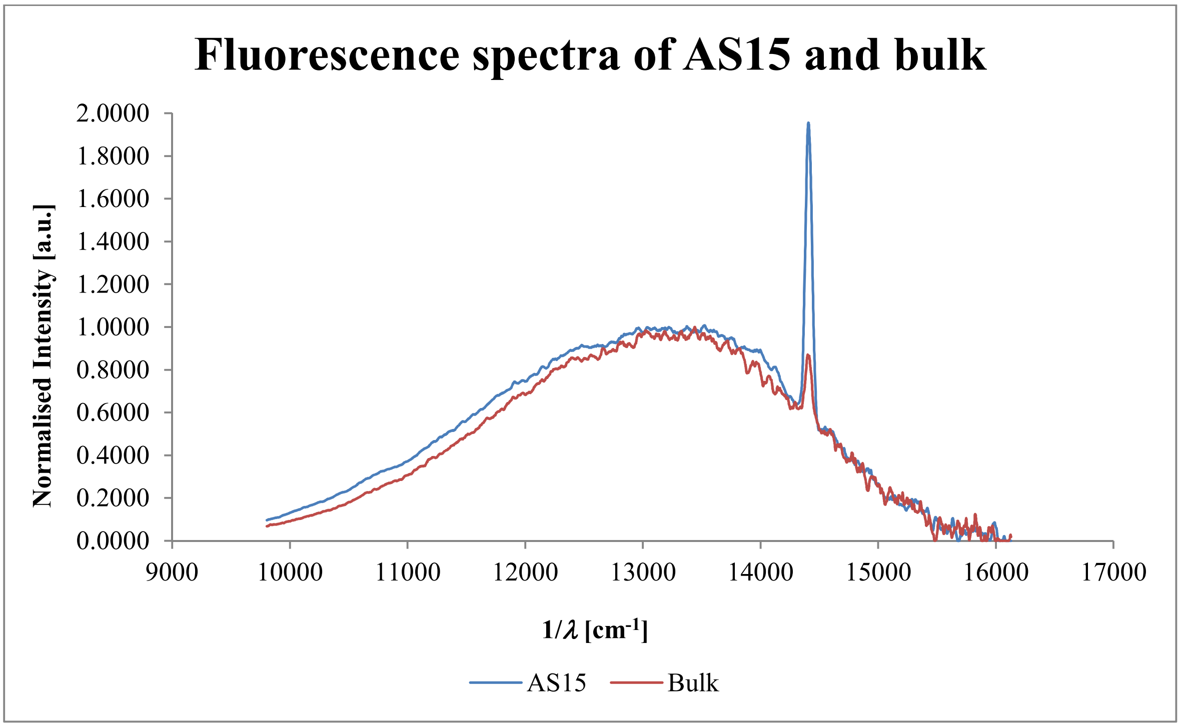

Figure 5.2.6. Fluorescence spectrum of AS15, compared with bulk Ti:sapphire – $1/\lambda$ = (10000 - 17000) cm^{-1}. The peaks at ~694 nm are due to Cr^{3+} impurities [17].

Figure 5.2.6 shows the fluorescence spectrum of sample AS15 in comparison with that from a bulk piece of Ti:sapphire. When plotted as a function of frequency, both spectra appear symmetric without any dip (visible in the spectra in Figure 5.2.1 and Figure 5.2.2), meaning that there is no re-absorption from Ti^{4+} ions.

These preliminary experiments were helpful for the optimisation of the PLD setup and deposition procedures and also to understand the growth dynamics of Ti:sapphire by PLD. However, in order to optimise the deposition conditions of Ti:sapphire further experiments were needed and these are described in the next paragraphs.

From these preliminary depositions it was observed that target pre-ablation is important for the minimisation of surface roughness and particle density. However, the presence of hexagonal-shaped features (see Figure 5.2.3, 5.2.4 and 5.2.5) suggests that they are not particles, but crystallites, which are thus unavoidable as they are intrinsic to the growth mode of Ti:sapphire, limiting the minimum surface roughness of films grown by PLD.

The lack of holes in most films leads to exclusion of the Volmer-Weber growth mode (island formation only), whereas the presence of 3D islands cannot be explained with the Frank–van der Merwe growth mode (layer by layer only); so, the film growth must happen by Stranski-Krastanov mode, i.e. 2D layer and 3D island growth [22]. This means that island formation cannot be avoided, being an intrinsic growth mode of Ti:sapphire by

PLD, and the crystallite presence on the film surface can be a problem for the fabrication of waveguides and lasers, as they would cause scattering and losses, due to Ti:sapphire being an anisotropic material. However, if this problem relates only to the film surface (Stranski-Krastanov growth mode, as assumed here, and not Volmer-Weber growth mode), then it could be overcome by polishing the surface or by depositing an un-doped capping layer on the waveguiding film, in order to reduce scattering losses.

A preliminary study of the effect of background gas and its pressure on Ti:sapphire film properties was performed. However, it was not systematic enough and it did not shed enough light on variation of Ti concentration and fluorescence with oxygen pressure. For this reason a new study was performed with an optimised PLD setup and procedures and is described in the following paragraphs. Although depositions in high vacuum ($P_{\mathrm{VAC}} \sim 10^{-2}$ Pa) gave interesting results, especially in terms of fluorescence, they were abandoned for other troublesome reasons: the plume in high vacuum expands more than in low vacuum and ablated material is deposited on laser windows, which causes reduction of transmitted CO_2 laser power and consequently reduction of substrate temperature and of excimer laser fluence and consequently undesirable changes in plume dynamics and composition.

5.3. OPTIMISATION OF OXYGEN PRESSURE

Five thin test films (AS16-AS18 and AS31-AS32) were deposited in one hour each (72,000 laser pulses) under the same conditions (summarised in Table 5.2.1), except for different values of oxygen pressure, in order to understand its effect on surface roughness, crystallinity, composition and fluorescence of Ti:sapphire films. Film thickness is ~4 μm for all samples. The most relevant data collected from these samples are reported in Table 5.3.1. XRD analysis showed that all samples are crystalline with the same orientation as the substrate, as only the peak due to the *c*-plane was found in a wide scan ($2\theta = 10° - 80°$).

ID	**P_{O2} [Pa]**	**S_q [nm]**	**Ti conc. [at. %]**	**Fluorescence/t_f [μm^{-1}]**
AS18	0.2	23.8	0.03	0.0064
AS31	0.5	3.9	0.01	0.0027
AS16	1	13.7	0.02	0.0032
AS32	5	18.0	0.02	0.0280
AS17	10	31.8	0.02	0.0045

Table 5.3.1. Oxygen pressure (P_{O2}), RMS surface roughness (S_q), Ti concentration and intensity of fluorescence normalised to film thickness **(t_f)** of samples AS16-AS18 and AS31-AS32.

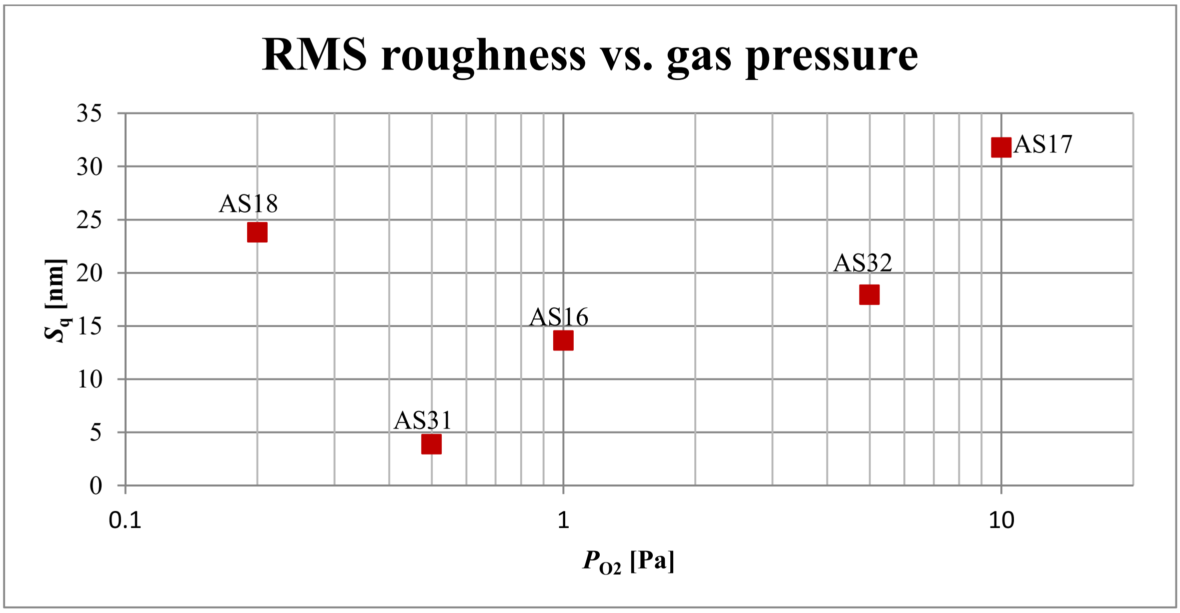

Figure 5.3.1. Variation of RMS roughness (S_q) with oxygen pressure (P_{O2}). Samples AS16-AS18 and AS31-AS32.

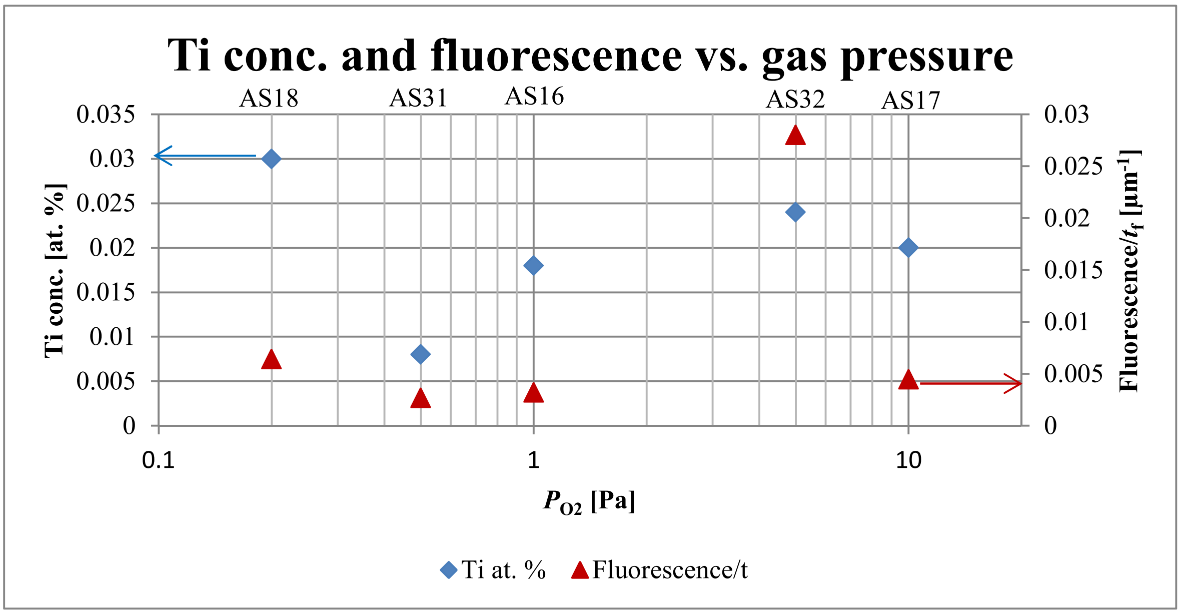

Figure 5.3.2. Variation of Ti concentration and fluorescence normalised to thickness with oxygen pressure (P_{O2}). Samples AS16-AS18 and AS31-AS32.

Figure 5.3.1 and Figure 5.3.2 show the variation of surface roughness, Ti concentration (as measured by EDX) and fluorescence with oxygen pressure.

Sample AS31 is the smoothest, but also the one with the lowest Ti concentration and fluorescence. Surface roughness tends to increase with increasing gas pressure from 0.5 Pa to 10 Pa. Although fluorescence is expected to be correlated to Ti concentration, there is no clear correlation between them, with only AS32 standing out from the low fluorescence level (average: ~0.0042 µm^{-1}) of the other samples. As explained earlier, this may be due to the presence of Ti^{4+} ions in the film or inaccuracy of EDX measurements.

Sample AS17 is the only domed film (thicker in the centre than the edges) of the set: this is probably due to the fact that the plume is smaller and more confined in low vacuum, thus causing a higher deposition rate in the centre than the edges and non-uniformity of film thickness. Also, the surface of this sample and AS32 does not appear uniform to the eye: in particular, the regions around the shadowed corners look denser and more opaque.

5.4. OPTIMISATION OF SUBSTRATE TEMPERATURE

Five thin test films (AS18, AS21-AS22 and AS33-AS34) were deposited in one hour each (72,000 laser pulses) under the same conditions (summarised in Table 5.2.1), except for substrate temperature, in order to understand its effect on surface roughness, crystallinity, composition and fluorescence of Ti:sapphire films. The oxygen pressure was set to 0.2 Pa for all depositions. Film thickness is ~4 μm for all samples, except for AS34 ($t_f \approx 2.5$ μm). The most relevant data collected from these samples are reported in Table 5.4.1.

ID	T [K]	S_q [nm]	Ti conc. [at. %]	Fluorescence/t_f [μm^{-1}]
AS33	1250	4.6	0.02	0.0215
AS22	1300	9.3	0.02	0.0522
AS18	1350	23.8	0.03	0.0064
AS21	1400	6.3	0.01	0.0404
AS34	1450	2.8	0.03	0.0448

Table 5.4.1. Substrate temperature (T), RMS surface roughness (S_q), Ti concentration and intensity of fluorescence normalised to film thickness (t_f) of samples AS18, AS21-AS22 and AS33-AS34.

XRD analysis showed that all samples are crystalline with the same orientation as the substrate: even at the lowest temperature only the α-Al_2O_3 (006) peak is observed at ~41.4°, as shown in Figure 5.4.1 for sample AS33. All samples but AS18 have a surface roughness $S_q < 10$ nm. Figure 5.4.2 and Figure 5.4.3 show the variation of surface roughness, Ti concentration and fluorescence with substrate temperature.

There is no clear correlation between fluorescence and Ti concentration. The former should increase with increasing Ti concentration; however, the sample with the highest Ti concentration (AS18) features the lowest fluorescence. Unfortunately, as already stated, EDX does not give accurate measurement of low-weight elements such as Ti, whose peak is also very close to the one due to oxygen in the EDX spectra; so EDX measurements cannot be fully trusted. Moreover, EDX does not provide any information on valence state of Ti ions and, as stated in Section 5.2, Ti^{4+} causes a re-absorption band centred between

750 nm and 800 nm; so, a high concentration of Ti does not imply high fluorescence and lasing, as all the Ti atoms present may not be in the correct valence state (Ti^{3+}).

The highest fluorescence is observed at $T \approx 1300$ K, but the highest Ti concentration at $T \approx 1350$ K. So, we considered these two values as optimum substrate temperatures.

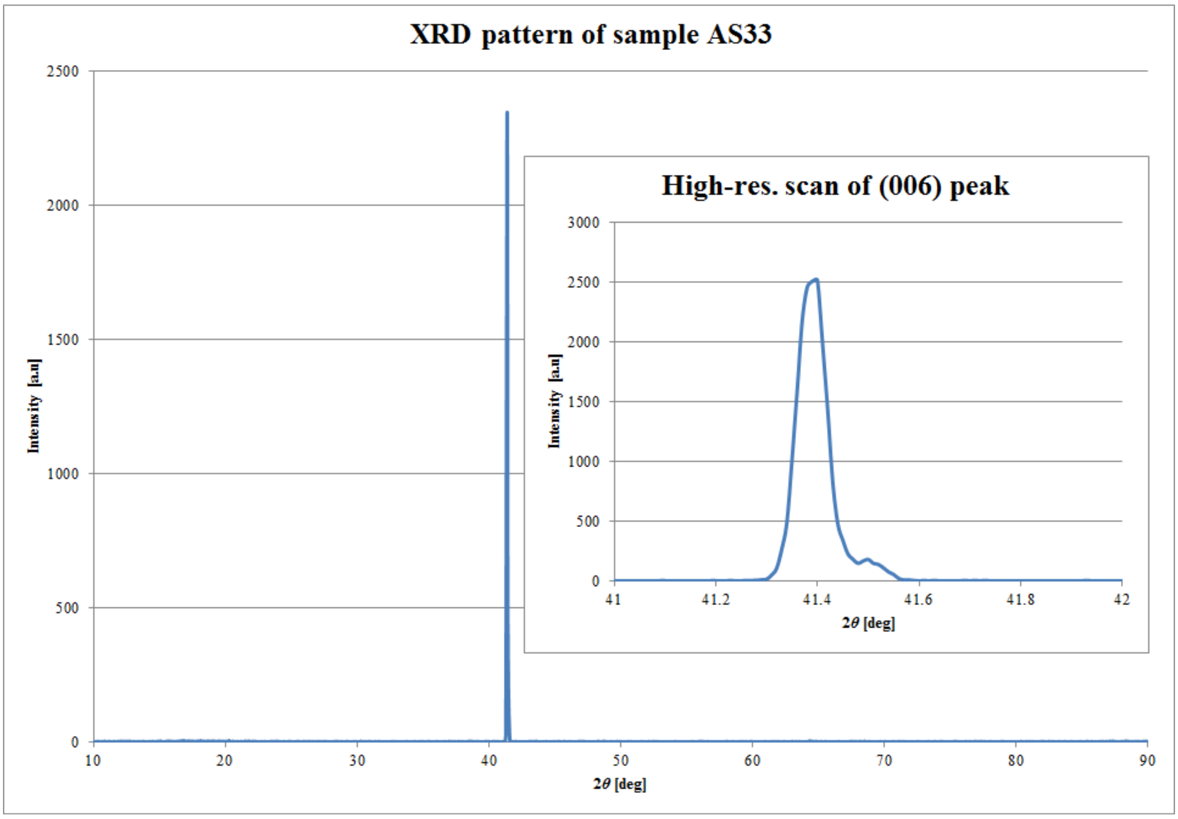

Figure 5.4.1. XRD pattern of sample AS33.
The inset shows a higher resolution scan of the α-Al_2O_3 (006) peak.

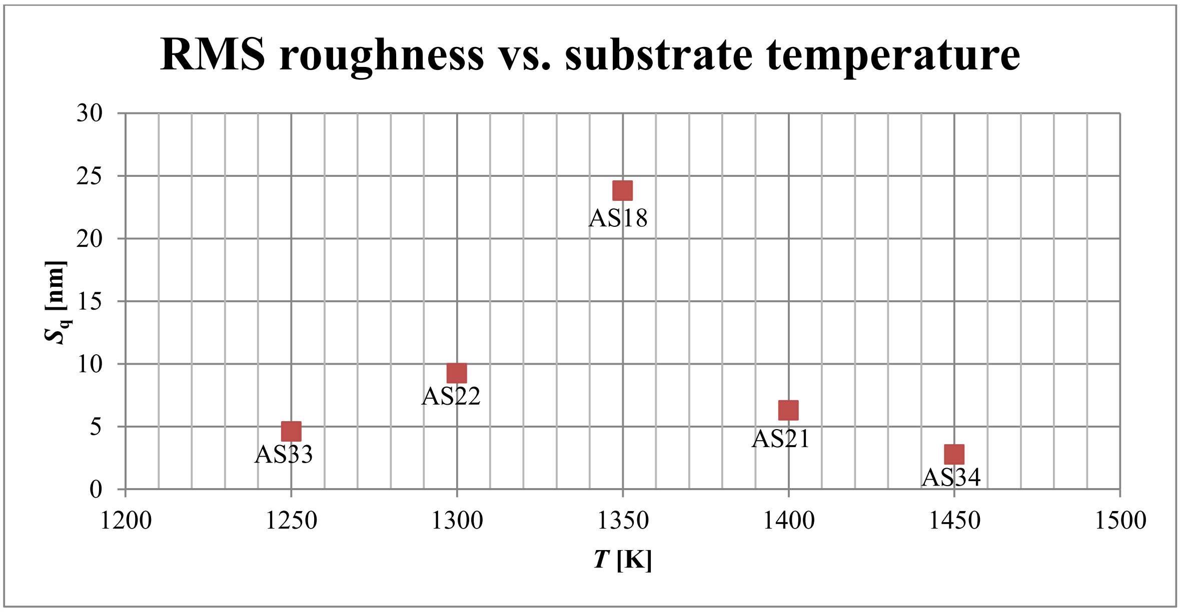

Figure 5.4.2. Variation of RMS roughness (S_q) with substrate temperature (T).
Samples AS16-AS18 and AS31-AS32.

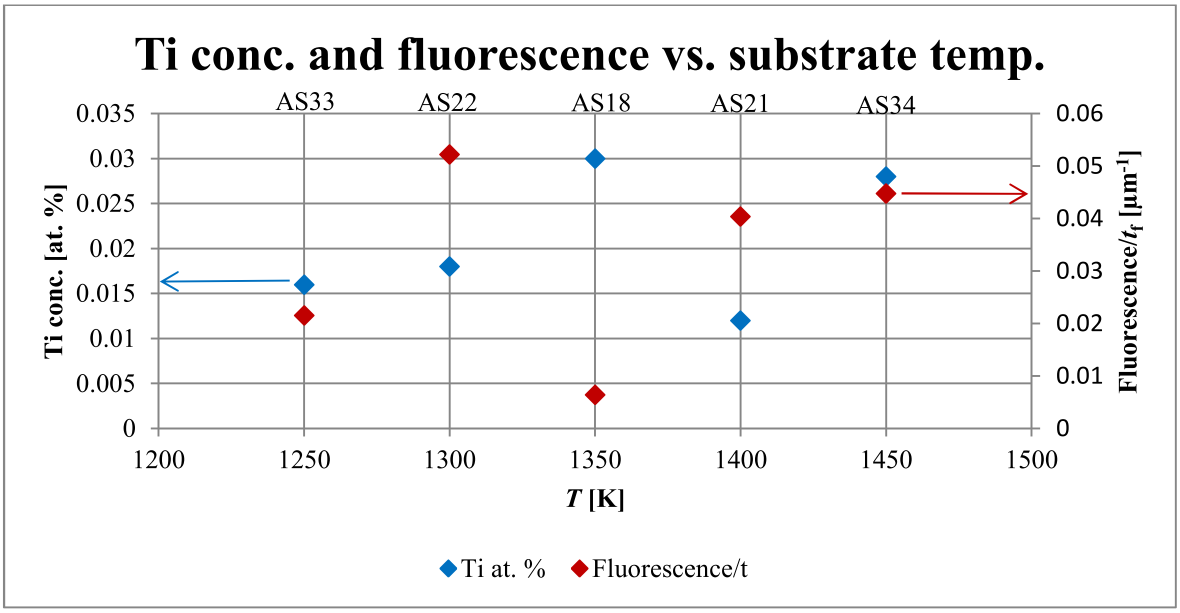

Figure 5.4.3. Variation of Ti concentration and fluorescence normalised to thickness with substrate temperature. Samples AS16-AS18 and AS31-AS32.

5.5. EFFECT OF VARIATION OF BACKGROUND GAS

Four thin test films (AS18-AS20 and AS23) were deposited in one hour each (72,000 laser pulses) under the same conditions (summarised in Table 5.2.1), except for different background gas, in order to understand its effect on surface roughness, crystallinity, composition and fluorescence of Ti:sapphire films. Gas pressure was set to $P_{\mathrm{GAS}} \approx 0.2$ Pa and substrate temperature to $T \approx 1350$ K. A fifth film (AS24) was deposited in Ar, under the same conditions as AS23, but at a slightly lower temperature, $T \approx 1300$ K. Film thickness varies between ~3 µm and ~5 µm. The most relevant data collected from these samples are reported in Table 5.5.1.

ID	Gas	t_f [µm]	S_q [nm]	Ti conc. [at. %]	Fluorescence/t_f [µm^{-1}]
AS18	O_2	4	~23.8	0.03	0.0064
AS20	N_2	4.5	~6.4	0.02	0.0504
AS19	Ar	3.0	~15.3	0.02	0.0773
AS23	Ar	3.0	~10.4	0.02	0.0773
AS24	Ar	3.0	~11.0	0.01	0.0464

Table 5.5.1. Background gas, film thickness (t_f), RMS surface roughness (S_q), Ti concentration and intensity of fluorescence normalised to film thickness **(t_f)** of samples AS18-AS20 and AS23-AS24.

Figure 5.5.1 shows fluorescence spectra from sample AS18-20: they are normalized to the highest value of fluorescence due to Ti^{3+}, found in AS19. The high and sharp peak centred at 694.37 nm, due to Cr^{3+} impurities [17], was ignored for normalisation.

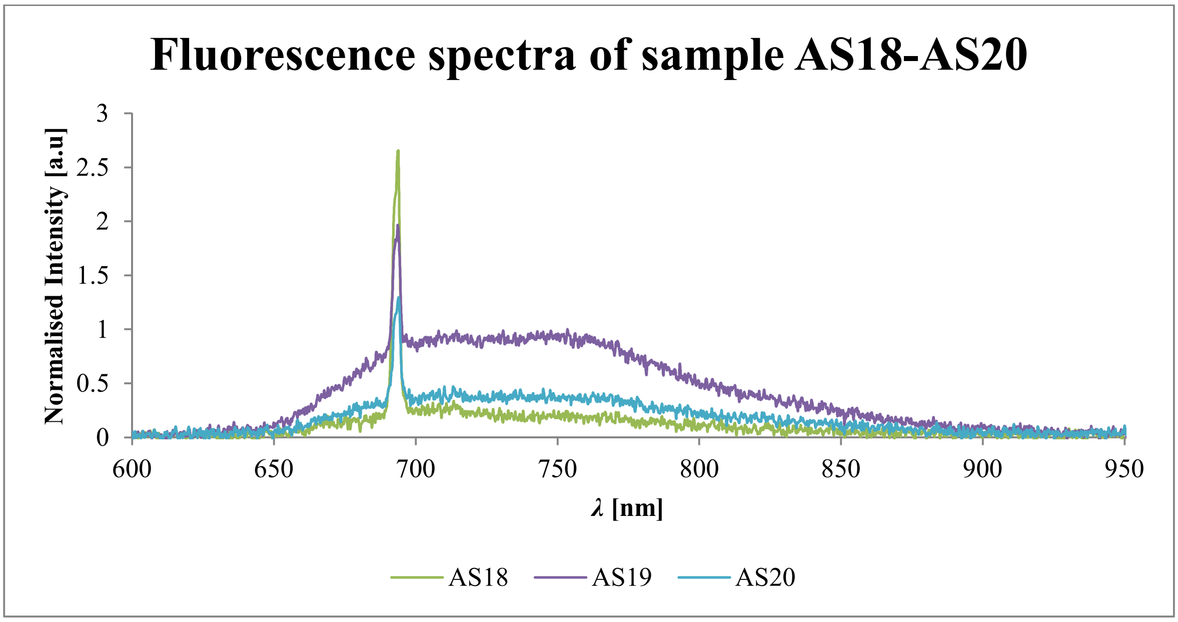

Figure 5.5.1. Fluorescence spectra of samples AS18-AS20: λ = (600 - 950) nm. The peaks at ~694 nm are due to Cr^{3+} impurities [17].

Considering the AS18-AS20 set, the different thickness (highest in AS20 and lowest in AS19) and surface roughness (lowest in AS20 and highest in AS18) suggest a difference in the plume dynamics and nucleation. Ballistics of the material ejected from the target depends on size and mass of the atomic species of the background gas: the interaction of ablated material with heavier and bigger atoms produces increased scatter (and therefore a lower mean free path) and reduces the deposition rate and the kinetic energy of the ablated material arriving on the substrate, which affects the film growth dynamics and thus the final film quality. In fact, the film deposited in N_2 (lightest atomic species) is the thickest (AS20: 4.5 μm), whereas the one deposited in Ar (heaviest atomic species) is the thinnest (AS19: 3 μm).

Also, in spite of the lower surface roughness, samples AS19 and AS20 are not uniform and clear. Moreover sample AS20 features a blue tint, except for a colourless and translucent corner; the blue tint could be due to colour centres caused by oxygen vacancies [21]. Probably the reaction of the plume with N_2, used as background gas, altered the composition of the plume itself and of the film deposited on the substrate. However, a thick film (AS30) deposited under the same conditions as AS20 does not feature the same blue tint as AS20.

In terms of composition, the highest Ti concentration is found in AS18. However, it features the lowest fluorescence, whereas the highest value is reported from samples AS19 and AS23, both deposited in Ar at $T \approx 1350$ K. Also, lowering the substrate temperature to $T \approx 1300$ K (AS24) causes a decrease in both Ti concentration and fluorescence, as expected from literature [20]. These findings suggest that background gas plays an important role not only in the plume dynamics, but also on the composition of plume and film: oxygen, being reactive, probably oxidises the Ti in the plume, thus causing formation of Ti^{4+} ions in the films, which re-absorb emitted radiation [17, 20]; on the contrary, inert Ar preserves the correct valence state of Ti ions in the plume, which are then oxidised in the film as Ti^{3+}, which allows fluorescence and lasing. In summary, although films deposited in Ar are more fluorescent than those deposited in O_2, EDX analysis showed higher Ti concentration in the latter.

5.6. DEPOSITION OF WAVEGUIDING FILMS

Three thick films (AS25, AS27 and AS28) were deposited under similar conditions to those summarised in Table 5.2.1: O_2 pressure was set to ~0.2 Pa, considered the optimum value in terms of film quality and Ti concentration, although delivering less fluoresence (see Section 5.3); substrate temperature was set to $T \approx 1350$ K for AS25 and $T \approx 1300$ K for AS27-AS28. Deposition time was changed too and is reported in Table 5.6.1 for all samples.

Two more thick films were deposited under the conditions reported in Table 5.2.1 at $T \approx 1350$ K in Ar (AS29) and N_2 (AS30), at the same gas pressure as stated above (~0.2 Pa).

XRD analysis showed that all samples are crystalline with the same orientation as the substrate. The most relevant data collected from these samples are reported in Table 5.6.1.

ID	Gas	T [K]	Deposition time [min.]	t_f [µm]	S_q [nm]	Ti conc. [at. %]	Fluorescence/t_f [μm^{-1}]
AS25	O_2	1350	180	10.0	15.2	0.02	0.0232
AS27	O_2	1300	300	18.5	119.1	0.02	0.0098
AS28	O_2	1300	240	13.0	77.3	0.01	0.0102
AS29	Ar	1350	240	14.0	23.8	0.03	0.0144
AS30	N_2	1350	240	14.0	19.6	0.02	0.0109

Table 5.6.1. Background gas, substrate temperature (T), deposition time, film thickness (t_f), RMS surface roughness (S_q), Ti concentration and intensity of fluorescence normalised to film thickness (t_f) of samples AS25-AS30.

All films appear non-uniform and rough (compared to thinner films and blank sapphire substrates), even those with RMS roughness $S_q < 20$ nm.

From data collected in Table 5.6.1 and plotted in the chart in Figure 5.6.1 it is clear that surface roughness increases with increasing thickness for samples deposited in O_2 (AS25, AS27 and AS28). A similar trend can be expected for films with different thickness in Ar or N_2. From a comparison between Table 5.5.1 and Table 5.6.1 it can be noticed that the thick film deposited in Ar (AS29) features roughly the same fluorescence as that coming from films deposited in O_2 and ~5.4 times lower than that reported for AS19, thin Ti:sapphire film deposited in Ar under the same conditions as AS29. However, Ti concentration in AS29 is even higher than that in AS19. For this reason, the lower fluorescence level could be explained by assuming that the light is waveguided away from the sensor (see the schematic of the set-up for measurement of fluorescence described in Section 4.11.1).

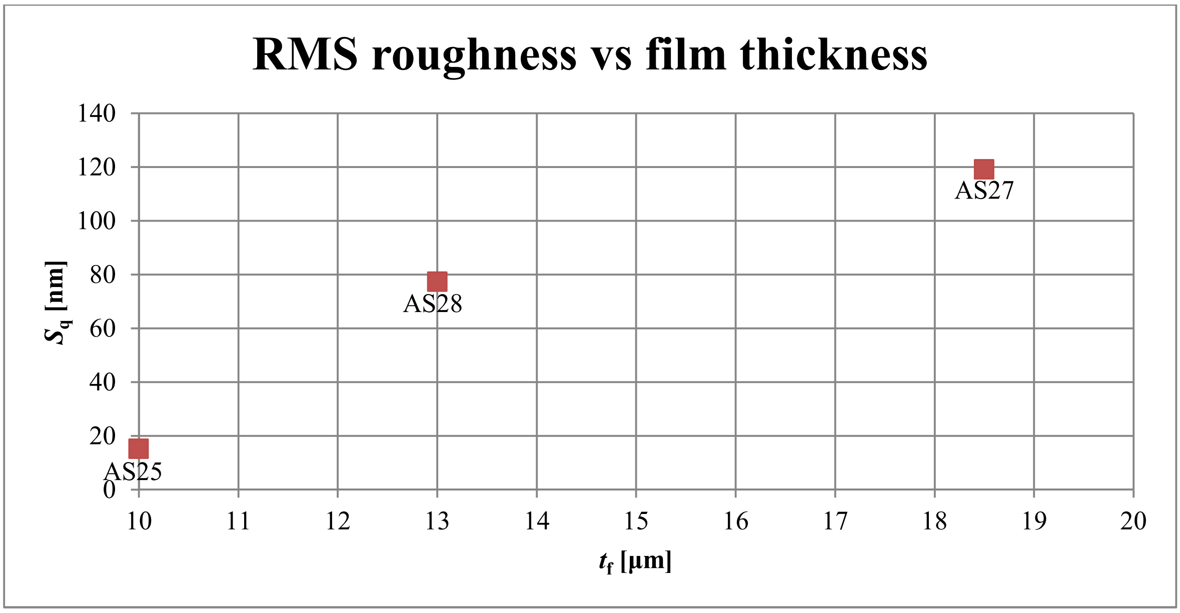

Figure 5.6.1. Variation of RMS roughness with film thickness (samples AS25 and AS27-AS28).

Further depositions of thick films were performed from a single-crystal Ti:sapphire target with a nominally higher Ti concentration than the one used for the depositions described so far, i.e. (0.17 – 0.34) at. % instead of (0.08 – 0.17) at. %. The following films were all deposited at $T \approx 1350$ K and $P_{GAS} \approx 0.2$ Pa:

ID	Gas	Deposition time [min.]	t_f [µm]	S_q [nm]
AS37	O_2	240	17.5	271.3
AS38	N_2	240	18.0	32.3
AS39	Ar	240	14.0	146.0
AS40	Ar	180	8.0	42.5
AS42	N_2	180	15	291.3
AS43	O_2	180	14	58.0

Table 5.6.2. Background gas, deposition time, film thickness (t_f) and RMS surface roughness (S_q) of samples AS37-AS43.

No EDX and fluorescence measurements were performed on these samples. Waveguide characterisation and lasing experiments are described in the next section.

5.7. WAVEGUIDE CHARACTERISATION AND LASING EXPERIMENTS

In order to characterise thick waveguiding Ti:sapphire films, the samples must be lapped and polished, as described in Section 4.7. The methods used for waveguide characterisation and lasing experiments are listed and described in Section 4.8. In this section the results of characterisation and lasing experiments with the waveguiding Ti:sapphire films, described in the previous section, are reported.

Samples AS25-AS30 were lapped and polished together; sample length was reduced to ~4.64 mm. Sample AS30 cracked at the end of the lapping/polishing process and was therefore discarded for subsequent characterisation.

The first step of waveguide characterisation was the measurement of waveguide losses or transmission coefficient. This was done by using a Ti:sapphire laser, tuned at $\lambda \approx 908$ nm and polarised perpendicular to the *c*-axis of the sample, and 10× objectives (focal length: 16.9 mm) to couple the laser beam into the waveguide and collect the output. Observation of a single back-reflection from all the waveguides suggested that the end-facets are parallel to each other. Table 5.7.1 shows the average values of Fresnel losses (F), launch efficiency (L), waveguide transmission coefficient (T^*), estimated as explained in Section 4.11:

ID	t_f [µm]	F	L	T^* [dB/cm]
AS25	10	0.909	0.697	-1.12
AS27	18.5	0.879	0.712	-0.74
AS28	13	0.933	0.561	-0.84
AS29	14	0.927	0.558	-0.88

Table 5.7.1. Results of waveguide characterisation of samples AS25 and AS27-AS29.

These results compare quite well with the waveguide losses reported by Anderson in [18]: ~1.6 dB/cm at $\lambda = 720$ nm. Estimated Fresnel losses agree with the theoretical value ($F \approx 0.93$) expected for sapphire ($n \approx 1.75$): $F = (1 - R^2)$, with: $R = |r|^2$ and $r = (1 - n)/(1 + n)$, for the air/sapphire interface.

Lasing experiments were attempted on all these waveguides with different configurations, but lasing was observed only once on sample AS27 at $\lambda = 750$ nm with the configuration reported in Table 5.7.2.

Input lens (focal length [mm]):	6.3× (22.5)
Input mirror:	HR @ $\lambda = 750$ nm, HT @ $\lambda = 532$ nm
Output coupler, R:	97% @ $\lambda = 750$ nm
Output lens (focal length [mm]):	10× (16.9)

Table 5.7.2. Set-up used for lasing experiments on AS27.

The lasing threshold (average absorbed power) was estimated to be $P_{abs} \approx P_{th} \approx 364$ mW (corresponding to an input power of ~2 W, incident on the input mirror), half the value reported by Anderson ($P_{th} \approx 720$ mW @ $\lambda = 800$-820 nm) with a similar configuration (output coupler with $R = 95\%$ @ $\lambda = 800$ nm) [20]. The maximum output power was $P_{out} \approx 7.5$ mW at $P_{abs} \approx 770$ mW, and slope efficiency was estimated to be ~4% (see Figure 5.7.1), the same value as reported by Anderson in [20]. The results obtained from AS27 were promising, but unfortunately we were not able to replicate them.

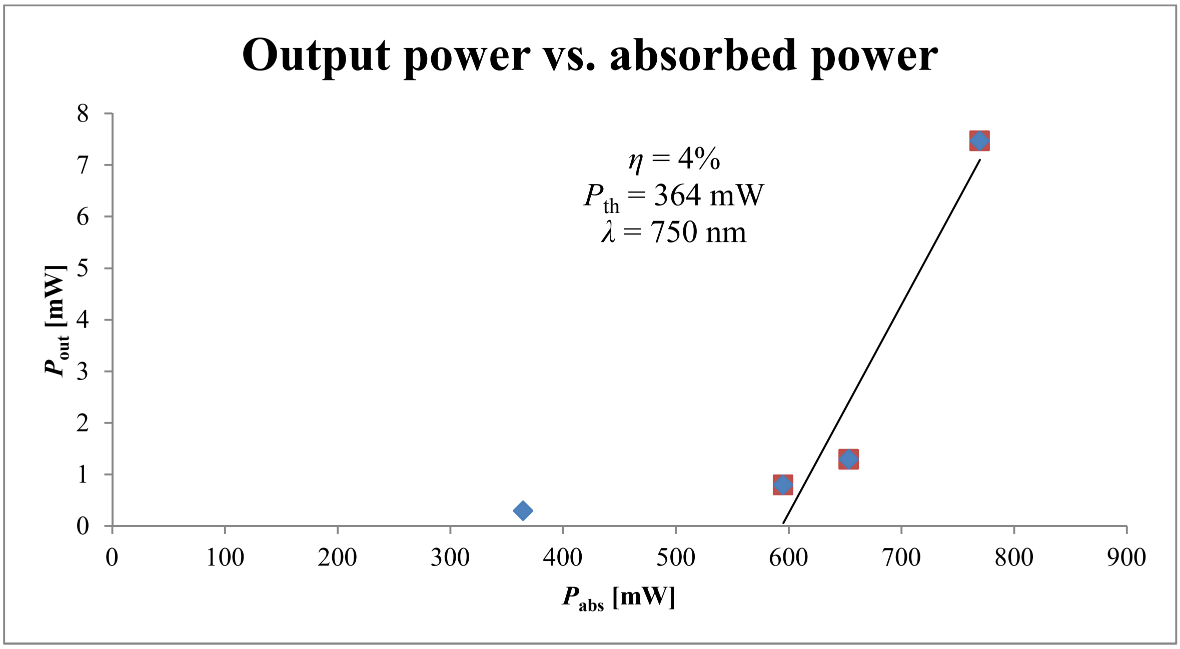

Figure 5.7.1. Slope efficiency with respect to absorbed power (P_{abs}) for sample AS27 with HR input mirror and 3% output coupler.

Further experiments were performed on the other waveguiding films, AS37-43, which were reduced to a length of ~4.64 mm after lapping and polishing, during which sample AS37 cracked. Unfortunately the end-facets were not parallel to each other, as inferred from double back-reflections; lasing experiments were attempted anyway, but with no success, probably due to the misaligned end-facets, which can be very critical in waveguide lasers with low dopant concentration. The samples were then re-lapped and re-polished, reducing their length to $l \approx 3.98$ mm. Again lasing experiments gave no good results, however transmission losses were estimated for these samples from waveguide characterisation using a Ti:sapphire laser beam. Waveguide transmission losses at $\lambda \approx 725$ nm were in the range (0.7 – 1.3) dB/cm for polarization perpendicular to the *c* axis and (0.8 – 1.0) dB/cm for polarization parallel to the *c* axis; these values are low enough to ensure lasing, which is probably hindered by low Ti^{3+} concentration, as suggested also by the lasing experiments on the other set of samples.

Another recurring issue, which made lasing experiment even more difficult, was the damaging of the input mirror, due to the high power density required to pump Ti:sapphire lasers, due to low peak emission cross-section (41×10^{-20} cm^2 at $\lambda = 720$ nm) and short fluorescence lifetime (3.2 μs).

5.8. CONCLUSIONS

In this chapter PLD of Ti:sapphire has been discussed. The process of optimisation of deposition conditions has been described throughout the chapter: it was not easy to interpret the data collected from the characterisation of the films, due to uncertainty in the measurements of Ti concentration (see Section 4.5) and lack of correlation between these and fluorescence measurements. The latter are more reliable than the former, considering also that re-absorption from Ti^{4+} ions in the lattice can be taken into account in fluorescence measurements; however, EDX measurements of Ti concentration were used as a guide too in the optimisation process.

In any case, lasing was observed just once from one of the waveguiding films and the results obtained from it were comparable (slope efficiency), if not better (lower lasing threshold) than those reported by Anderson in [1, 20], suggesting that the actual deposition conditions may not be far from optimum. The problem in making all the Ti:sapphire waveguides lase may lie in the low gain of the lasing medium, i.e. to in the low concentration of Ti^{3+} in the film, due to non-stoichiometric transfer from the target, and in the difficulty in producing perfectly parallel end-facets during polishing, which is a critical factor in waveguide lasers with such a low doping concentration. In fact, waveguide transmission losses in the NIR are actually lower than previously reported, suggesting that the problem lies in the triggering of lasing action, either due to low concentration of Ti^{3+}, misaligned end-facets or a combination of both.

5.9. REFERENCES

1. A. A. Anderson, R. W. Eason, L. M. B. Hickey, M. Jelinek, C. Grivas, D. S. Gill, and N. A. Vainos, "Ti:sapphire planar waveguide laser grown by pulsed laser deposition," Opt. Lett. **22**, 1556-1558 (1997).

2. M. Jelinek, R. W. Eason, A. A. Anderson, C. Grivas, D. S. Gill, J. Sonsky, J. Lancok, L. M. B. Hickey, N. A. Vainos, and P. Hribek, "Planar waveguide lasers of Ti:Sapphire and Nd:YAG (YAP) grown by PLD," NATO ASI 3 HIGH TECH **45**, 419-425 (1998).

3. M. Jelinek, J. Lancok, J. Sonsky, L. Jastrabik, C. Grivas, C. Fotakis, A. A. Anderson, R. W. Eason, and F. Flory, "Planar waveguide structures created by PLD," in *Alt '97 International Conference on Laser Surface Processing*, V. I. Pustovoy, ed. (Spie-Int Soc Optical Engineering, Bellingham, 1998), pp. 22-26.

4. N. A. Vainos, C. Grivas, C. Fotakis, R. W. Eason, A. A. Anderson, D. S. Gill, D. P. Shepherd, M. Jelinek, J. Lancok, and J. Sonsky, "Planar laser waveguides of Ti:sapphire, Nd:GGG and Nd:YAG grown by pulsed laser deposition," Appl. Surf. Sci. **127**, 514-519 (1998).

5. C. Grivas, T. C. May-Smith, D. P. Shepherd, R. W. Eason, M. Pollnau, and M. Jelinek, "Broadband single-transverse-mode fluorescence sources based on ribs fabricated in pulsed laser deposited Ti : sapphire waveguides," Appl. Phys. A-Mater. Sci. Process. **79**, 1195-1198 (2004).

6. C. Grivas, D. P. Shepherd, T. C. May-Smith, R. W. Eason, and M. Pollnau, "Single-transverse-mode Ti:sapphire rib waveguide laser," Opt. Express **13**, 210-215 (2005).

7. J. Lancok, M. Jelinek, and J. Oswald, "Deposition of Ti:sapphire film on quartz and sapphire substrates by laser," in *Technical Digest. CLEO/Pacific Rim '99*(IEEE, Seoul, South Korea, 1999), pp. 961-962 vol.963.

8. H. Uetsuhara, S. Goto, Y. Nakata, N. Vasa, T. Okada, and M. Maeda, "Fabrication of a Ti:sapphire planar waveguide by pulsed laser deposition," Appl. Phys. A-Mater. Sci. Process. **69**, S719-S722 (1999).

9. M. Jelinek, R. W. Eason, J. Lancok, A. A. Anderson, C. Grivas, C. Fotakis, L. Jastrabik, and F. Flory, "Study of Ti:sapphire layers created by PLD," P. Soc. Photo-opt. Ins. **2888**, 51-59 (1996).

10. P. E. Dyer, J. Gonzalo, P. H. Key, D. Sands, and M. J. J. Schmidt, "Studies of target materials and wavelength for laser ablation-deposition of Ti:sapphire," Appl. Surf. Sci. **109-110**, 345-349 (1997).

11. A. A. Anderson, R. W. Eason, M. Jelinek, C. Grivas, D. Lane, K. Rogers, L. M. B. Hickey, and C. Fotakis, "Growth of Ti:sapphire single crystal thin films by pulsed laser deposition," Thin Solid Films **300**, 68-71 (1997).

12. M. Jelinek, R. W. Eason, J. Lancok, A. A. Anderson, C. Grivas, C. Fotakis, L. Jastrabik, and F. Flory, "Planar waveguide lasers created by pulsed laser deposition," in *Ninth International School on Quantum Electronics: Lasers-Physics and Applications*, P. A. Atanasov, ed. (SPIE - Int. Soc. Optical Engineering, Bellingham, 1996), pp. 85-97.

13. P. E. Dyer, S. R. Jackson, P. H. Key, W. J. Metheringham, and M. J. J. Schmidt, "Excimer laser ablation and film deposition of Ti:Sapphire," Appl. Surf. Sci. **96-8**, 849-854 (1996).

14. J. Gonzalo, P. H. Key, and M. J. J. Schmidt, "Growth of Ti : sapphire thin films by pulsed laser deposition," Laser Phys. **8**, 265-269 (1998).

15. P. H. Key, J. Kral, and M. J. J. Schmidt, "Ion beam analysis of pulsed laser deposited Ti : sapphire," Appl. Surf. Sci. **138**, 503-506 (1999).

16. M. Pollnau, R. Salathé, T. Bhutta, D.P. Shepherd, and R. W. Eason, "Continuous-wave broadband emitter based on a transition-metal-ion-doped waveguide,"Opt. Lett. **26**, 283-285 (2001).

17. H. Calvo del Castillo, J. L. Ruvalcaba, and T. Calderón, "Some new trends in the ionoluminescence of minerals," Anal. Bioanal. Chem. **387**, 869-878 (2007).

18. R. L. Aggarwal, A. Sanchez, M. M. Stuppi, R. E. Fahey, A. J. Strauss, W. R. Rapoport, and C. P. Khattak, "Residual infrared-absorption in as-grown and annealed crystals of Ti-Al_2O_3," IEEE J. Quantum Electron. **24**, 1003-1008 (1988).

19. R. W. Eason, ed.: *Pulsed Laser Deposition of Thin Films – Applications-led Growth of Functional Materials* (Wiley Interscience, 2007).

20. A. A. Anderson, "Crystalline planar waveguide lasers fabricated by pulsed laser deposition," PhD thesis at *Optoelectronics Research Centre* (University of Southampton, Southampton, 1998).

21. C. J. McHargue, E. Alves, C. Marques, and L. C. Ononye, "Comparison of the damage in sapphire due to implantation of boron, nitrogen, and iron," J. Nucl. Mater. **389**, 311-316 (2009).

22. K. Oura, V. G. Lifshits, A. A. Saranin, A. V. Zotov, and M. Katayama, *Surface Science: An Introduction* (Springer, 2010).

6. CHAPTER 6
SINGLE-PLD OF YIG:
OPTIMISATION OF GROWTH CONDITIONS

6.1. INTRODUCTION

The theory of magneto-optic garnets has been covered in Chapter 3. In this chapter the results of the growth of YIG by single-PLD are presented.

Several attempts to deposit YIG by PLD have been reported so far [1-28], mostly on GGG substrates, with only one report of PLD of thin ($t_f < 1$ μm) YIG films on YAG [20]. To the best of our knowledge, we are the first to grow crack-free μm-thick YIG films on YAG substrates by PLD.

The optimisation of the deposition conditions of YIG by PLD was performed, in order to grow YIG films with the best magnetic properties, using the FMR linewidth as the quality factor to be optimised; more details on the experiments and the results obtained are given in the next paragraphs. Table 6.1.1 summarises the typical deposition conditions of YIG reported in the literature [1-17]:

Substrate	GGG (111)
Laser (λ [nm])	KrF ($\lambda = 248$) or ArF ($\lambda = 193$)
Repetition frequency [Hz]	≥(20 – 30)
Fluence [J/cm^2]	~(2 – 3)
Target – substrate distance [cm]	~4
O_2 pressure [Pa]	~(0.665 – 13.3)
Substrate temperature [K]	~(850 – 1150)

Table 6.1.1. Optimum deposition conditions for PLD of YIG films.

Manuilov et al. [17] reported the narrowest FMR linewidth obtained so far in YIG films deposited by PLD: $\Delta H = 0.09$ mT at 9 GHz, comparable to the FMR linewidth of YIG films grown by LPE [29]. They attribute such a small value to the compressive strain accumulated in Fe-deficient YIG/GGG (111) films.

6.2. SINGLE-PLD OF YIG IN THE SINGLE-PLD CHAMBER

6.2.1. PRELIMINARY EXPERIMENTS

The first experiment (sample Y1) was an attempt to replicate Manuilov's optimum deposition conditions [17], reported in Table 6.2.1 for convenience:

Target	Single-crystal YIG
Substrate	GGG (111)
Laser (λ [nm])	KrF ($\lambda = 248$)
Repetition frequency [Hz]	20
Fluence [J/cm^2]	~3.0
Target – substrate distance [cm]	6.0
O_2 pressure [Pa]	3.3
Substrate temperature [K]	~1050

Table 6.2.1. Deposition conditions of sample Y1.

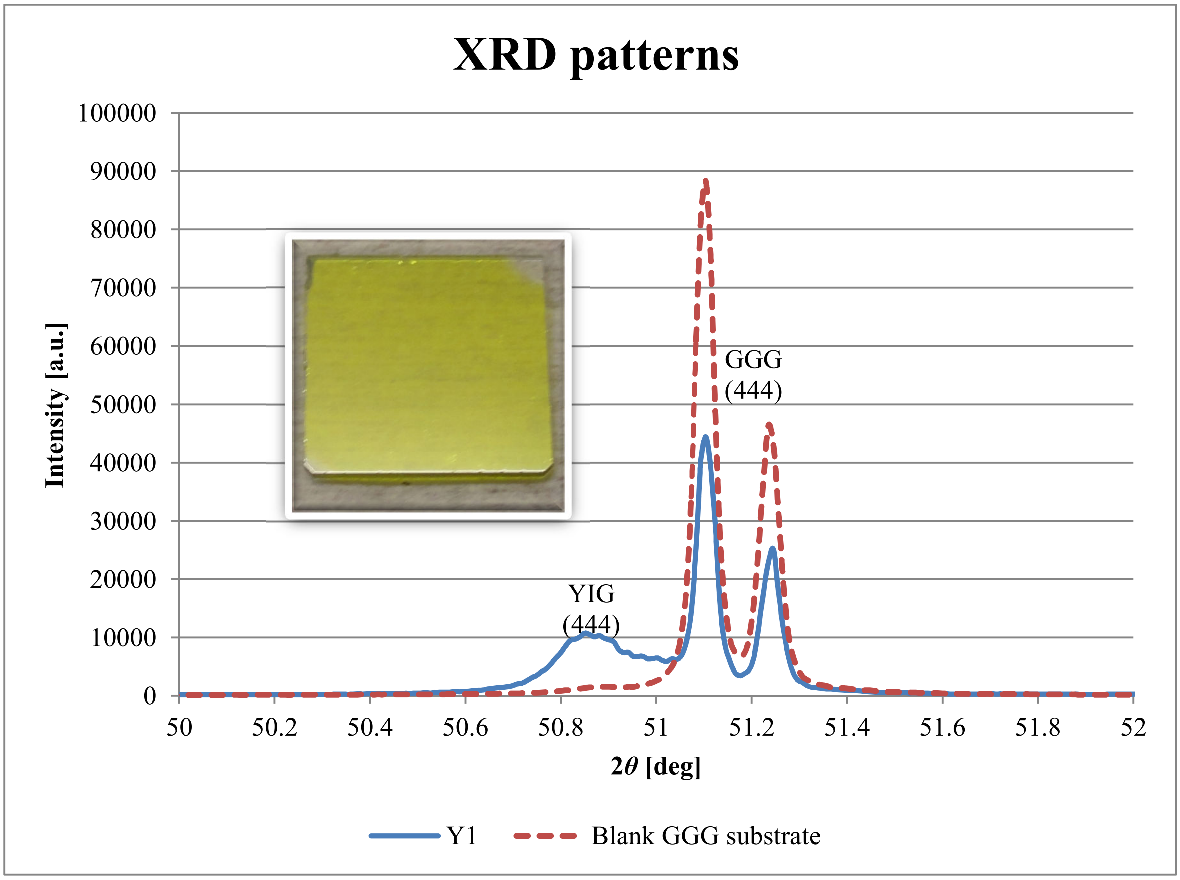

Figure 6.2.1. XRD patterns of sample Y1 and of a blank GGG (111) substrate, used as a reference. Peak doublets are due to Cu-K$_{\alpha2}$ radiation present in the diffractometer. The inset shows a photo of sample Y1.

XRD peak	**Database position $2\theta_d$ [deg]**	**Measured position $2\theta_m$ [deg]**	**Corrected position $2\theta_c$ [deg]**
GGG (444)	51.10 [30]	50.70	51.10
YIG (444)	51.22 [31]	50.45	50.85

Table 6.2.2. Measured and corrected XRD peak positions of sample Y1, compared to database values.

The as-deposited film is ~3 μm thick and features a yellow colour and a clear surface with low roughness (RMS roughness: $S_q \approx 6.2$ nm). XRD analysis confirmed the crystallinity of the YIG film, which has the same orientation as the GGG (111) substrate (see Figure 6.2.1); the measured peak positions were corrected by shifting the XRD pattern so that the first GGG (444) peak, due to the Cu-$K_{\alpha 1}$ wavelength from the x-ray source, is matched to the database value (see Table 6.2.2); the YIG (444) peak at the left of the GGG (444) peak means that the film is under compressive stress and has a larger lattice constant than bulk YIG and even GGG (see Section 4.6). According to EDX analysis, the film composition is $Y_{3.37}Fe_{4.63}O_{12}$, i.e. Y-rich and Fe-deficient, which agrees with the results reported in [17] and explains what was observed in the XRD analysis: the large ionic radius and the high concentration of Y cause lattice distortion and a larger lattice constant than stoichiometric bulk YIG. The FMR resonance linewidth measured at $v = 6$ GHz is $\Delta H \approx 3.81$ mT, which is more than one order of magnitude broader than the linewidth reported by Manuilov et al. ($\Delta H = 0.09$ mT at $v = 9$ GHz) [17]. As discussed in Section 4.10, the broader FMR linewidth, compared to literature values, may be due to instrumental issues (Manuilov et al. measure FMR linewidth with a microwave cavity apparatus [17, 32] instead of a coplanar waveguide) and the intrinsic FMR linewidth may be lower than actually measured.

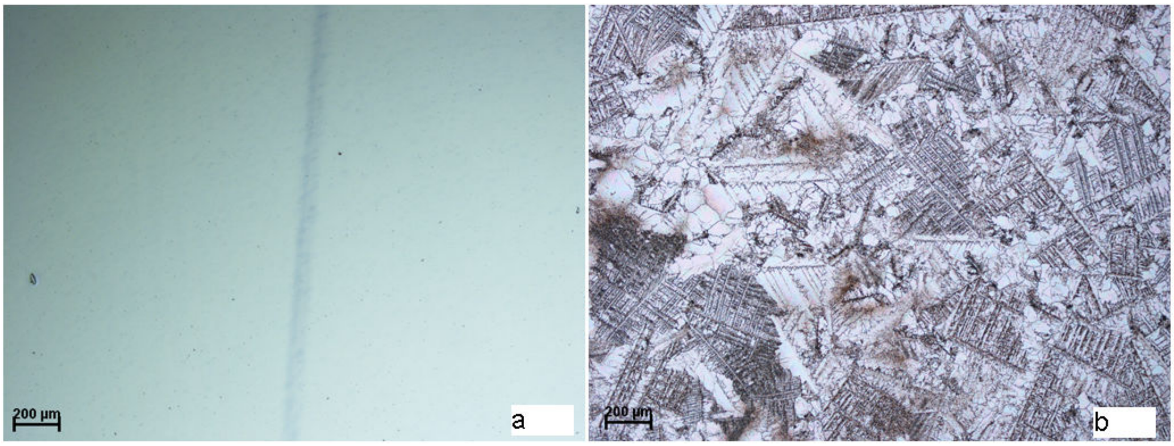

Figure 6.2.2. Optical microscope images (magnification factor: 5×) of the centre of the films in samples Y1 **(a)** and Y2 **(b)** after thermal annealing.
The line in the middle of Y1 is part of the sample label scratched on the back side of Y1 with a diamond scribe.

According to [15], thermal annealing improves magnetic properties of YIG films and Manuilov's samples were indeed post-annealed [17]. For this reason another YIG film (sample Y2) was deposited under the same conditions as those of Y1 and then annealed *in situ* for 7 hours with the CO_2 laser at full power (~25 W in chamber) and oxygen pressure $P_{O_2} \approx 50$ Pa. At the end of the thermal annealing, the sample was analysed: both surfaces appeared rough with odd morphology, as the analysis with microscope and ZeScope confirmed (see Figure 6.2.2). The annealing temperature was probably too high, causing partial fusion and/or transformation of both GGG substrate and YIG film, although XRD confirmed the crystallinity of both. Therefore no magnetic analysis was performed on sample Y2 and *in-situ* post-annealing abandoned.

6.2.2. DEPOSITIONS ON DIFFERENT SUBSTRATES

YIG films were deposited under the same conditions as specified in Table 6.2.1 on different substrates, to see how they affect the film quality and magnetic properties. Table 6.2.3 shows the results of the characterization of samples Y1, Y6, Y9 and Y10: it can be seen that the highlighted sample Y6, deposited on YAG (100), has a lower FMR linewidth (ΔH) than any of the three films deposited on lattice-matched GGG substrates, which agrees with the previous findings reported in literature [11, 17, 19, 21]. In fact, lattice mismatch between YIG and YAG is: $\Delta a/a_{\mathrm{SUB}} \approx 3.1\%$, whereas $\Delta a/a_{\mathrm{SUB}} \approx -0.056\%$ for YIG on GGG, where: $\Delta a = (a_{\mathrm{FILM}} - a_{\mathrm{SUB}})$, a_{FILM} = lattice constant of the film, a_{SUB} = lattice constant of the substrate. Film orientation plays a role too in the magnetic properties, as shown already in [11, 16, 17].

ID	**Substrate**	**ΔH [mT]**	**t_f [µm]**	**S_q [nm]**	**Y [formula number]**	**Fe [formula number]**	**Y/Fe**
Y1	GGG (111)	3.81	3	6.2	3.37	4.63	0.73
Y6	YAG (100)	3.37	1.2	0.4	3.56	4.44	0.80
Y9	GGG (111)	4.42	2.75	8.6	3.56	4.44	0.80
Y10	GGG (100)	9.27	2.75	3.4	3.47	4.53	0.75

Table 6.2.3. Substrates, FMR linewidth (ΔH), thickness (t_f), RMS surface roughness (S_q) and composition of samples Y1, Y6 and Y8-Y10. The best sample in terms of FMR is highlighted in grey.

Crystallinity and epitaxial growth of all samples was confirmed by XRD. EDX analysis showed that all films are yttrium (Y) rich and iron (Fe) deficient, as reported in [17] for films grown on GGG under similar deposition conditions.

The better magnetic properties of our lattice-mismatched YIG/YAG samples, compared to our lattice matched YIG/GGG samples, can be explained with the same theory proposed in [19] for BIG films grown on GSGG and Nd:GSGG, that has also been confirmed in [17] for lattice-matched Fe-deficient and lattice-mismatched stoichiometric YIG films grown on GGG.

According to [19], a large lattice mismatch induces a strain that can be more easily relieved through misfit dislocations than the strain induced by a smaller lattice mismatch; consequently the films having a small lattice mismatch, such as BIG/Nd:GSGG(111) ($\Delta a/a_{\mathrm{SUB}} \approx 0.13\%$), have larger strain and worse magnetic properties (e.g. higher FMR linewidth ΔH, higher coercivity H_{C}, lower saturation magnetisation $4\pi M_{\mathrm{S}}$ and lower Faraday rotation θ_{F}) than films with higher lattice mismatch, such as BIG/GSGG(001) ($\Delta a/a_{\mathrm{SUB}} \approx 0.45\%$), as shown in Table 6.2.4, where data from [19] are compared.

SAMPLES	$\mathbf{\Delta a/a_{SUB}}$	ΔH **[mT]**	H_{C} **[kA/m]**	$4\pi M_{\mathrm{S}}$ **[kA/m]**	θ_{F} **[deg/µm] @ λ = 633 nm**
BIG/Nd:GSGG(111)	0.13%	35	27.85	95.5	-6.7
BIG/GSGG(001)	0.45%	2.5	3.18	111.4	-7.8

Table 6.2.4. Comparison of data from [19].

From this same reasoning it can be inferred that our off-stoichiometric YIG/YAG samples accommodate the strain induced by the large lattice-mismatch ($\Delta a/a_{\mathrm{SUB}} \approx 3.1\%$ for stoichiometric YIG/YAG) better than our YIG/GGG samples ($\Delta a/a_{\mathrm{SUB}} \approx -0.056\%$ for stoichiometric YIG/GGG), thus inducing better magnetic properties.

Also, the better relief of the strain induced in YIG/YAG than in YIG/GGG can be explained by taking into account the thermal expansion coefficients (TEC, ρ) of the materials: $\rho_{\mathrm{YIG}} = 10\times10^{-6}$ K^{-1} [33, 34], $\rho_{\mathrm{YAG}} = 7.5\times10^{-6}$ K^{-1} [35], $\rho_{\mathrm{GGG}} = 9.3\times10^{-6}$ K^{-1} [33, 34]. The lattice mismatch in YIG/YAG ($\Delta a/a_{\mathrm{SUB}} \approx 3.1\%$) causes a compressive strain; however, the TEC mismatch in YIG/YAG ($\Delta\rho/\rho_{\mathrm{SUB}} \approx 33.3\%$) causes a tensile stress that may compensate the lattice-mismatch-induced compressive strain during the cooling-down of the sample at the end of the deposition. As for YIG/GGG, the lattice-mismatch ($\Delta a/a_{\mathrm{SUB}} \approx -0.056\%$ for stoichiometric YIG) induces a tensile strain that is increased even more by the TEC-mismatch ($\Delta\rho/\rho_{\mathrm{SUB}} \approx 7.5\%$) during the cooling-down of the sample after the film growth; however, as observed and explained in 6.2.1, our YIG/GGG films are off-stoichiometric and under compressive stress, which apparently may not be fully relieved or may be over-compensated by the tensile stress induced by the TEC-mismatch during the cooling-down.

Having obtained the best results on YAG (100) substrates, subsequent experiments were focussed on optimisation of deposition conditions of YIG on these substrates.

6.2.3. OPTIMISATION OF SUBSTRATE TEMPERATURE

Subsequent samples Y11-Y18 were deposited on YAG (100) substrates at the same oxygen pressure ($P_{O2} \approx 3.3$ Pa) and different substrate temperatures, as shown in Table 6.2.5 (best sample in grey). It can be seen that all samples are Fe-deficient, with an average Y/Fe ratio of ~0.8. The substrate temperatures reported in Table 6.2.5 and shown in the chart in Figure 6.2.3 are estimated as described in Section 4.2.4.3 and should not be taken as definitive: there is likely an error of ±25 K. Thickness was not measured in order to save time in the optimisation process, however, from growth time (1 hour), it is expected to be ~2.5 μm.

ID	*T* [K]	Δ*H* [mT]	Y [formula number]	Fe [formula number]	Y/Fe	YIG peaks in XRD pattern	Sample colour
Y18	300	-	3.60	4.40	0.82	NO	Black
Y17	700	-	3.54	4.46	0.79	NO	Black
Y16	900	-	3.46	4.54	0.76	NO	Dark red
Y15	1000	13.02	3.60	4.40	0.82	YES	Dark yellow
Y14	1050	9.05	3.56	4.44	0.81	YES	Yellow
Y8	1100	4.21	3.53	4.47	0.79	YES	Yellow
Y11	1200	2.91	3.55	4.45	0.80	YES	Yellow
Y12	1250	2.55	3.63	4.37	0.83	YES	Yellow
Y13	1300	3.43	3.59	4.41	0.81	YES	Yellow

Table 6.2.5. Deposition conditions, FMR linewidth (Δ*H*), composition, XRD and colour of samples Y11-Y18 and Y8. The best sample in terms of FMR is highlighted in grey.

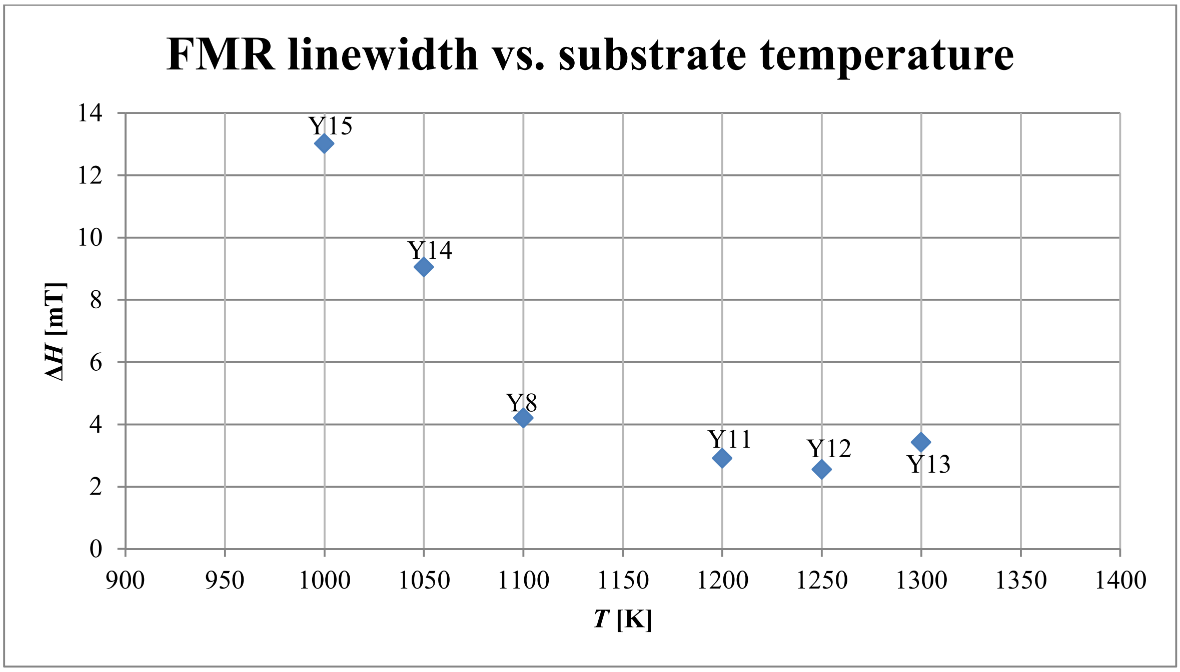

Figure 6.2.3. Variation of FMR linewidth (Δ*H*) with substrate temperature.

Table 6.2.5 and Figure 6.2.3 show a clear correlation between FMR linewidth and substrate temperature. Figure 6.2.3 shows the trend of the FMR linewidth with substrate temperature: once the substrate temperature is high enough to ensure crystallization ($T \approx 1000$ K), FMR is observed and the linewidth decreases with increasing temperature until the minimum value (2.55 mT – sample Y12) is reached at $T \approx 1250$ K.

XRD analysis showed the presence of diffraction peaks due to the YIG (100) phase only in the samples deposited at a substrate temperature $T \geq 1000$ K, meaning that samples Y16-18, deposited at $T \leq 900$ K, are amorphous, as expected from literature [6, 10], and thus do not feature any FMR. Indicators of crystal and magnetic quality of µm-thick YIG films are also their colour, as shown in Table 6.2.5, and their optical transmission: YIG films deposited at $T \geq 1050$ K have a light yellow tint and high optical transmission in the visible and near infra-red (NIR), with an absorption edge typically between 450 nm and 550 nm (see Figure 6.2.4); samples deposited at $T \leq 1000$ K have a darker colour, going from dark yellow through red to black as substrate temperature drops, and lower optical transmission with red-shifted absorption edge (see Y16-18 in Figure 6.2.4). The ripples in the transmission spectra are etalon fringes [36] due to Fabry-Pérot modes resonating in the cavity between the air/film ($|\Delta n| \approx 1.23$) and film/substrate ($|\Delta n| \approx 0.39$) interfaces.

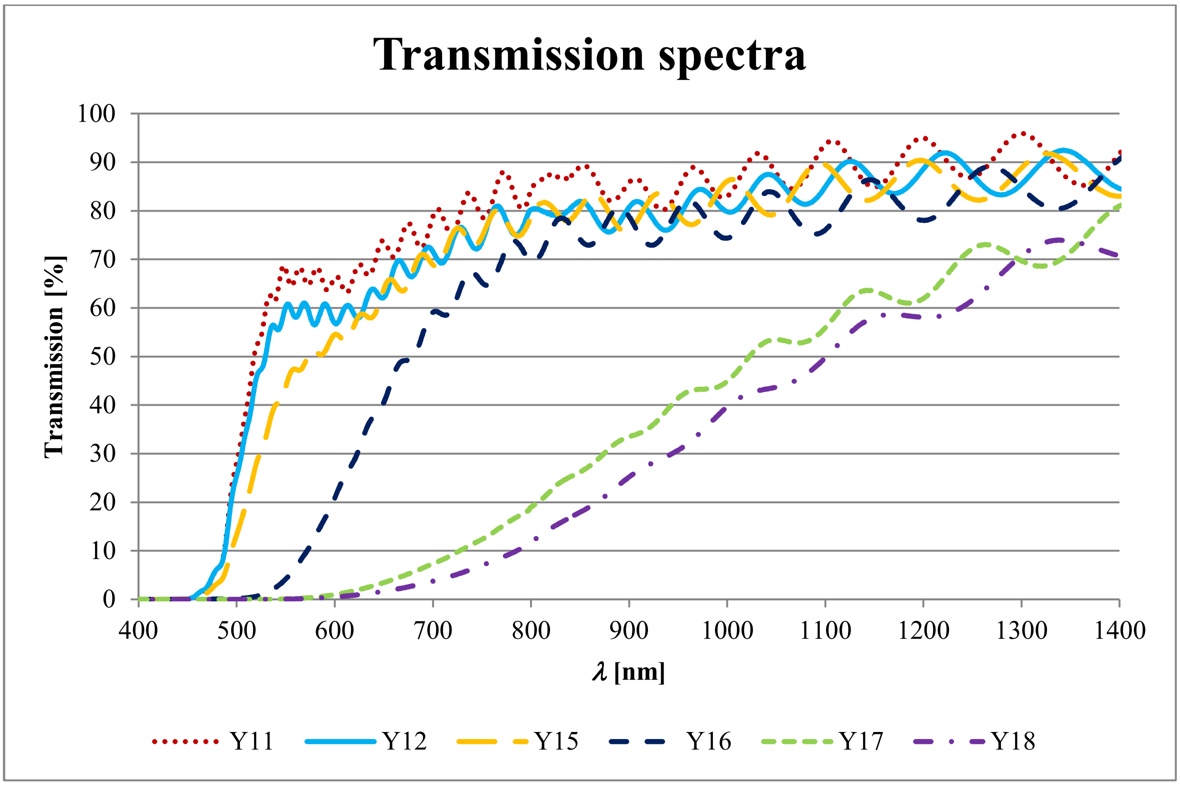

Figure 6.2.4. Transmission spectra of representative samples Y11 and Y15-Y18.
Samples Y8, Y13 and Y14 are omitted for clarity, as they lie between those of Y11 and Y15.
Ripples are etalon fringes [36].

6.2.4. OPTIMISATION OF OXYGEN PRESSURE

Samples Y19-Y21 were deposited at the optimum substrate temperature ($T \approx 1250$ K), found from the characterization of samples Y11-18, and at different values of oxygen pressure (P_{O2}); all the other deposition conditions are the same as specified in Table 6.2.1. Table 6.2.6 summarizes the results of sample characterization. No significant change with oxygen pressure is observed in transmission spectra.

ID	P_{O2} **[Pa]**	ΔH **[mT]**	t_f **[µm]**	S_q **[nm]**	**Y [formula number]**	**Fe [formula number]**	**Y/Fe**
Y20	1	1.75	2.4	1.8	3.55	4.45	0.80
Y19	3.3	2.75	2.5	11.2	3.58	4.42	0.81
Y21	6	2.97	1.8	3.0	3.55	4.45	0.80

Table 6.2.6. Deposition conditions, FMR linewidth (ΔH), thickness (t_f), RMS surface roughness (S_q) and composition of samples Y19-Y23. The best sample in terms of FMR is highlighted in grey.

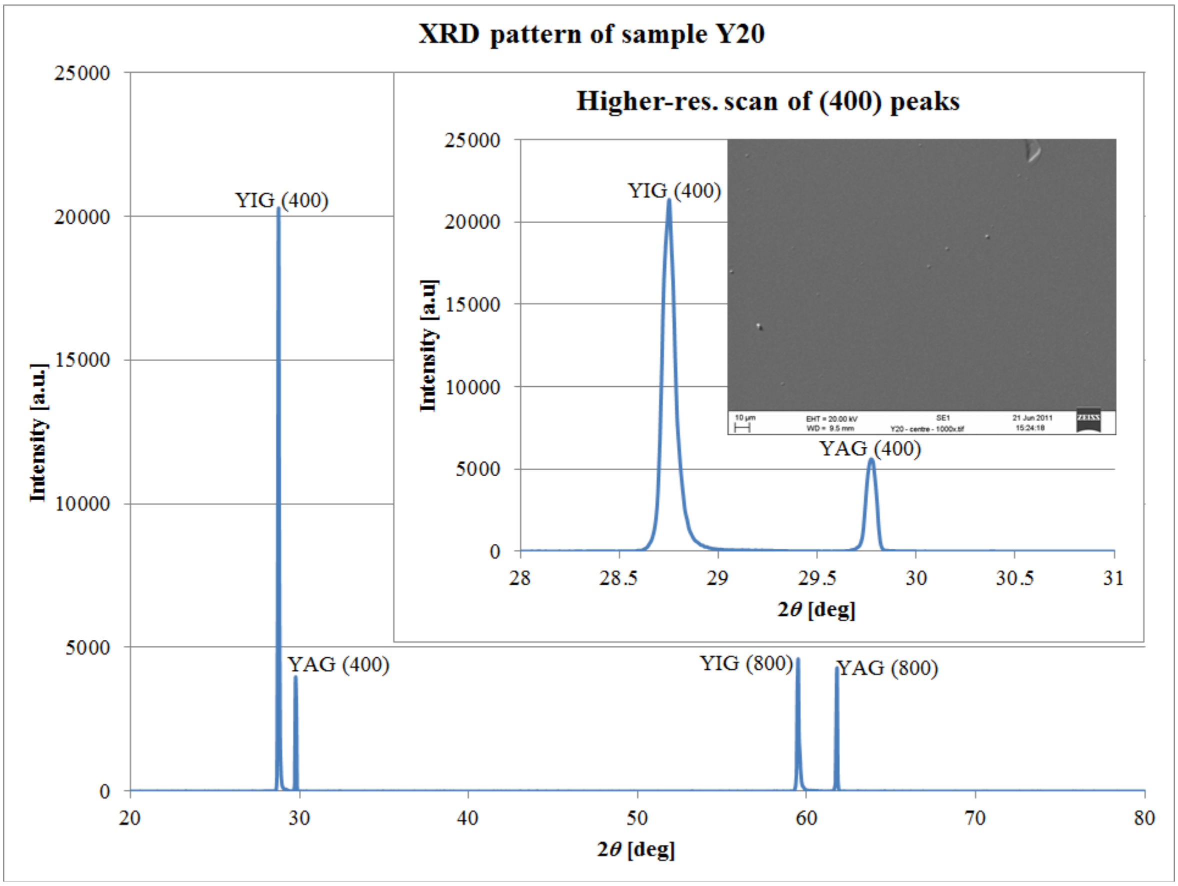

Figure 6.2.5. XRD pattern of Y20.
The insets show a higher resolution scan of (400) peaks and a SEM picture of the film surface.

According to XRD analysis, all films are crystalline with the same orientation as the YAG (100) substrates, with no relevant difference in the XRD patterns. No significant change can be noticed in terms of stoichiometry, when changing the oxygen pressure in the range $P_{O2} = (1 - 6)$ Pa. The narrowest FMR linewidth was achieved at $P_{O2} \approx 1$ Pa (Y20): $\Delta H \approx 1.75$ mT.

Figure 6.2.5 shows the XRD pattern of our best sample, Y20: the peaks from the YIG film and the YAG substrate are close to the positions reported in the database [31, 37], but suffer instrumental error, which was compensated by shifting the XRD pattern so that the YAG peaks are matched to the database values, as shown in Table 6.2.7.

XRD peak	**Database position $2\theta_d$ [deg]**	**Measured position $2\theta_m$ [deg]**	**Corrected position $2\theta_c$ [deg]**
YAG (400)	29.8	29.77	29.8
YIG (400)	28.9	28.75	28.78

Table 6.2.7. Database, measured and corrected XRD peak positions for Y20.

Figure 6.2.6 shows the FMR absorption plot of the best sample, Y20, i.e. the variation of the scattering *S*-parameter S_{21}, which is the transmission of microwaves across the sample (see Section 4.10), as a function of the intensity of the applied magnetic field (B_a). The graph presents a number of satellites to the main FMR resonance peak: these occur at applied fields both greater and smaller than the main FMR peak and are due to the orientation of the RF excitation field relative to the DC applied field, causing magneto-static modes [38-40], which may hinder the measurement of the intrinsic FMR linewidth, as discussed in section 4.10.

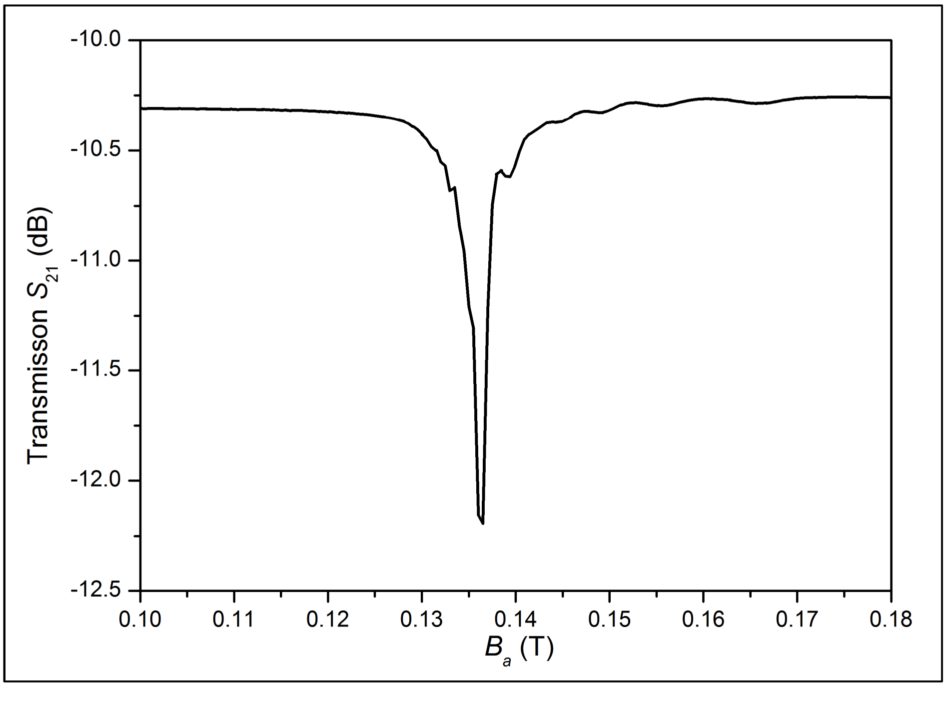

Figure 6.2.6. FMR absorption plot of Y20 at ν = 6 GHz.

A few deposition trials were also carried out at oxygen pressures below 1 Pa, but the broadening of the plume causes a decrease in deposition rate, window coating and consequent decrease in KrF laser fluence and CO_2 laser power, making the study of material properties with changing parameters difficult: variation of crystallinity and magnetic properties cannot be related to just one growth condition and may be due to different factors, such as lower gas pressure, decreasing laser fluence and substrate temperature during the deposition. However a dramatic increase in FMR linewidth (10×) was noticed when decreasing O_2 pressure at 0.5 Pa.

6.2.5. COMPARISON OF DEPOSITIONS FROM SINGLE-CRYSTAL AND POLYCRYSTALLINE YIG TARGETS

Samples Y26-Y29 were deposited from a poly-crystalline YIG target on YAG (100) substrates under similar conditions to those reported in Table 6.2.1, except for substrate temperature, which was set to the optimum value ($T \approx 1250$ K) found from Y20, and oxygen pressure (see Table 6.2.8). Results from samples Y26-Y29 are reported again in Table 6.2.8, together with the data from sample Y20, used as a reference, deposited from the single-crystal YIG target under the same deposition conditions as Y26 and Y29.

ID	**P_{O2} [Pa]**	**ΔH [mT]**	**t_f [µm]**	**S_q [nm]**	**Y [formula number]**	**Fe [formula number]**	**Y/Fe**	**$2\theta_{YIG(400)}$ [deg]**
Y20	1	1.75	2.4	1.8	3.55	4.45	0.80	28.78
Y26	1	4.80	4.5	87.8	3.62	4.38	0.83	28.76
Y29	1	2.10	4.5	14.1	3.74	4.26	0.88	28.65
Y27	2	3.70	4.0	27.1	3.89	4.11	0.95	28.58
Y28	10	3.40	2.0	30.1	3.70	4.30	0.86	28.67

Table 6.2.8. Deposition conditions, FMR linewidth (ΔH), thickness (t_f), RMS surface roughness (S_q), composition and YIG (400) peak position ($2\theta_{YIG(400)}$) in corrected XRD patterns of samples Y26-Y29 and Y20.

One of the most striking differences is the higher thickness of samples Y26 and Y29, ~1.9 times thicker than Y20. This can be explained with the higher absorptivity of UV radiation ($\lambda = 248$ nm) from the poly-crystalline target compared to the single-crystal[13], so that more material is ablated and deposited from the former. The decrease in film thickness with increasing oxygen pressure, observed also in Y19 and Y21, can be explained with the scattering of ablated species with the background gas, reducing the amount of material impinging on the substrate.

The only difference between Y26 and Y29 is that the former was deposited from a fresh target surface, with only 10 minutes of pre-ablation, whereas Y29 was deposited from the same target side with more than 3 hours of ablation. Sample Y26 is ~3.2 times rougher

---

[13] Higher absorptivity in the polycrystalline target can be explained with light scattering from crystallites with random orientation.

than Y29, which means that the ablation of a long-ablated surface produces smoother film surfaces; nevertheless Y29 is still ~7.8 times rougher than Y20, although the difference in FMR linewidth is relatively small (0.35 mT, ~19%).

From data in Table 6.2.8 there seems to be a correlation between surface roughness and FMR linewidth. These data were plotted for convenience in Figure 6.2.7, where it is clear that FMR linewidth tends to increase with increasing surface roughness.

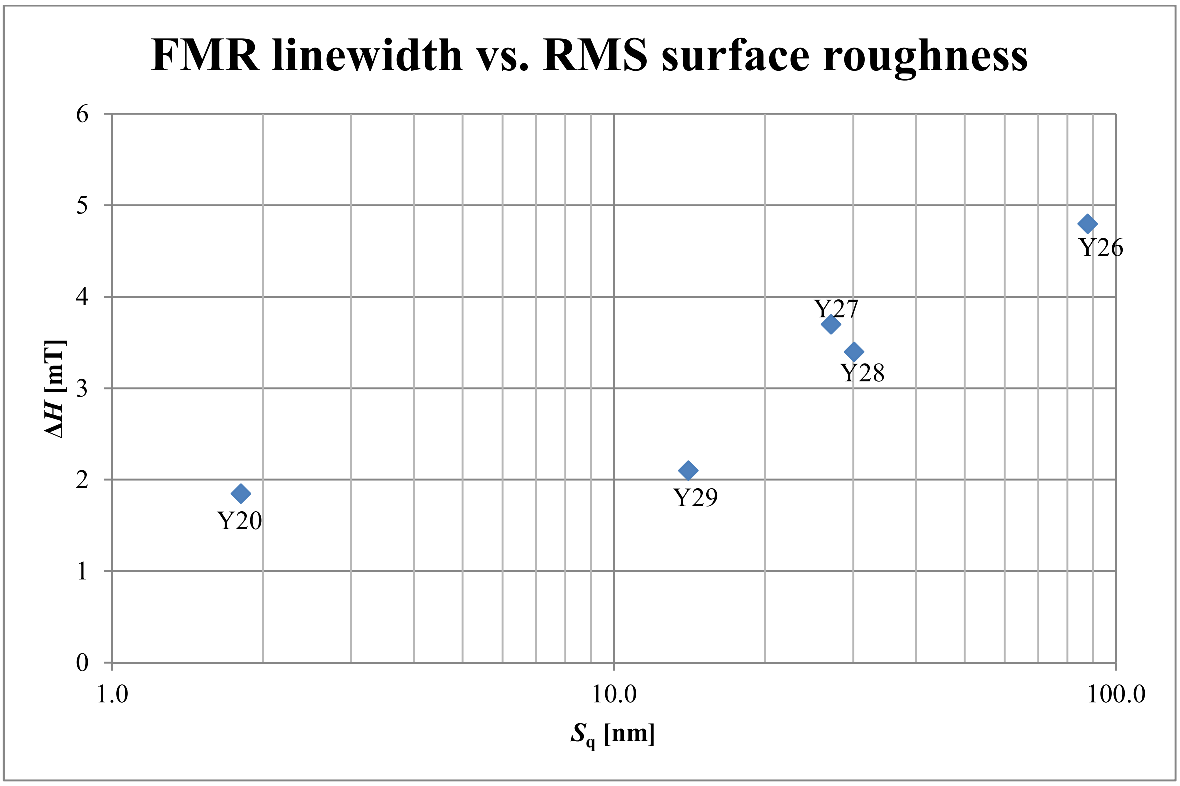

Figure 6.2.7. Variation of FMR linewidth with RMS surface roughness (samples Y26-Y29 and Y20).

Figure 6.2.8 compares the film surface of samples Y26 and Y29: the latter, although having a relatively high density of particulates (compare Figure 6.2.8.c with Figure 6.2.2.a), do not feature any of the flakes clearly visible in Y26, which are supposedly caused by the ablation of the fresh surface of the polycrystalline YIG target. These features were already observed, although at a less extent, in YIG films grown soon after reconditioning the single-crystal target. Y27 features a lower density of these flakes, whereas they completely disappear in Y28. We think that these features are due to contamination in the (re)conditioned target surface and, in particular, to lapping powder embedded in it, which probably is not completely removed during the cleaning process (see section 4.3). Later experiments showed that reconditioning the targets with sandpaper, instead of lapping, considerably reduces the formation and density of these flakes from the first deposition. In any case, this demonstrate the importance of a relatively long (30 minutes at least) target pre-ablation, in order to get rid of dirt on the target before the first deposition from a freshly reconditioned target surface, especially in polycrystalline and ceramic targets, probably due to the fact that they are less dense and more porous than single-crystal targets, thus trapping lapping powder more easily.

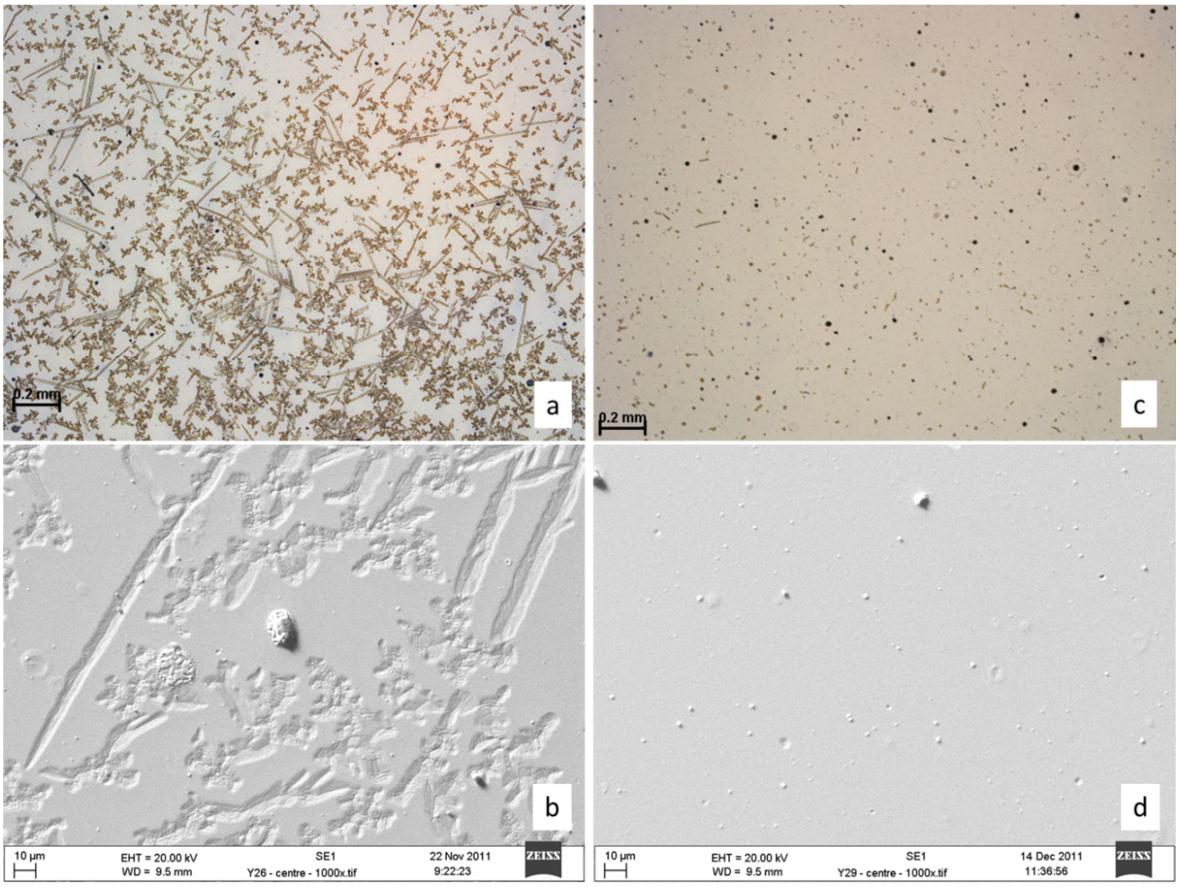

Figure 6.2.8. (a) Optical microscope (5×) and **(b)** SEM (1000×) pictures of the film surface of sample Y26; **(c)** optical microscope (5×) and **(d)** SEM (1000×) pictures of the film surface of samples Y29.

Table 6.2.8 shows also that YIG films Y26-29, deposited from the polycrystalline target, are Y-richer and more Fe-deficient than the YIG samples grown from the single-crystal target, Y20 and all the previous ones (see also Tables 6.2.3, 6.2.5 and 6.2.6); this agrees also with the YIG (400) peak position of Y26-Y29, shifted towards lower diffraction angles, compared to YIG films deposited from the single-crystal target. Moreover, only Y26 has a composition and a YIG (400) peak position similar to Y20, whereas subsequent samples (Y27-Y29) have significantly different composition and YIG (400) peak positions, suggesting that the problem lies in the different changes in the polycrystalline and single-crystal YIG targets during ablation. However, usage and pricing of the latter forced us to switch to the polycrystalline YIG target. Finally, no significant difference was noticed in the optical transmission spectra of samples Y26-29 compared to Y20, except for lower absolute transmission values in the NIR, probably due to the light scattering caused by the rougher film surfaces in Y26-29.

6.3. SINGLE-PLD OF YIG IN THE MULTI-PLD CHAMBER

Optimisation of YIG growth conditions was conducted in the multi-PLD chamber too, with both KrF and Nd:YAG lasers, before performing any multi-PLD experiments, described in the next chapter.

6.3.1. DEPOSITIONS OF YIG WITH THE KRF LASER

First of all, a deposition test (sample E1) was performed under the same conditions as Y20, the best YIG film grown on YAG in our single-PLD system, except for the target (polycrystalline instead of single-crystal) and the substrate temperature ($T \approx 1150$ K), which is limited by the heating method in our multi-PLD system. All deposition conditions are summarised in Table 6.3.1.

Target	Polycrystalline YIG
Substrate	YAG (100)
Laser (λ [nm])	KrF ($\lambda = 248$)
Repetition frequency [Hz]	20
Fluence [J/cm^2]	~3.0
Target – substrate distance [cm]	6.0
O_2 pressure [Pa]	1.0
Substrate temperature [K]	~1150

Table 6.3.1. Deposition conditions of sample E1

As shown in Table 6.3.2, there are only two big differences between Y20 and E1: film thickness and FMR linewidth (ΔH). The lower film thickness in E1, compared to Y20, is due to the continuous tilting of the targets during their ablation and to the target configuration in the multi-PLD chamber, where the target holders are symmetrically off-axis with respect to the substrate, thus causing a lower deposition rate, compared to film growth in the single-PLD system with the on-axis configuration. The FMR linewidth of E1 is ~1.7 times the value of Y20, most likely because of the lower substrate temperature: in fact, the FMR linewidth of E1 ($\Delta H \approx 3.00$ mT) is roughly the same as that of Y11 ($\Delta H \approx 2.91$ mT), grown under similar conditions ($T \approx 1200$ K, $d = 6$ cm, $P_{O2} \approx 3.3$ Pa).

ID	P_{O2} [Pa]	d [cm]	ΔH [mT]	t_f [µm]	S_q [nm]	Y conc. [formula number]	Fe conc. [formula number]	Y/Fe	Sample colour
Y20	1	6	1.75	2.4	1.8	3.55	4.45	0.80	Yellow
E1	1	6	3.00	1.4	2.0	3.54	4.46	0.79	Yellow
E2	1	4	7.15	3.3	9.1	3.36	4.64	0.72	Dark yellow
E3	3.4	4	3.87	2.5	2.8	3.52	4.48	0.78	Yellow
E4	6.8	4	6.65	2	3.3	3.47	4.53	0.77	Yellow

Table 6.3.2. Deposition conditions, FMR linewidth (ΔH), thickness (t_f), RMS surface roughness (S_q) and composition of samples E1-E4. Sample Y20 is shown as a reference.

In order to increase the deposition rate, the target – substrate distance was decreased from 6 cm to 4 cm. This also caused a change in growth dynamics, which affected the quality of sample E2, featuring a darker yellow colour and a broader FMR linewidth than E1. However, XRD analysis revealed that the YIG film is still crystalline with (100) orientation.

In order to keep the same growth dynamics as in Y20 and E1, oxygen pressure must be increased accordingly to the rule of thumb $P_{O2} \cdot d^3$ = const. [41] (see Section 3.2.2), which gives a value of $P_{O2} \approx 3.4$ Pa. This restored the growth dynamics of Y20 and E1, giving acceptable growth rate (~2.5 µm/hour) and FMR linewidth in E3: $\Delta H \approx 3.87$ mT.

Doubling the oxygen pressure (E4) resulted in a lower deposition rate (~2.0 µm/hour), most likely due to increased scattering of ablated species with the background gas, and in a broader FMR linewidth ($\Delta H \approx 6.65$ mT) than E3, suggesting a deterioration of film quality with increasing oxygen pressure, although the sample features high and sharp YIG (400) and (800) peaks in the XRD pattern and a yellow colour.

Optical transmission spectra of samples E1-4 are shown in Figure 6.3.1: E2 features a low and rapidly decreasing transmission with decreasing wavelength, as expected from its dark yellow colour and its film quality.

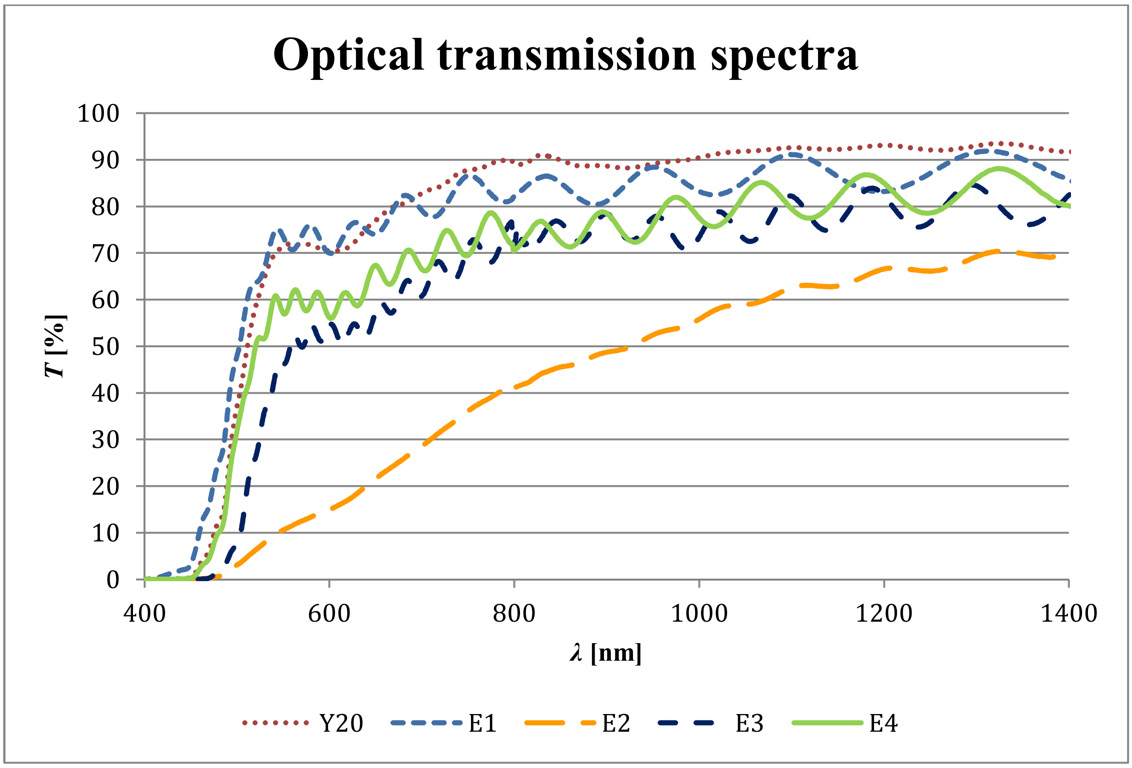

Figure 6.3.1. Optical transmission spectra of E1-4 and Y20. Ripples are etalon fringes [36].

6.3.2. DEPOSITIONS OF YIG WITH THE ND:YAG LASER

The depositions with the frequency-quadrupled Nd:YAG laser were performed with the following laser settings: fluence on the target set at $F_{\mathrm{Nd:YAG}} \approx 1.3$ J/cm^2, and pulse repetition rate fixed at $f_{\mathrm{Nd:YAG}} \approx 10$ Hz. Again we studied the effect of changes in target-substrate distance and oxygen pressure on film properties, which are summarised in Table 6.3.3. XRD analysis confirmed crystallinity and epitaxial growth of all YIG films.

ID	P_{O2} **[Pa]**	d **[cm]**	ΔH **[mT]**	t_f **[μm]**	S_q **[nm]**	**Y conc. [formula number]**	**Fe conc. [formula number]**	**Y/Fe**	**Sample colour**
Y20	1	6	1.75	2.4	1.8	3.55	4.45	0.80	Yellow
N1	1	6	4.34	1	1.8	3.46	4.54	0.76	Yellow
N2	1	4	13.25	2.2	13.4	3.33	4.67	0.71	Dark yellow
N3	3.4	4	4.67	2	2.3	3.37	4.63	0.73	Yellow
N4	6.8	4	5.11	1.2	3.6	3.38	4.62	0.73	Yellow

Table 6.3.3. Deposition conditions, FMR linewidth (ΔH), thickness (t_f), RMS surface roughness (S_q) and composition of samples N1-N4. Sample Y20 is shown as a reference.

Sample N1 was deposited under the same conditions as Y20 and E1, i.e. at $T \approx 1150$ K, $P_{O2} \approx 1$ Pa and $d \approx 6$ cm, but it has a broader FMR linewidth ($\Delta H = 4.34$ mT) than Y20 (by a factor of ~2.5) and E1 (by a factor of ~1.5). Film thickness is just ~1 μm.

Reducing the target – substrate distance from 6 cm to 4 cm without compensation of oxygen pressure (N2) allows a doubling of the growth rate, but it also causes a dramatic increase in FMR linewidth: ΔH = 13.25 mT, which can be explained as originating from a worsening of crystal quality, according to the dark yellow colour and the transmission spectrum (see Figure 6.3.2).

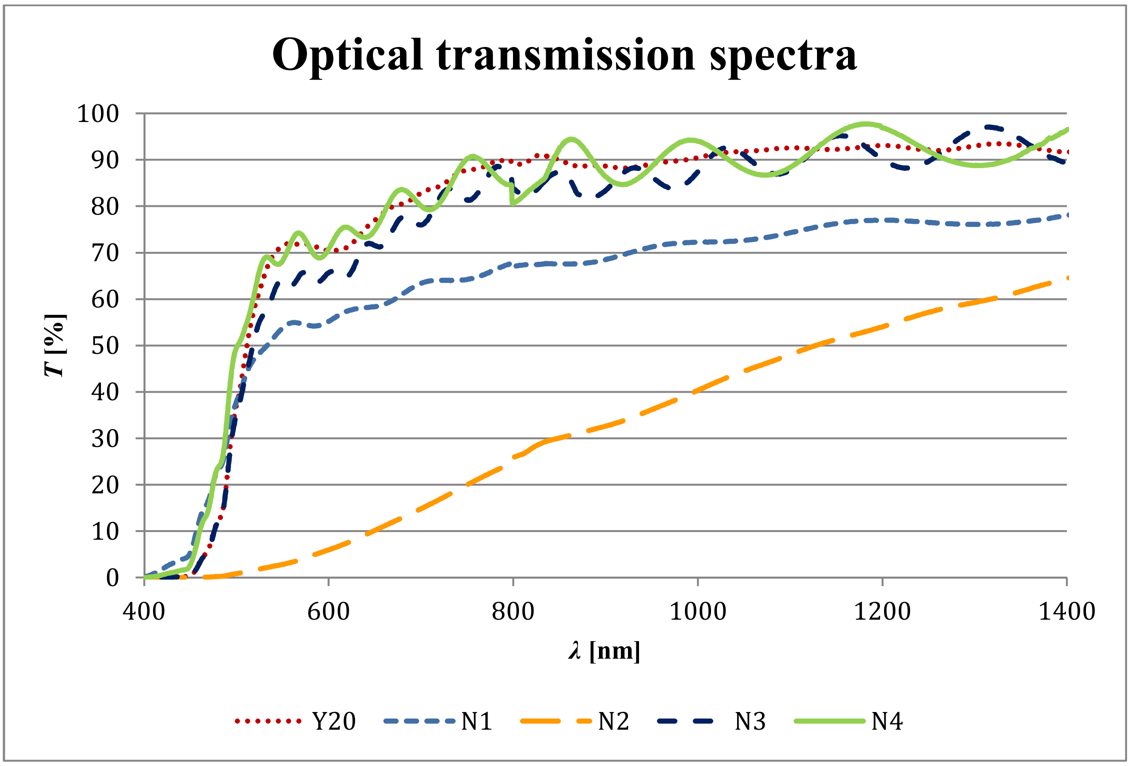

Figure 6.3.2. Optical transmission spectra of N1-4 and Y20. Ripples are etalon fringes [36].

The sample (N3) grown with the same growth dynamics as Y20 and N1, i.e. at $P_{O2} \approx 3.4$ Pa and $d \approx 4$ cm, features a similar thickness, but a narrower FMR linewidth (ΔH = 4.67 mT) than N2. When doubling the oxygen pressure ($P_{O2} \approx 6.8$ Pa), the growth rate is almost halved and no improvement in FMR linewidth is observed (ΔH = 5.11 mT from N4). In any case we observe a broader FMR linewidth in this batch of YIG films, compared to the previous set of samples (batch “E”).

6.4. CONCLUSIONS

In this chapter the process of optimization of deposition conditions of YIG has been shown. Starting from Manuilov's deposition conditions [17] of YIG on GGG, a larger FMR linewidth was observed, probably due to instrumental issues, as explained in Section 6.2.1 and, in more detail, in Section 4.10. PLD growth of YIG on different substrates showed that a narrower FMR linewidth can be obtained in YIG films grown on YAG (100) substrates, probably due to the larger lattice mismatch, compared to YIG on GGG substrates, as discussed in Section 6.2.2. For this reason and the better pricing of YAG substrates than GGG, the deposition conditions of YIG were optimized for growth on YAG (100). FMR linewidth was minimized to $\Delta H \approx 1.75$ mT at a substrate temperature $T \approx 1250$ K, in oxygen ambient at a pressure $P_{O2} \approx 1$ Pa. The deposition conditions of the best YIG film (Y20) are reported in Table 6.4.1.

Target	Single-crystal YIG
Substrate	YAG (100)
Laser (λ [nm])	KrF ($\lambda = 248$)
Repetition frequency [Hz]	20
Fluence [J/cm^2]	~3.0
Target – substrate distance [cm]	6.0
O_2 pressure [Pa]	1.0
Substrate temperature [K]	~1250

Table 6.4.1: Deposition conditions of sample Y20.

Lowering the substrate temperature causes an increase in FMR linewidth, until FMR absorption disappears together with crystallinity, as explained in Section 6.2.3. Changing the oxygen pressure in either direction causes a broadening of the FMR linewidth (see Section 6.2.4).

Because of the usage of the single-crystal YIG target and the pricing for a new one, a poly-crystalline target was used for subsequent experiments. In spite of an increase in surface roughness and a change in composition in the films deposited from the new polycrystalline target, we managed to grow a YIG film (Y29) with an FMR linewidth ($\Delta H \approx 2.10$ mT) close to the best result achieved in Y20, as discussed in Section 6.2.5. An increasing trend of FMR linewidth with increasing surface roughness was noticed in Y26-Y29, although no correlation was observed in other samples, e.g. Y9-Y10 (see Table 6.2.3) and Y19 and Y21 (see Table 6.2.6).

Preliminary experiments for multi-PLD of YIG were performed in the multi-PLD chamber with the single-PLD set-up, using the polycrystalline YIG target, in order to optimise deposition conditions to the following, with either the KrF (see Section 6.3.1) or the Nd:YAG laser (see Section 6.3.2).

Target	Polycrystalline YIG
Substrate	YAG (100)
Target – substrate distance [cm]	4.0
O_2 pressure [Pa]	3.4
Substrate temperature [K]	~1150

Table 6.4.2. Optimum deposition conditions of YIG on YAG in the multi-PLD chamber.

Target – substrate distance and oxygen pressure were changed to optimise YIG film growth in terms of FMR linewidth and growth rate. The substrate temperature, although not optimal, is limited by the heating system used in the multi-PLD chamber.

Ablation of the YIG target with the KrF laser gave slightly better results than Nd:YAG laser: $\Delta H \approx 3.87$ mT for E3 versus $\Delta H = 4.67$ mT for N3.

A few annealing experiments were also performed, both *in situ* and *ex situ*. The *in-situ* thermal annealing of Y2 caused a dramatic change in morphology of both film and substrate (see Section 6.2.1). *Ex-situ* thermal annealing was performed on Y19-Y21 in a furnace at ~1400 K with flowing O_2 (at 1.5 l/min) and N_2 (at 0.5 l/min) for ~12 hours: no significant change in morphology, composition and crystallinity was noticed in any of the samples; only Y19 showed an improvement of 20% in FMR linewidth (from 2.75 mT to 2.2 mT).

6.5. REFERENCES

1. P. C. Dorsey, S. E. Bushnell, R. G. Seed, and C. Vittoria, "Magnetic and structural characteristics of pulsed-laser deposited epitaxial $Y_3Fe_5O_{12}$ films," IEEE Trans. Magn. **29**, 3069-3071 (1993).

2. P. C. Dorsey, S. E. Bushnell, R. G. Seed, and C. Vittoria, "Epitaxial yttrium-iron-garnet films grown by pulsed-laser deposition," J. Appl. Phys. **74**, 1242-1246 (1993).

3. B. M. Simion, R. Ramesh, V. G. Keramidas, G. Thomas, E. Marinero, and R. L. Pfeffer, "Magnetic characterization of epitaxial $Y_3Fe_5O_{12}$ $Bi_3Fe_5O_{12}$ and $Y_3Fe_5O_{12}$ $Eu_1Bi_2Fe_5O_{12}$ heterostructures grown by pulsed-laser deposition," J. Appl. Phys. **76**, 6287-6289 (1994).

4. C. J. Yang, S. W. Kim, and Y. S. Kim, "Polycrystalline $Y_3Fe_5O_{12}$ garnet-films grown by a pulsed-laser ablation technique," IEEE Trans. Magn. **30**, 4527-4529 (1994).

5. H. Buhay, J. D. Adam, M. R. Daniel, N. J. Doyle, M. C. Driver, G. W. Eldridge, M. H. Hanes, R. L. Messham, and M. M. Sopira, "Thick yttrium-iron-garnet (YIG) films produced by pulsed-laser deposition (PLD) for integration applications," IEEE Trans. Magn. **31**, 3832-3834 (1995).

6. B. M. Simion, G. Thomas, R. Ramesh, V. G. Keramidas, and R. L. Pfeffer, "Growth and characterization of ($Y_3Fe_5O_{12}$-$Bi_3Fe_5O_{12}$) heterostructures by pulsed-laser deposition," Appl. Phys. Lett. **66**, 830-832 (1995).

7. M. Y. Chern, C. C. Fang, J. S. Liaw, J. G. Lin, and C. Y. Huang, "Study of ultrathin $Y_3Fe_5O_{12}/Gd_3Ga_5O_{12}$ superlattices," Appl. Phys. Lett. **69**, 854-856 (1996).

8. A. Morimoto, Y. Maeda, T. Minamikawa, Y. Yonezawa, and T. Shimizu, "LPE-like growth of YIG ferrimagnetic thin films by pulsed laser ablation with molten droplets," Appl. Phys. A-Mater. Sci. Process. **69**, S703-S706 (1999).

9. N. B. Ibrahim, C. Edwards, and S. B. Palmer, "Pulsed laser ablation deposition of yttrium iron garnet and cerium-substituted YIG films," J. Magn. Magn. Mater. **220**, 183-194 (2000).

10. E. Popova, N. Keller, F. Gendron, M. Guyot, M. C. Brianso, Y. Dumond, and M. Tessier, "Structure and magnetic properties of yttrium-iron-garnet thin films prepared by laser deposition," J. Appl. Phys. **90**, 1422-1428 (2001).

11. S. Kahl, and A. M. Grishin, "Pulsed laser deposition of $Y_3Fe_5O_{12}$ and $Bi_3Fe_5O_{12}$ films on garnet substrates," J. Appl. Phys. **93**, 6945-6947 (2003).

12. N. B. Ibrahim, C. Edwards, and S. B. Palmer, "Yttrium iron garnet surface modification during pulsed laser ablation deposition," Mater. Sci. **22**, 111-115 (2004).

13. N. Kumar, D. S. Misra, N. Venkataramani, S. Prasad, and R. Krishnan, "Magnetic properties of pulsed laser ablated YIG thin films on different substrates," J. Magn. Magn. Mater. **272**, E899-E900 (2004).

14. Y. Dumont, N. Keller, E. Popova, D. S. Schmool, S. Bhattacharya, B. Stahl, M. Tessier, and M. Guyot, "Superexchange and iron valence control by off-stoichiometry in

yttrium iron garnet thin films grown by pulsed laser deposition," J. Appl. Phys. **97**, 10G108 (2005).

15. N. Kumar, S. Prasad, D. S. Misra, N. Venkataramani, M. Bohra, and R. Krishnan, "The influence of substrate temperature and annealing on the properties of pulsed laser-deposited YIG films on fused quartz substrate," J. Magn. Magn. Mater. **320**, 2233-2236 (2008).

16. Y. Krockenberger, K. S. Yun, T. Hatano, S. Arisawa, M. Kawasaki, and Y. Tokura, "Layer-by-layer growth and magnetic properties of $Y_3Fe_5O_{12}$ thin films on $Gd_3Ga_5O_{12}$," J. Appl. Phys. **106**, 123911 (2009).

17. S. A. Manuilov, R. Fors, S. I. Khartsev, and A. M. Grishin, "Submicron $Y_3Fe_5O_{12}$ Film Magnetostatic Wave Band Pass Filters," J. Appl. Phys. **105**, 033917 (2009).

18. H. Kidoh, A. Morimoto, and T. Shimizu, "Synthesis of ferromagnetic bisubstitued yttrium-iron-garnet films by laser ablation," Appl. Phys. Lett. **59**, 237-239 (1991).

19. A. A. Jalali-Roudsar, V. P. Denysenkov, S. I. Khartsev, A. M. Grishin, N. Adachi, and T. Okuda, "Microwave and magneto-optic properties of pulsed laser deposited bismuth iron garnet films," IEEE Trans. Magn. **37**, 2454-2456 (2001).

20. E. Popova, N. Keller, F. Jomard, L. Thomas, M. C. Brianso, F. Gendron, M. Guyot, and M. Tessier, "Exchange coupling in ultrathin epitaxial yttrium iron garnet films," Eur. Phys. J. B **31**, 69-74 (2003).

21. S. Leitenmeier, T. Korner, J. Griesbauer, M. Herbort, A. Heinrich, and B. Stritzker, "Studies on the growth of epitaxial bismuth-substituted iron garnet on gadolinium gallium garnet single crystals by pulsed laser deposition," J. Cryst. Growth **310**, 5392-5401 (2008).

22. S. A. Manuilov, S. I. Khartsev, and A. M. Grishin, "Pulsed laser deposited $Y_3Fe_5O_{12}$ films: Nature of magnetic anisotropy I," J. Appl. Phys. **106**, 123917 (2009).

23. S. A. Manuilov, and A. M. Grishin, "Pulsed laser deposited $Y_3Fe_5O_{12}$ films: Nature of magnetic anisotropy II," J. Appl. Phys. **108**, 013902 (2010).

24. S. Yiyan, S. Young-Yeal, and W. Mingzhong, "Growth and ferromagnetic resonance of yttrium iron garnet thin films on metals," Appl. Phys. Lett. **101**, 082405 (2012).

25. S. Yiyan, S. Young-Yeal, C. Houchen, M. Kabatek, M. Jantz, W. Schneider, W. Mingzhong, H. Schultheiss, and A. Hoffmann, "Growth and ferromagnetic resonance properties of nanometer-thick yttrium iron garnet films," Appl. Phys. Lett. **101**, 152405 (2012).

26. B. Bhoi, N. Venkataramani, R. Aiyar, and S. Prasad, "FMR and Magnetic Studies on Polycrystalline YIG Thin Films Deposited Using Pulsed Laser," IEEE Trans. Magn. **49**, 990-994 (2013).

27. M. Kubota, K. Shibuya, Y. Tokunaga, F. Kagawa, A. Tsukazaki, Y. Tokura, and M. Kawasaki, "Systematic control of stress-induced anisotropy in pseudomorphic iron garnet thin films," J. Magn. Magn. Mater. **339**, 63-70 (2013).

28. E. Popova, A. F. F. Galeano, M. Deb, B. Warot-Fonrose, H. Kachkachi, F. Gendron, F. Ott, B. Berini, and N. Keller, "Magnetic anisotropies in ultrathin bismuth iron garnet films," J. Magn. Magn. Mater. **335**, 139-143 (2013).

29. M. Shone, "The technology of YIG film growth," Circ. Syst. Signal Pr. **4**, 89-103 (1985).

30. H. Sawada, "Electron density study of garnets: $Y_3X_2Al_3O_{12}$; X = Al and X = (Al, Cr)," J. Solid State Chem. **134**, 182-186 (1997).

31. D. Rodic, M. Mitric, R. Tellgren, H. Rundloef, and A. Kremenovic, "True magnetic structure of the ferrimagnetic garnet $Y_3Fe_5O_{12}$ and magnetic moments of iron ions.," J. Magn. Magn. Mater. **191**, 137-145 (1999).

32. V. P. Denysenkov, and A. M. Grishin, "Broadband ferromagnetic resonance spectrometer," Rev. Sci. Instrum. **74**, 3400-3405 (2003).

33. T. Boudiar, B. Payet-Gervy, M. F. Blanc-Mignon, J. Rousseau, M. Le Berre, and H. Joisten, "Magneto-optical properties of yttrium iron garnet (YIG) thin films elaborated by radio frequency sputtering," J. Magn. Magn. Mater. **284**, 77-85 (2004).

34. S. M. Shahrokhvand, A. S. H. Rozatian, M. Mozaffari, S. M. Hamidi, and M. M. Tehranchi, "Preparation and investigation of Ce:YIG thin films with a high magneto-optical figure of merit," J. Phys. D-Appl. Phys. **45**, 235001 (2012).

35. R. Paschotta, "RP Photonics Encyclopedia," http://www.rp-photonics.com/, Accessed December 2013.

36. R. Swanepoel, "Determination of the thickness and optical-constants of amorphous-silicon," J. Phys. E-Sci. Instr. **16**, 1214-1222 (1983).

37. L. Dobrzycki, E. Bulska, D. A. Pawlak, Z. Frukacz, and K. Wozniak, "Structure of YAG crystals doped/substituted with erbium and ytterbium," Inorg. Chem. **43**, 7656-7664 (2004).

38. R. W. Damon, and J. R. Eshbach, "Magnetostatic modes of a ferromagnet slab," J. Phys. Chem. Solids. **19**, 2 (1960).

39. J. F. Dillon, "Magnetostatic modes in disks and rods," J. Appl. Phys. **31**, 10 (1960).

40. L. R. Walker, "Resonant modes of ferromagnetic spheroids," J. Appl. Phys. **29**, 318–323 (1958).

41. R. Castro-Rodriguez, D. R. Coronado, A. Iribarren, B. E. Watts, F. Leccabue, and J. L. Pena, "Correlation between target-substrate distance and oxygen pressure in pulsed laser deposition of complex oxide thin films," Appl. Phys. A Mater. Sci. **81**, 1503-1507 (2005).

7. CHAPTER 7
MULTI-PLD OF YIG

7.1. INTRODUCTION

This chapter focuses on the multi-PLD growth of YIG films. Preliminary experiments for optimisation of deposition conditions of YIG in the multi-PLD chamber, with either the KrF or the Nd:YAG laser, were described and discussed in Section 6.3. Single-PLD of YIG from a stoichiometric target usually leads to films that are Fe-deficient, as previously reported in the literature [1] and confirmed in the experiments described in Chapter 6. The experiments described in this chapter were carried out to understand how the change in the composition of YIG films affects the other properties (crystallinity, surface roughness and morphology, optical transmission and FMR linewidth), as no systematic study has been done before by multi-PLD. In particular, Section 7.2 describes multi-PLD of YIG and Fe_2O_3, performed in order to study the compensation of Fe-deficiency; the results of multi-PLD of YIG and Y_2O_3 are discussed in Section 7.3; multi-PLD of Fe_2O_3 and Y_2O_3 for growth of YIG and $YFeO_3$ films is described in Section 7.4. An important experimental point to note is that the Y_2O_3 target cannot be ablated with the Nd:YAG laser and for this reason the experiments with it were performed only with the laser set-ups described below in Table 7.1.1.

Section \ TARGETS	**YIG**	**Fe_2O_3**	**Y_2O_3**
7.2.1	Nd:YAG	KrF	-
7.2.2	KrF	Nd:YAG	-
7.3	Nd:YAG	-	KrF
7.4	-	Nd:YAG	KrF

Table 7.1.1. Summary table of targets and lasers used, as described in each section of this chapter.

7.2. MULTI-PLD OF YIG AND FE_2O_3

In this section the results achieved by multi-PLD of YIG and Fe_2O_3 are discussed. In the first sub-section the results obtained from ablating the YIG target with the frequency-quadrupled Nd:YAG laser and the Fe_2O_3 target with the KrF laser are presented, whereas the results attained with the inverted laser set-up are discussed in the second sub-section.

7.2.1. ABLATION OF YIG WITH ND:YAG AND FE$_2$O$_3$ WITH KRF

The batch of YIG samples whose growth conditions and properties are summarised in Table 7.2.1 was deposited by multi-PLD, ablating the YIG target with the Nd:YAG laser (fluence: $F_{\mathrm{Nd:YAG}} \approx 1.3$ J/cm^2; pulse repetition frequency: $f_{\mathrm{Nd:YAG}} = 10$ Hz) and the Fe$_2$O$_3$ target with the KrF laser, whose fluence F_{KrF} and pulse repetition rate f_{KrF} were systematically changed, in order to grow YIG films with different Fe concentration. The other conditions are the same as in Table 6.4.2. The deposition duration was ~72,000 Nd:YAG laser pulses (i.e. 2 hours) for all samples. The target ablation ratio in Table 7.2.1 is defined as $r = f_{\mathrm{KrF}}/f_{\mathrm{Nd:YAG}}$.

ID	F_{KrF} [J/cm^2]	r	ΔH [mT]	t_f [µm]	S_q nm]	Y conc. [formula number]	Fe conc. [formula number]	Y/Fe	Sample colour
Y20	-	0	1.75	2.4	1.8	3.55	4.45	0.80	Yellow
N3	-	0	4.67	2	2.3	3.37	4.63	0.73	Yellow
YF1	2.4	0.1	30.4	2	217.4	2.92	5.08	0.57	Dark red
YF2	1.3	0.1	17.25	1.4	7.4	3.11	4.89	0.64	Orange
YF3	1.3	0.2	21.12	1.8	12.1	3.02	4.98	0.61	Light red
YF4	1.3	0.3	24.05	1.7	203.6	2.93	5.07	0.58	Dark red
YF5	1.3	0.4	29.81	1.7	216.5	2.92	5.08	0.57	Dark red

Table 7.2.1. Deposition conditions and results of samples YF1-YF5, grown by ablating the YIG target with the Nd:YAG laser and the Fe$_2$O$_3$ target with the KrF laser. Samples Y20 and N3 are shown as reference.

All the films of this batch have a darker colour than YIG films grown by ablating only the YIG target and show a non-uniform and hazy surface, with a more opaque region in the centre, which appears to have higher particulate density than the rest of the film surface from inspection by optical microscopy and stylus profiler (see Figure 7.2.1): the high surface roughness did not allow the correct measurement of transmission spectra, due to undesirable surface light scattering. XRD analysis confirmed crystallinity and epitaxy of all YIG films.

Table 7.2.1 shows that Fe deficiency was compensated at the first attempt: YF1 is actually slightly Fe-overstoichiometric; however the film has a very broad FMR linewidth ($\Delta H \approx$ 30.4 mT), a dark reddish colour and a very rough surface ($S_q \approx 217.4$ nm), featuring a high particulate density region in the centre, similar to a Fe$_2$O$_3$ tester film (~1.5 µm thick) grown on a *c*-cut sapphire (α-Al$_2$O$_3$) substrate, which suggests that the problem lies in the ablation of the Fe$_2$O$_3$ target with the KrF laser, whose fluence on the Fe$_2$O$_3$ target was therefore reduced, in the hope that this would produce better-quality films. Lowering F_{KrF} from ~2.4 J/cm^2 to ~1.3 J/cm^2 in fact allowed the growth of a smoother, but thinner (~0.6

µm thick) Fe_2O_3 tester film, with low particulate density in the central region, as in Figure 7.2.1.b.

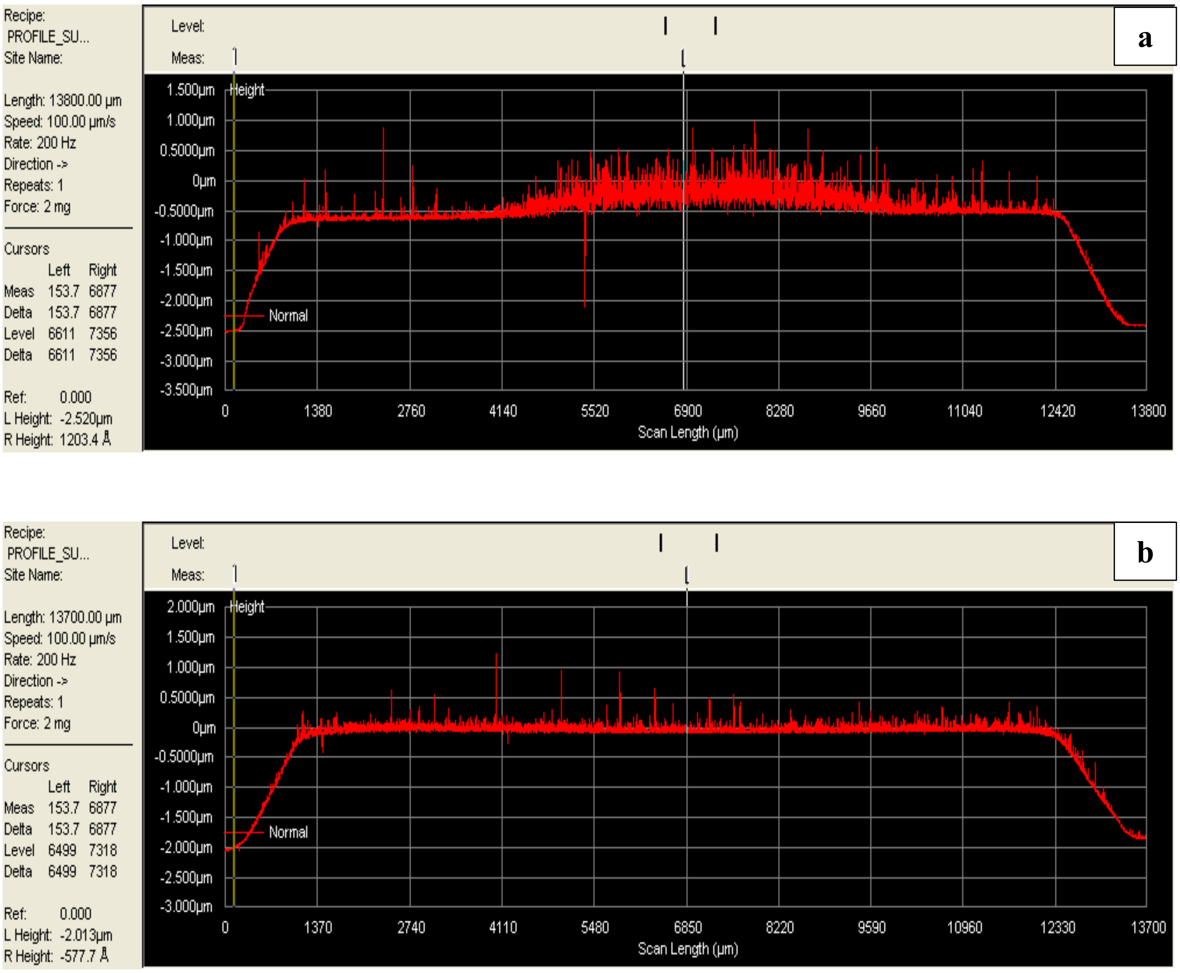

```
Recipe:
 PROFILE_SU...
Site Name:

Length: 13800.00 µm
Speed: 100.00 µm/s
Rate: 200 Hz
Direction ->
Repeats: 1
Force: 2 mg

Cursors
        Left   Right
Meas    153.7  6877
Delta   153.7  6877
Level   6611   7356
Delta   6611   7356

Ref:      0.000
L Height: -2.520µm
R Height: 1203.4 Å
```

```
Recipe:
 PROFILE_SU...
Site Name:

Length: 13700.00 µm
Speed: 100.00 µm/s
Rate: 200 Hz
Direction ->
Repeats: 1
Force: 2 mg

Cursors
        Left   Right
Meas    153.7  6877
Delta   153.7  6877
Level   6499   7318
Delta   6499   7318

Ref:      0.000
L Height: -2.013µm
R Height: -577.7 Å
```

Figure 7.2.1. Comparison of surface profiles of samples **(a)** YF1 and **(b)** N3.

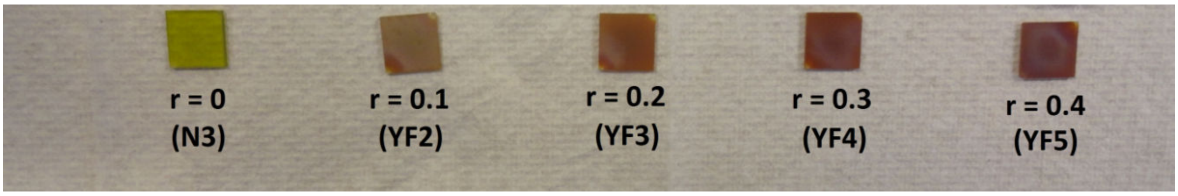

Figure 7.2.2. Samples YF2-YF5 compared to sample N3. *r* is the target ablation ratio.

As already observed, lower KrF laser fluence (F_{KrF}) means lower deposition rate from the Fe_2O_3 target, thus lower Fe in the YIG films: in fact, overstoichiometry was reached at f_{KrF} = 3 Hz (YF4) and f_{KrF} = 4 Hz (YF5) instead of f_{KrF} = 1 Hz as in YF1, but the film quality became worse as the KrF laser repetition frequency and the target ablation ratio were increased, as seen in Figure 7.2.2: films became less reflective, more opaque, redder and rougher – film colour, particulate density and surface roughness seem to be related to concentration of Fe (see Table 7.2.1). Figure 7.2.3 shows the variation of FMR linewidth and RMS surface roughness with Fe concentration, which increases with increasing KrF laser repetition frequency f_{KrF} or target ablation ratio r (see Table 7.2.1). The broadening of FMR linewidth with increasing Fe concentration in the YIG films agrees with previous findings in the single-PLD-grown films (N1-N4, but also E1-E4) and with the results in YIG films grown by single-PLD from a Fe-overstochiometric YIG target reported in [1].

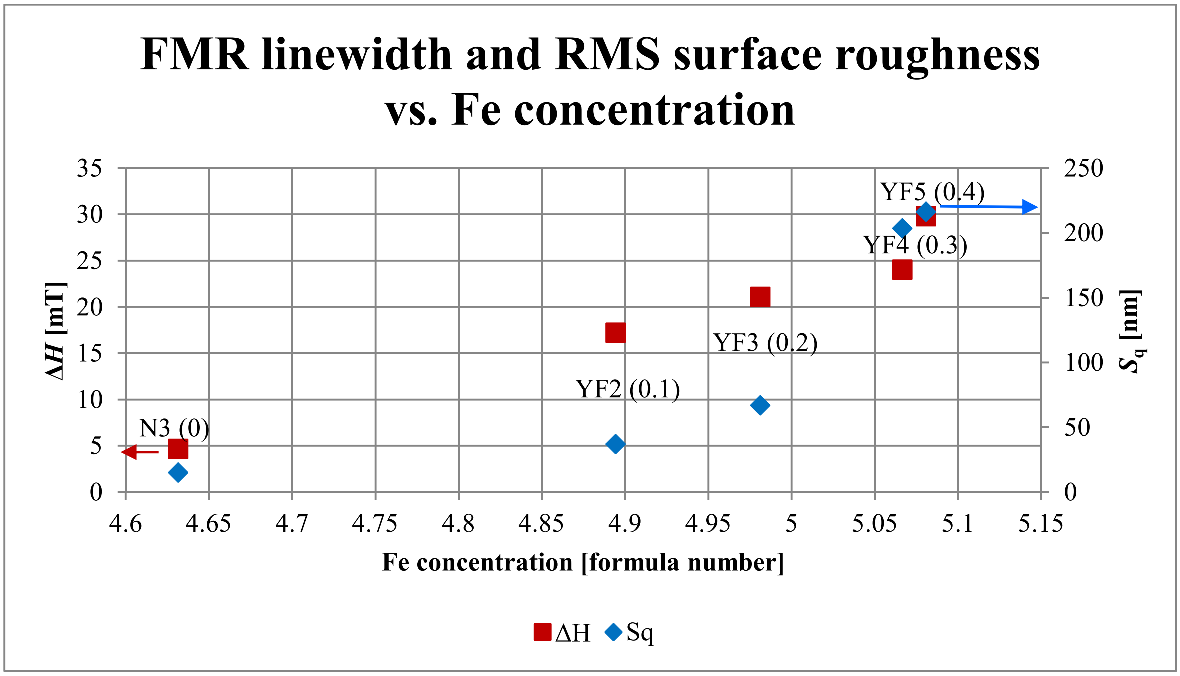

Figure 7.2.3. Variation of FMR linewidth (ΔH) and RMS roughness (S_q) with Fe concentration. Samples YF2-YF5 and N3 – The number in parentheses is the target ablation ratio r.

Although a correlation between RMS surface roughness and FMR linewidth has already been shown and discussed in Section 6.2.5, the broadening in FMR linewidth here is likely due to a direct effect of increase of Fe concentration or a change in crystallinity, induced by the change in composition; in fact, in Y26 the FMR linewidth is relatively low ($\Delta H \approx$ 4.8 mT) compared to YF2 ($\Delta H \approx$ 17.25 mT), in spite of the higher surface roughness of Y26 ($S_q \approx$ 87.8 nm), compared to the same sample, YF2 ($S_q \approx$ 37.2 nm). However, the increase in surface roughness is surely related to the increase in Fe concentration (see trend in Figure 7.2.3), as it can be observed also in N1-N4 (see Table 6.3.3) and E1-E4 (see Table 6.3.2).

Considering that a variation in target-substrate distance or in oxygen pressure causes a significant change in deposition rate and in FMR linewidth in pure YIG films (see samples N1-N4), as discussed in Section 6.3.2, the only option available to improve film quality was changing laser set-up (i.e. actually swapping target positions) and therefore ablating the Fe_2O_3 target with the Nd:YAG laser and the YIG target with the KrF laser (although this required higher fluence and use of the KrF laser at maximum output energy), as discussed in the next paragraph.

7.2.2. Ablation of YIG with KrF and Fe_2O_3 with Nd:YAG

The batch of YIG samples whose growth conditions and properties are summarised in Table 7.2.2 was deposited by multi-PLD, ablating the YIG target with the KrF laser ($F_{\mathrm{KrF}} \approx$ 2.8 J/cm^2 and f_{KrF} = 20 Hz, except for YFi3, deposited with f_{KrF} = 16 Hz) and the Fe_2O_3 target with the Nd:YAG laser, whose fluence was set to $F_{\mathrm{Nd:YAG}} \approx$ 1.3 J/cm^2. To achieve this co-deposition, pulses were gated with a shutter with different open and close times, in order to grow YIG films with different Fe concentration. The other growth conditions are the same as in Table 6.4.2. Deposition duration was 72,000 excimer laser pulses for all samples.

The inverted target ablation ratio, *ir,* in Table 7.2.2 is defined as the ratio of the number of Nd:YAG laser pulses per second on the Fe_2O_3 target to the number of excimer laser pulses per second (i.e. the excimer laser repetition rate, f_{KrF}) on the YIG target: $ir = f_{\mathrm{Nd:YAG}}/f_{\mathrm{KrF}}$. This was done in order to avoid the somewhat illogical infinite target ablation ratio r for $f_{\mathrm{Nd:YAG}}$ = 0 Hz, according to the definition adopted in Section 7.2.1, and this batch of samples (YFi) can be compared with the “YF” batch, by referring to the ratio of the number of laser pulses per second on the Fe_2O_3 target over the number of laser pulses per second on the YIG target.

ID	*ir*	ΔH [mT]	t_f [µm]	S_q [nm]	Y conc. [formula number]	Fe conc. [formula number]	Y/Fe	Sample colour
Y20	0	1.75	2.4	1.8	3.55	4.45	0.8	Yellow
E3	0	3.87	2.5	2.8	3.52	4.48	0.78	Yellow
YFi1	0.05	6.03	2.2	5.1	3.40	4.60	0.74	Yellow
YFi2	0.1	6.50	3	4.0	3.22	4.78	0.67	Dark yellow
YFi3	0.125	9.21	3	7.9	3.03	4.97	0.61	Brownish / dark yellow
YFi4	0.15	8.70	4	8.6	2.88	5.12	0.56	Light brown
YFi5	0.2	16.00	3.5	395.6	2.89	5.11	0.56	Brown

Table 7.2.2. Deposition conditions and results of samples YFi1-YFi5, grown ablating the YIG target with the KrF laser and the Fe_2O_3 target with the Nd:YAG laser. Samples Y20 and E3 are shown as reference.

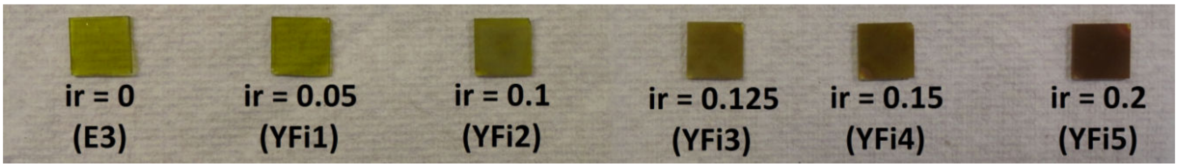

Figure 7.2.4. Samples YFi1-YFi5 compared to sample E3. *ir* is the inverted target ablation ratio.

As shown in Figure 7.2.4, the films of this batch have a progressively darker colour with increasing inverted target ablation ratio, but they show a smoother and more uniform film surface than the “YF” batch. Also the Fe_2O_3 tester (~1.5 µm thick) grown on a *c*-cut sapphire substrate with the Nd:YAG laser compares better (more uniform and smoother) than the one grown ablating the Fe_2O_3 target with the KrF laser, suggesting that the problem lies in the ablation of the Fe_2O_3 target with the KrF laser, which probably causes the formation of a more energetic plume that adversely affects the film growth.

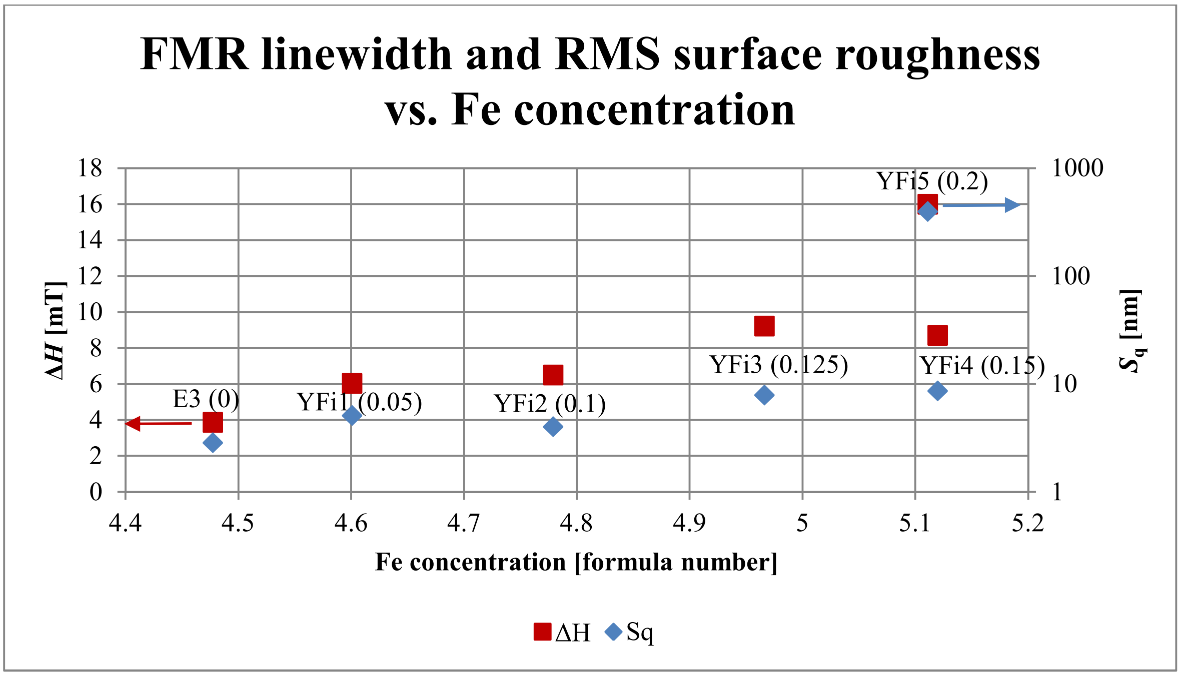

Figure 7.2.5. Variation of FMR linewidth (Δ*H*) and RMS surface roughness (S_q) with Fe concentration. Samples YFi1-YFi5 and E3 – The number in parentheses is the inverted target ablation ratio *ir*.

Table 7.2.2 shows that Fe deficiency was almost compensated in YFi3, whereas samples YFi4 and YFi5 are Fe-overstoichiometric. As in the multi-PLD batch with swapped laser configuration (YF1-YF5), the film colour becomes darker, opacity increases, reflectivity decreases, surface roughness increases and FMR linewidth broadens with increasing Fe concentration (see Figure 7.2.5). However, the increase of surface roughness and the broadening of FMR linewidth in this set of samples are not as strong as in the previous batch: RMS surface roughness is below 10 nm and FMR linewidth below 10 mT for all samples except for YFi5 ($S_q \approx 395.6$ nm and $\Delta H \approx 16$ mT), unlike most of the "YF" samples, featuring $S_q > 10$ nm and $\Delta H > 10$ mT; the largest value of FMR linewidth is $\Delta H \approx 16$ mT in YFi5, with an Fe concentration of 5.11 formula units, versus $\Delta H \approx 30.4$ mT in YF1, with an Fe concentration of 5.08 formula units, suggesting that YIG ablation by KrF laser produces better quality films, as already observed in single-PLD experiments (see Section 6.3). Moreover, EDX analysis showed that Fe concentration is more uniform across the film surface in this batch than in the "YF" batch, suggesting that the plume from the Fe_2O_3 target ablated by the Nd:YAG laser is broader than the plume formed by the KrF laser, which also agrees with the idea that the KrF laser plume is more energetic and hence more forward-directed than the plume formed by the Nd:YAG laser.

Ablation of Fe_2O_3 by the Nd:YAG laser produces better quality films too: in fact, the Fe_2O_3 tester film grown on sapphire with the Nd:YAG laser is smoother and more uniform than the one grown with the KrF laser, which instead featured a large hazy area and a dark and opaque region in its centre, with a higher density of particulates. This is reflected in multi-PLD-grown YIG films using the same laser set-up, as observed above, suggesting that optimum ablation of both targets is crucial for deposition of high-quality YIG films with a higher Fe concentration and that successful growth might require a different set of conditions that satisfies neither laser source for ablation of Fe_2O_3.

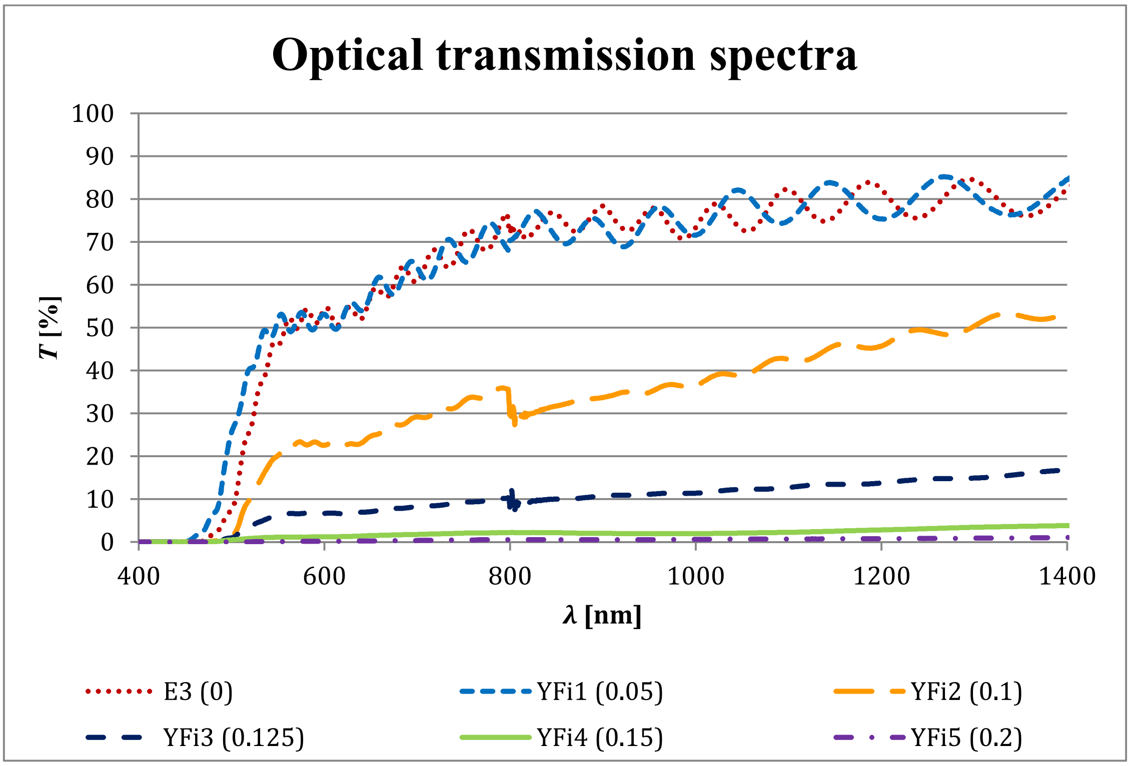

Figure 7.2.6. Optical transmission spectra of YFi1-YFi5 and E3. Ripples are etalon fringes [2]. The number in parentheses is the inverted target ablation ratio *ir*.

Optical transmission spectra are shown in Figure 7.2.6, where it is clear how optical transmission in the near infrared and visible decreases with increasing Fe concentration in the YIG films. The darkening of film colour and the increase of opacity agree with the trend of optical transmission with Fe concentration. A shift towards longer wavelengths (red-shift) with increasing Fe concentration can be noticed too, which agrees with the transmission spectra of the Fe_2O_3 testers, featuring an absorption edge at ~600 nm (typically between ~550 nm and ~450 nm for our YIG films grown by single-PLD).

7.3. MULTI-PLD OF YIG AND Y_2O_3

In this section the results achieved by multi-PLD of YIG and Y_2O_3 are discussed. All the experiments were performed at the same deposition conditions as in Table 6.4.2, by ablating the YIG target with the Nd:YAG laser ($F_{\mathrm{Nd:YAG}} \approx 1.3$ J/cm^2 and $f_{\mathrm{Nd:YAG}} = 10$ Hz) and the Y_2O_3 target with the KrF laser, whose fluence was set to $F_{\mathrm{KrF}} \approx 1.3$ J/cm^2 and pulse repetition rate was changed in the range $f_{\mathrm{KrF}} = (1 - 4)$ Hz, in order to grow YIG films with different Y concentration (see Table 7.3.1). Deposition duration was ~72,000 Nd:YAG laser pulses.

The original definition of target ablation ratio r (see Section 7.2.1) is used again here. Thickness measurements of YY2-YY4 were not conclusive, due to the high curvature of the YAG substrates used; however, from deposition time, it is expected to be ~(1.7 – 2) μm.

ID	r	ΔH [mT]	t_f [μm]	S_q [nm]	Y conc. [formula number]	Fe conc. [formula number]	Y/Fe	YIG peak in XRD pattern	Sample colour
Y20	0	1.75	2.4	1.8	3.55	4.45	0.8	YES	Yellow
N3	0	4.67	2	2.3	3.37	4.63	0.73	YES	Yellow
YY1	0.1	5.08	1.7	18.9	3.64	4.36	0.83	YES	Yellow
YY2	0.2	10.05	N.A.	9.5	3.91	4.09	0.96	YES	Yellowish
YY3	0.3	–	N.A.	10.5	4.40	3.6	1.22	NO	Orange / pinkish
YY4	0.4	–	N.A.	4.1	4.72	3.28	1.44	NO	Orange / pinkish

Table 7.3.1. Deposition conditions and results of samples YY1-YY4, grown ablating the YIG target with the Nd:YAG laser and the Y_2O_3 target with the KrF laser. Samples Y20 and N3 are shown as reference.

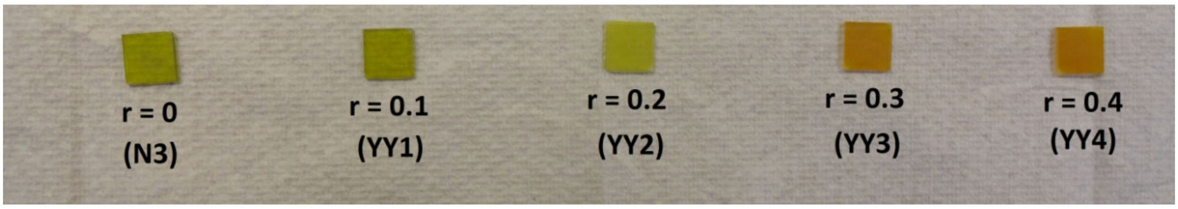

Figure 7.3.1. Samples YY1-YY4 compared to sample N3. r is the target ablation ratio. Samples YY2-YY4 appear more opaque due to the rougher surface of the back side of the substrates (polished only on one side).

XRD analysis showed that only YY1 and YY2 are epitaxial crystalline YIG films, as their diffraction patterns feature YIG (400) and YIG (800) peaks, which are missing in the patterns of YY3 and YY4, where only YAG (400) and (800) peaks due to the substrate appear. YY3 and YY4 differ from YY1 and YY2 also in terms of film colour, as shown in Figure 7.3.1.

Table 7.3.1 shows an obvious increase in Y concentration, a decrease in Fe concentration and an increase of FMR linewidth with increasing target ablation ratio r from 0 to 0.4, i.e. with increasing KrF laser repetition rate f_{KrF} from 0 Hz to 4 Hz; actually, FMR absorption disappears in YIG films grown with $r \geq 0.3$, i.e. $f_{\mathrm{KrF}} \geq 3$ Hz. From the results of Fe-doping experiments, a decrease of FMR linewidth with decreasing Fe concentration (or increasing Y concentration) was expected. The opposite trend observed may be due to either the dilution of magnetic Fe ions in Y-rich films or the lattice distortion, whereas the lack of FMR absorption in YY3-YY4 is likely due to the fact that the films are not crystalline.

Figure 7.3.2 shows the variation of composition of YIG films (N3 + YY1-YY4) with target ablation ratio. It can be noticed that Y-doping in these samples is heavier than Fe-doping in previous experiments: this is because less material is lost or the KrF laser ablates more material from the Y_2O_3 target than from the Fe_2O_3, despite using the same KrF laser fluence as in the "YF" batch ($F \approx 1.3$ J/cm^2). In fact, under the same conditions, the Y_2O_3 growth rate is ~0.025 nm/pulse versus ~0.0083 nm/pulse for the Fe_2O_3 growth rate. Also, during the deposition of YY1-YY4 the YIG growth rate was probably lower than before (N3), due to a decrease in Nd:YAG laser fluence, thus making these YIG films even more Y-doped.

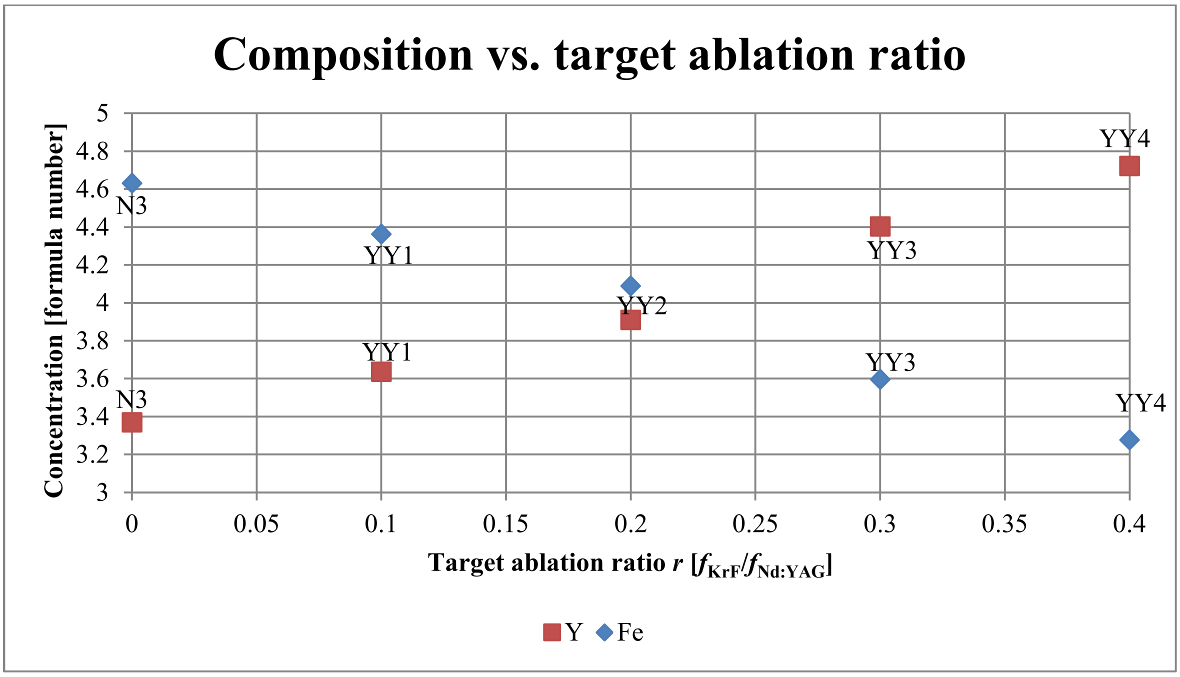

Figure 7.3.2. Variation of film composition with target ablation ratio – samples YY1-YY5 and N3.

Figure 7.3.3 shows the XRD patterns of N3, YY1 and YY2: a large shift towards lower angles can be noticed for the YIG (400) peaks, whose positions are plotted versus Y concentration in Figure 7.3.4. The higher the Y concentration, the lower the YIG (400) peak position, which means larger lattice constant, which agrees with the expected theoretical trend: Y has a larger ionic radius, so the higher the Y concentration in the YIG film, the larger the lattice constant. The lack of crystallinity in YY3 and YY4 can be explained as follows: when the Y concentration becomes too high, the YIG crystal cannot accommodate any more Y ions in lattice positions or even in interstitial positions, as they would cause excessive lattice distortion that cannot be accommodated by the crystal, so that the material prefers growing in an amorphous phase, as suggested also by the different film colour.

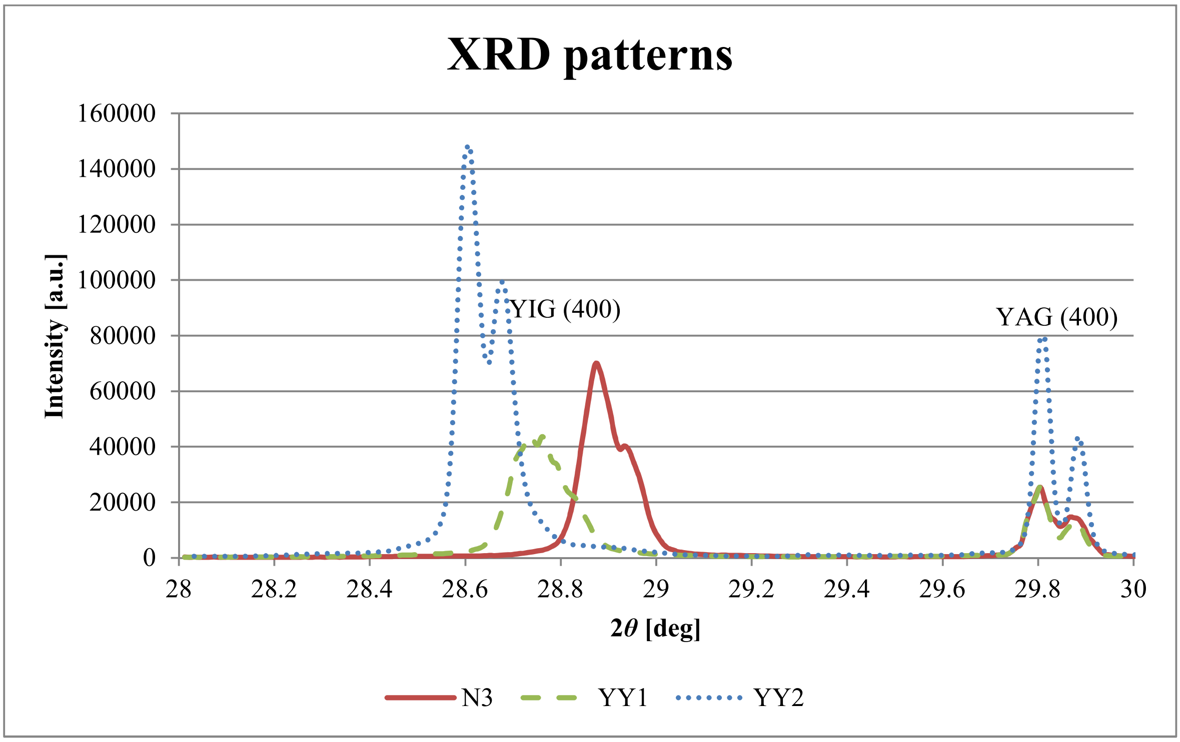

Figure 7.3.3. XRD patterns of samples YY1-YY2 and N3.
All diffraction peaks appear as double, due to Cu-K$_{\alpha 2}$ radiation present in the diffractometer.

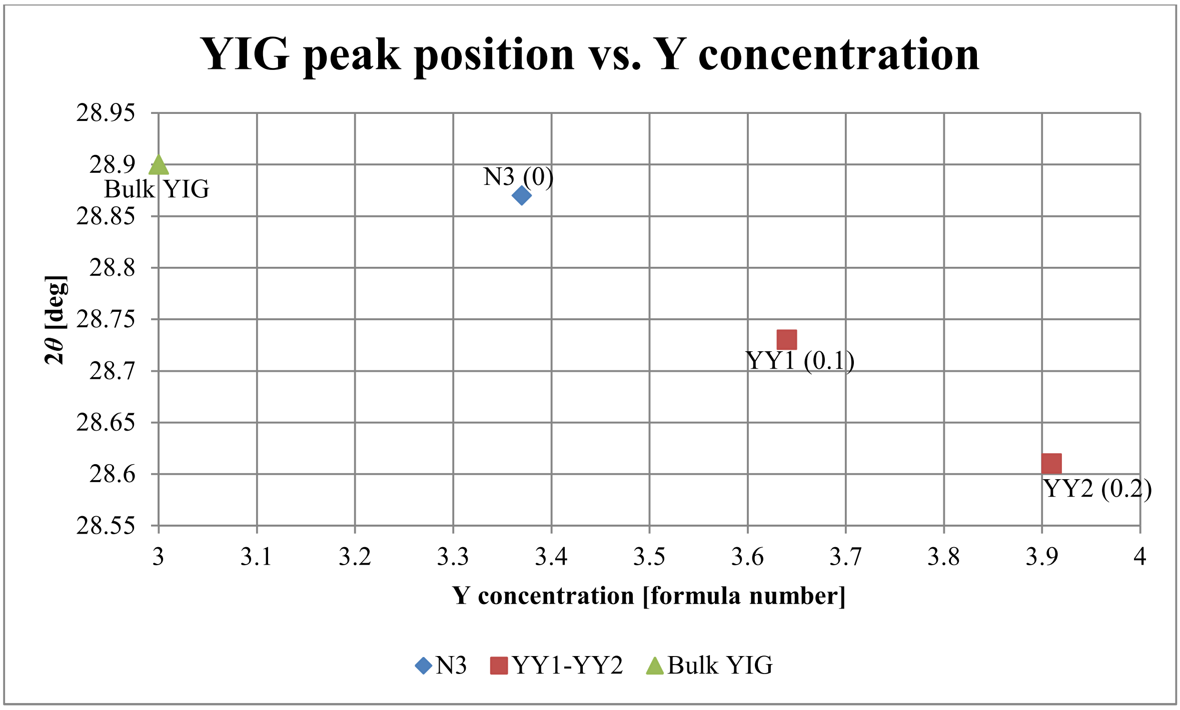

Figure 7.3.4. Variation of YIG (400) peak position with Y concentration.
The number in parentheses is the target ablation ratio *r*.

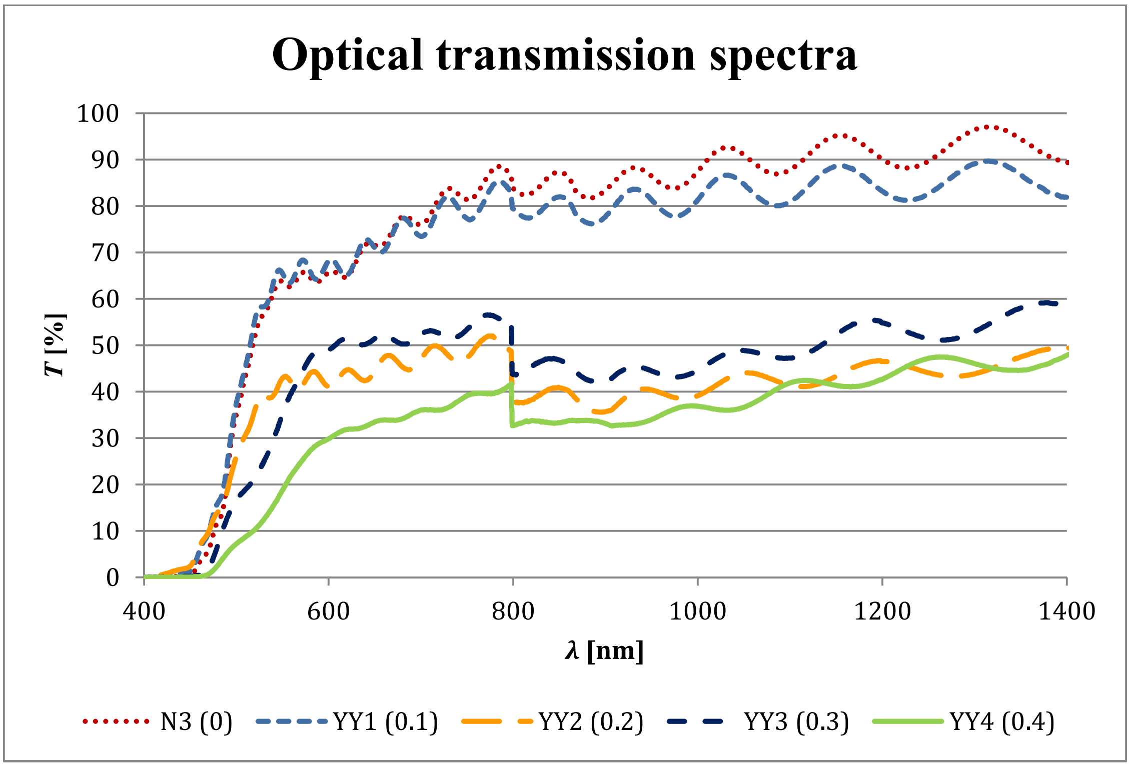

Figure 7.3.5. Optical transmission spectra of YY1-YY4 and N3. Ripples are etalon fringes [2]. The number in parentheses is the target ablation ratio *r*. The step change at ~800 nm is due to a combination of detector changeover and the rough surface of the back side of the YAG substrates used for YY2-YY4.

Figure 7.3.5 shows optical transmission spectra of N3 and YY1-YY4: a tiny shift to lower wavelengths (blue shift) in the absorption edge can be observed in YY1 and YY2, with increasing Y concentration: this may be due to Fe dilution in Y-rich films, as stated above, and agrees with the opposite trend (red-shift with increasing Fe concentration) observed in samples YFi2-YFi5, compared to E3 in Figure 7.2.6. However, when increasing the Y doping even more with higher target ablation ratio, a clear red-shift is observed in YY3 and YY4, which also feature an orange/pink colour (see Figure 7.3.1). The red-shift of the absorption edge and the different colour of YY3 and YY4 can be explained better with the very different composition and, in particular, the severe Fe deficiency rather than with change in crystallinity (amorphous YIG is dark and absorbs in the near-infrared, NIR, and in the visible): in fact, in YIG it is Fe ions that are responsible for optical absorption [3-5], as explained in Section 3.6.3; also, Fe_2O_3 films are red and absorb in the visible, whereas Y_2O_3 films are colourless and transparent, with no optical absorption in the visible and in the NIR.

7.4. MULTI-PLD OF Y_2O_3 AND FE_2O_3

This section covers the multi-PLD experiments of Y_2O_3 and Fe_2O_3. In Section 7.4.1 the growth of YIG from its precursors is demonstrated by depositing films on YAG (100) substrates; compositional tuning via a change in target ablation ratio is described and variation of film properties with changing composition discussed. In Section 7.4.2 the growth of yttrium ferrite ($YFeO_3$ or YFO) on sapphire is demonstrated too, thus proving, for the first time to our knowledge, the capability of multi-PLD to grow different crystalline complex oxides, such as YIG and YFO, from the same precursors (Y_2O_3 and Fe_2O_3) by choosing the appropriate substrate (YAG or sapphire), and to tune the material composition by adjusting the repetition frequency of the lasers.

7.4.1. YIG GROWTH

Table 7.4.1 summarises the different deposition conditions and results of the YIG samples grown by multi-PLD of Y_2O_3 and Fe_2O_3. The original definition of target ablation ratio r (see Section 7.2.1) is used again. All the experiments were performed at the same deposition conditions as in Table 6.4.2, by ablating the Fe_2O_3 target with the Nd:YAG laser ($F_{\mathrm{Nd:YAG}} \approx 1.2$ J/cm^2 and $f_{\mathrm{Nd:YAG}} = 10$ Hz) and the Y_2O_3 target with the KrF laser, whose pulse repetition frequency was changed in the range $f_{\mathrm{KrF}} = (4 - 9)$ Hz, in order to grow YIG films with different composition, whereas the laser fluence was tuned to $F_{\mathrm{KrF}} \approx$ 1.1 J/cm^2 in a few deposition trials to grow stoichiometric YFO with both lasers set at the same repetition rate $f_{\mathrm{KrF}} = f_{\mathrm{Nd:YAG}} = 10$ Hz, i.e. with a target ablation ratio $r = 1$, and stoichiometric YIG with the KrF laser set at $f_{\mathrm{KrF}} = 6$ Hz and the Nd:YAG laser set at $f_{\mathrm{Nd:YAG}} = 10$ Hz, i.e. with a target ablation ratio $r = 0.6 = \mathrm{Y/Fe}$ for stoichiometric YIG.

ID	***r***	**Δ*H* [mT]**	***S*q [nm]**	**Y conc. [formula number]**	**Fe conc. [formula number]**	**Y/Fe**	**Sample colour**
Y20	0	1.75	1.8	3.55	4.45	0.80	Yellow
FY1	0.4	57.31	104.4	2.28	5.72	0.40	Red
FY2	0.5	40.01	134.0	2.67	5.33	0.50	Red
FY3	0.6	13.29	9.2	2.99	5.01	0.60	Brown / dark yellow
FY4	0.7	6.27	12.4	3.40	4.60	0.74	Yellow
FY5	0.8	5.98	10.0	3.70	4.30	0.86	Yellow
FY6	0.9	9.58	10.5	3.93	4.07	0.96	Yellow

Table 7.4.1. Deposition conditions and results of samples FY1-FY6, grown ablating the Fe_2O_3 target with the Nd:YAG laser and the Y_2O_3 target with the KrF laser. Sample Y20 is shown as reference.

Figure 7.4.1 is a photo of all the YIG samples of this batch, ordered from left to right according to the target ablation ratio (*r*). It is evident that the film's colour becomes brighter (less red and more yellow) with decreasing Fe concentration, i.e. with increasing target ablation ratio. Moreover FY3 (stoichiometric YIG), FY1 and FY2 (Fe-rich films) are less uniform, hazier and rougher than FY4-FY6 (Fe-deficient samples), as shown also in the SEM pictures in Figure 7.4.2.

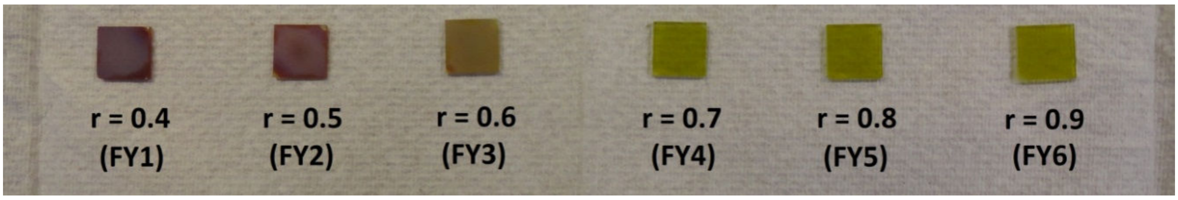

Figure 7.4.1. Photo of samples FY1-FY6. r is the target ablation ratio: $r = f_{KrF}/f_{Nd:YAG}$.

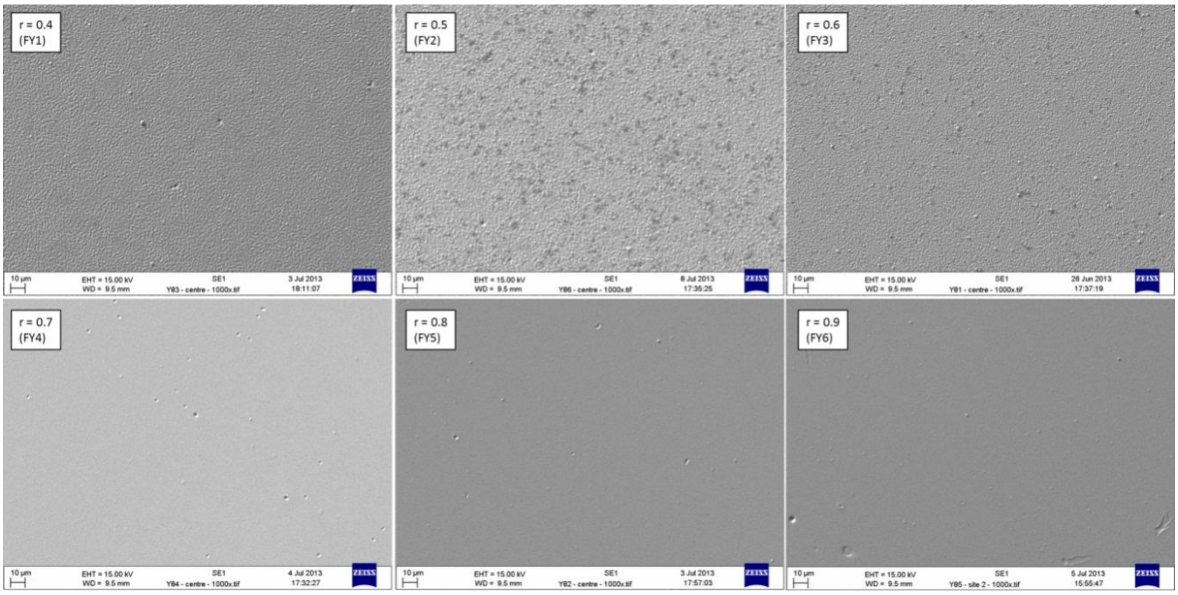

Figure 7.4.2. SEM pictures of samples FY1-FY6. r is the target ablation ratio: $r = f_{KrF}/f_{Nd:YAG}$.

Table 7.4.1 shows an obvious increase in Y concentration, a decrease in Fe concentration and a decrease of FMR linewidth with increasing target ablation ratio r from 0.4 to 0.8, i.e. with increasing KrF laser repetition rate f_{KrF} from 4 Hz to 8 Hz; at $r = 0.9$ or $f_{KrF} = 9$ Hz, FMR linewidth starts broadening again, as already observed in "YY" samples grown by multi-PLD of YIG + Y_2O_3 (see Section 7.3). No further depositions were performed with higher target ablation ratio r, i.e. with higher KrF laser frequency f_{KrF}, as we already observed FMR disappearing and a change in crystallinity in "YY" samples (see Section 7.3), when the Y/Fe ratio was raised above 1, i.e. composition similar to $YFeO_3$. The trend shown for the new "FY" samples in Figure 7.4.3 agrees with those previously observed in the other sets of samples ("YF", "YFi" and "YY") grown by multi-PLD of YIG and either Fe_2O_3 or Y_2O_3, as discussed in the previous sections of this chapter (7.2.1, 7.2.2 and 7.3) and summarised in the same figure. This confirms that the FMR linewidth in YIG films grown on YAG by PLD is minimised when the composition is off-stoichiometric and in particular, in Fe-deficient films with the following estimated formulation: $Y_{3.5}Fe_{4.5}O_{12}$, which may be explained with a change in microstructure and morphology induced by the different composition or with a direct effect: as explained in Section 3.6.2, ferrimagnetism in YIG derives from the fact the octahedral sub-lattice [*a*] and the tetrahedral one (*d*), where Fe ions are located in the garnet structure $\{c^{3+}\}_3[a^{3+}]_2(d^{3+})_3O_{12}$, are coupled anti-ferromagnetically but are not equivalent, yielding a ferrimagnetic crystal; however, Fe deficiency in one of the two sub-lattices may enhance ferrimagnetism, so that – on the contrary – compensation of Fe deficiency induces anti-ferromagnetism.

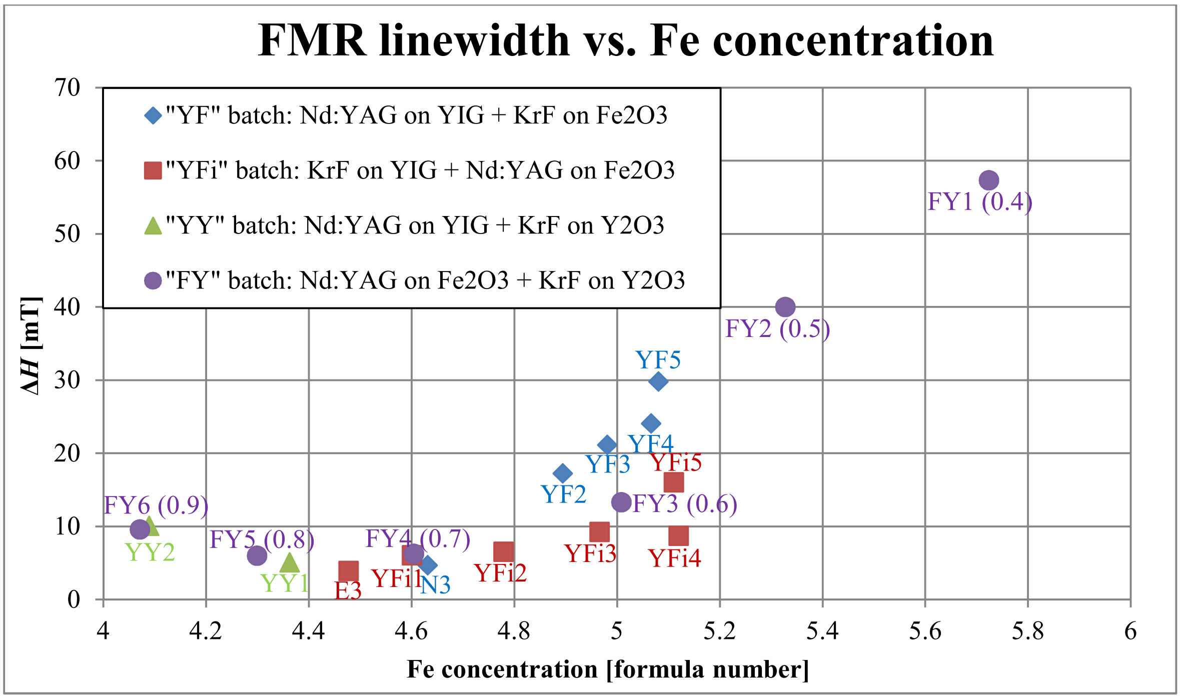

Figure 7.4.3. Variation of FMR linewidth (Δ*H*) with Fe concentration.
The number in parentheses is the target ablation ratio.

Figure 7.4.4 shows the variation of composition of YIG films (FY1-FY6) with target ablation ratio. An obvious increase of Y concentration and a decrease of Fe concentration are observed with increasing target ablation ratio *r*, i.e. with increasing repetition frequency f_{KrF} of the KrF laser ablating the Y_2O_3 target. Sample FY6 has a composition very close to that of $YFeO_3$, but it still features the YIG phase in its XRD pattern and FMR, as in YY2.

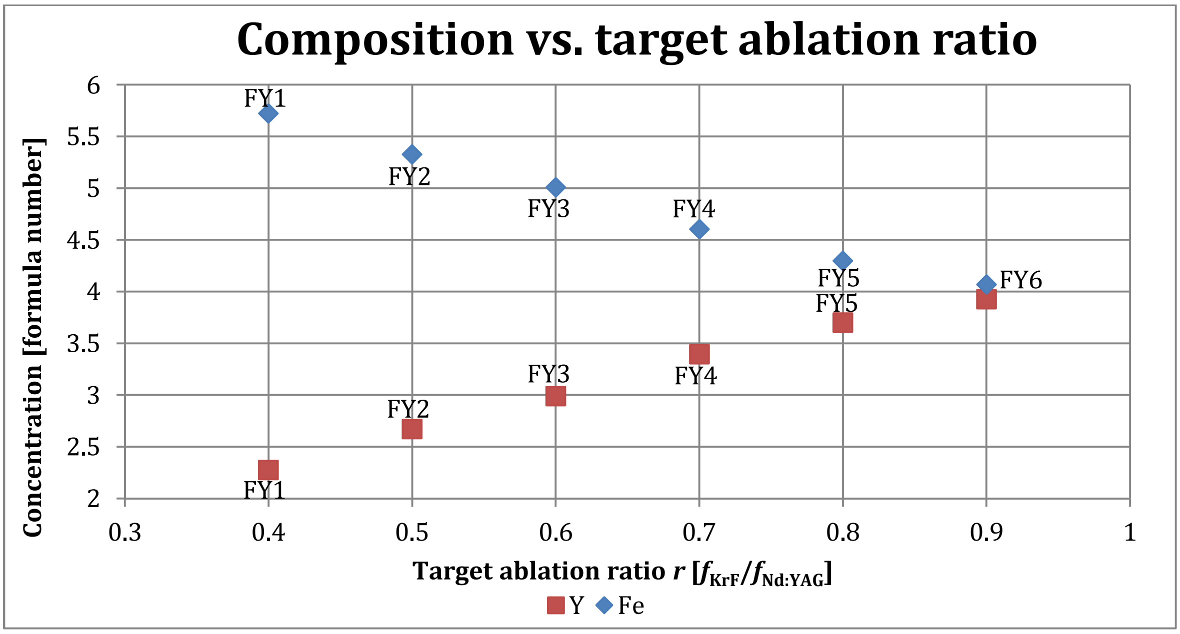

Figure 7.4.4. Variation of film composition with target ablation ratio – samples FY1-FY5.

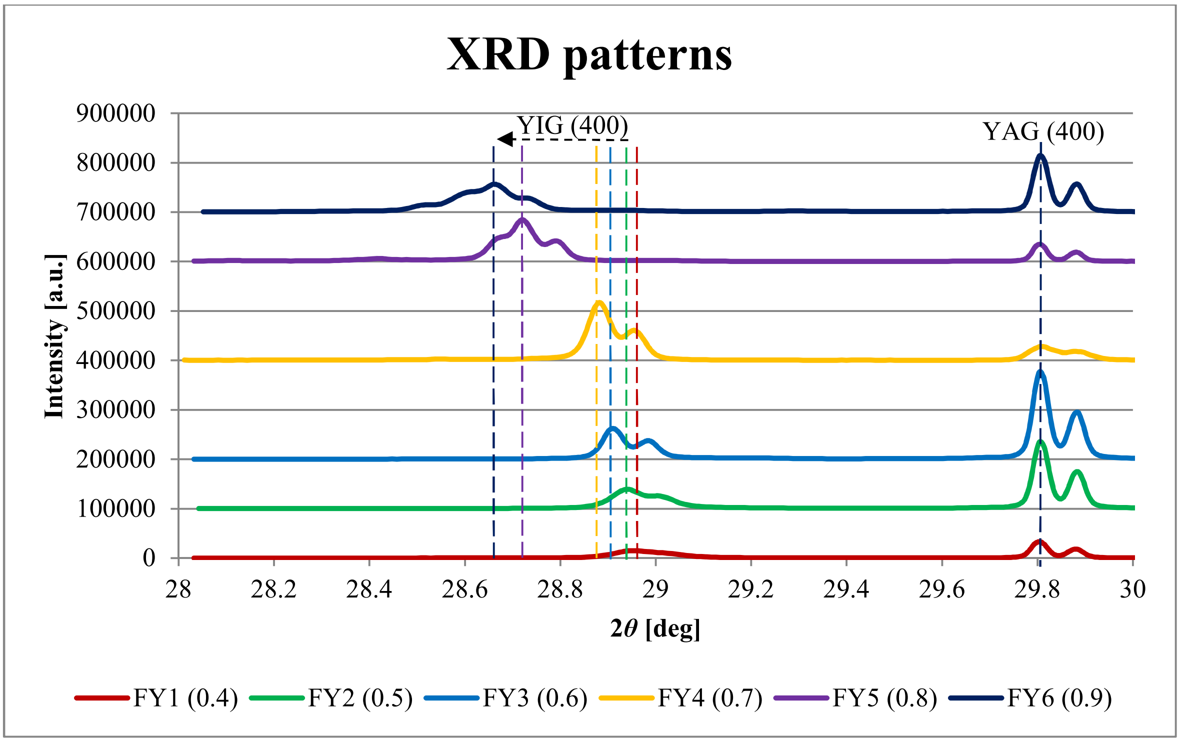

Figure 7.4.5. XRD patterns of samples FY1-FY6. All traces are vertically offset for better clarity. The second peak is due to Cu-K$_{\alpha 2}$ radiation in the diffractometer**.**

Figure 7.4.5 shows the XRD patterns of FY1-FY6 in the range 2θ = (28° – 30°): all films feature a YIG (400) peak from the film and a YAG (400) peak from the substrate, indicating epitaxial growth of crystalline YIG on YAG; a clear shift towards lower diffraction angles with increasing target ablation ratio can be noticed for the YIG (400) peaks, whose positions are plotted versus Y concentration in Figure 7.4.6. The higher the Y concentration, the lower the YIG (400) peak position, which means higher lattice constant, which agrees with the trend observed in samples YY1-YY2 and the expected theoretical trend explained in Section 7.3. Also, distortion and broadening of the YIG peaks can be noticed with composition diverging from stoichiometry, meaning a degrading crystal quality: sample FY4, with a composition of $Y_{3.4}Fe_{4.6}O_{12}$, features the highest and sharpest YIG (400) peak, as shown in Figure 7.4.5.

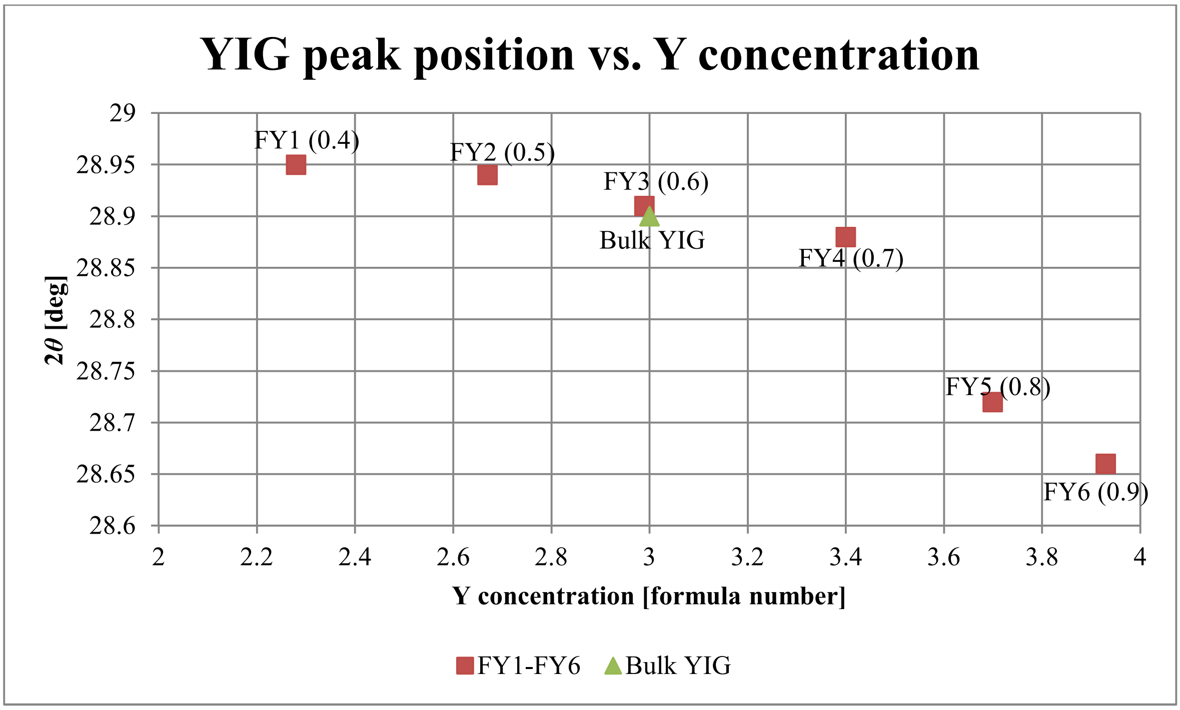

Figure 7.4.6. Variation of YIG (400) peak position with Y concentration. The number in parentheses is the target ablation ratio.

As a final experiment, a Fe-overstoichiometric YIG target was purchased and ablated in the single-PLD chamber with the KrF laser under optimum conditions for YIG growth (see Table 6.4.1). The film featured a composition close to stoichiometric YIG ($Y_{3.04}Fe_{4.96}O_{12}$), a red colour, a uniform, but hazy and rough surface ($S_q \approx 85$ nm) and a broad FMR linewidth ($\Delta H \approx 11.65$ mT), everything in line with the results from the multi-PLD experiments, confirming that the worsening of YIG film properties is closely related to its composition and not due to an interaction of the plumes from the co-ablated targets. However, plume interaction is unlikely, considering the random delay between asynchronous laser pulses, which, from a statistical point of view, is likely to be higher than ~200 μs, the threshold below which plume interaction is observed to affect film growth [6, 7].

7.4.2. YFO GROWTH

Co-ablating the Y_2O_3 and Fe_2O_3 targets with the same laser repetition frequency (f_{KrF} = $f_{\mathrm{Nd:YAG}}$ =10 Hz), at the same deposition conditions as in Table 6.4.2 and with the same laser fluences as stated in Section 7.4.1 ($F_{\mathrm{KrF}} \approx 1.1$ J/cm^2 and $F_{\mathrm{Nd:YAG}} \approx 1.2$ J/cm^2), and using *c*-cut sapphire (α-Al_2O_3) as substrate resulted in the growth of a polycrystalline stoichiometric $YFeO_3$ film: Figure 7.4.7 shows the XRD pattern of this sample, where the highest sharp peak is due to the sapphire substrate, whereas the smaller ones are assigned to $YFeO_3$ phases with different orientations.

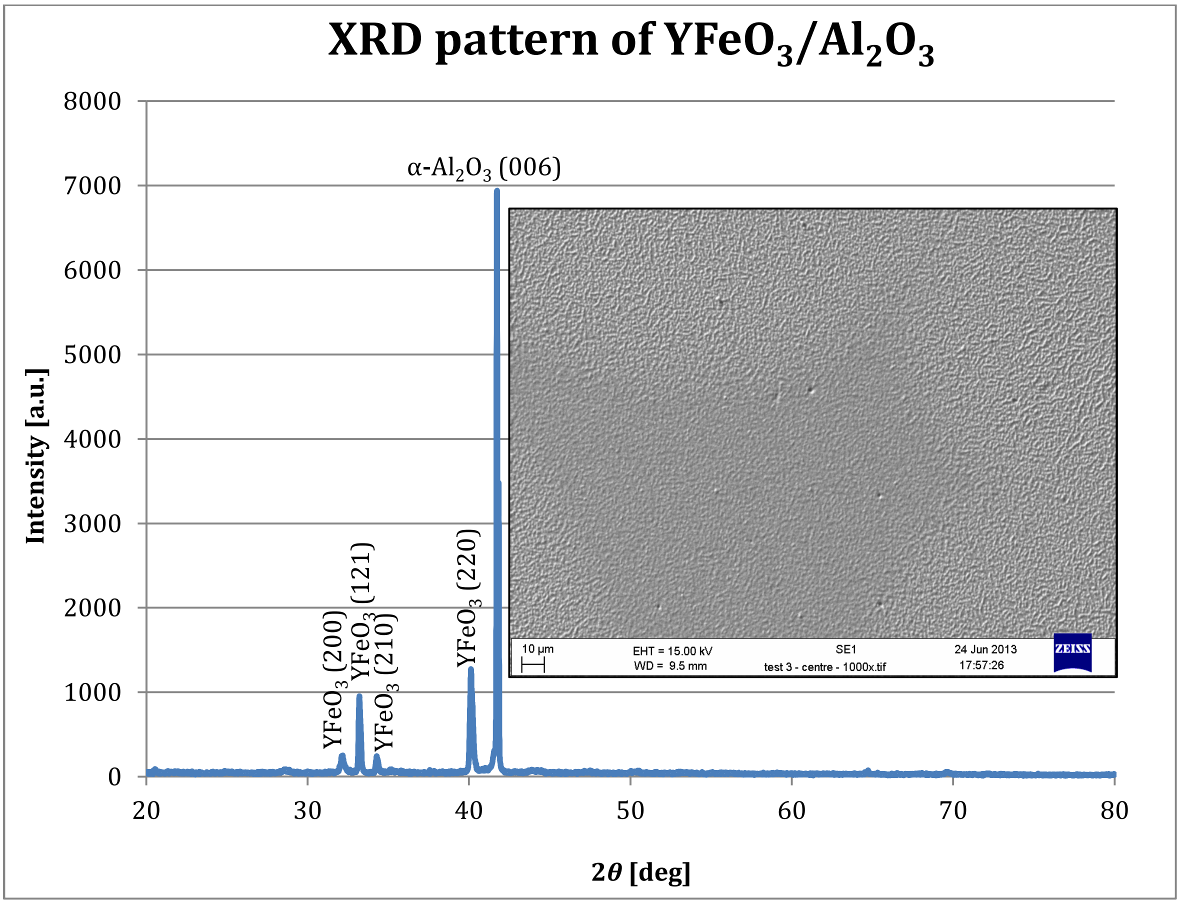

Figure 7.4.7. XRD pattern of polycrystalline stoichiometric $YFeO_3$ film grown on *c*-cut sapphire (α-Al_2O_3). The inset shows a SEM picture of the film surface.

FMR analysis showed that the film has got an FMR linewidth of 70.28 mT, which is large, compared to typical FMR linewidth from YIG; however, it must be considered that the film is polycrystalline and that $YFeO_3$ is a canted anti-ferromagnetic crystal with a weak ferrimagnetic behaviour. In fact, a slight off-stoichiometry (~7%) observed in another YFO film, grown while trying to optimise the laser fluence to produce stoichiometric $YFeO_3/Al_2O_3$, was enough to impede observation of FMR absorption, thus suggesting a relatively good crystal quality of the stoichiometric YFO film.

The YFO films are not uniform, but partly red/pink and partly orange/yellow, featuring a rough appearance, as shown also in the SEM picture included in Figure 7.4.7, and particulate hiding a network of micro-cracks, visible by optical microscopy. This and the polycrystalline structure of the film are likely due to the lattice and TEC-mismatch with the substrate: unlike YIG and YAG, which are both cubic crystals with a lattice mismatch of $\Delta a/a_{\mathrm{YAG}} \approx 3.1\%$, YFO is an orthorhombic perovskite [8] with lattice constants a_{YFO} = 0.5593 nm, b_{YFO} = 0.7604 nm and c_{YFO} = 0.5282 nm, whereas sapphire can be described as either rhombohedral or hexagonal [9, 10] with lattice parameters $a_{\mathrm{Al2O3}} = b_{\mathrm{Al2O3}}$ = 0.4785 nm and c_{Al2O3} = 1.2991 nm; as for TECs, $\rho_{\mathrm{YFO}} = -1.72\times10^{-6}$ K^{-1} at $T < 593$ K and $\rho_{\mathrm{YFO}} = 2.28\times10^{-6}$ K^{-1} at $T > 593$ K, whereas $\rho_{\mathrm{Al2O3},//} = 6.66\times10^{-6}$ K^{-1} parallel to optical axis and $\rho_{\mathrm{Al2O3},\perp} = 5\times10^{-6}$ K^{-1} perpendicular to optical axis. As explained in Section 3.2.3.4, it is probably the TEC-mismatch and, in this particular case, the change of sign in the TEC of YFO to cause the cracking of the sample. Epitaxial growth of YFO may be performed on better lattice-matched substrate to improve its properties.

7.5. CONCLUSIONS

This chapter covered the multi-PLD growth of YIG. Compositional tuning by co-ablation of YIG and Fe_2O_3 was examined in Section 7.2, in order to study the compensation of Fe-deficiency and its effects on the properties of YIG films (colour and appearance, surface roughness and morphology, crystallinity, FMR and optical transmission). The experiments showed that the choice of lasers for target ablation is important: ablation of Fe_2O_3 with the Nd:YAG laser produces smoother and more uniform YIG films, with narrower FMR linewidth than YIG samples grown ablating the Fe_2O_3 target with the KrF laser. However, in both cases, the compensation of Fe-deficiency did not improve the properties of YIG, but actually the films became darker, surface roughness increased, optical transmission became worse and FMR linewidth broadened with increasing Fe concentration.

Conversely, an increase in Y concentration was thought to improve ferromagnetic properties of YIG; however the multi-PLD experiments carried out co-ablating YIG and Y_2O_3 target, as described in Section 7.3, showed a broadening of FMR linewidth also with increasing Y concentration, until FMR disappeared completely when the film became amorphous and orange in colour.

The experiments described in Section 7.4 demonstrated that it is possible to grow different materials (e.g. YIG and YFO) by multi-PLD of their precursors (Y_2O_3 and Fe_2O_3), choosing appropriate substrates and adjusting the target ablation ratio accordingly to the desired composition. The results of multi-PLD of YIG described in the sub-section 7.4.1 agree with those reported in the previous sections and with that obtained by ablation of a Fe-rich YIG target in the single-PLD chamber under optimum deposition conditions, thus confirming that it is the variation of composition in YIG films to induce the change in the other properties (colour, appearance, crystallinity, surface roughness and morphology, optical transmission and FMR) and not something related to target co-ablation (e.g. plume interaction). The optimum composition of YIG films in terms of FMR (minimum FMR linewidth) is estimated as: $Y_{3.5}Fe_{4.5}O_{12}$. The worsening of FMR linewidth with composition diverging from this optimum value may be due to a direct effect or indirect through a change in crystallinity and/or lattice constant, affecting the film strain and magnetic properties.

7.6. REFERENCES

1. S. A. Manuilov, R. Fors, S. I. Khartsev, and A. M. Grishin, "Submicron $Y_3Fe_5O_{12}$ Film Magnetostatic Wave Band Pass Filters," J. Appl. Phys. **105**, 033917 (2009).

2. R. Swanepoel, "Determination of the thickness and optical-constants of amorphous-silicon," J. Phys. E-Sci. Instr. **16**, 1214-1222 (1983).

3. W. R. Eppler, and M. H. Kryder, "Garnets for short-wavelength magnetooptic recording," J. Phys. Chem. Solids **56**, 1479-1490 (1995).

4. V. R. Sobol, T. V. Volchik, S. M. Arabei, B. V. Korzun, and N. A. Kalanda, "Optical constants of yttrium-iron garnet single-crystal film structures," J. Appl. Spectrosc. **76**, 203-208 (2009).

5. S. H. Wemple, S. L. Blank, J. A. Seman, and W. A. Biolsi, "Optical properties of epitaxial iron garnet thin films," Physical Review B **9**, 2134-2144 (1974).

6. K. A. Sloyan, T. C. May-Smith, R. W. Eason, and J. G. Lunney, "The effect of relative plasma plume delay on the properties of complex oxide films grown by multi-laser, multi-target combinatorial pulsed laser deposition," Appl. Surf. Sci. **255**, 9066-9070 (2009).

7. C. Sanchez-Ake, R. Camacho, and L. Moreno, "Deposition and composition-control of Mn-doped ZnO thin films by combinatorial pulsed laser deposition using two delayed plasma plumes," J. Appl. Phys. **112**, 044904 (2012).

8. H. Shen, J. Y. Xu, A. H. Wu, J. T. Zhao, and M. L. Shi, "Magnetic and thermal properties of perovskite $YFeO_3$ single crystals," Mater. Sci. Eng. B-Adv. Funct. Solid-State Mater. **157**, 77-80 (2009).

9. "MolTech GmbH sapphire datasheet," http://www.mt-berlin.com/frames_cryst/descriptions/sapphire.htm, Accessed December 2013.

10. A. A. Anderson, "Crystalline planar waveguide lasers fabricated by pulsed laser deposition," PhD thesis at *Optoelectronics Research Centre*(University of Southampton, Southampton, 1998).

8. CHAPTER 8
MULTI-PLD OF BI:YIG

8.1. INTRODUCTION

Faraday rotation in magneto-optic garnets can be increased by substituting the yttrium (Y) in the YIG lattice with bismuth (Bi): it has already been demonstrated that the Verdet constant in Bi:YIG films increases with increasing Bi concentration (from V = 60.4 deg/(T×µm) for $Bi_1Y_2Fe_5O_{12}$ to V = 160 deg/(T×µm) for $Bi_2Y_1Fe_5O_{12}$ at λ = 500 nm) [1]. There are several reports of PLD growth of Bi:YIG and fully-substituted BIG films by ablation of a single target [1-19], mostly on GGG substrates. This chapter describes the investigation of Bi:YIG and BIG growth by multi-PLD of Bi_2O_3 and either YIG (Section 8.2) or Fe_2O_3 (Section 8.3).

8.2. MULTI-PLD OF BI_2O_3 AND YIG

When growing films containing Bi, the melting points of metallic Bi ($T_{m,\ Bi} \approx 545$ K) and of its oxide ($T_{m,\ Bi2O3} \approx 1090$ K) must be taken into account; moreover the depression of melting points of materials in thin-film form must be considered too. A substrate temperature higher than $T_{m,\ Bi2O3}$ will tend to boil off both Bi and Bi_2O_3 species impinging on the substrate.

The growth conditions reported in Table 6.4.2 were used, with the YIG target ablated by the Nd:YAG laser ($F_{Nd:YAG} \approx 1.1$ J/cm^2 and $f_{Nd:YAG} = 10$ Hz) and the Bi_2O_3 target ablated by the KrF laser ($F_{KrF} \approx 2.1$ J/cm^2). Attempts at growing Bi_2O_3 tester samples on *c*-cut sapphire resulted in no film growth at temperatures $T \geq 1000$ K: although optical microscopy and profilometry revealed the presence of particulates scattered across the substrate surface, no film was revealed by stylus profiler and XRD analysis. Room temperature (RT) allowed the growth of Bi_2O_3 on sapphire at a high deposition rate (~0.21 nm/pulse), but with an amorphous phase, as revealed by XRD analysis (no diffraction peak between $2\theta = 20°$ and $80°$) of a ~15 µm-thick film grown in 1 hour at 20 Hz.

Following these first trials, Bi:YIG growth was tried on YAG (100) substrates over a wide range of substrate temperatures, from RT up to the maximum $T \approx 1150$ K, fixing the KrF laser repetition rate at 1 Hz for most depositions: the results are summarised in Table 8.2.1, where pure YIG samples PY1 (N3), PY4 and PY5, grown under the same conditions as BY1a, BY4 and BY5a respectively, are listed for reference. Samples BY1b and BY5b were grown under the same conditions as BY1a and BY5a respectively, with the KrF laser set at f_{KrF} = 2 Hz. The substrate temperatures reported in Table 8.2.1 are estimated as described in Section 4.2.4.3 and should not be taken as definitive: there is likely an error of ±25 K.

ID	***T* [K]**	**f_{KrF} [Hz]**	**ΔH [mT]**	**S_q [nm]**	**Bi [formula number]**	**Y [formula number]**	**Fe [formula number]**	**Sample colour**
PY1	1150	0	4.67	2.3	0.00	3.37	4.63	Yellow
BY1a	1150	1	6.18	19.4	0.07	3.32	4.61	Yellow
BY1b	1150	2	6.23	17.1	0.13	3.27	4.60	Yellow
BY2	1050	1	7.95	1.7	0.07	3.36	4.57	Yellow
BY3	1000	1	9.96	27.4	0.06	3.27	4.66	Yellow
PY4	950	0	19.24	5.1	0	3.31	4.69	Yellow
BY4	950	1	13.20	1.2	0.22	3.20	4.57	Yellow
PY5	900	0	23.46	3.6	0	3.29	4.71	Dark yellow
BY5a	900	1	8.79	0.6	0.22	3.45	4.32	Yellow
BY5b	900	2	10.41	0.9	0.30	3.33	4.38	Yellow
BY6	875	1	12.22	3.2	0.30	3.28	4.42	Yellow
BY7	850	1	54.53	2.6	1.49	3.04	3.47	Dark yellow
BY8	750	1	–	2.0	2.94	2.14	2.91	Orange/red
BY9	300	1	–	0.9	3.16	1.96	2.88	Black/red

Table 8.2.1. Deposition conditions, FMR linewidth (ΔH), RMS surface roughness (S_q), composition and colour of Bi:YIG samples BY1-BY9 and of pure YIG samples PY1, PY4 and PY5, used as a reference.

All samples have a RMS surface roughness $S_q < 10$ nm, except for BY1a, BY1b and BY3. All Bi:YIG films grown at temperature $T \geq 875$ K feature the yellow colour typical of Fe-deficient YIG samples, whereas the reference YIG sample PY5 is dark yellow at $T \approx 900$ K. At $T \approx 850$ K the Bi:YIG film colour becomes darker and then orange with a red tint at $T \approx 750$ K. The sample grown at RT (~300 K), although showing good specular reflection, in transmission appears black with a faint red tint (effectively zero transmission). As already shown in Chapter 6, the film colour is an indicator of crystal quality. XRD analysis showed that Bi:YIG samples BY1-BY6 only have crystalline YIG (100) peaks, whereas the XRD pattern of BY7 (shown in Figure 8.2.1) features two distinct BIG and YIG peaks, respectively at $2\theta \approx 28.24°$ and $2\theta \approx 28.86°$. BY8 shows no evidence of any garnet phase, with only a peak at $2\theta \approx 29.2°$, attributable to (111)-oriented Y_2O_3 (shown via the (222) peak, as in Figure 8.2.1); BY9 does not show any crystalline phase, as no diffraction peaks are observed in its XRD pattern, except for those attributable to the YAG substrate. Table

8.2.2 shows the database peak positions for BIG (400), YIG (400), YAG (400) and Y_2O_3 (222) for reference.

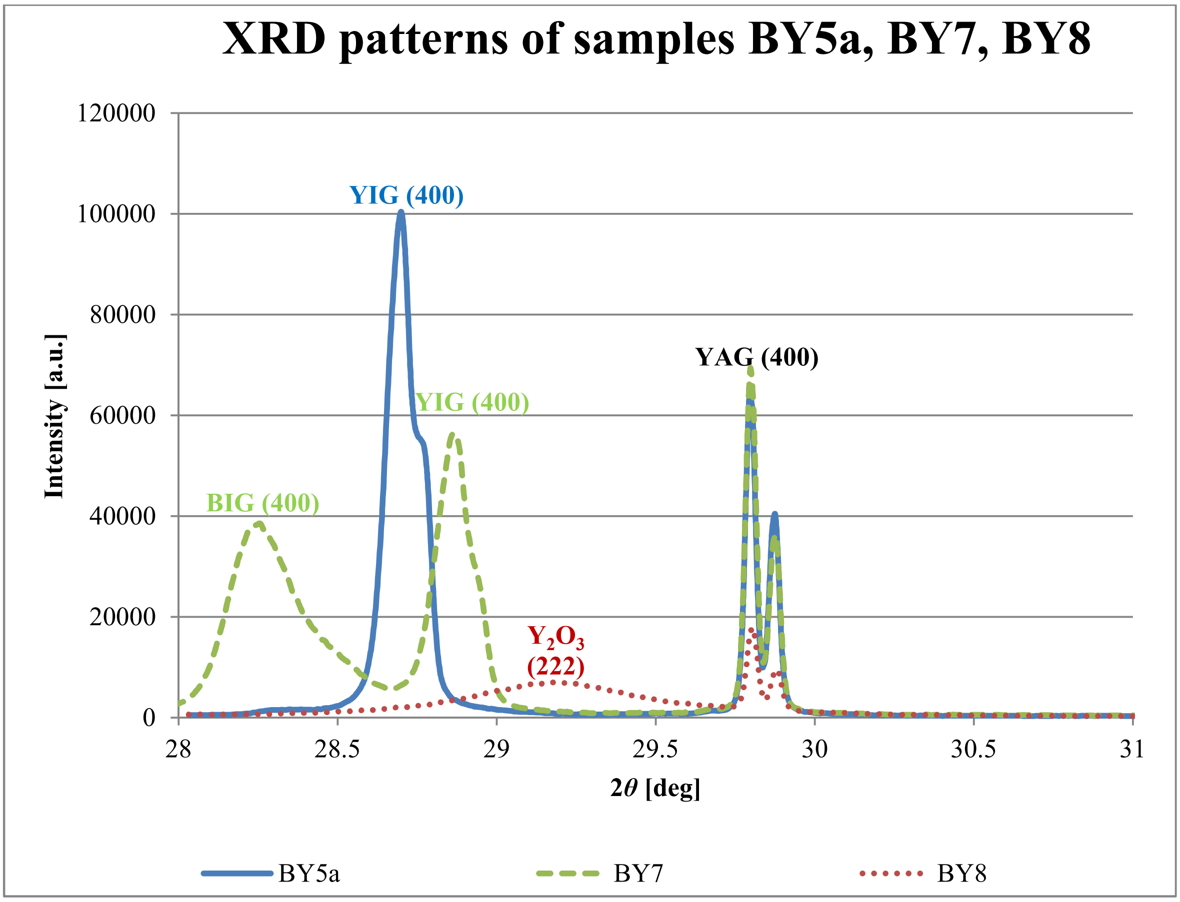

Figure 8.2.1. Comparison of XRD patterns of BY5a, BY7 and BY8.
Peak doublets are due to Cu-$K_{\alpha2}$ radiation present in the diffractometer.

XRD peak:	BIG (400)	YIG (400)	YAG (400)	Y_2O_3 (222)
Database peak position:	28.22°	28.90°	29.80°	29.20°
Reference:	[20]	[21]	[22]	[23]

Table 8.2.2. Database peak positions for BIG, YIG and YAG (100) phases and Y_2O_3 (111) and their references.

XRD analysis of samples BY1-BY6, grown at $T \geq 875$ K, showed a shift of the YIG peak position with changing substrate temperature, as shown in Figure 8.2.2: while the XRD patterns of pure YIG samples PY1, PY4 and PY5 feature a YIG (400) peak at roughly the same diffraction angle (~28.87°), the YIG (400) peak in Bi:YIG films tends to shift towards lower diffraction angles with decreasing substrate temperature, meaning an increase in lattice constant.

Figure 8.2.3 shows the variation of film composition for Bi:YIG samples grown at $f_{\mathrm{KrF}} = 1$ Hz with substrate temperature. The film composition changes dramatically with temperature and a transition region is clearly observed around $T \approx 850$ K, the same range of substrate temperature where the change in crystallinity is observed, as discussed above.

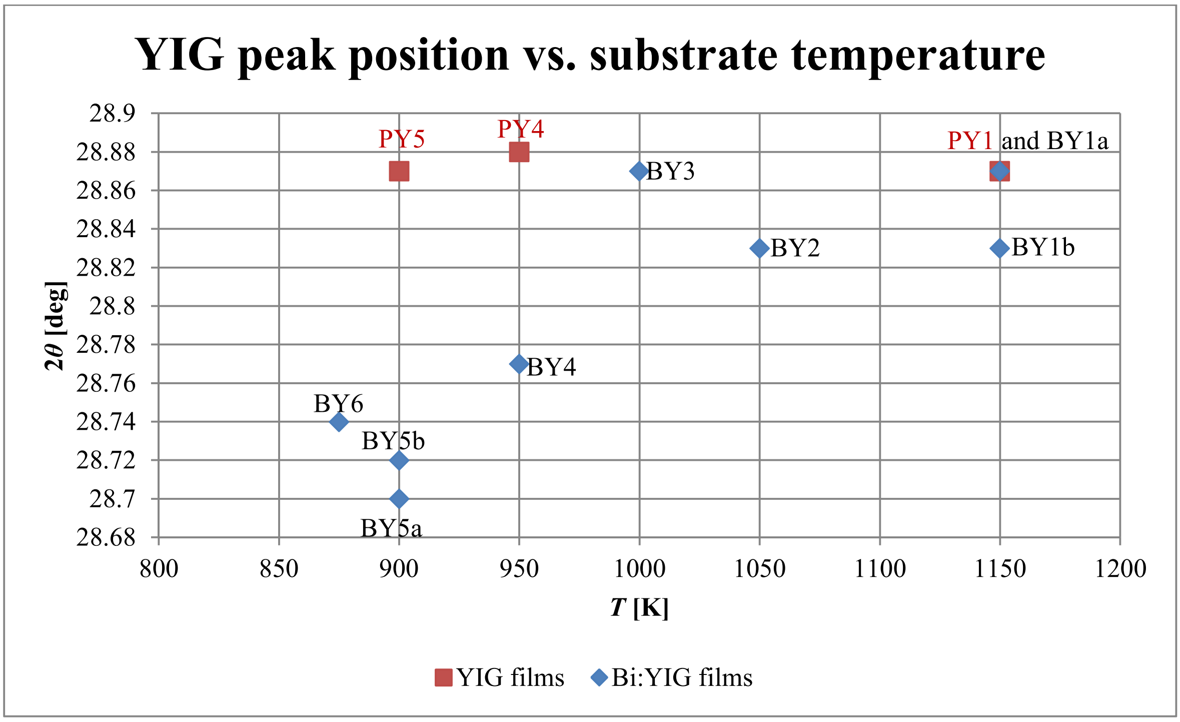

Figure 8.2.2. Trend of YIG (400) peak position in the XRD patterns of YIG and Bi:YIG films with substrate temperature.

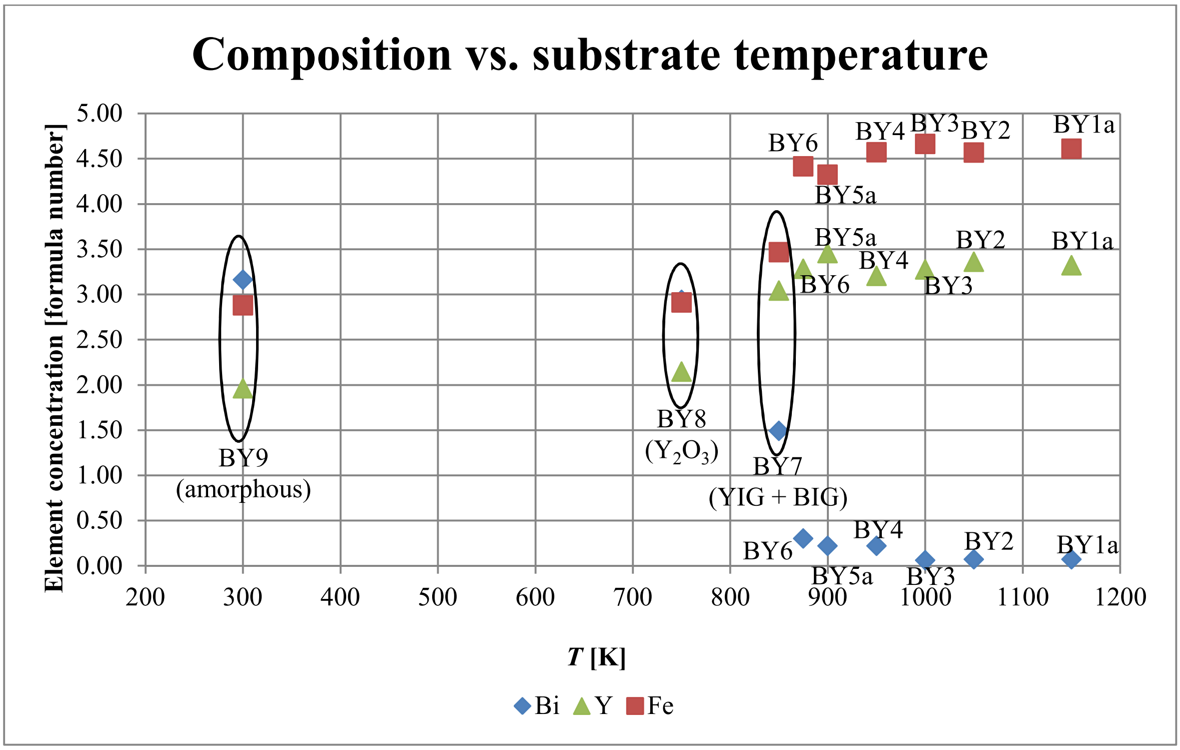

Figure 8.2.3. Trend of composition with substrate temperature. The samples highlighted with an ellipse have peculiar crystallinity, as show in this figure and in Figure 8.2.1.

Figure 8.2.4 shows the trend of FMR linewidth with substrate temperature: as already found in Section 6.2.3 for pure YIG films grown by PLD with the KrF laser, FMR linewidth tends to increase with decreasing temperature, but more slowly for Bi:YIG films, compared to pure YIG (PY1, PY4 and PY5); also, at a temperature $T \approx 900$ K there appears to be a local minimum for FMR linewidth, as opposed to the values for YIG, where the lowest value is at $T \approx 1150$K and increases steadily with decreasing temperature.

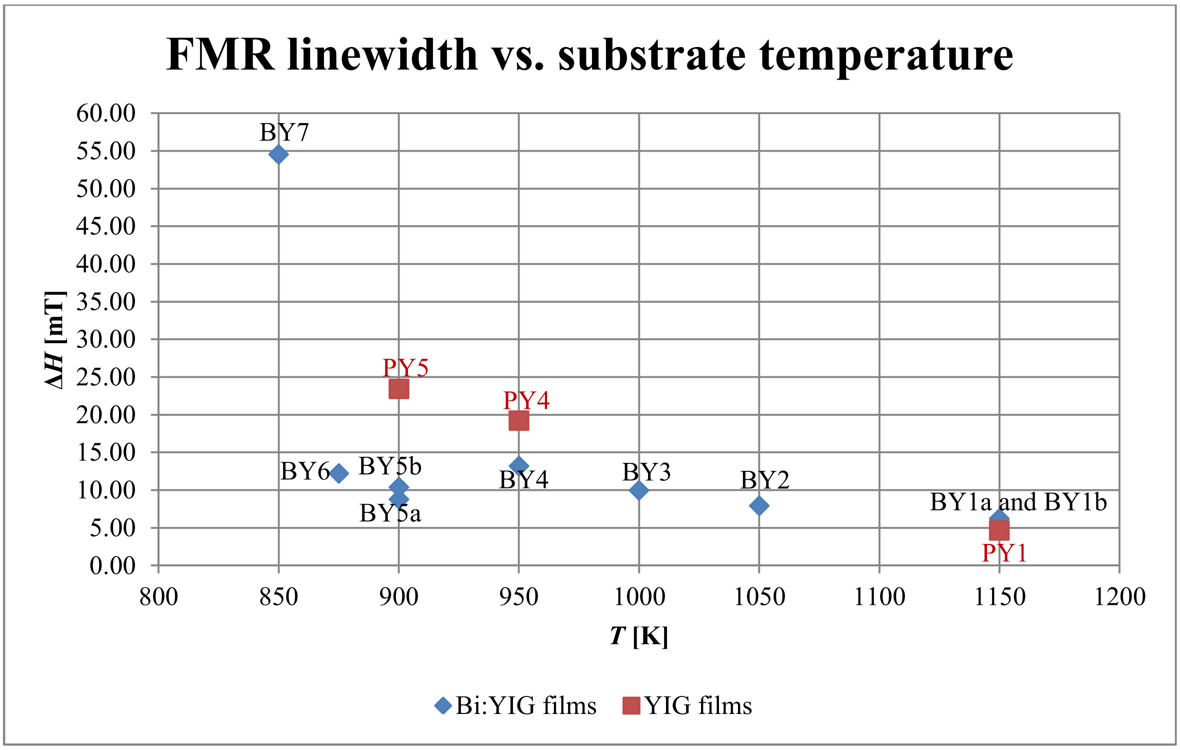

Figure 8.2.4. Trend of FMR linewidth with substrate temperature.

The observed phenomena require further discussion to try to identify the primary cause of change of YIG properties with substrate temperature, Bi concentration and crystallinity. At very high temperatures ($T \geq 1000$ K) only a small fraction of the bismuth present within the plume is incorporated into the final garnet structure, because of re-evaporation from the hot surface of the sample, resulting in a very low doping level (~0.07 formula units – see Table 8.2.1), which causes a small change in lattice constant (see Figure 8.2.2), due to the larger ionic radius of Bi, compared to Y. This doping level is also too low to cause a significant change in magnetic properties and FMR linewidth ΔH initially increases with decreasing temperature (see Figure 8.2.4), as already observed in Section 6.2.3 for YIG films. At $T \approx (900 - 950)$ K the Bi doping increases by a factor of ~3 (~0.22 formula units – see Table 8.2.1), suggesting that the substrate temperature is closer to the melting point of Bi_2O_3 in thin-film form, and the lattice constant increases accordingly (as seen in the large YIG (400) peak shift in Figure 8.2.2, ~0.17° between BY5a and BY1a); it is at $T \approx$ 900 K (BY5a) that the local minimum of $\Delta H(T)$ is observed and this can be explained with the change in YIG film properties with Bi doping. Also, these results agree with previous findings in the literature of PLD growth of Bi:YIG by single-PLD, where optimum growth temperatures of ~900 K for Bi:YIG on GGG [24, 25] and ~1100 K for YIG on GGG [25-27] are reported.

Two factors can be taken into account to explain the change in the FMR linewidth trend with substrate temperature:

1. a direct change of magnetic properties of YIG with Bi doping;
2. an indirect effect of Bi doping on magnetic properties via a change in crystallinity.

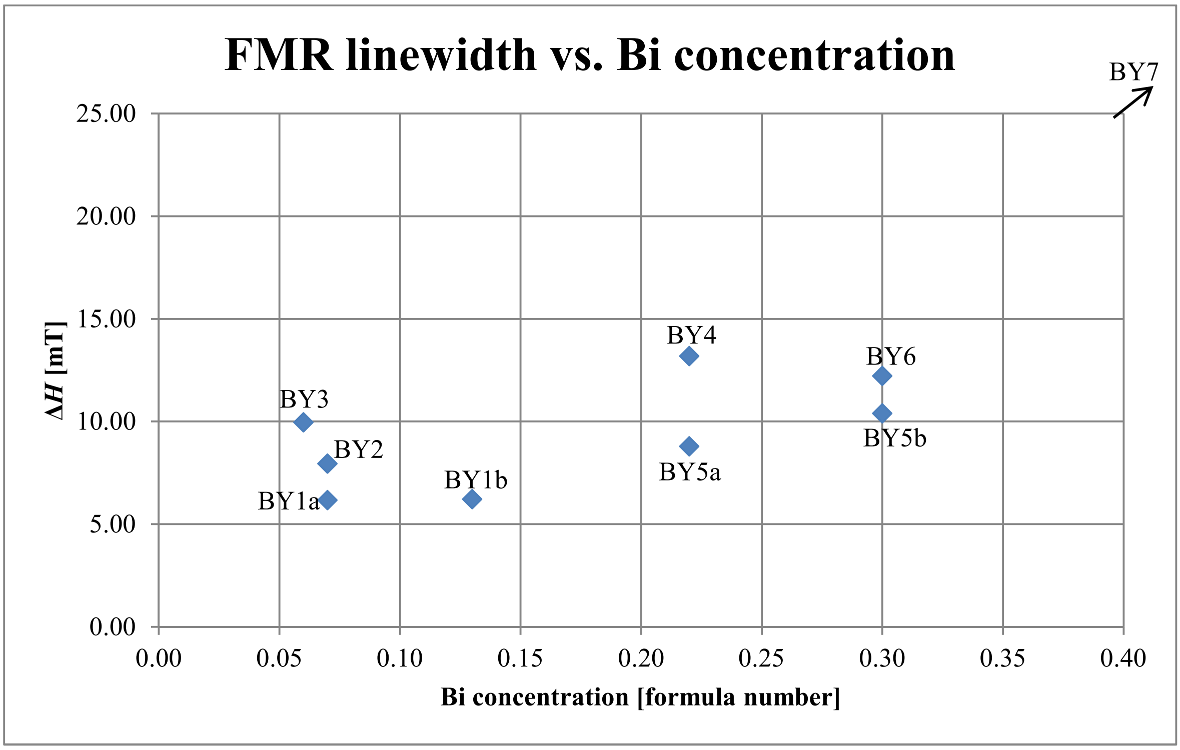

Figure 8.2.5. Trend of FMR linewidth with Bi concentration.

Regarding the first aspect of Bi inclusion, Figure 8.2.5 shows the variation of FMR linewidth with Bi concentration: although there is an increase of FMR linewidth with Bi concentration, the trend is not systematic (e.g. the Bi doping of BY3 is one fifth that of BY5b, but they have roughly the same FMR linewidth, $\Delta H \approx 10$ mT); also, there is no significant change in FMR linewidth ($\Delta H \approx 6.2$ mT), when doubling the KrF laser repetition rate (f_{KrF}) and thus the Bi concentration at $T \approx 1150$ K (BY1a and BY1b – see Table 8.2.1 and Figure 8.2.4 and Figure 8.2.5). Also, when doubling f_{KrF} at $T \approx 900$ K (samples BY5a and BY5b), the Bi concentration increases by ~36%, but the FMR linewidth increases by ~18% (see Table 8.2.1, Figure 8.2.4 and Figure 8.2.5), meaning that Bi doping has a more dramatic role when it reaches a level > 0.2 formula units.

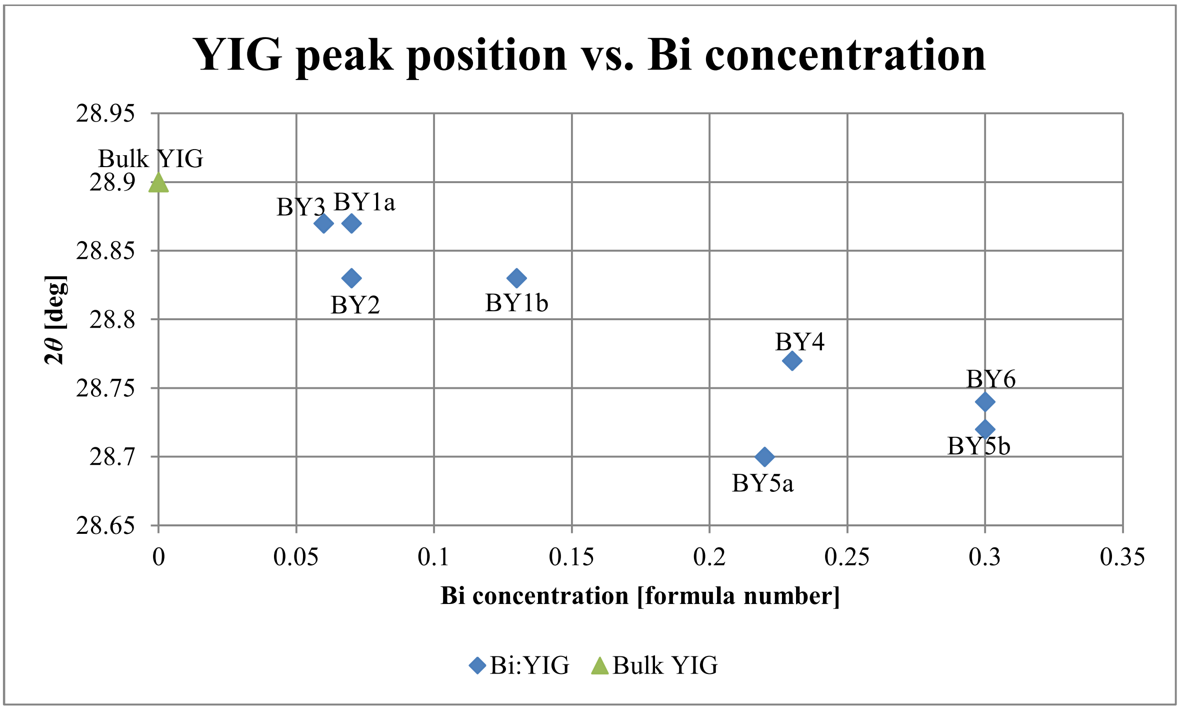

Figure 8.2.6. Trend of YIG (400) peak position with Bi concentration.

On the other hand, the second factor is reinforced by a clear change in YIG (400) peak position with changing temperature (see Figure 8.2.2) and by the decreasing trend of YIG (400) peak position (i.e. an increase in lattice constant) with increasing Bi concentration, shown in Figure 8.2.6, as expected from theory, due to the larger ionic radius of Bi^{3+} (117 pm) compared to Y^{3+} (104 pm) [28]. While the change in YIG peak position and lattice constant is clearly due to Bi doping, no change in YIG peak position with temperature is observed in pure YIG films (see Figure 8.2.2); however, at very high temperature ($T \geq$ 1000 K) the deterioration of crystal quality has a stronger effect than that of Bi doping (quite low, ~0.07 formula units), which instead prevails only at $T \approx 900$ K – BY5a, and the observed local minimum of $\Delta H(T)$. A further decrease in temperature causes further deterioration of crystal quality, until at $T \approx 850$ K the substrate temperature probably reaches the depressed melting point of Bi_2O_3 ($T_{m,\ Bi2O3}$) and Bi concentration increases abruptly at 1.49 formula units, whereas both Y and Fe concentration decrease (see BY7 in Table 8.2.1 and Figure 8.2.3): this is the most likely cause of the formation of two separate BIG and YIG phases in the film (BY7 in Figure 8.2.1), which are detrimental for magnetic properties (see point BY7 in Figure 8.2.4). Further decrease in substrate temperature ($T \approx$ 750 K) will lead to the growth of an yttria phase (see BY8 in Figure 8.2.1) heavily doped with Bi and Fe, at similar concentrations (~3 formula units – see BY8 in Figure 8.2.3). The completely different crystal phase produces no magnetic properties and no FMR absorption. Growth at RT results in an amorphous film (BY9) with composition similar to BY8 and again no FMR.

To sum up, there is a complex interplay between substrate temperature (*T*), Bi concentration (Bi conc.), YIG peak position (2θ), crystal quality and FMR linewidth (ΔH), whose general trends are summarised schematically in Figure 8.2.7.

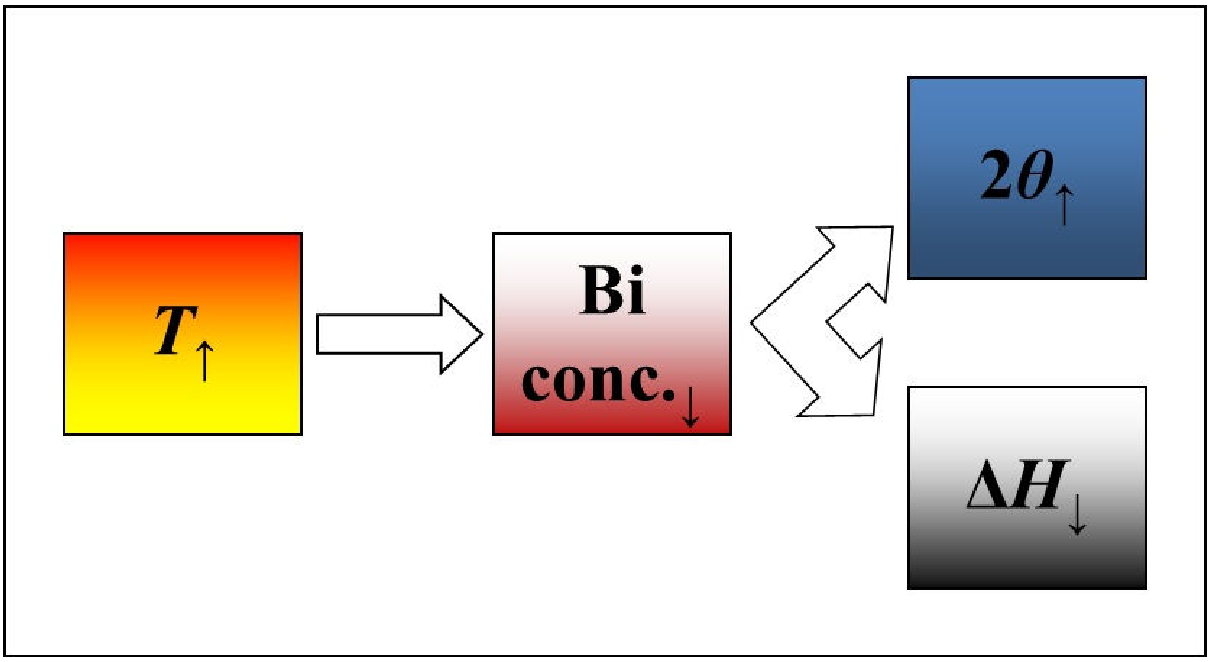

Figure 8.2.7. Schematic of the interplay between substrate temperature (*T*), Bi concentration (Bi conc.), YIG peak position (2θ) and FMR linewidth (ΔH) in the multi-PLD growth of Bi:YIG.

Finally a highly doped Bi:YIG film was grown using a substrate temperature $T \approx 900$ K, considered as a compromise between Bi-doping level and crystalline and magnetic properties. Setting the KrF laser repetition rate at $f_{\mathrm{KrF}} = 10$ Hz resulted in a heavily doped Bi:YIG film, with a composition of $Bi_{2.38}Y_{2.81}Fe_{2.81}O_{12}$, showing a strong Fe deficiency and a low Y-substitutional level, suggesting that Bi is probably substituting Fe rather than Y, as already observed in BY7-BY9. The film featured also an XRD pattern similar to that of BY7, with two separate YIG and BIG peaks, and an FMR linewidth $\Delta H \approx 47.76$ mT. This eventually suggests that Bi doping level plays a big role: if excessive and substituting for Fe instead of Y, it causes the formation of different crystalline phases, which results in a large broadening of FMR linewidth.

8.3. MULTI-PLD OF BI_2O_3 AND FE_2O_3

Multi-PLD of pure BIG was attempted by co-ablation of Bi_2O_3 and Fe_2O_3. The deposition conditions reported in Table 6.4.2 were used, with the exception of different substrate temperatures; the Fe_2O_3 target was ablated by the Nd:YAG laser ($F_{\mathrm{Nd:YAG}} \approx 1.1$ J/cm^2 and $f_{\mathrm{Nd:YAG}} = 10$ Hz) and the Bi_2O_3 target ablated by the KrF laser, set at $F_{\mathrm{KrF}} \approx 1.1$ J/cm^2.

Firstly, a 2 µm-thick BFO tester film was grown in 2 hours on a *c*-cut sapphire substrate, heated up to $T \approx 900$ K, with a target ablation ratio $r = f_{\mathrm{KrF}}/f_{\mathrm{Nd:YAG}} = 1$, i.e. with both lasers set at the same pulse repetition rate (10 Hz). XRD analysis showed that the film is polycrystalline BFO with (1 0 -1) or equivalent preferential orientation, as can be inferred from the diffraction pattern in Figure 8.3.1, though one of the minor peaks was not identified.

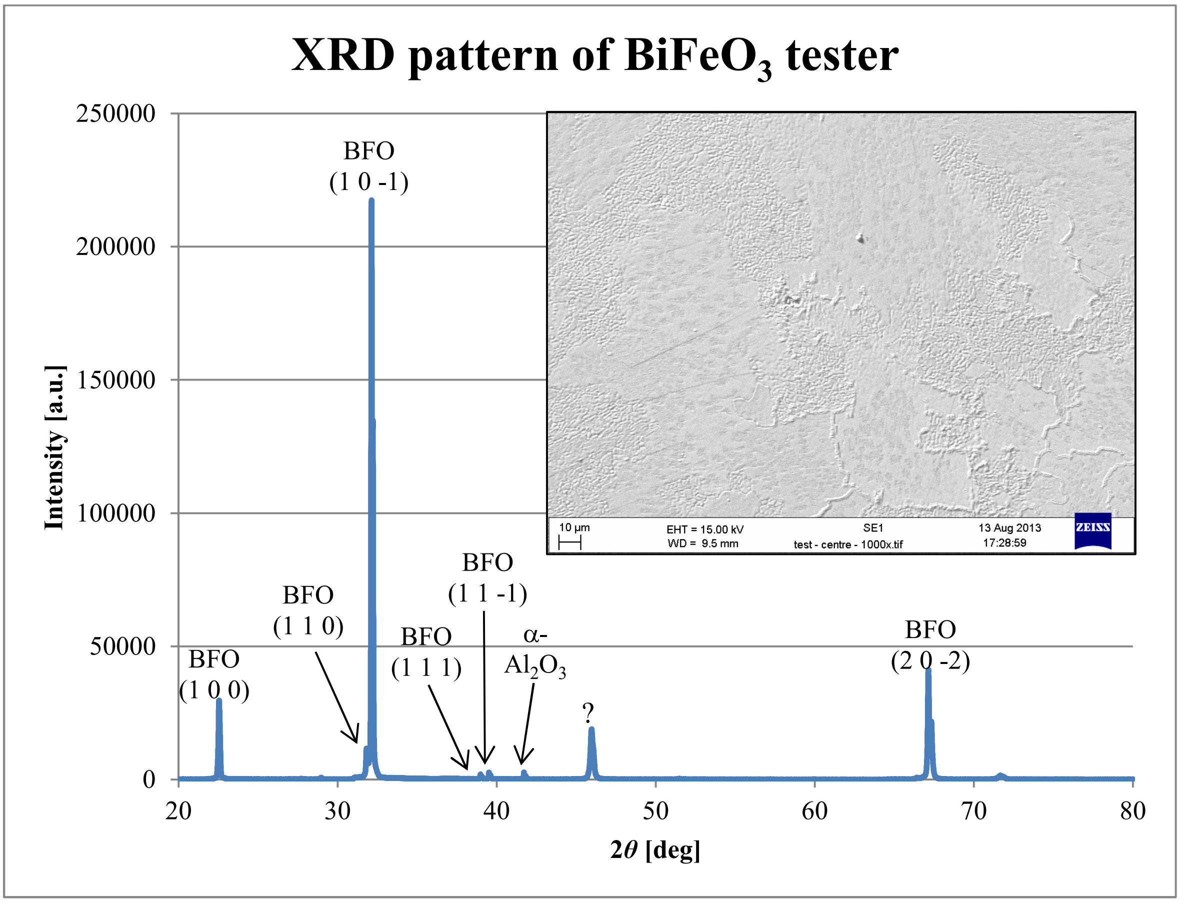

Figure 8.3.1. XRD pattern of the BFO tester film. – The inset shows a SEM picture of the film surface.

The surface of the BFO film appears rough ($S_q \approx 30.6$ nm) and non-uniform, as visible also at microscopic level by SEM analysis (see picture in the inset of Figure 8.3.1). This may be due to the high lattice mismatch ($\Delta a/a_{\mathrm{SUB}} \approx 17.6\%$) and to the fact that BFO is a rhombohedrally distorted perovskite [29] ($a_{\mathrm{BFO}} = b_{\mathrm{BFO}} = 0.558$ nm, $c_{\mathrm{BFO}} = 1.390$ nm in the hexagonal setting at RT), whereas sapphire has a rhombohedral or hexagonal structure [30, 31] ($a_{\mathrm{Al2O3}} = b_{\mathrm{Al2O3}} = 0.4785$ nm and $c_{\mathrm{Al2O3}} = 1.2991$ nm in the hexagonal setting at RT); TEC-mismatch may play a role too, with TEC of BFO non completely linear, nor isotropic with values $\rho_{\mathrm{BFO}} \approx (6.5 - 13)\times10^{-6}$ K^{-1} and TECs of sapphire $\rho_{\mathrm{Al2O3},//} = 6.66\times10^{-6}$ K^{-1} parallel to optical axis and $\rho_{\mathrm{Al2O3},\perp} = 5\times10^{-6}$ K^{-1} perpendicular to optical axis. However, what is important for our purposes is that the film composition is close to stoichiometric, as confirmed by EDX: $Bi_{1.02}Fe_{0.98}O_3$, thus suggesting that laser fluences were correctly tuned to grow BFO at $r = 1$ and BIG at $r = 0.6$ at this substrate temperature ($T \approx 900$ K).

The first attempt (sample BF1) to grow a BIG film with $r = 0.6$ and $T \approx 900$ K resulted in a non-uniform surface with an orange/red colour and some blue dots scattered across it. SEM/EDX analysis revealed the presence of slightly shallower areas in the centre of the sample, as shown in Figure 8.3.2, where the dark (shallower) areas are Bi-deficient ($Bi_{0.61}Fe_{7.39}O_{12}$), whereas the light grey region has a composition close to BIG: $Bi_{2.79}Fe_{5.21}O_{12}$. However, XRD analysis showed diffraction peaks at $2\theta \approx 31.84°$ and $2\theta \approx 32.15°$, which can be assigned respectively to BFO with (110) and (1 0 -1) orientations or equivalent.

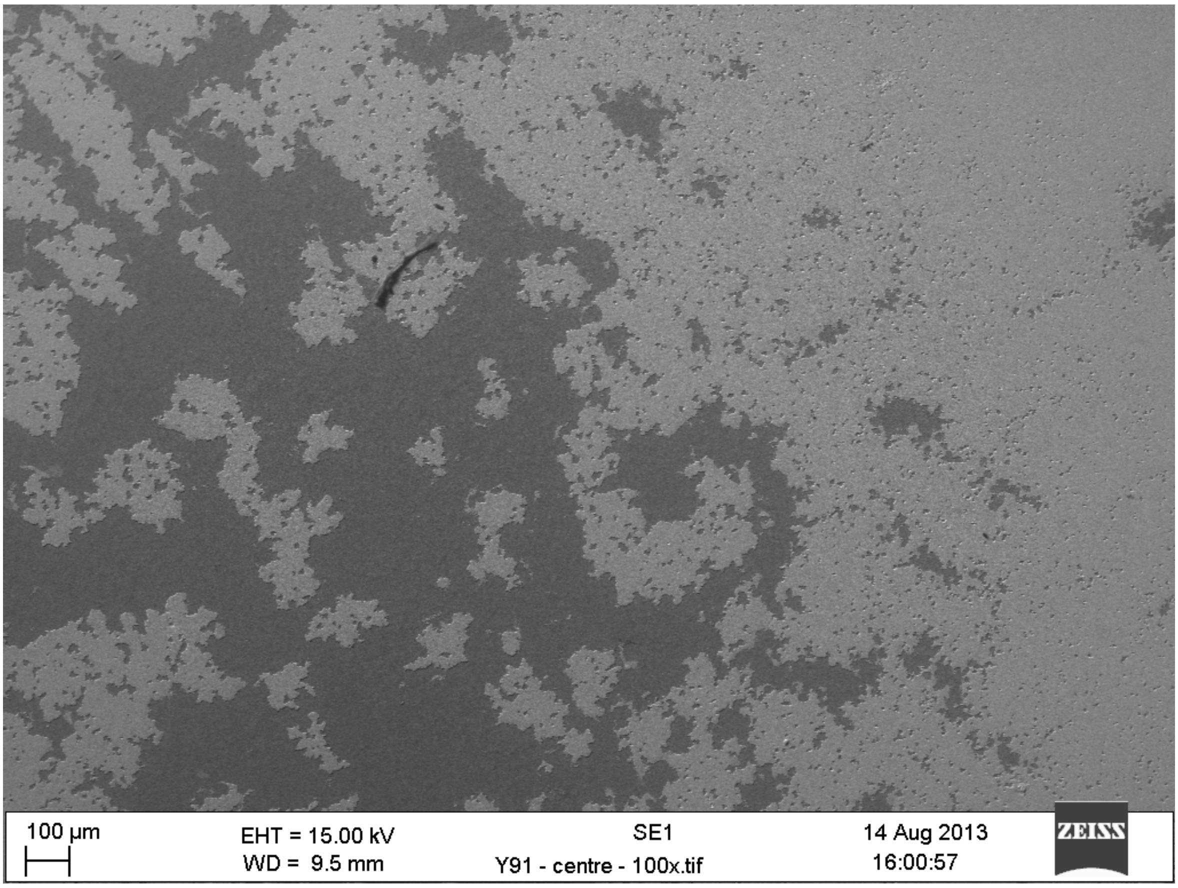

Figure 8.3.2. SEM picture of the surface of sample BF1.

Further attempts were performed under different conditions, as summarised in Table 8.3.1. No FMR absorption was observed in any sample. XRD patterns are shown in Figure 8.3.3.

ID	*T* [K]	*r*	S_q [nm]	Bi [formula number]	Fe [formula number]	Bi/Fe	Sample colour
BF1	900	0.6	285.3	2.79	5.21	0.54	Red/orange
BF2	950	0.6	32.9	0.06	7.94	0.008	Dark red
BF3	850	0.6	132.6	5.57	2.43	2.29	Red
BF4	875	0.6	54.5	3.98	4.02	0.99	Red/orange
BF5	850	0.3	18.9	4.13	3.87	1.07	Red/orange
BF6	900	0.6	202.7	2.54	5.46	0.46	Red/orange
BF7	800	0.6	46.1	5.77	2.23	2.59	Orange
BF8	850	0.5	103.6	4.84	3.16	1.53	Dark red

Table 8.3.1. Deposition conditions, RMS surface roughness (S_q), composition, colour of BIG samples BF1-BF8.

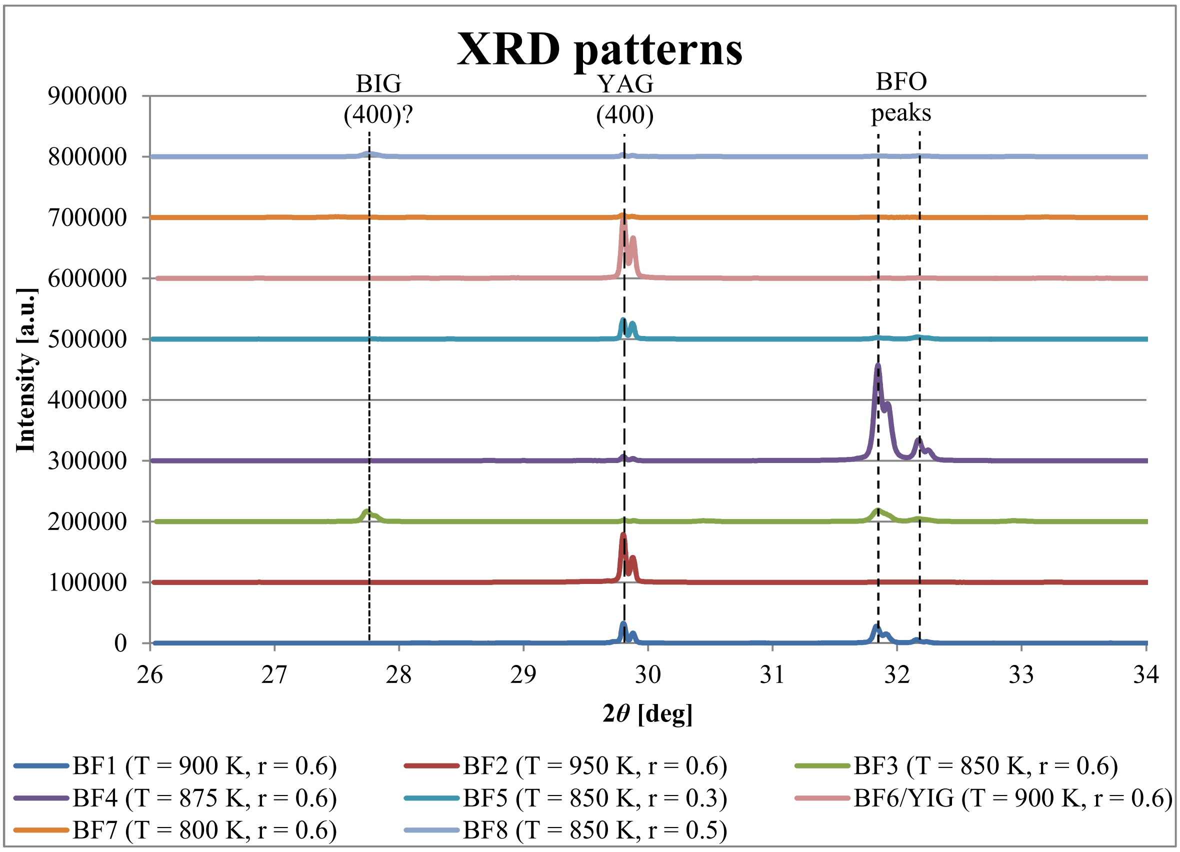

Figure 8.3.3. XRD patterns of "BIG" samples BF1-BF8.

Increasing the substrate temperature up to $T \approx 950$ K (sample BF2) resulted in a completely Bi-deficient Fe_2O_3 film with no crystalline phase. The severe Bi-deficiency is most likely due to the substrate temperature being higher than the melting point of Bi_2O_3 ($T > T_{m,\ Bi2O3}$), causing re-evaporation of the species ablated from the Bi_2O_3 target, whereas the lack of crystallinity (red trace in Figure 8.3.3) is probably due to the high lattice mismatch ($\Delta a/a_{SUB} \approx -58\%$) between the YAG substrate (cubic crystal with $a_{YAG} = b_{YAG} = c_{YAG} = 1.2006$ nm [32]) and the Fe_2O_3 crystal (hexagonal or rhombohedral with $a_{Fe2O3} = b_{Fe2O3} = 0.5034$ nm and $c_{Fe2O3} = 1.3752$ nm for the most common and stable phase, i.e. hematite or α-Fe_2O_3 [33]).

Lowering the substrate temperature to $T \approx 850$ K (sample BF3) produced a Bi-rich polycrystalline film ($Bi_{5.57}Fe_{2.43}O_{12}$) with BIG (400) and BFO phases, as visible from the green trace in Figure 8.3.3. The film surface appears quite rough (see Figure 8.3.4).

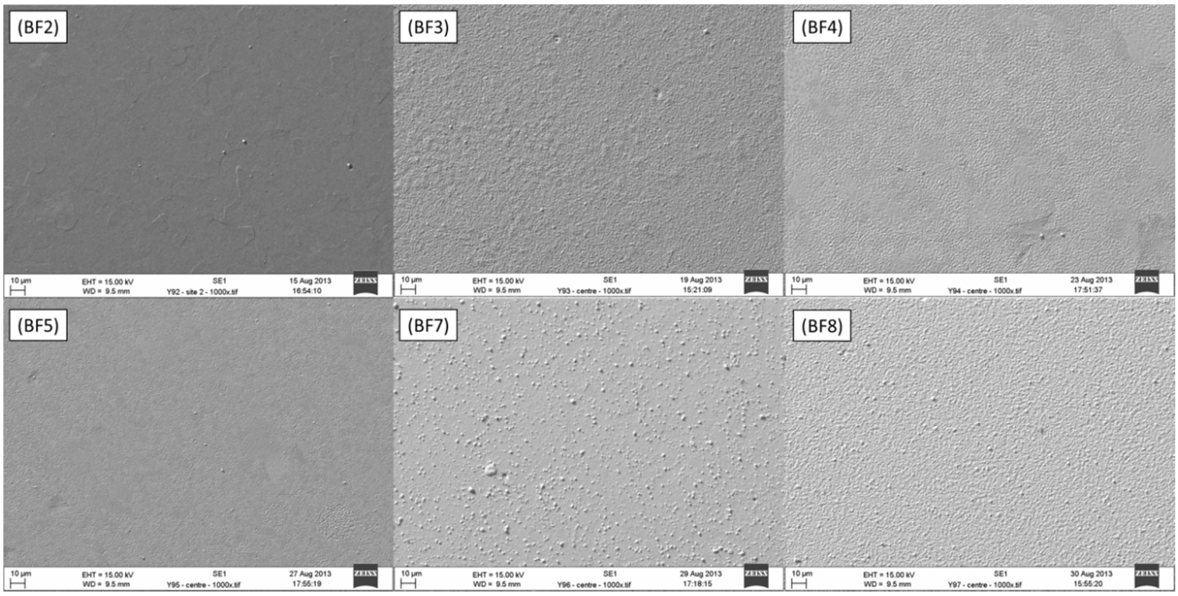

Figure 8.3.4. SEM pictures of samples BF2-5 and BF7-8. Sample BF6 looks like BF1 (see Figure 8.3.2).

Using an intermediate substrate temperature ($T \approx 875$ K) between those of BF1 and BF3 resulted in a polycrystalline $BiFeO_3$ film (sample BF4 in Table 8.3.1) with preferential (110) or equivalent orientation (see purple trace in Figure 8.3.3).

BIG growth was then attempted at $T \approx 850$ K, reducing r from 0.6 to 0.3, which gave a Bi/Fe ratio of 1.07 in BF5, roughly half the value (~47%) of the Bi/Fe ratio in BF3. A 50% reduction in Bi concentration was wrongly expected. In any case, XRD analysis showed two low BFO peaks at $2\theta \approx 31.84°$ and $2\theta \approx 32.15°$.

BIG growth was attempted again at $T \approx 900$ K and $r = 0.6$, but on a buffer YIG layer (~100 nm-thick) previously deposited under optimum conditions (see Table 6.4.1) in the single-PLD chamber. The film composition of this sample (BF6) was Fe-overstoichiometric BIG: $Bi_{2.54}Fe_{5.46}O_{12}$, similar to that of BF1, but no crystalline phase was detected by XRD, except for the YAG (400) substrate peak. The film morphology is also like BF1 (see Figure 8.3.2) and it is probably related to the substrate temperature, close to the depressed melting point of Bi_2O_3 nanoparticles and thin films.

Lowering the temperature to $T \approx 800$ K, while keeping the target ablation ratio at $r = 0.6$, produced a film (sample BF7) with a rough film surface (see Figure 8.3.4) and the following Bi-overstoichiometric composition: $Bi_{5.77}Fe_{2.23}O_{12}$. XRD showed the presence of very low diffraction peaks at $2\theta \approx 27°$, 27.5°, 28.1°, 31.76° and 32.15°: except for the last two that can be assigned to BFO, respectively with (110) and (1 0 -1) orientations or equivalent, the other peaks are not easily identifiable; the peak at $2\theta \approx 27.5°$ may be due to distorted BIG (400), as it is the peak at $2\theta \approx 27.7°$ in BF3 – the database value of the BIG (400) peak position is $2\theta \approx 28.22°$ [20].

A final attempt was made under similar conditions to those which gave a clear BIG phase in the XRD pattern (BF3 – green trace in Figure 8.3.3): in particular the same temperature as BF3 was used ($T \approx 850$ K), whereas the target ablation ratio was lowered to $r = 0.5$, resulting in a film (BF8) with Bi-overstoichiometric BIG composition ($Bi_{4.84}Fe_{3.16}O_{12}$), rough surface (see Figure 8.3.4) and an XRD pattern with low BIG ($2\theta \approx 27.75°$) and BFO peaks.

In all cases, as stated above, no FMR absorption was observed from these films, most likely because of their crystallinity.

8.4. ABLATION OF BI_2O_3 WITH ND:YAG

An ablation test of the Bi_2O_3 target was performed with the Nd:YAG laser ($F_{Nd:YAG} \approx 1.1$ J/cm^2 and $f_{KrF} = 10$ Hz) using a *c*-cut sapphire substrate, at $d \approx 4$ cm away from the target, in oxygen ambient ($P_{O2} \approx 3.4$ Pa) and at room temperature (RT, i.e. ~300 K). A 4 μm-thick Bi_2O_3 film was grown in 2 hours (growth rate: ~0.0556 nm/pulse), confirming the possibility of ablating the Bi_2O_3 target.

No multi-PLD experiments were performed with the inverted laser set-up, as the main problem with growth of Bi:YIG and BIG is the substrate temperature, as demonstrated in the experiments described in Sections 8.2 and 8.3, rather than the target ablation.

8.5. CONCLUSIONS

In this chapter the results of the multi-PLD experiments of Bi_2O_3 and either YIG or Fe_2O_3 were presented. In both cases of growth of Bi:YIG and BIG the substrate temperature was found to play a critical role, due to the melting points of Bi ($T_{m,\,Bi} \approx 545$ K) and Bi_2O_3 ($T_{m,\,Bi2O3} \approx 1090$ K), which are further depressed for materials in thin-film form. In particular, the depressed melting point of Bi_2O_3 is estimated to be $T \approx 950$ K from experimental results.

Section 8.2 covered multi-PLD growth of Bi:YIG films: a detailed discussion of the complex correlation between substrate temperature, Bi concentration, crystallinity and FMR linewidth was given after presenting the results of Bi:YIG depositions at different substrate temperatures. In summary, high temperatures ($T > 950$ K) allow growth of Bi:YIG films with high crystal quality and narrow FMR linewidth ($\Delta H < 10$ mT), but low Bi concentration (<0.2 formula units); low temperatures ($T \leq 950$ K) cause a degradation of crystal quality and magnetic properties ($\Delta H \geq 10$ mT), but higher Bi doping levels (≥0.2 formula units). A compromise ($\Delta H \approx 8.8$ mT with a Bi concentration of 0.22 formula units) was thought to be found at $T \approx 900$ K, however increasing the Bi concentration at this temperature caused degradation of crystal quality and magnetic properties, meaning that the problem may lie not only in the substrate temperature, but also in the incorporation of Bi in the garnet lattice, as the decrease in Fe concentration suggests that Bi substitutes both Y and Fe in the YIG crystal.

Section 8.3 covered multi-PLD of BIG: although co-ablation of Bi_2O_3 and Fe_2O_3 at $T \approx 900$ K and with $r = 1$ allowed the growth of a polycrystalline stoichiometric BFO on sapphire, the film grown at the same temperature with $r = 0.6$ was off-stoichiometric BIG ($Bi_{2.79}Fe_{5.21}O_{12}$), but polycrystalline BFO, as shown by XRD analysis; moreover the film is highly inhomogeneous with large shallow and Bi-deficient areas. Decreasing the substrate temperature to $T \approx 850$ K allowed the observation of what is possibly a BIG (400) peak, although highly shifted (around –0.5°), compared to the database value, suggesting a larger lattice constant of the BIG phase, which would also agree with the high Bi concentration in the same sample (BF3: $Bi_{5.57}Fe_{2.43}O_{12}$); however, BFO phases were observed at the same time and all attempts performed by changing either the substrate temperature or the target ablation ratio were unsuccessful, suggesting that the bismuth and iron species ablated from their respective targets prefer aggregating to form amorphous or BFO phases (see sample BF4 in Figure 8.3.3) and that the BIG (400) phase observed in a few samples may be due to Bi in excess, as it only appears in Bi-overstoichiometric films. Depositing on a YIG buffer layer (BF6) did not help crystal growth of stoichiometric BIG and a surface morphology similar to BF1 (see Figure 8.3.2) was observed, indicating that the growth of crystalline BIG film is actually limited by the substrate temperature (a value $T \geq 950$ K causes a critical loss of Bi in the film, as observed in BF2 and BY1-BY3).

8.6. REFERENCES

1. H. Hayashi, S. Iwasa, N. J. Vasa, T. Yoshitake, K. Ueda, S. Yokoyama, and S. Higuchi, "Characteristics of Bi:YIG magneto-optic thin films fabricated by pulsed laser deposition method for an optical current transformer," Jpn. J. Appl. Phys. **41**, 410-411 (2002).

2. K. Kawano, R. A. Chakalov, G. Kong, J. S. Abell, S. Kahl, and A. M. Grishin, "BIG films fabricated by PLD for magnetic flux visualisation of YBCO," Physica C **372**, 696-699 (2002).

3. M. Laulajainen, P. Paturi, J. Raittila, H. Huhtinen, A. B. Abrahamsen, N. H. Andersen, and R. Laiho, "$Bi_xY_{3-x}Fe_5O_{12}$ thin films prepared by laser ablation for magneto-optical imaging of superconducting thin films," J. Magn. Magn. Mater. **279**, 218-223 (2004).

4. B. Vertruyen, R. Cloots, J. S. Abell, T. J. Jackson, R. C. da Silva, E. Popova, and N. Keller, "Curie temperature, exchange integrals, and magneto-optical properties in off-stoichiometric bismuth iron garnet epitaxial films," Phys. Rev. B: Condens. Matter **78**, 094429 (2008).

5. N. Adachi, V. P. Denysenkov, S. I. Khartsev, A. M. Grishin, and T. Okuda, "Epitaxial $Bi_3Fe_5O_{12}$(001) films grown by pulsed laser deposition and reactive ion beam sputtering techniques," J. Appl. Phys. **88**, 2734-2739 (2000).

6. S. Kahl, and A. M. Grishin, "Evolution of properties of epitaxial bismuth iron garnet films with increasing thickness," J. Magn. Magn. Mater. **278**, 244-255 (2004).

7. S. H. Wee, H. S. Hong, Y. H. Kim, S. I. Yoo, and J. H. Kang, "Fabrication and characterization of Bi-substituted yttrium iron garnet films by pulsed laser deposition," Met. Mater.-Int. **9**, 507-511 (2003).

8. H. Hayashi, S. Iwasa, N. J. Vas, T. Yoshitake, K. Ueda, S. Yokoyama, S. Higuchi, H. Takeshita, and M. Nakahara, "Fabrication of Bi-doped YIG optical thin film for electric current sensor by pulsed laser deposition," Appl. Surf. Sci. **197**, 463-466 (2002).

9. E. Popova, A. F. F. Galeano, M. Deb, B. Warot-Fonrose, H. Kachkachi, F. Gendron, F. Ott, B. Berini, and N. Keller, "Magnetic anisotropies in ultrathin bismuth iron garnet films," J. Magn. Magn. Mater. **335**, 139-143 (2013).

10. M. Deb, E. Popova, A. Fouchet, and N. Keller, "Magneto-optical Faraday spectroscopy of completely bismuth-substituted $Bi_3Fe_5O_{12}$ garnet thin films," J. Phys. D-Appl. Phys. **45**, 455001 (2012).

11. A. A. Jalali-Roudsar, V. P. Denysenkov, S. I. Khartsev, A. M. Grishin, N. Adachi, and T. Okuda, "Microwave and magneto-optic properties of pulsed laser deposited bismuth iron garnet films," IEEE Trans. Magn. **37**, 2454-2456 (2001).

12. S. Kahl, V. Popov, and A. M. Grishin, "Optical transmission and Faraday rotation spectra of a bismuth iron garnet film," J. Appl. Phys. **94**, 5688-5694 (2003).

13. T. Tepper, and C. A. Ross, "Pulsed laser deposition and refractive index measurement of fully substituted bismuth iron garnet films," J. Cryst. Growth **255**, 324-331 (2003).

14. S. Kahl, and A. M. Grishin, "Pulsed laser deposition of $Y_3Fe_5O_{12}$ and $Bi_3Fe_5O_{12}$ films on garnet substrates," J. Appl. Phys. **93**, 6945-6947 (2003).

15. R. Lux, A. Heinrich, S. Leitenmeier, T. Korner, M. Herbort, and B. Stritzker, "Pulsed-laser deposition and growth studies of $Bi_3Fe_5O_{12}$ thin films," J. Appl. Phys. **100**, 113511 (2006).

16. M. Y. Chern, F. Y. Lo, D. R. Liu, K. Yang, and J. S. Liaw, "Red shift of Faraday rotation in thin films of completely bismuth-substituted iron garnet $Bi_3Fe_5O_{12}$," Jpn. J. Appl. Phys. **38**, 6687-6689 (1999).

17. S. Kahl, S. I. Khartsev, A. M. Grishin, K. Kawano, G. Kong, R. A. Chakalov, and J. S. Abell, "Structure, microstructure, and magneto-optical properties of laser deposited $Bi_3Fe_5O_{12}/Gd_3Ga_5O_{12}(111)$ films," J. Appl. Phys. **91**, 9556-9560 (2002).

18. S. Leitenmeier, T. Korner, J. Griesbauer, M. Herbort, A. Heinrich, and B. Stritzker, "Studies on the growth of epitaxial bismuth-substituted iron garnet on gadolinium gallium garnet single crystals by pulsed laser deposition," J. Cryst. Growth **310**, 5392-5401 (2008).

19. H. Kidoh, A. Morimoto, and T. Shimizu, "Synthesis of ferromagnetic bisubstitued yttrium-iron-garnet films by laser ablation," Appl. Phys. Lett. **59**, 237-239 (1991).

20. H. Toraya, and T. Okuda, "Crystal-structure analysis of polycrystalline $Bi_3Fe_5O_{12}$ thin-film by using asymmetric and symmetrical diffraction techniques," J. Phys. Chem. Solids **56**, 1317-1322 (1995).

21. D. Rodic, M. Mitric, R. Tellgren, H. Rundloef, and A. Kremenovic, "True magnetic structure of the ferrimagnetic garnet $Y_3Fe_5O_{12}$ and magnetic moments of iron ions.," J. Magn. Magn. Mater. **191**, 137-145 (1999).

22. L. Dobrzycki, E. Bulska, D. A. Pawlak, Z. Frukacz, and K. Wozniak, "Structure of YAG crystals doped/substituted with erbium and ytterbium," Inorg. Chem. **43**, 7656-7664 (2004).

23. G. Baldinozzi, J. F. Berar, and G. Calvarin, "Rietveld refinement of two-phase Zr-doped Y_2O_3," Mater. Sci. Forum **278-281**, 680-685 (1998).

24. E. Popova, L. Magdenko, H. Niedoba, M. Deb, B. Dagens, B. Berini, M. Vanwolleghem, C. Vilar, F. Gendron, A. Fouchet, J. Scola, Y. Dumont, M. Guyot, and N. Keller, "Magnetic properties of the magnetophotonic crystal based on bismuth iron garnet," J. Appl. Phys. **112**, 093910 (2012).

25. B. M. Simion, G. Thomas, R. Ramesh, V. G. Keramidas, and R. L. Pfeffer, "Growth and characterization of ($Y_3Fe_5O_{12}$-$Bi_3Fe_5O_{12}$) heterostructures by pulsed-laser deposition," Appl. Phys. Lett. **66**, 830-832 (1995).

26. S. A. Manuilov, R. Fors, S. I. Khartsev, and A. M. Grishin, "Submicron $Y_3Fe_5O_{12}$ Film Magnetostatic Wave Band Pass Filters," J. Appl. Phys. **105**, 033917 (2009).

27. S. Yiyan, S. Young-Yeal, C. Houchen, M. Kabatek, M. Jantz, W. Schneider, W. Mingzhong, H. Schultheiss, and A. Hoffmann, "Growth and ferromagnetic resonance properties of nanometer-thick yttrium iron garnet films," Appl. Phys. Lett. **101**, 152405 (2012).

28. R. D. Shannon, "Revised effective ionic radii and systematic studies of interatomic distances in halides and chalcogenides," Acta Crystallogr. A, Cryst. Phys. Diffr. Theor. Gen. Crystallogr. **A32**, 751-767 (1976).

29. G. Catalan, and J. F. Scott, "Physics and Applications of Bismuth Ferrite," Adv. Mater. **21**, 2463-2485 (2009).

30. "MolTech GmbH sapphire datasheet," http://www.mt-berlin.com/frames_cryst/descriptions/sapphire.htm, Accessed December 2013.

31. A. A. Anderson, "Crystalline planar waveguide lasers fabricated by pulsed laser deposition," PhD thesis at *Optoelectronics Research Centre* (University of Southampton, Southampton, 1998).

32. A. Nakatsuka, A. Yoshiasa, and T. Yamanaka, "Cation distribution and crystal chemistry of $Y_3Al_{5-x}Ga_xO_{12}$ ($0 \leq x \leq 5$) garnet solid solutions," Acta Crystallogr. Sect. B-Struct. Sci. **55**, 266-272 (1999).

33. F. O. Gulshan, K., "Preparation of alumina-iron oxide compounds by coprecipitation method and its characterization," American Journal of Materials Science and Engineering **1**, 6-11 (2013).

9. CHAPTER 9
MULTI-PLD OF CE:YIG

9.1. INTRODUCTION

Ce:YIG has the advantage over pure YIG films of a higher Faraday rotation, which increases linearly with increasing Ce concentration ($\phi = 3.3x + 0.008$ [deg/μm] for $Ce_xY_{3-x}Fe_5O_{12}$ at $\lambda = 750$ nm), as demonstrated in [1], thus allowing fabrication of more compact Faraday rotators/isolators and other magneto-optic devices. Also, cerium and its oxides have higher melting points ($T_{m,\,Ce} = 1068$ K, $T_{m,\,Ce2O3} = 2450$ K and $T_{m,\,CeO2} = 2673$ K) than bismuth and its oxides ($T_{m,\,Bi} = 545$ K and $T_{m,\,Bi2O3} = 1090$ K), which would therefore indicate that multi-PLD of Ce:YIG films at high temperatures should be feasible.

There are a few reports of PLD growth of Ce:YIG films by ablation of a Ce:YIG target [1-9], mostly on GGG substrates, but also on non-garnet substrates (Si or cubic quartz). This chapter investigates the possibility of growing Ce:YIG films on YAG (100) substrates by multi-PLD of YIG and CeO_2, using the same conditions as in Table 6.4.2.

9.2. ABLATION OF YIG WITH ND:YAG AND CEO_2 WITH KRF

Multi-PLD growth of Ce:YIG was tried by co-ablating the CeO_2 target with the KrF laser, set at $F_{KrF} \approx 1.0$ J/cm^2 and $f_{KrF} = (1 - 2)$ Hz, and the YIG target with the Nd:YAG laser, set at $F_{Nd:YAG} \approx 1.1$ J/cm^2 and $f_{KrF} = 10$ Hz. The depositions were performed under the usual near-optimum growth conditions for YIG, i.e. those listed in Table 6.4.2.

Both samples grown at $f_{KrF} = 1$ and 2 Hz feature the typical yellow colour of YIG films, a uniform and smooth surface (3 nm < S_q < 4 nm – see inset in Figure 9.2.1), but two clearly distinct phases in the XRD patterns, as shown in Figure 9.2.1, and attributable to YIG (100) and CeO_2 (111). This suggests that the Ce^{4+} species ablated from the CeO_2 target are neither reduced nor included in the garnet lattice, but instead they form a separate phase intermixed with the YIG crystal structure, thus resulting in no FMR absorption. The composition of the two films grown was: $Ce_{0.64}Y_{3.1}Fe_{4.26}O_{12}$ and $Ce_{1.61}Y_{2.67}Fe_{3.72}O_{12}$ for the samples grown respectively at $f_{KrF} = 1$ Hz and $f_{KrF} = 2$ Hz, showing that, as in Bi:YIG films (see Chapter 7), not only the concentration of Y, but also that of Fe tends to decrease with increasing level of Ce doping.

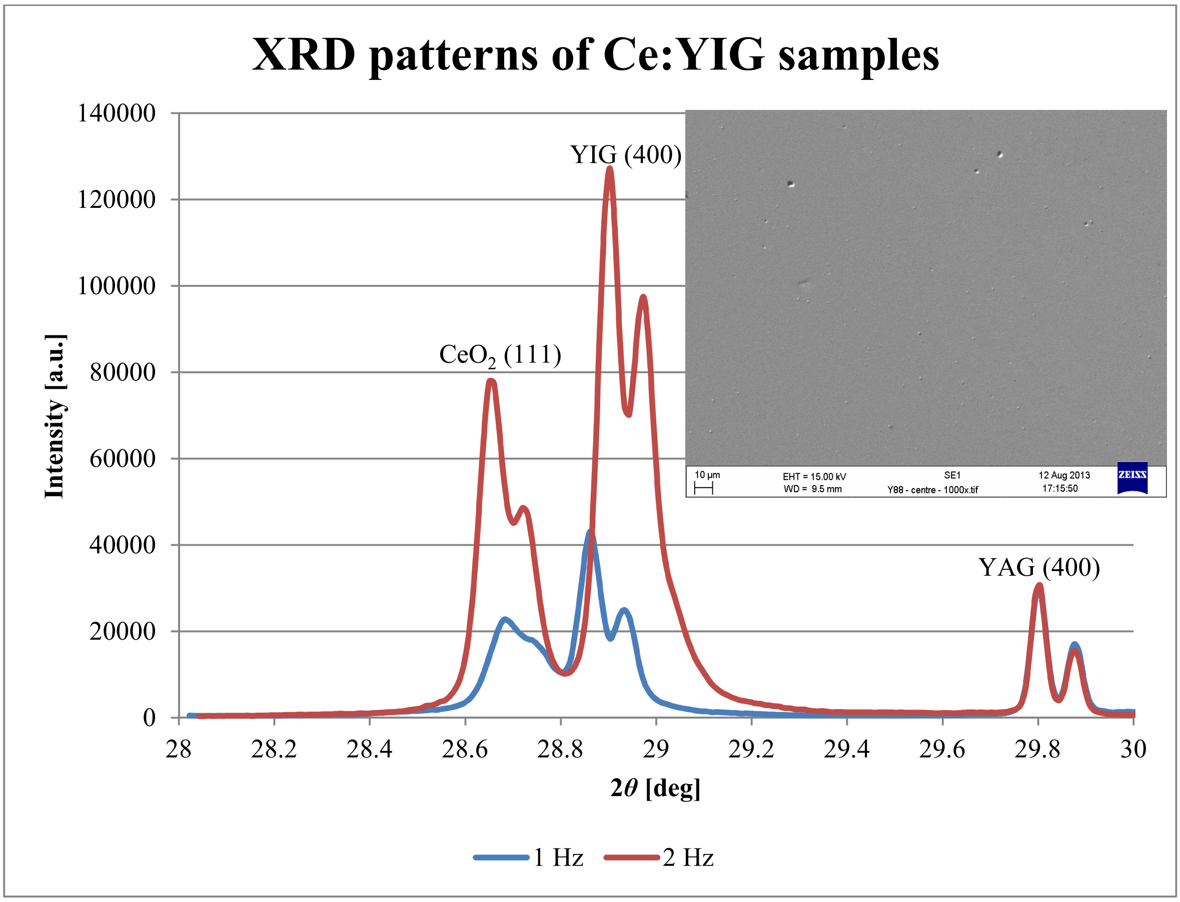

Figure 9.2.1. XRD patterns of Ce:YIG samples.
Peak doublets are due to Cu-K$_{\alpha 2}$ radiation present in the diffractometer.
The inset shows a SEM picture of the samples grown at f_{KrF} = 1 Hz.

No further multi-PLD experiments were performed for Ce inclusion as no magnetic properties were observed in our intended Ce:YIG samples; an investigation of the ablation of the CeO_2 target and the growth of cerium oxide on *c*-cut sapphire substrates, heated at high temperature ($T \approx 1150$ K), was carried out instead.

The CeO_2 target was ablated with the KrF laser, set at f_{KrF} = 20 Hz and different fluences ($F_{\mathrm{KrF}} \approx 1$ and 2 J/cm^2), and with different background gases (oxygen, O_2, and argon, Ar). XRD analysis (see Figure 9.2.2) showed that the film grown in O_2 at $F_{\mathrm{KrF}} \approx 2$ J/cm^2 is polycrystalline CeO_2 with two different orientation: (111) and (100). When depositing at lower fluence ($F_{\mathrm{KrF}} \approx 1$ J/cm^2), either in O_2 or Ar, the film grows as CeO_2 (111). For all cases however, as confirmed also by EDX, the film composition was CeO_2, meaning that Ce species ablated from the CeO_2 target maintain the 4+ valence state, even in an Ar ambient, as reported in the literature for a wide range of deposition conditions [10-14]. Growth rates were: ~0.069 nm/pulse and ~0.035 nm/pulse in O_2, respectively at $F_{\mathrm{KrF}} \approx 2$ J/cm^2 and 1 J/cm^2, and ~0.028 nm/pulse in Ar at $F_{\mathrm{KrF}} \approx 1$ J/cm^2.

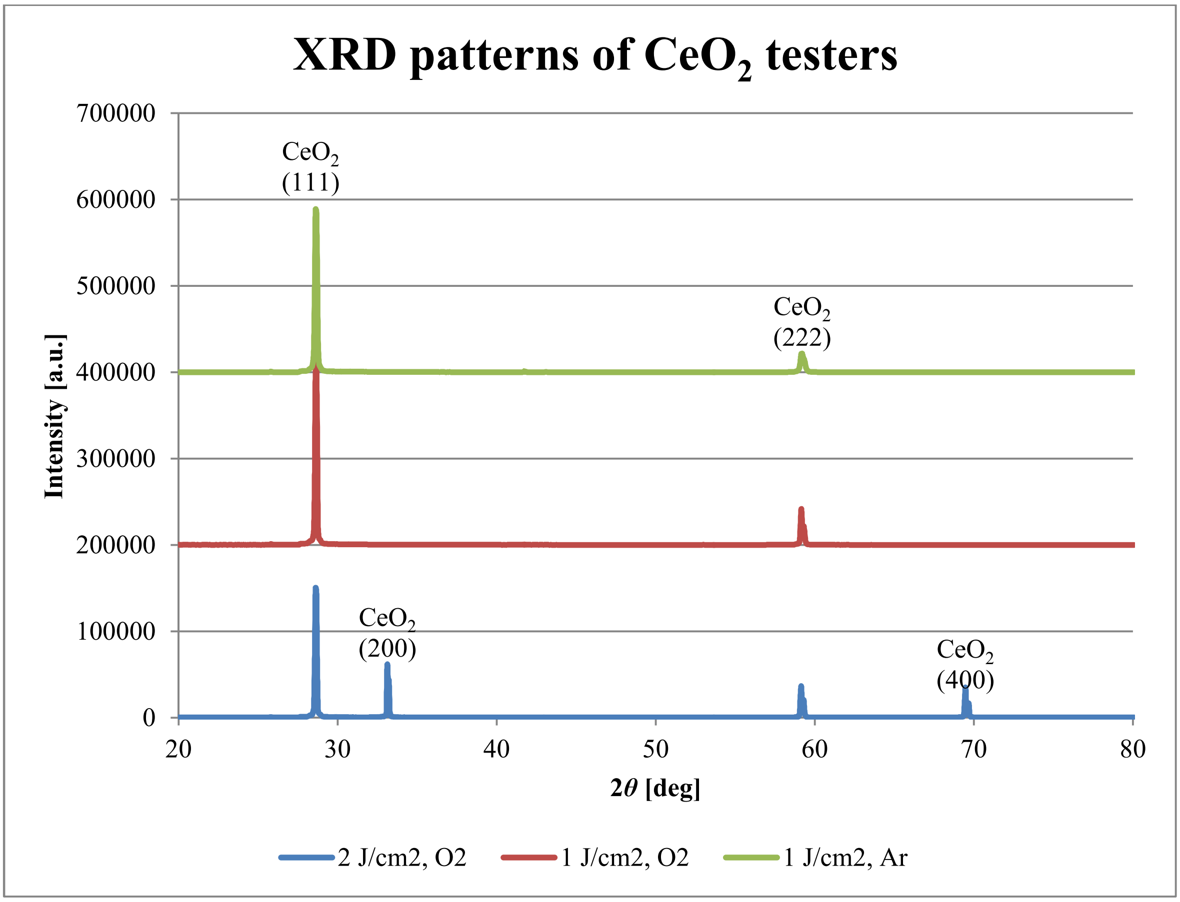

Figure 9.2.2. Comparison of XRD patterns of CeO2 testers.

All CeO_2 tester samples featured a network of cracks across the whole film surface. This, which is probably responsible of the high RMS surface roughness measured by optical profilometry (S_q of the order of 10 nm, but less than 100 nm), is likely due to the mismatch of the lattice constants and the TECs between the µm-thick CeO_2 films (2 µm $\leq t \leq$ 5 µm) and the *c*-cut sapphire substrates: $\Delta a/a_{SUB} \approx 13\%$ from $a_{CeO2} = 0.5411$ nm [11, 13, 14], $a_{\alpha\text{-}Al2O3} = 0.4785$ nm [15]; $\rho_{CeO2} = 12.68$ K^{-1} [16], $\rho_{Al2O3,//} = 6.66\times10^{-6}$ K^{-1} parallel to optical axis of sapphire and $\rho_{Al2O3,\perp} = 5\times10^{-6}$ K^{-1} perpendicular to optical axis of sapphire [15].

However, the results of depositions of cerium oxide on sapphire substrates under different growth conditions confirmed what was observed in the attempts of growing Ce:YIG films by multi-PLD: the cerium in the ablation plume from the CeO_2 target is incorporated in the film as crystalline CeO_2 with (111) preferential orientation, thus disrupting the magnetic properties of YIG.

9.3. ABLATION OF CEO$_2$ WITH ND:YAG

An ablation test of the CeO$_2$ target was performed with the Nd:YAG laser ($F_{\mathrm{Nd:YAG}} \approx 1.1$ J/cm^2 and $f_{\mathrm{KrF}} = 10$ Hz) under the same deposition conditions as in Table 6.4.2, using a *c*-cut sapphire substrate. A 1.25 µm-thick CeO$_2$ (111) film was grown in 2 hours (growth rate: ~0.0174 nm/pulse) and, although it did not feature any cracks, it appeared to be highly porous, as shown in Figure 9.3.1.b.

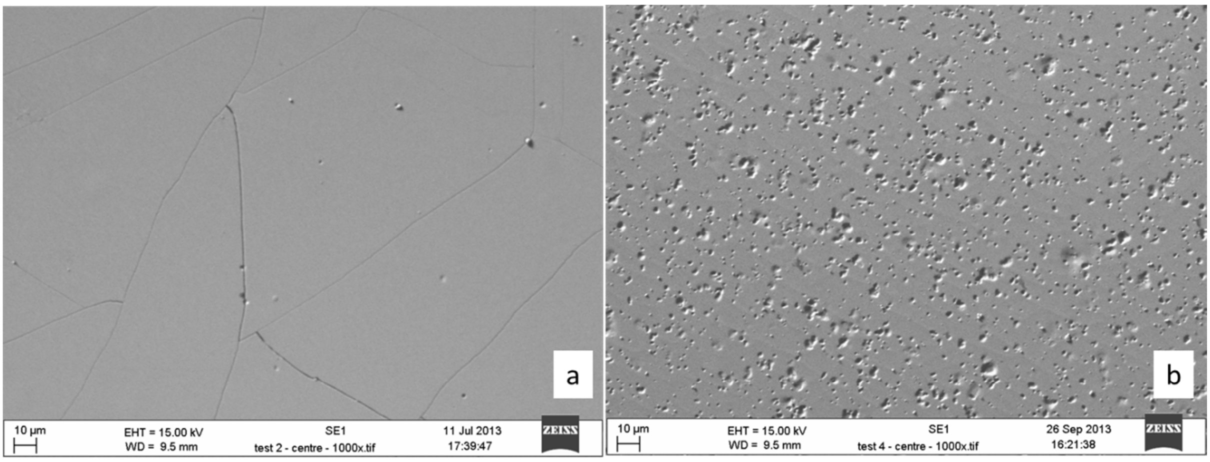

Figure 9.3.1. SEM pictures of film surface of the CeO$_2$ testers grown in O$_2$ ambient with (**a**) the KrF laser ($F_{\mathrm{KrF}} \approx 1$ J/cm^2) and (**b**) the Nd:YAG laser ($F_{\mathrm{Nd:YAG}} \approx 1$ J/cm^2).

No multi-PLD experiments were performed with the inverted laser set-up, because of the quality of this tester and of its CeO$_2$ phase and composition, suggesting that no improvement in attempts of growing Ce:YIG could have been obtained with it.

9.4. CONCLUSIONS

This chapter presented the results of the attempts of growing Ce:YIG by multi-PLD of YIG and CeO$_2$. The higher melting points of cerium and its oxides, compared to bismuth and its oxide, should allow the growth of heavily doped Ce:YIG at high temperatures. However, the lack of Ce$_2$O$_3$ targets and the fact that the ablated species from a CeO$_2$ target maintain their 4+ valence state, as confirmed also by cerium oxide deposition tests on sapphire in different growth conditions, do not allow the inclusion of Ce into the YIG lattice as Ce^{3+}, so that multi-PLD of YIG and CeO$_2$ produces polycrystalline films with intermixed CeO$_2$ and YIG phases and no FMR. Lacking Ce$_2$O$_3$ targets, the problem may be overcome using a metallic Ce target, although it tarnishes slowly in air, its ablation may cause formation of droplets and its ablated species may be easily oxidised in the wrong valence state (3+

instead of 4+) in an oxygen ambient; however multi-PLD of Ce and YIG may be successful in Ar.

9.5. REFERENCES

1. S. Higuchi, K. Ueda, F. Yahiro, Y. Nakata, H. Uetsuhara, T. Okada, and M. Maeda, "Fabrications of cerium-substituted YIG thin films for magnetic field sensor by pulsed-laser deposition," IEEE Trans. Magn. **37**, 2451-2453 (2001).

2. K. Hyonju, A. M. Grishin, K. V. Rao, S. C. Yu, R. Sbiaa, and H. Le Gall, "Ce-substituted YIG films grown by pulsed laser deposition for magneto-optic waveguide devices," IEEE Trans. Magn. **35**, 3163-3165 (1999).

3. S. M. Hamidi, M. M. Tehranchi, and S. Sadeghi, "Effect of magnetic annealing on magneto-optical properties of Ce:YIG thin films incorporating gold nanoparticles," J. Phys. D-Appl. Phys. **44**, 305003 (2011).

4. Y. Nakata, T. Okada, M. Maeda, S. Higuchi, and K. Ueda, "Effect of oxidation dynamics on the film characteristics of Ce : YIG thin films deposited by pulsed-laser deposition," Opt. Lasers Eng. **44**, 147-154 (2006).

5. X. T. Zhou, W. J. Cheng, F. T. Lin, X. M. Ma, and W. Z. Shi, "Effect of post-annealing temperature on the microstructure and magnetic properties of Ce : YIG thin films deposited on Si substrates," Appl. Surf. Sci. **253**, 2108-2112 (2006).

6. S. M. Hamidi, and M. M. Tehranchi, "Magneto-Optical Faraday Rotation in Ce:YIG Thin Films Incorporating Gold Nanoparticles," J. Supercond. Nov. Magn **25**, 2713-2717 (2012).

7. T. Goto, M. C. Onbasli, and C. A. Ross, "Magneto-optical properties of cerium substituted yttrium iron garnet films with reduced thermal budget for monolithic photonic integrated circuits," Opt. Express **20**, 28507-28517 (2012).

8. S. M. Shahrokhvand, A. S. H. Rozatian, M. Mozaffari, S. M. Hamidi, and M. M. Tehranchi, "Preparation and investigation of Ce:YIG thin films with a high magneto-optical figure of merit," J. Phys. D-Appl. Phys. **45**, 235001 (2012).

9. N. B. Ibrahim, C. Edwards, and S. B. Palmer, "Pulsed laser ablation deposition of yttrium iron garnet and cerium-substituted YIG films," J. Magn. Magn. Mater. **220**, 183-194 (2000).

10. S. Amirhaghi, Y. H. Li, J. A. Kilner, and I. W. Boyd, "Growth of pure and doped cerium oxide thin-film bilayers by pulsed-laser deposition," Mater. Sci. Eng. B **34**, 192-198 (1995).

11. R. P. Wang, S. H. Pan, Y. L. Zhou, G. W. Zhou, N. N. Liu, K. Xie, and H. B. Lu, "Fabrication and characteristics of CeO_2 films on Si (100) substrates by pulsed laser deposition," J. Cryst. Growth **200**, 505-509 (1999).

12. D. Q. Shi, M. Ionescu, J. McKinnon, and S. X. Dou, "Growth orientation and surface morphology of CeO_2 films deposited by PLD using different deposition atmospheres," Physica C **356**, 304-310 (2001).

13. R. Bhattacharya, T. Chaudhuri, and S. Phok, "Pulsed-laser deposition of textured cerium oxide thin films on glass substrates at room temperature," Thin Solid Films **515**, 6971-6974 (2007).

14. Y. T. Ho, K. S. Chang, K. C. Liu, L. Z. Hsieh, and M. H. Liang, "Room temperature epitaxial growth of (001) CeO_2 on (001) $LaAlO_3$ by pulsed laser deposition," Cryst. Res. Technol. **48**, 308-313 (2013).

15. "MolTech GmbH sapphire datasheet," http://www.mt-berlin.com/frames_cryst/descriptions/sapphire.htm, Accessed December 2013.

16. H. T. Handal, and V. Thangadurai, "Evaluation of chemical stability, thermal expansion coefficient, and electrical properties of solid state and wet-chemical synthesized Y and Mn-codoped CeO_2 for solid oxide fuel cells," J. Power Sources **243**, 458-471 (2013).

10. CHAPTER 10
CONCLUSIONS AND FUTURE WORK

10.1. PLD OF TI:SAPPHIRE

The project of fabrication of Ti:sapphire waveguide lasers by PLD of Ti-doped sapphire films on undoped *c*-cut sapphire substrate was not as straightforward as the project on investigation of magneto-optic garnets, due to several difficulties encountered. First of all, optimisation of growth conditions was not as easy as for PLD of YIG, due to limitation of EDX in measuring very low concentrations (of the order of 0.01 at. %), as in the case of Ti doping, and in resolving energy peaks due to different elements, as in the case of O and Ti; moreover EDX cannot distinguish the valence state of Ti ions in the lattice, as can be done by XPS for example, which however has a high detection threshold (≥0.1 at. %) – see Section 4.5 for more details. Having no routine access to facilities allowing measurement of Ti concentration at the requied level of accuracy (e.g. PIXE) and also having obtained different results from various compositional analysis techniques (EDX, PIXE and SIMS) performed by some collaborators, the results of fluorescence measurements could have been used as an optimisation parameter, but such measurements also introduce their own characteristic complications: in fact, an unexpected decrease in fluorescence intensity (normalised with film thickness) was observed with increasing film thickness, although this may be explained with the light being waveguided away from the detector, as explained in Section 5.6.

There are also other problems intrinsic with film growth and properties of Ti:sapphire:

1. High substrate temperatures ($T \approx 1300$ K) are needed to ensure formation of high quality crystalline α-Al_2O_3, otherwise the film grows polycrystalline or amorphous [1]: poor crystal quality may give rise to light scattering, thus increasing transmission losses, and to a parasitic absorption band centred at ~750 nm [2], overlapping with the Ti^{3+} fluorescence band and thus hindering fluorescence and subsequent lasing; on the other side, too high a temperature tends to reduce the Ti concentration in the film [1]. However, to tackle this issue, most of the depositions described in Chapter 5 were performed at temperatures near the melting point of gold ($T \approx 1337$ K), which was approximated to $T \approx 1350$ K, after calibration with metal balancing experiments on sapphire substrates.

2. High Ti-doping levels (≥0.4 at. %) cause a deterioration of optical quality [1, 3].

3. Titanium can be oxidised in the wrong valence state (4+), which causes a re-absorption band centred between 750 nm and 800 nm [1, 4], overlapping with the Ti^{3+} fluorescence band and thus hindering fluorescence and inhibiting lasing: this may be avoided by depositing either in high vacuum or in Ar, instead of an O_2 ambient. In fact, higher fluorescence levels were often observed from films deposited in vacuum and Ar than films grown in O_2; however, the only lasing Ti:sapphire waveguide was grown in O_2 and also growth in high vacuum tends to reduce film growth rate and coat the chamber windows faster.

4. Low Ti^{3+} concentration means low pump absorption, thus requiring a longer waveguide, which means also higher transmission losses at the lasing wavelength and may consequently hinder lasing, if the gain is not high enough to compensate all the losses in the cavity, including the misalignment of end-facets and mirrors, which can then be critical to achieve lasing.

5. Ti^{3+} ions have low peak emission cross-section (41×10^{-20} cm^2 at $\lambda = 720$ nm) and short fluorescence lifetime (3.2 μs), thus requiring high pump power density (of the order of 1 MW/cm^2), which can damage the input mirror, as it frequently happened.

6. The Stranski-Krastanov mode, i.e. 2D layer and 3D island growth, cause formation of hexagonal crystallites, which are the most likely cause of high surface roughness and waveguide transmission losses.

7. Sapphire is one of the hardest materials (9 on the Mohs scale, compared to 10 for diamond), making lapping and polishing processes lengthy, thus slowing the process of optimisation of deposition conditions, if lasing performances are to be taken into account.

In spite of all these difficulties, we managed to make one of the thick waveguiding Ti:sapphire films lase, measuring a lasing wavelength $\lambda = 750$ nm, a lasing threshold (average absorbed power) $P_{\mathrm{th}} \approx 364$ mW, a maximum output power $P_{\mathrm{out}} \approx 7.5$ mW at $P_{\mathrm{abs}} \approx 770$ mW and a slope efficiency $\eta \approx 4\%$, using a HR mirror and a 3% output coupler. Although these results compare well with the best reported so far by Anderson [1, 5], unfortunately we were not able to replicate the experiment and to make any of the other Ti:sapphire waveguides lase.

A more systematic and rigorous optimisation procedure may be carried out in the future, by using fluorescence measurements as optimisation parameters. Having demonstrated the feasibility of growing doped films by multi-PLD in Chapters 8 and 9, multi-PLD of Ti:sapphire may be attempted too by co-ablation of a single-crystal Ti:sapphire target (pure single crystal sapphire cannot be ablated by KrF) and of a Ti_2O_3 target. Following the results of CeO_2 ablation, the usage of a TiO_2 target is strongly discouraged, as the Ti species ablated from this target may retain the 4+ valence state, and hence be incorporated as Ti^{4+} in the sapphire crystal and thus cause re-absorption at ~750 nm, hindering fluorescence and lasing, as explained above. Metallic Ti or, even better, a Ti_2O_3 target is suggested: in particular the latter may avoid formation of droplets, which are typical when ablating metallic target.

10.2. PLD OF MAGNETO-OPTIC GARNETS

The research work carried out on PLD of magneto-optic garnets has allowed investigation of the growth of μm-thick YIG films on YAG substrates, which has not been reported extensively to date [6], most likely because of the relatively high lattice mismatch ($\Delta a/a_{\mathrm{SUB}} \approx 3.1\%$), which was probably thought to hinder the growth of high-quality YIG films with good crystallinity, ferromagnetic and magneto-optical properties. On the contrary, the work described in Chapter 6 demonstrated the feasibility of growing crack-free μm-thick YIG films on YAG (100) by PLD and their better ferromagnetic properties, compared to lattice-matched YIG/GGG samples ($\Delta a/a_{\mathrm{SUB}} \approx -0.056\%$) reported in these thesis. The mechanism by which the lattice-mismatch causes better magnetic properties has been explained through strain-relief by misfit dislocation and by TEC-mismatch (see Section 6.2.2).

Variation of film quality and magnetic properties as a function of substrate temperature, oxygen pressure, target-substrate distance, laser wavelength and crystallinity of the target was studied, in order to find the optimum deposition conditions for PLD growth of YIG films on YAG with the narrowest FMR linewidth possible, which was found to be $\Delta H \approx 1.75$ mT from our best sample (Y20), grown by single-PLD from a single-crystal YIG target ablated with the KrF laser ($\lambda = 248$ nm) at $T \approx 1250$ K, $P_{O2} = 1$ Pa, $d = 6$ cm. As explained in Section 4.10 and discussed also in Chapter 6, the actual FMR linewidth may be even narrower than measured, but the limitations of the FMR set-up used may hinder the measurement of the intrinsic FMR linewidth. Deposition on colder substrates causes a broadening of FMR linewidth and then a disappearance of FMR absorption, probably due to the deterioration of crystal quality with decreasing substrate temperature. Deviation of oxygen pressure from the optimum value in either direction caused a broadening of FMR linewidth. Target-substrate distance can be reduced to allow faster growth rates, provided that the film growth dynamics is maintained by increasing the oxygen pressure accordingly. Ablation of a polycrystalline YIG target tends to produce rougher films, with slightly broader FMR linewidth than ablation of a single-crystal target, and the KrF laser ablates it better than the frequency-quadrupled Nd:YAG laser (λ = 266 nm) does and produces YIG samples with narrower FMR linewidth.

Having observed a strong Fe-deficiency in all YIG films grown by single-PLD, a systematic study of variation of YIG film properties (colour and appearance, surface roughness and morphology, crystallinity, FMR and optical transmission) followed by quantitative comparison was performed by multi-PLD of YIG with either an Y_2O_3 or Fe_2O_3 target, as discussed in Chapter 7. These experiments showed that compensation of Fe-deficiency causes deterioration, instead of the expected improvement of the properties of YIG films, which become darker (redder), more opaque, rougher and with broader FMR linewidth with increasing Fe concentration; however, co-ablation of YIG with KrF and Fe_2O_3 with Nd:YAG produced better films than the inverted laser set-up, although featuring the same trends with increasing Fe concentration as observed before, suggesting that the choice of appropriate ablation wavelength for each target is important. Conversely, an increase in Y concentration, by co-ablation of YIG and Y_2O_3, was thought to improve ferromagnetic properties of YIG, but, on the contrary, a broadening of the FMR linewidth with larger off-stoichiometry was observed, until FMR absorption disappears when the film becomes amorphous (no YIG or other crystalline phases observed in XRD patterns) and orange in colour. All these results indicated that the optimum composition of YIG films in terms of film quality and FMR linewidth is close to $Y_{3.5}Fe_{4.5}O_{12}$, i.e. the same as YIG films grown by single-PLD. The worsening of FMR linewidth with composition diverging from this optimum value was explained with either a direct or an indirect effect, through a change in crystallinity and/or lattice constant, affecting the film strain and magnetic properties. In any case, these experiments proved that multi-PLD is a viable technique to tailor thin film properties by tuning the material composition: for YIG and magneto-optic garnets in particular, multi-PLD can be used to tune FMR linewidth and

Faraday rotation of the material for applications in microwave and optical communications (rotators and isolators).

YIG films were also grown on YAG substrates "from scratch", i.e. by multi-PLD of precursors of YIG (Y_2O_3 and Fe_2O_3). Once the laser fluences were tuned to grow stoichiometric YIG with a target ablation ratio equal to the stoichiometric ratio (r = Y/Fe = 0.6), film composition was varied by changing the repetition rate of one of the lasers (and thus *r)*; the results obtained from this new set of depositions agreed with those collected from the other batches, as discussed above, and with that obtained by ablation of a Fe-rich YIG target in the single-PLD chamber under optimum deposition conditions, thus confirming the validity of the study of film composition by multi-PLD: it is the intrinsic variation of composition in YIG films that induces the change in the other properties (colour, appearance, crystallinity, surface roughness and morphology, optical transmission and FMR) and not plume interaction or something else related to target co-ablation. Moreover, the successful deposition of a polycrystalline stoichiometric $YFeO_3$ film on sapphire substrate demonstrated that it is possible to grow different materials (e.g. YIG and YFO) by multi-PLD of their precursors (Y_2O_3 and Fe_2O_3) by choosing appropriate substrates and adjusting the target ablation ratio accordingly to the desired composition. With an appropriate multi-PLD set-up one could first grow a thin-film compositional library on a large wafer by combinatorial PLD, for high throughput screening and optimisation, and then tune the laser fluences and/or repetition rates to grow films with the desired composition on smaller substrates for functional devices.

Growth of Bi-doped YIG and pure BIG films was attempted by multi-PLD, as discussed in Chapter 8. In this case, substrate temperature not only affects crystallinity, but it also plays a critical role in terms of film growth and composition. In fact, the species ablated from the Bi_2O_3 target that impinge on the hot substrate can re-evaporate, due to their low melting points ($T_{\mathrm{m,\,Bi}} \approx 545$ K and $T_{\mathrm{m,\,Bi2O3}} \approx 1090$ K for bulk, further depressed for materials in thin-film form and nanoparticles), relative to the optimum substrate temperature for YIG growth ($T \approx 1250$ K). This severely constrains the Bi concentration in Bi:YIG films and completely inhibits BIG growth at high temperatures ($T \geq 950$ K); moreover, the Bi-doping level was observed to affect crystalline growth, when it is higher than 0.3 formula units. Several Bi:YIG films were deposited, allowing a systematic study of the variation of Bi:YIG properties (colour, appearance, crystallinity, surface roughness and morphology, and FMR) as a function of substrate temperature and composition; a complex correlation between substrate temperature, Bi concentration, crystallinity and FMR was observed and discussed in detail in Section 8.2. The investigation of Bi:YIG films could be completed in future with attempts of growing samples with high Bi-doping level at high temperature ($T \approx 1150$ K), using higher pulse repetition frequency ($f_{\mathrm{KrF}} > 2$ Hz) for the laser ablating the Bi_2O_3 target, although a deterioration in crystallinity and FMR with increasing Bi concentration is suspected to happen even at this temperature, as observed in the films grown at $T \approx 900$ K and $f_{\mathrm{KrF}} = (1, 2 \text{ and } 10)$ Hz.

Growth of BIG by co-ablation of Bi_2O_3 and Fe_2O_3 targets was not successful, in spite of successful growth of polycrystalline stoichiometric $BiFeO_3$ on sapphire, at $T \approx 900$ K and $r = 1$, and in spite of variation of substrate temperature over quite a broad range of values, $T \approx (800 - 950)$ K, and of target ablation ratio r between 0.3 and 0.6; growth of BFO phases seems to be preferential over BIG, even on a thin YIG buffer layer, as shown by XRD analysis of all samples. A more systematic study may be performed, for instance reducing substrate temperature, although it may deteriorate crystallinity even further and it would cause higher Bi concentration, which would require lower laser fluence on the Bi_2O_3 target or higher fluence on the Fe_2O_3 target to control the BIG composition; as the problem appears to be related to substrate temperature and Bi inclusion, any change in other deposition conditions (e.g. gas pressure or laser parameters) is probably not relevant.

Finally, growth of Ce:YIG films was attempted by multi-PLD of YIG and CeO_2, as described in Chapter 9. The higher melting points of Ce and its oxides ($T_{\mathrm{m, Ce}} = 1068$ K, $T_{\mathrm{m, Ce2O3}} = 2450$ K and $T_{\mathrm{m, CeO2}} = 2673$ K), compared to those of Bi and Bi_2O_3, were thought to allow the deposition of Ce:YIG films; however the films grown by multi-PLD featured intermixed phases of the YIG (100) and CeO_2 (111), which must disrupt the intrinsic magnetic properties of YIG, as no FMR absorption was observed from these samples. Testers grown by ablation of the CeO_2 target alone under different conditions (in O_2 and Ar) were always stoichiometric CeO_2, thus confirming what was observed in multi-PLD experiments, that the species ablated from the target retain the 4+ valence state and thus are not included in the YIG lattice, but form a separate CeO_2 phase. This may be circumvented only by using a metallic Ce target, although it slowly tarnishes in air and its ablation may cause formation of droplets, due to the unavailability of Ce_2O_3 targets; to avoid re-oxidisation of the ablated species in the wrong valence state (4+ instead of 3+) in O_2, multi-PLD of Ce and YIG may be tried in an Ar.

10.3. REFERENCES

1. A. A. Anderson, "Crystalline planar waveguide lasers fabricated by pulsed laser deposition," PhD thesis at *Optoelectronics Research Centre* (University of Southampton, Southampton, 1998).

2. P. F. Moulton, "Spectroscopic and laser characteristics of Ti-Al_2O_3," J. Opt. Soc. Am. B-Opt. Phys. **3**, 125-133 (1986).

3. I. T. McKinnie, A. L. Oien, D. M. Warrington, P. N. Tonga, L. A. W. Gloster, and T. A. King, "Ti3+ ion concentration and Ti:sapphire laser performance," IEEE J. Quantum Electron. **33**, 1221-1230 (1997).

4. M. Yamaga, T. Yosida, S. Hara, N. Kodama, and B. Henderson, "Optical and electron-spin-resonance spectroscopy of Ti^{3+} and Ti^{4+} in Al_2O_3," Journal of Applied Physics **75**, 1111-1117 (1994).

5. A. A. Anderson, R. W. Eason, L. M. B. Hickey, M. Jelinek, C. Grivas, D. S. Gill, and N. A. Vainos, "Ti:sapphire planar waveguide laser grown by pulsed laser deposition," Opt. Lett. **22**, 1556-1558 (1997).

6. E. Popova, N. Keller, F. Jomard, L. Thomas, M. C. Brianso, F. Gendron, M. Guyot, and M. Tessier, "Exchange coupling in ultrathin epitaxial yttrium iron garnet films," Eur. Phys. J. B **31**, 69-74 (2003).

A. APPENDIX A
LIFT OF CRYSTALLINE YIG

A.1. INTRODUCTION

This appendix covers a project for which I collaborated by providing YIG films grown by PLD on YAG substrates. The aim of the project was to demonstrate the possibility of laser-printing crystalline films by Laser-Induced Forward Transfer (LIFT). While all the YIG films were grown by myself, the pre-machining, LIFT experiments and subsequent characterisation measurements were performed by Dr. Collin L. Sones and Dr. Matthias Feinaeugle of the LIFT research group of the ORC at the University of Southampton. The basics of LIFT are introduced in the next section, whereas the results of the LIFT experiments of YIG are presented and briefly discussed in Section A.3. More details can be found in [1].

A.2. LASER-INDUCED FORWARD TRANSFER (LIFT)

Laser-Induced Forward Transfer, often abbreviated as LIFT, is a serial laser-printing or direct-write technique consisting of transferring a material, called the “donor”, from the “carrier”, i.e. the substrate on top of which the donor is deposited, to the “receiver” or “acceptor”, i.e. another substrate on top of which the donor is to be transferred. This approach allows the printing of user-defined high-resolution 1-D, 2-D or even 3-D (i.e. multi-layer) patterns on top of a substrate, which may well be incompatible with the LIFT-printed material in terms of direct growth. The definition of 1-D or 2-D patterns can be performed by either moving the source (carrier + donor) and the receiver at the same time [2] or by raster scanning the laser beam on the source, using a digital multi-mirror device (DMD) [3, 4]. The LIFT technique typically uses UV lasers (e.g. excimers) or high repetition rate Ti:sapphire fs-lasers, tuned at λ = 800 nm, exploiting multi-photon absorption in the donor, whereas the carrier must be transparent to the laser wavelength and its harmonics; unlike several deposition and patterning methods, LIFT does not require vacuum chambers and clean-room equipment. The working principle of LIFT is schematically illustrated in Figure A.2.1: a laser beam is focussed or imaged on the region of the donor to be printed; if the laser fluence is above a certain threshold (generally close the ablation threshold), which depends on the material, the laser energy is absorbed by the donor, which partially evaporates and the irradiated region is thus propelled away from the carrier and transferred on top of the receiver/acceptor.

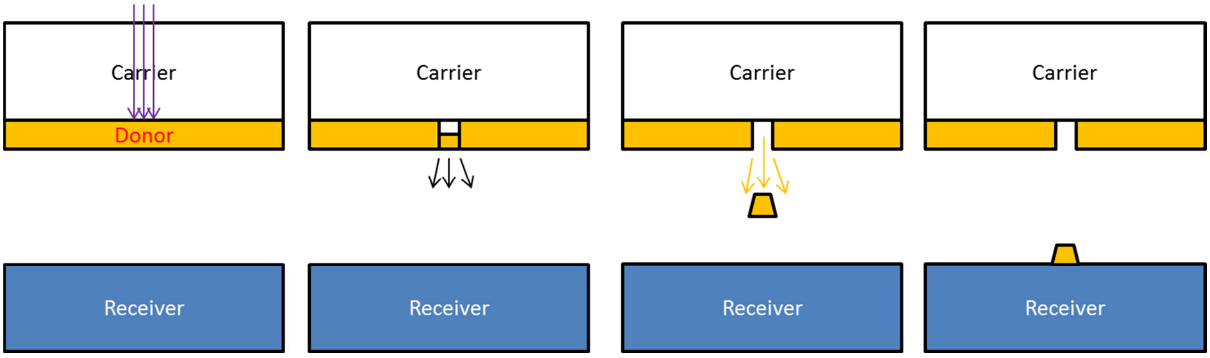

Figure A.2.1: Schematic illustration of the LIFT mechanism

A major problem in LIFT-printing is the transfer of debris-free 3D volumetric pixels (voxels) with precise shapes or high-quality edges. In conventional LIFT there are two main issues:

I. partial ablation of the donor;
II. shearing and tearing of the donor around its edges during the transfer.

The first issue can often be overcome by use of a sacrificial layer, also called a dynamic release layer (DRL), sandwiched between the carrier and the donor and which absorbs UV light and vaporises, thus pushing the donor away from the carrier and towards the receiver. However, the DRL is normally a polymer, which prevents the epitaxial growth of donors at the high temperatures needed for ensuring the crystallisation of the film [1].

The second issue is more closely related to the formation of debris during the transfer, which is especially true for brittle donors such as crystalline µm-thick films. This problem can be circumvented with a pre-patterning approach: a laser-based pre-indentation can be performed to weaken the boundaries of the voxel intended for transfer, but the approach adopted in [5], for example, does not routinely lead to the printing of high-quality material with the exact shape required; a pre-machining of the donor by focussed ion beam (FIB) has proven successful in the transfer of amorphous ZnO voxels with well-defined shapes and smooth edge quality [6]. The results presented in the next section show that FIB-pre-machining of PLD-grown crystalline YIG films allows, for the first time, a demonstration of transfer of precisely defined voxels without the often encountered and highly undesirable shattering and formation of debris.

A.3. LIFT OF YIG

A ~1-µm thick YIG film was grown by PLD on a YAG substrate under the deposition conditions summarised in Table A.3.1, which are known to produce high-quality crystalline YIG, as also confirmed by XRD analysis.

Target	Single-crystal YIG
Substrate	YAG (100)
Laser (λ [nm])	KrF (λ = 248)
Repetition frequency [Hz]	20
Fluence [J/cm^2]	~3.2
Target – substrate distance [cm]	6.0
O_2 pressure [Pa]	3.3
Substrate temperature [K]	~1150

Table A.3.1. Deposition conditions of sample Y6, used for LIFT experiments.

A YIG/YAG sample was chosen as a donor/carrier because of the high contrast of UV absorption: in fact, as shown in Figure A.3.1, the YAG substrate is transparent (~80% transmission) at 800 nm and 400 nm, whereas YIG features the typical absorption edge between ~450 and ~550 nm and a strong UV absorption at λ ≈ 400 nm (zero transmission), thus matching the two-photon absorption induced by the Ti:sapphire fs-laser tuned at λ = 800 nm, used for LIFT experiments. Earlier attempts to LIFT crystalline GGG donors from YAG carriers were unsuccessful because of the mismatched absorption criteria (see Figure A.3.1).

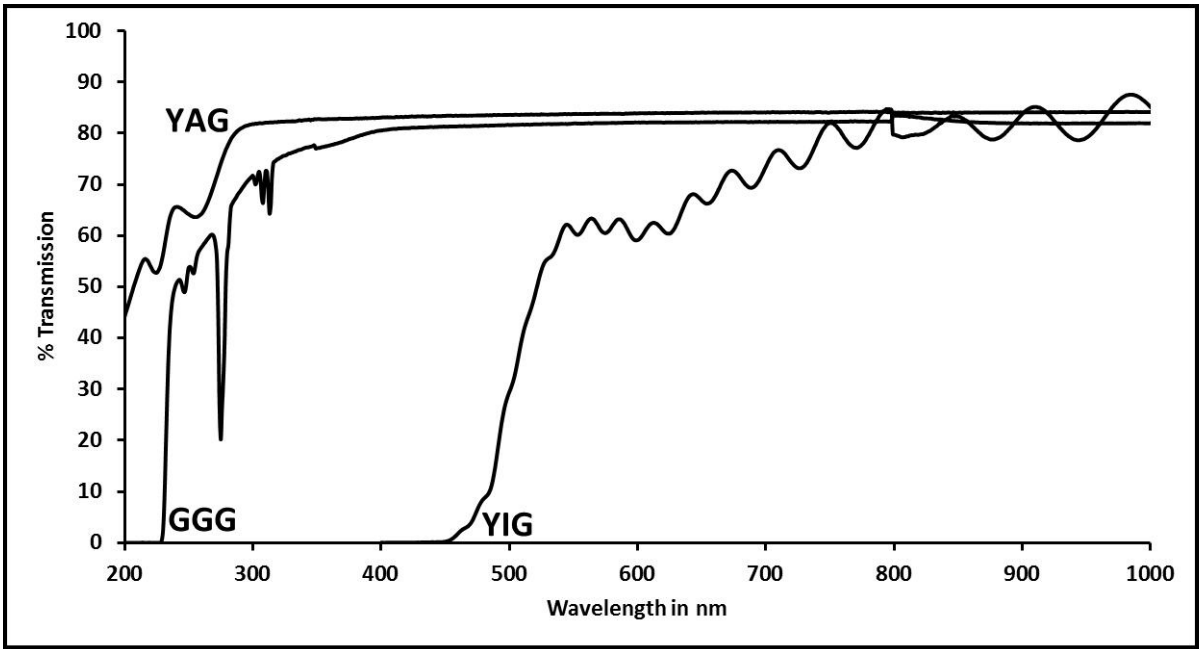

Figure A.3.1. Optical transmission spectra for YAG carrier and the YIG and GGG donors (used in previous unsuccessful LIFT trials) grown by PLD. The ripples in the YIG spectra are thin-film etalon fringes [7]. Figure taken from reference [1].

Pre-machining of circular ring patterns with outer and inner diameters of ~10 μm and 9.5 μm respectively was performed by FIB into the YIG donor films. Arrays of rings with different depths were pre-machined in order to understand the dependence of the laser fluence on the LIFT-printing process. The machining depth was limited in the range (40 – 80) % of the initial thickness of the donor, because machining throughout the entire depth of the donor would not allow the laser-induced pressure build-up behind the material intended for transfer.

The LIFT experiments were performed by using a tunable ultrafast Ti:sapphire laser system operating at $\lambda = 800$ nm, with a repetition rate of 1 kHz, a pulse duration of ~150 fs and a maximum energy of ~2 mJ/pulse. A spatially uniform top-hat intensity profile with a diameter of ~6 mm was obtained by collimating and then homogenising the laser beam with a refractive optical element, in order to ensure a uniform intensity profile, resulting in a uniform laser energy deposition and thus in a uniform thrust from the laser onto the voxel to transfer. Shape and size of the incident laser beam were varied via an aperture positioned in the path of the beam after the homogeniser; the laser beam was then imaged onto the carrier-donor interface with a large value of demagnification using a microscope objective lens. The diameter of the imaged circular beam profile was intentionally set to match the diameter of the pre-machined donor (~10 μm).

The YIG/YAG sample was placed in near proximity to a glass receiver, which was coated with Parafilm to ensure better adhesion of the LIFT-printed donor voxels. A 1 mm-thick Mylar spacer was introduced between the donor and the receiver in order to maintain a uniform separation between them. The incident laser fluence for the LIFT printing was varied from ~0.2 to ~5.8 J/cm^2.

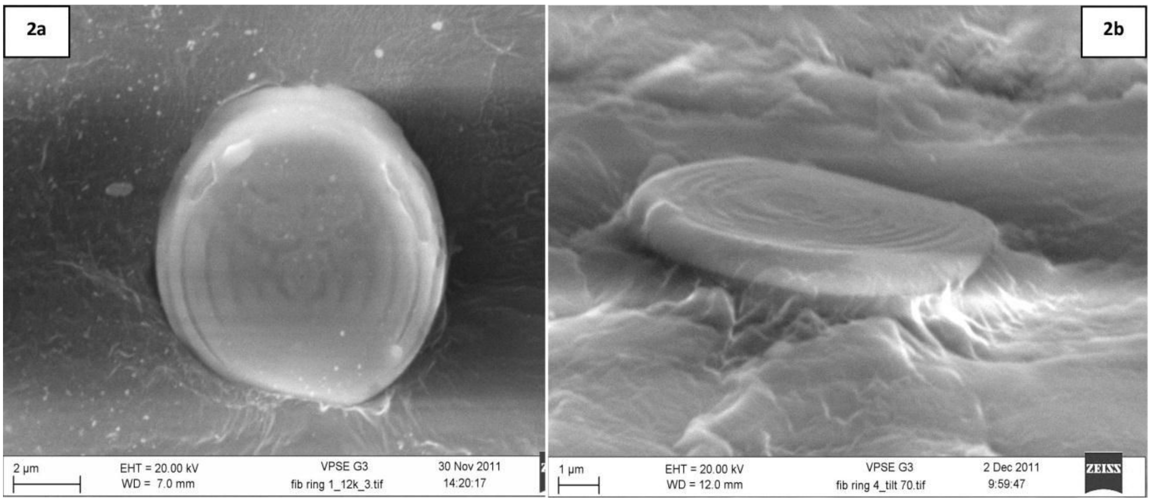

Figure A.3.2. SEM images of **(a)** top-view and **(b)** side-view of FIB pre-machined LIFTed YIG voxels. [1]

Figure A.3.2 shows the first results for LIFT-printing from the pre-machined YIG donor film. Figure A.3.2.a and Figure A.3.2.b show respectively the top and side-view of two different discs LIFT-printed from a donor that had been FIB pre-machined down to depths of ~70%. The laser fluences necessary for the transfer of these pre-machined discs was ~5.8 J/cm^2, well above the threshold of ~1.7 J/cm^2, below which not even a partial transfer of the pre-machined discs was possible. The circular disc in Figure A.3.2.a appears to be slightly non-circular; in reality, this is due to the front section of the LIFT-printed disc being slightly embedded in the soft Parafilm coating of the glass receiver; for this reason, Figure A.3.2.b shows an SEM image of the edge of another FIB pre-machined LIFT-printed voxel (taken with the SEM stage tilted at 70°) rather than an image of the side of the same LIFT-printed voxel as in Figure A.3.2.a. The circular concentric rings that can be seen on the surface of the LIFT-printed discs in Figure A.3.2.a are probably due to incorrect imaging of the aperture or due to an optical standing wave effect resulting from multiple reflections from within the various carrier, donor and receiver surfaces [1, 8].

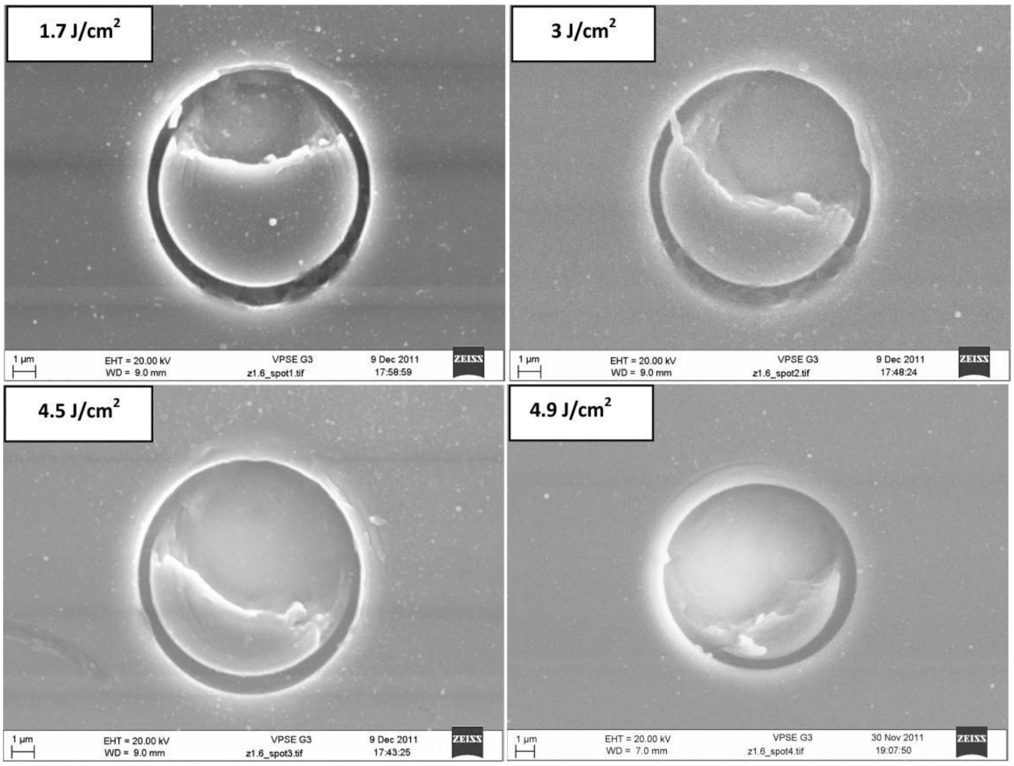

Figure A.3.3. SEM images of different pre-machined donor rings after LIFT-transfer with different laser fluences. The images are for donors that were pre-machined to a depth of 80% of the donor thickness. The fractional percentage of the donor material that has been LIFT-printed from the pre-machined donor rings at the incident laser fluences of 1.7J/cm^2, 3J/cm^2, 4.5J/cm^2, and 4.9J/cm^2, has been measured to be approximately 29%, 51%, 63% and 72% respectively. [1]

Figure A.3.3 shows a set of SEM pictures of pre-machined (down to depths of 80%) donor spots after their LIFT-transfer with increasing incident laser fluence. As seen in Figure A.3.3, the amount of donor material that is transferred onto the receiver increases with increasing fluence, thus showing the importance of incident laser fluence for successful LIFT-transfer of pre-machined crystalline material. The non-uniform LIFT-printing results (of Figure A.3.3) at non-optimal fluence could possibly be due to:

a. a small non-uniformity in the incident laser intensity profile;
b. the strong non-linear two-photon absorption in the donor material or…
c. a possible slight error in the alignment of the incident laser beam.

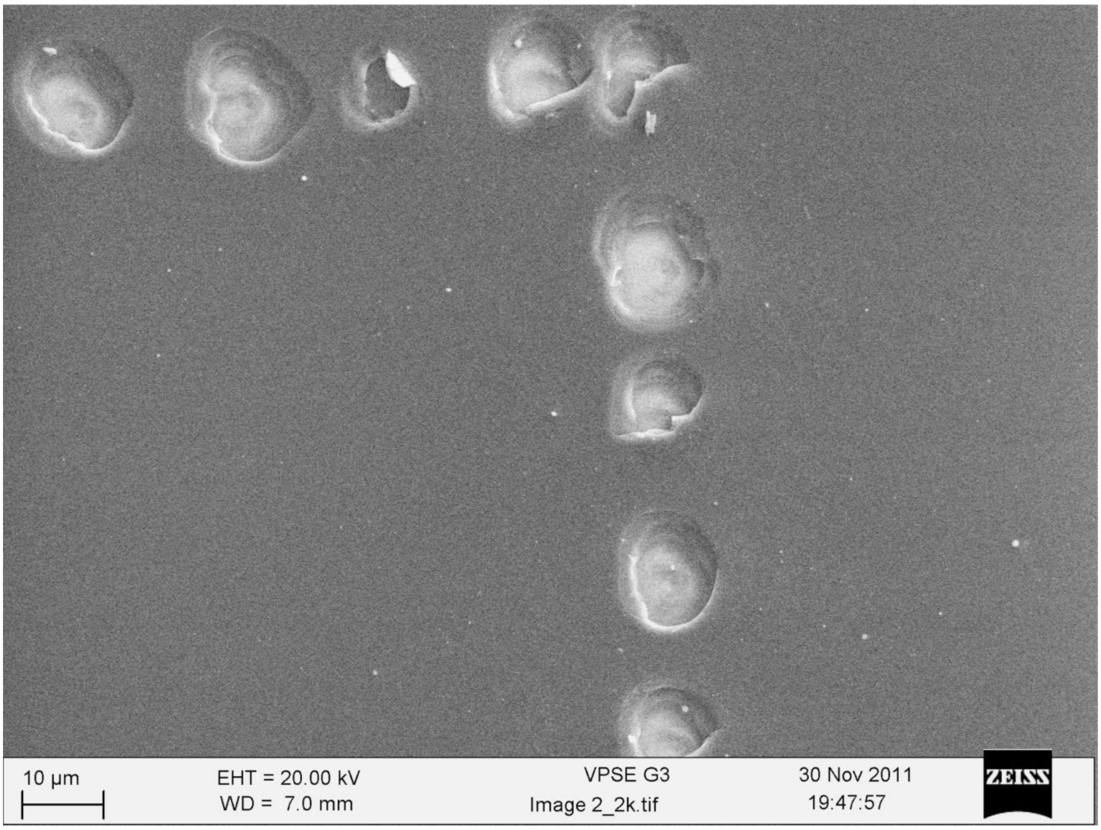

Figure A.3.4. SEM picture of a non-machined donor after LIFT-printing of an array of spots. [1]

By comparison, Figure A.3.4 shows a non-machined donor after LIFT-printing an array of many voxels: it is clear that there is an inherent non-repeatability involved in LIFT-printing from a non-machined donor; moreover the printed voxels from non-machined donors are worse than those printed from FIB-machined donor in terms of shape and edge-quality.

The SEM images in Figure A.3.5 show the top and side-view of an irregularly shaped and partially fragmented voxel, LIFT-printed using a circular laser spot, but from a non-machined section of the donor. Compared to Figure A.3.2, the SEM pictures in Figure A.3.5 show the importance of the pre-machining step to avoid the undesirable and otherwise unavoidable shattering, associated with voxels deposited with similar laser fluences but without the pre-machining. The inevitable non-uniformity of a non-machined LIFT-printed voxel along its edge and in its thickness is evident in Figure A.3.5.b (taken with the sample tilted to 70°), which also shows a large semi-circular fragmented section (indicated by an arrow) from another non-machined LIFT-printed pixel. This debris results from the fragmentation of LIFT-printed non-machined donors and its formation is due to the excessive force that the transferred donor voxel experiences while shearing-off from the remaining non-machined donor material; in contrast, for pre-machined donors, a smaller shearing force in the transfer of donor pixels consequently results in better edge quality and almost no fragmentation [1].

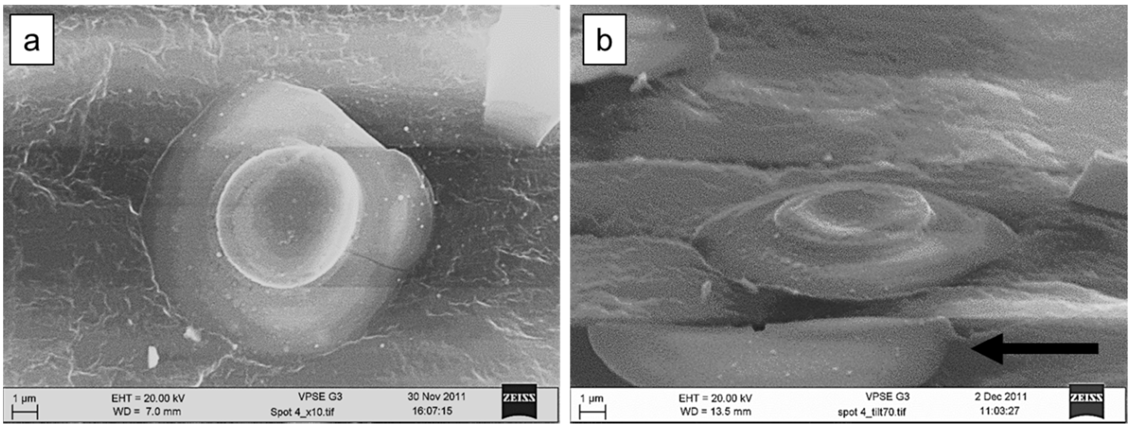

Figure A.3.5. SEM images showing **(a)** top-view and **(b)** side-view of a non-machined LIFT-printed YIG voxel. The arrow in **(b)** shows fragmented pixel debris associated with typical non-machined LIFT-printing [1].

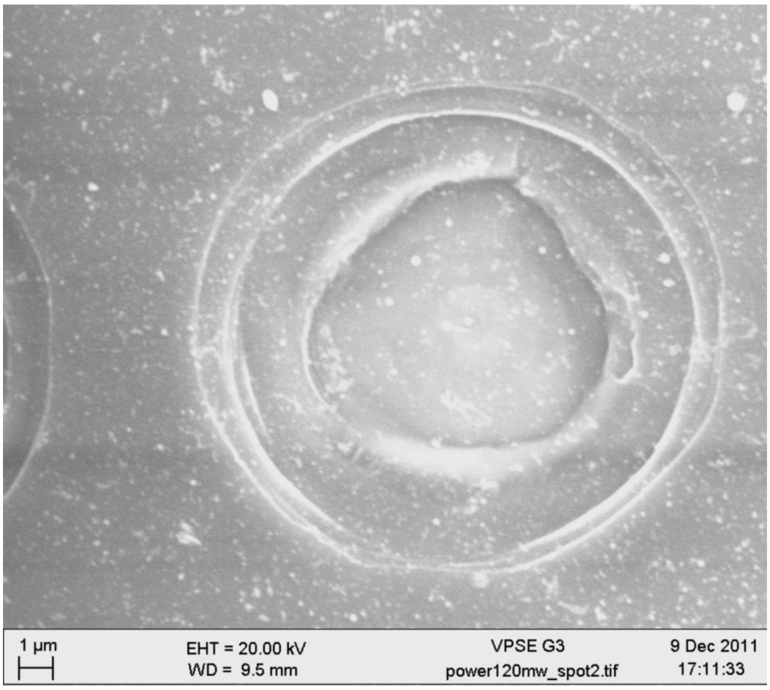

Figure A.3.6. SEM image of a non-machined donor after LIFT-transfer [1].

Figure A.3.6 shows a close-up SEM image of a non-machined donor after LIFT-printing, which can be compared with the SEM images in Figure A.3.3, further emphasizing the importance of the pre-machining step for the deposition of donor voxels with better edge quality and well defined shapes. The facetted ring features of the donor (in Figure A.3.6), showing depth-dependent cracking, can possibly be attributed to the preferential cleaving of the crystal along different planes during LIFT [1]. The result of this is evident in the complementary ‘flying-saucer-like’ shape of the corresponding LIFT-printed voxel shown in Figure A.3.5.b. Moreover, the area on the donor influenced by the LIFT-printing is restricted to the size of the incident laser beam of pre-machined voxels (Figure A.3.3), whereas in non-machined donors the region affected by the LIFT process is larger than the incident laser beam (whose size was of the order of the inner hollow ring feature formed in the donor, as visible in Figure A.3.6) and extends over a large area of the donor.

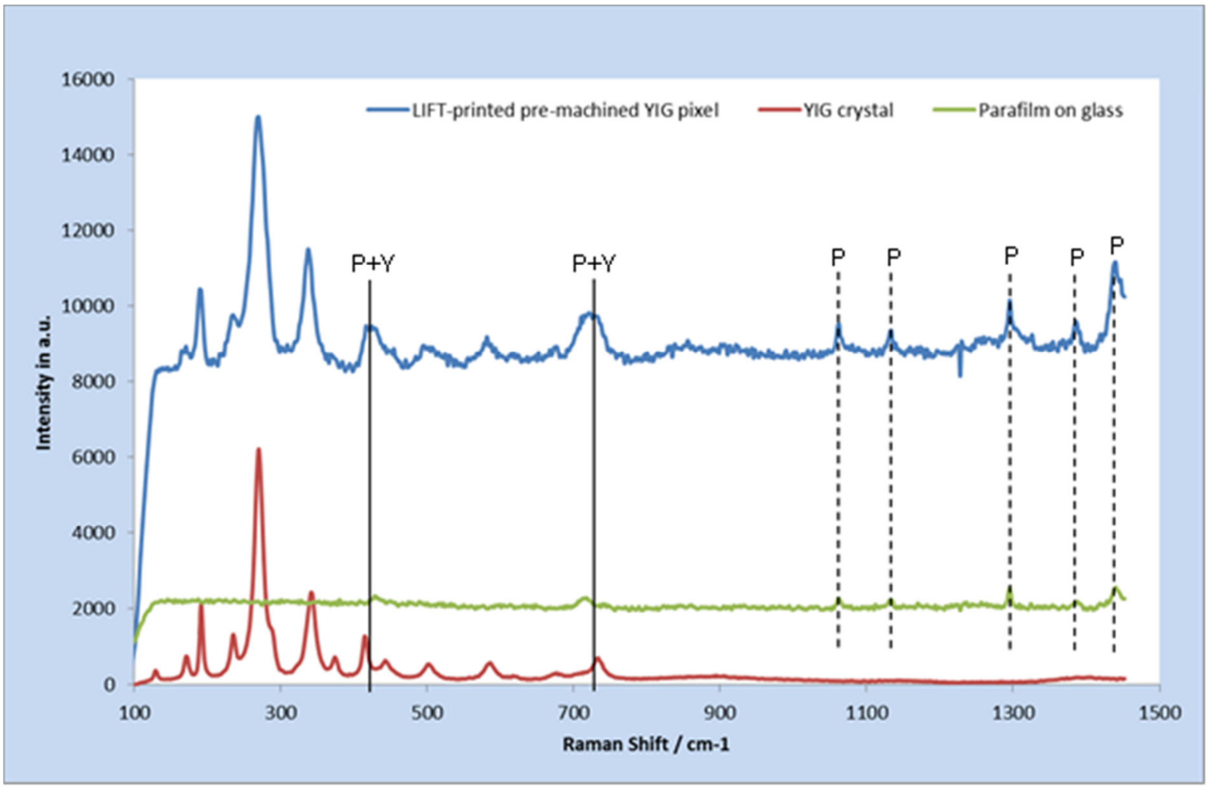

Figure A.3.7. Micro-Raman measurements of a pre-machined disc LIFT-printed on a Parafilm-coated glass receiver, YIG crystal donor, and Parafilm on glass [1].

Finally, the crystallinity of pre-machined LIFT-printed YIG voxels was confirmed by micro-Raman characterisation performed using a Renishaw inVia Raman Microscope. The Raman scans were acquired with an incident laser wavelength of λ = 633 nm and a grating with a resolution of 1200 lines/mm. The blue trace in Figure A.3.7 is the micro-Raman spectrum for a circular disc LIFT-printed from a pre-machined donor. Since these discs were transferred onto a Parafilm-coated glass receiver, a micro-Raman trace (green) was acquired from an identical blank Parafilm-coated glass substrate. The red trace in Figure A.3.7 is the measurement for the YIG crystal which was used for the PLD of YIG. Acquisition of micro-Raman measurements from the YIG donor on the YAG carrier was attempted, but it was not possible to separate the contributions of YAG and YIG crystals in the measured spectrum, due to the overwhelmingly contribution from the underlying YAG substrate.

The scan data for the YIG crystal have been reduced to half of their original value, in order to separate the different traces in Figure A.3.7 for better clarity. Similarly, the data for the Parafilm on glass have been shifted upwards by 1000 arbitrary units. The crystalline nature of the LIFT-printed voxels is quite evident from the relative coincidence between at least the first five peaks of the Raman spectra for the LIFT-printed pre-machined donor pixel and the YIG crystal.

The peaks marked “P” in the spectrum for the LIFT-printed pre-machined YIG disc are due to the underlying Parafilm, onto which the pre-machined YIG disc has been transferred, and these have been indicated via the dashed lines in Figure A.3.7. The broadened peaks marked “P+Y” in the scan for the LIFT-printed pre-machined YIG disc are probably due to a convolution of the peaks observed for the YIG donor crystal and the Parafilm [1].

A.4. CONCLUSIONS

This chapter has covered the successful demonstration of debris-free, intact, LIFT-printing of FIB pre-machined crystalline YIG voxels with very good edge quality. This is the first report to our knowledge of LIFT-printing of intact crystalline materials from thin film donors [1]. Considering the difficulty in detaching a section of an epitaxially-grown (YIG) film from a single-crystal (YAG) substrate, the results of these experiments here described are particularly encouraging and represent an important step that will help spread the applicability of PLD and LIFT-printing for photonic single-crystal devices, where crystal and edge quality and feature shape are crucial parameters.

A.5. REFERENCES

1. C. L. Sones, M. Feinaeugle, A. Sposito, B. Gholipour, and R. W. Eason, "Laser-Induced Forward Transfer-printing of focused ion beam pre-machined crystalline magneto-optic yttrium iron garnet micro-discs," Opt. Express **20**, 15171-15179 (2012).

2. C. B. Arnold, P. Serra, and A. Pique, "Laser direct-write techniques for printing of complex materials," MRS Bulletin **32**, 23-31 (2007).

3. B. Mills, J. A. Grant-Jacob, M. Feinaeugle, and R. W. Eason, "Single-pulse multiphoton polymerization of complex structures using a digital multimirror device," Opt. Express **21**, 14853-14858 (2013).

4. B. Mills, M. Feinaeugle, C. L. Sones, N. Rizvi, and R. W. Eason, "Sub-micron-scale femtosecond laser ablation using a digital micromirror device," J. Micromech. Microeng. **23**, 035005 (2013).

5. D. P. Banks, C. Grivas, I. Zergioti, and R. W. Eason, "Ballistic laser-assisted solid transfer (BLAST) from a thin film precursor," Opt. Express **16**, 3249-3254 (2008).

6. K. S. Kaur, M. Feinaeugle, D. P. Banks, J. Y. Ou, F. Di Pietrantonio, E. Verona, C. L. Sones, and R. W. Eason, "Laser-induced forward transfer of focussed ion beam pre-machined donors," Appl. Surf. Sci. **257**, 6650-6653 (2011).

7. R. Swanepoel, "Determination of the thickness and optical-constants of amorphous-silicon," J. Phys. E-Sci. Instr. **16**, 1214-1222 (1983).

8. D. P. Banks, K. Kaur, and R. W. Eason, "Influence of optical standing waves on the femtosecond laser-induced forward transfer of transparent thin films," Appl. Optics **48**, 2058-2066 (2009).

B. APPENDIX B
APPLICATIONS OF YIG IN MAGNETIC META-MATERIALS

B.1. INTRODUCTION

During the collaboration with Dr. Gavin Stenning, previously a PhD student in the School of Physics and Astronomy of the University of Southampton, efforts were made to find new applications of magneto-optic and ferromagnetic properties of YIG. This appendix shows the results obtained during the demonstration of one of the YIG films I provided in the research field of magnetic meta-materials. All the experiments described here were performed by Dr. Gavin Stenning during his doctoral studies at the School of Physics and Astronomy of the University of Southampton, in collaboration with the Meta-materials research group of the Optoelectronics Research Centre at the University of Southampton: the data collected were analysed and interpreted by Dr. Gavin Stenning and collaborators. After a short introduction about meta-materials, necessary to place this project in context, the experiments and the results achieved are described and discussed in Section B.3. More details can be found in [1].

B.2. META-MATERIALS

Meta-materials are artificial materials exhibiting properties which cannot be found in natural materials, e.g. negative refractive index [2], resulting for instance in “invisibility cloaking” and super-lenses with sub-wavelength spatial resolution, i.e. beyond diffraction limit. Meta-materials are usually made of periodic structures (meta-molecules) with sub-wavelength size, i.e. features smaller than the wavelength that they are designed to affect. However the properties of meta-materials are achieved only at the resonance frequency of these meta-molecules, but, if the meta-material comprises tunable elements, e.g. ferromagnetic materials, it is possible to tune the resonance frequency of the meta-material and thus overcome the intrinsic narrow-bandwidth limitations, for instance by varying the FMR frequency of a YIG slab by changing the intensity of the magnetising field [3]. The work presented in the next section describes the magnetic control of a meta-molecule and, in particular, the tunability via an external magnetic field of a composite structure made of an insulating ferromagnetic YIG film grown by PLD on a diamagnetic YAG substrate and a high-conductivity split ring resonator (SRR): the strong interaction between the two elements of the hybrid structure is discussed in more detail below.

The SRR is one of the most common meta-molecules used to fabricate meta-materials, as it has been extensively studied since its first proposal by Pendry *et al.* [4]. It is made of a pair of concentric C-shaped rings, patterned on a dielectric substrate, with gaps on opposite sides (see Figure B.2.1.c) and with a size typically 10% that of the incident frequency used to excite the structure. The resonant frequency of a SRR derives from the capacitance (C_{mm}) and inductance (L_{mm}) of the geometry of the single meta-molecule:

$$\omega_{mm} = \frac{1}{\sqrt{L_{mm}C_{mm}}} \tag{B.2.1}$$

SRR-based meta-materials have therefore a narrow bandwidth due to the resonant character of the individual meta-molecule; however, this can be changed with a magnetic hybrid structure, as aforementioned and shown schematically in Figure B.2.1 and discussed in detail in Section B.3.

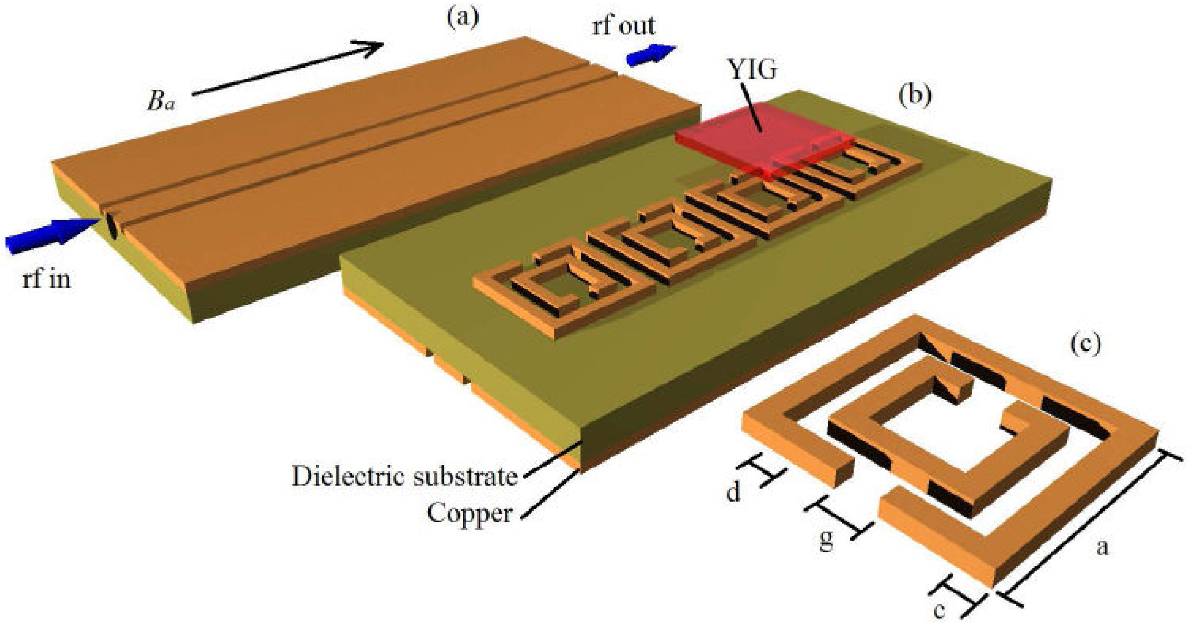

Figure B.2.1. Schematic of **(a)** top view of coplanar waveguide (CPW), **(b)** SRR meta-material on the underside of the CPW (the YIG film is placed in a flip-chip configuration on top of one of the SRRs), **(c)** single SRR, whose dimensions are: a = 3.93 mm, c = 0.375 mm, d = 0.45 mm, g = 0.69 mm. Field direction as shown by *B*a. Figure taken from [1].

B.3. MAGNETIC CONTROL OF A META-MOLECULE

The YIG film used for the experiments described in this section was Y20, the best sample grown on a YAG substrate by PLD, deposited under the optimum growth conditions discussed in Chapter 6 and reported in Table B.3.1 for convenience, featuring an FMR linewidth $\Delta H \approx 1.75$ mT; although this value is ~100 times higher than the intrinsic FMR linewidth of bulk YIG spheres, it was good enough for the purposes of this project. YIG was chosen not only for its strong and narrow FMR and low microwave losses, but also for its negative permeability on resonance [5], its wide tunability in the microwave and its insulating properties, avoiding eddy current losses.

Target	Single-crystal YIG
Substrate	YAG (100)
Laser (λ [nm])	KrF ($\lambda = 248$)
Repetition frequency [Hz]	20
Fluence [J/cm^2]	~3.0
Target – substrate distance [cm]	6.0
O_2 pressure [Pa]	1.0
Substrate temperature [K]	~1250

Table B.3.1. Deposition conditions of sample Y20.

The experimental set-up is schematically depicted in Figure B.2.1 and finds applications in broadband tunable devices [1]. SRRs can be excited by the electromagnetic field of a microwave signal propagating through a coplanar waveguide (CPW – shown in Figure B.2.1.a), even if they are patterned on the reverse side of the CPW (Figure B.2.1.c), actually resulting in lower microwave losses, while still featuring strong meta-material resonances [1, 6]. The experimental rig is otherwise the same as used for FMR characterisation of YIG films, as described in Section 4.10, with the YIG film placed on top of an SRR (*flip-chip* method) [7] in order to allow strong coupling to the CPW and good microwave excitation.

Figure B.3.1 shows a colour plot of the normalised S_{21} transmission vs. frequency and field (ν-B_a), in the range 1-20 GHz and 0-0.5 T, for the CPW/SRR/YIG composite system: the colour at a given point in the map represents the magnitude of S_{21}. All S_{21} map plots were normalized by subtracting the S_{21} transmission obtained in a small (approximately zero) magnetic field (B_a =0.001 T) from every subsequent frequency sweep: this gives a final value of $|S^N_{21}|$[14], leaving only field-dependent features in the resulting plots. Individual

---

[14] The *N* superscript refers to normalisation.

SRR and YIG resonances and strong anti-crossing behaviour, when the two resonances coincide, are clearly visible in such colour maps [8].

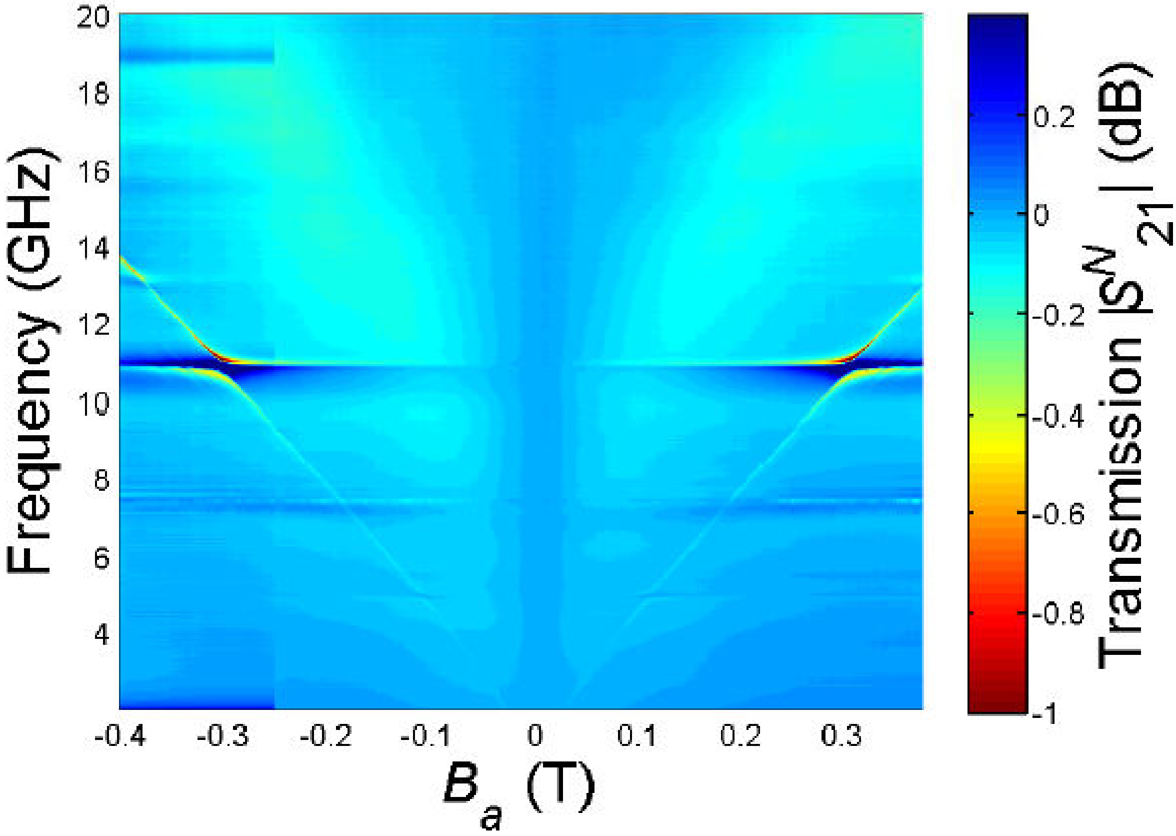

Figure B.3.1. Normalized S^N_{21} (ν-B_a) map of a YIG film coupled to a SRR. The transmission colour-bar on the right represents transmission (positive values/blue) and absorption (negative values/red). Figure taken from [8].

The normalized $|S^N_{21}|$ map in Figure B.3.1 was obtained from a single SRR coupled to a YIG film excited via the CPW: YIG being isotropic, the ν-Ba map results to be symmetrical at B_a = 0 T. The diagonal lines departing from B_a = 0 T, ν = 2 GHz (bottom line of the map) represent the expected YIG FMR absorption, whereas the SRR resonance appears as a horizontal line at 10.9 GHz; strong anti-crossing behaviour occurs at the point where the YIG and SRR resonances are expected to cross. Figure B.3.2 shows the positive field section of the $|S^N_{21}|$ map in Figure B.3.1 (right side) and two hybridised resonances arising from the different current excitations (electric and magnetic) of the SRR: the electric resonance mode of the SRR is highlighted in the red circle (at ν = 10.9 GHz), whereas its magnetic mode is highlighted in the black circle (at ν = 5 GHz). Figure B.3.3 shows a close-up of the YIG-SRR anti-crossing mode (electric resonance) highlighted in the red circle in Figure B.3.2; the arrow in Figure B.3.3 indicates the presence of FMR satellites, due to the excitation of backward volume magnetostatic waves (BVMSWs) [9-12].

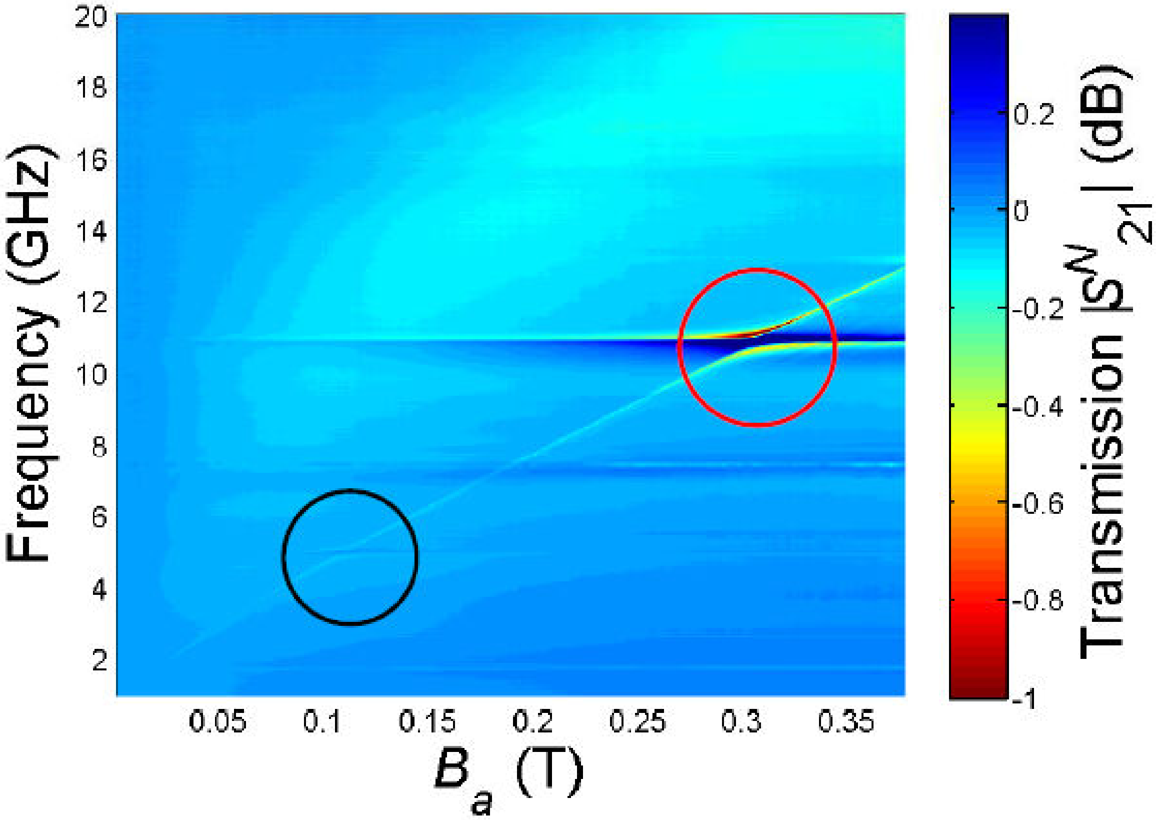

Figure B.3.2. (*v*-*B*a) map of hybridised interaction showing all anti-crossings present.
Red (black) circle represent the electric (magnetic) resonance mode of the SRR respectively [8].

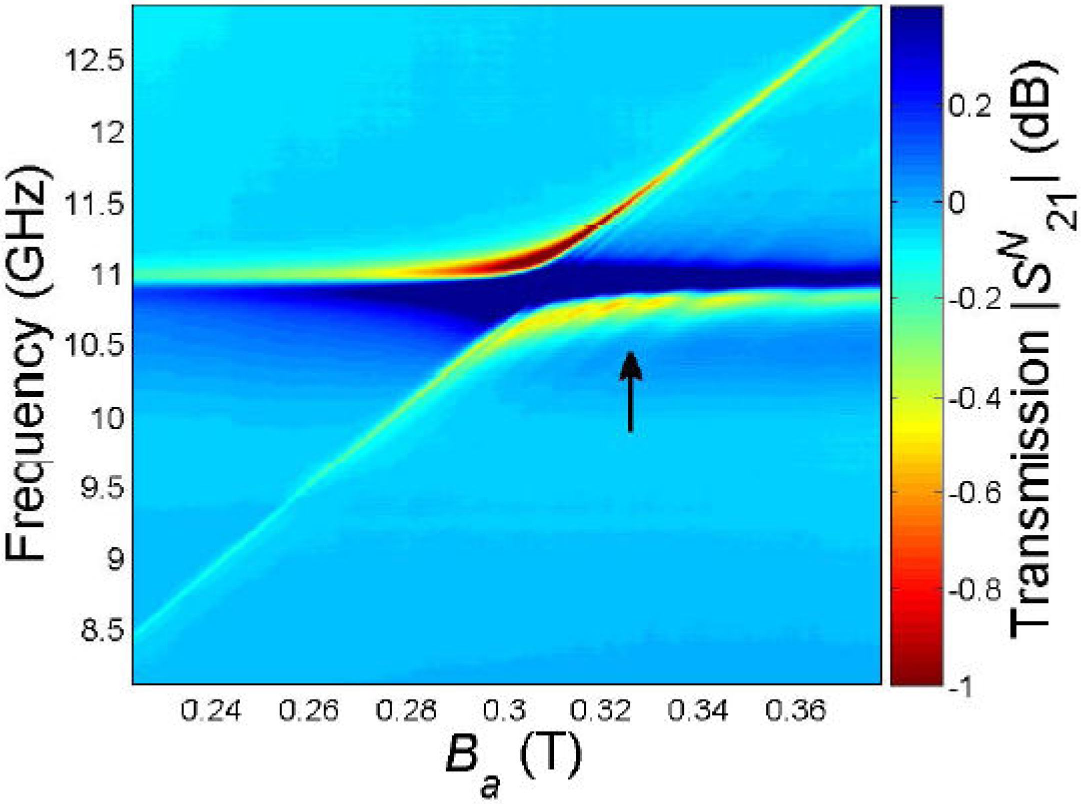

Figure B.3.3. Close-up of the YIG-SRR anti-crossing mode in the (*v*-*B*a) map in Figure B.3.2.
Satellites of the FMR are visible to the right of the anti-crossing and FMR shown by the black arrow [1].

A reduction in microwave losses for the SRR resonance at ν = 10.9 GHz is observed at a field of B_a = 0.3 T. This point is illustrated in Figure B.3.3 and Figure B.3.4 at the centre of the anti-crossing: above and below the anti-crossing (black and blue curves respectively in Figure B.3.4) there are absorption troughs (negative) associated with the field-dependent YIG FMR, while exactly at the centre of the anti-crossing, there is a reduction in the losses amounting to 1.6 dB (peak) [1]. This is indicative of an effective negative index of refraction, as obtained by He *et al.* [13], using the experimental *S*-parameter retrieval technique [14].

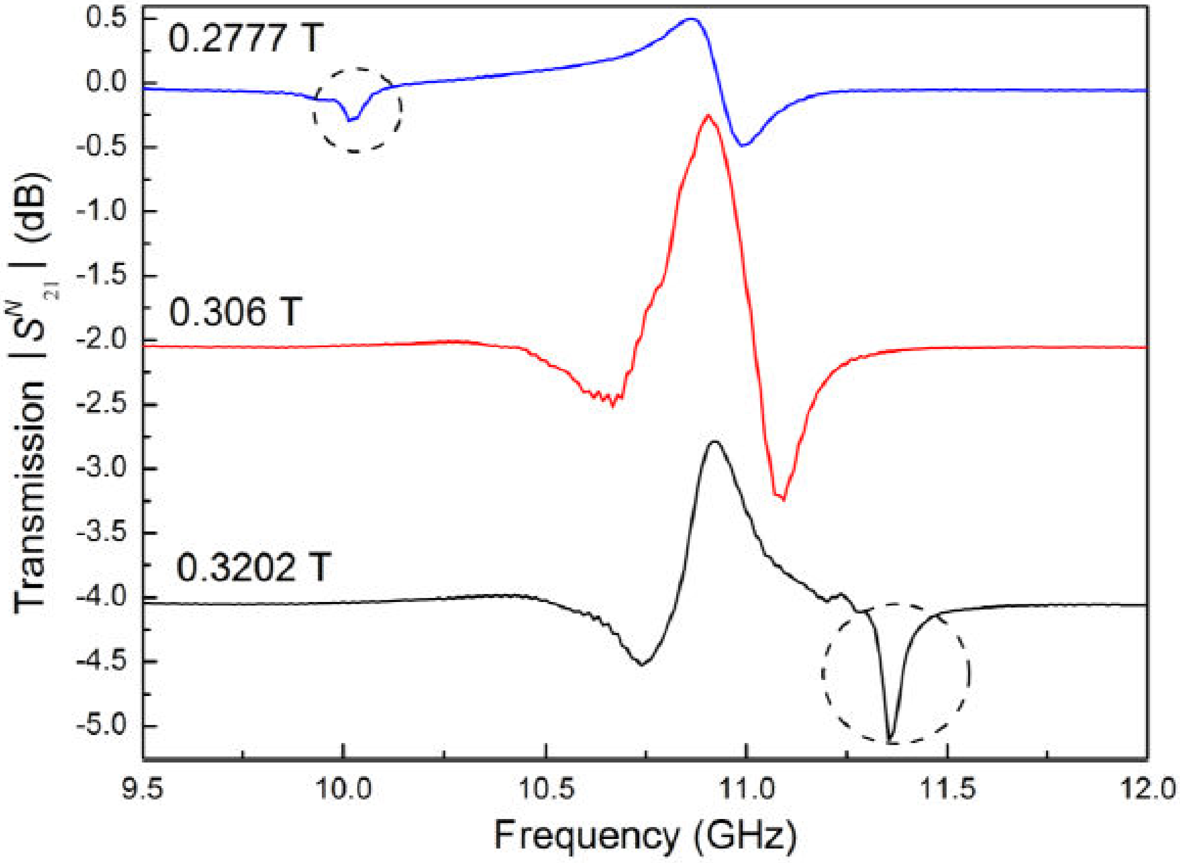

Figure B.3.4. Normalised transmission $|S^N_{21}|$ vs. frequency (ν) at three fixed values of magnetic field from Figure B.3.3: B_a = 0.278 T, 0.306 T and 0.320 T, blue, red and black respectively. Dashed circles represent the FMR peak which moves through the SRR resonance as the intensity of the magnetic field is increased. Each trace has been offset by 2 dB for better clarity [8].

The resonances shown in Figure B.3.4 are similar to those described theoretically in [15]. The low frequency trough of the blue trace (B_a = 0.2777 T) is the FMR resonance of YIG, whereas the high frequency peak is associated with the symmetric electric-dipole resonance of the SRR, as confirmed experimentally by shorting the gaps in the ring with a short strip of conducting wire, following [16]; in this way, the low frequency anti-symmetric magnetic resonance of the SRR at ~5 GHz is eliminated, while the symmetric electric-dipole resonance response at 10.9 GHz is left unchanged. As the intensity of the magnetic field is increased, the YIG resonance passes through the SRR resonance, distorting the hybridization, as shown in Figure B.3.4 (red trace, B_a = 0.306 T) revealing the 1.6 dB reduction in losses: the YIG resonance is no longer visible on either side of where the FMR would appear and the natural resonance of the SRR is observed. By increasing the intensity of the external magnetic field even further, the YIG resonance moves above that of the SRR resonance (black trace, B_a = 0.3202 T). A comparison the blue and black curves in Figure B.3.4, respectively at B_a = 0.2777 T and 0.3202 T, shows that the SRR effective frequency trace at B_a = 0.3202 T (black trace) is inverted in shape and shifted by 0.25 GHz with respect to the first trace at B_a = 0.2777 T (blue trace), in agreement with the observations reported in [15, 17].

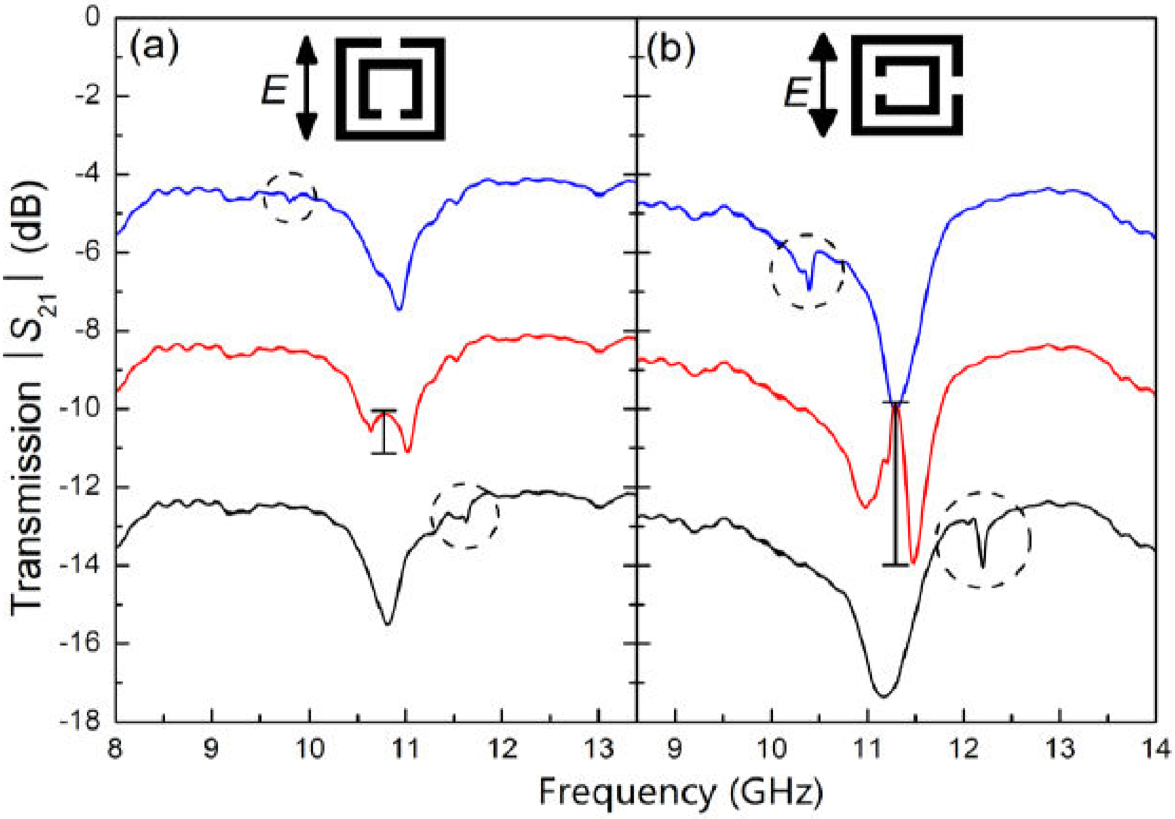

Figure B.3.5. Un-normalised data (S_{21}) for two orientations of the SRR. The black arrow represents the electric field polarisation supplied by the CPW. The resonance S_{21} curves blue, red and black were obtained for applied magnetic fields of 0.27 T, 0.30 T and 0.33 T respectively. The dashed circles indicate the YIG resonance, whereas the vertical black lines represent the modulation in microwave transmission. Each frequency trace has been offset vertically by 4 dB for better clarity [8].

The results of a 90° rotation of the SRR with respect to the direction of the magnetic field is shown in Figure B.3.5, where it is clear that the hybridization/interaction is much stronger for the orientation of the SRR as shown in Figure B.3.5.b: in particular, the transmission at the centre of the anti-crossing has increased to 4.0 dB; a shift in frequency of 0.25 GHz of the electric dipole resonance is apparent too as the YIG FMR passes across.

This demonstrates the importance of the SRR orientation with respect to the magnetization field in terms of optimisation of microwave transmission S_{21}. Concurrent increases in absorption can be noticed on both sides of the anti-crossing, as shown by the circles in Figure B.3.5.b.

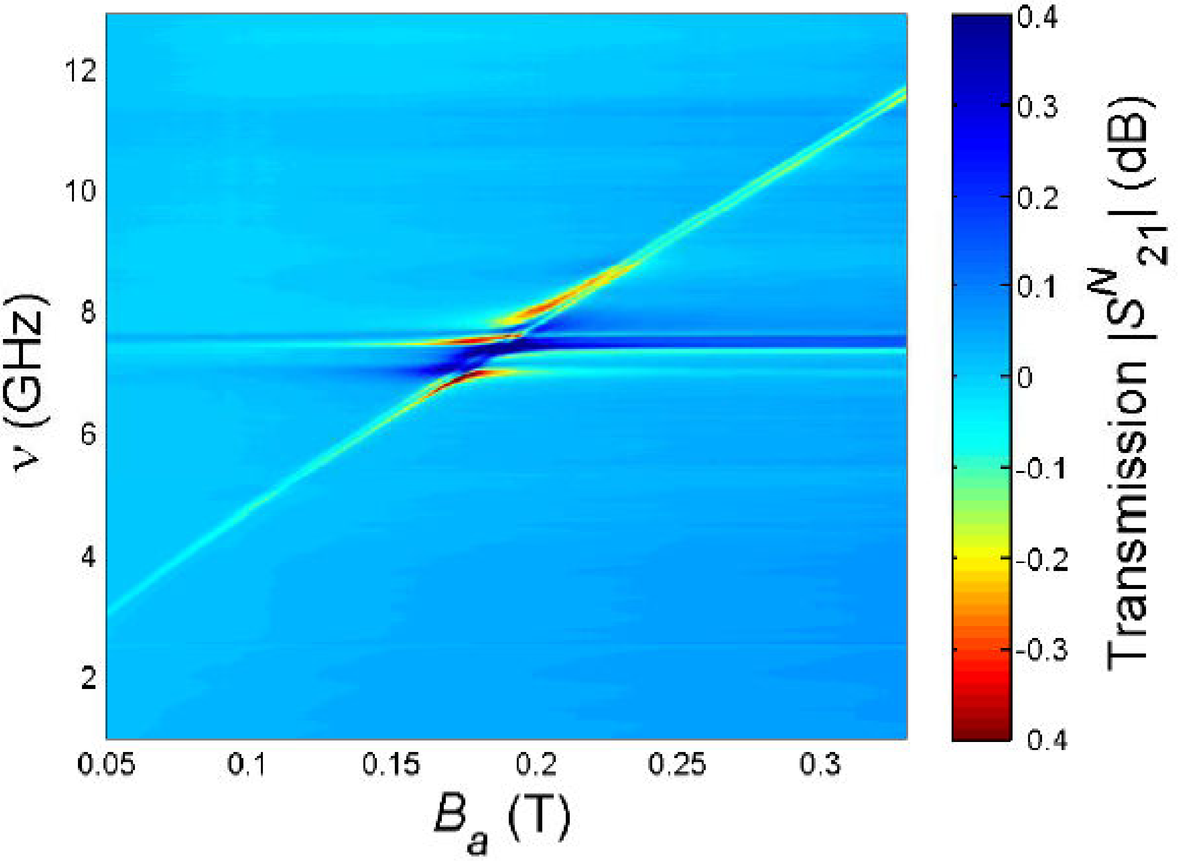

Figure B.3.6. (ν-Ba) map of multiple YIG films coupled to four SRRs [8].

Figure B.3.6 shows a $|S^N{}_{21}|(\nu\text{-}B\text{a})$ map of a linear array of 4 SRRs and multiple YIG films to replicate a meta-material structure, to prove that the coupling of a meta-molecule to an active magnetic material is scalable to an array. In these experiments, multiple YIG films were used as it was not possible to grow a film large enough that would be uniform across 4 SRRs. In any case, Figure B.3.6 shows evident crosstalk and/or differences in the individual electric-dipole resonances: in place of a single SRR resonance there would appear to be at least three electric-dipole resonances in the region of 7-8 GHz, compared to the original frequency of 10.9 GHz in the case of a single meta-molecule; this shift down to ~7 GHz arises from the crosstalk/mutual inductance between the 4 SRRs. Nevertheless the results are similar to those obtained for a single meta-molecule.

The anti-crossing mode was replicated using COMSOL: its results are shown in Figure B.3.7, whose low resolution is due to the need to cover wide magnetic field and frequency range, which otherwise would have taken long computing times: the simulation is in good agreement with the experimental results shown above (see Figure B.3.3 and Figure B.3.4 for comparison).

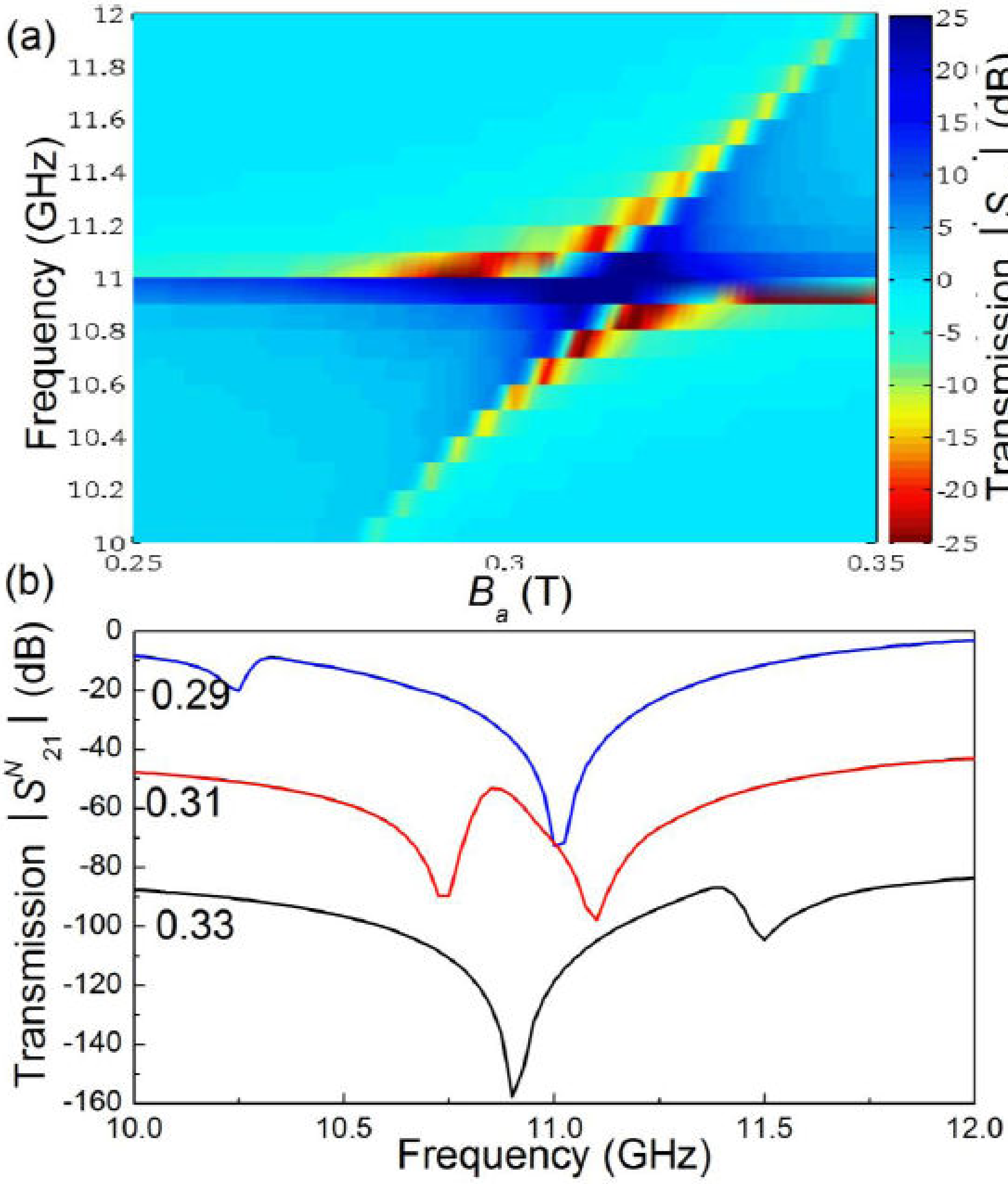

Figure B.3.7. COMSOL simulation of a SRR coupled to a YIG film. The microwaves are supplied by a plane wave normal to the SRR and the YIG. **(a)** *ν-Ba* map of the anti-crossing and **(b)** line-scans at 3 different values of the applied magnetic field respectively [8].

B.4. CONCLUSIONS

In summary, this chapter has presented an application of YIG films grown by PLD: CPW-based composite SRR meta-materials incorporating a magnetic component (YIG) tunable by applying an external magnetic field have been demonstrated. The coupling between the SRR and the YIG gives rise to hybridisation of the two resonances: in particular, the anti-crossing regime allows tuning over a frequency range of ~0.3 GHz. Good agreement has been found between the experiments and electromagnetic simulations obtained using COMSOL. It has also been shown that the orientation of the SRR with respect to the magnetisation of the YIG and CPW plays an important role: in particular, a rotation of the SRR by 90° allows an increase of the transmission at the centre of the anti-crossing up to 4.0 dB, thus demonstrating that device tunability can be performed by adjusting either the strength of the magnetic field or the orientation of the SRR relatively to the CPW.

B.5. REFERENCES

1. G. B. G. Stenning, G. J. Bowden, L. C. Maple, S. A. Gregory, A. Sposito, R. W. Eason, N. I. Zheludev, and P. A. J. De Groot, "Magnetic control of a meta-molecule," Opt. Express **21**, 1456-1464 (2013).

2. R. A. Shelby, D. R. Smith, and S. Schultz, "Experimental verification of a negative index of refraction," Science **292**, 77-79 (2001).

3. H. Yongxue, H. Peng, Y. Soack Dae, P. V. Parimi, F. J. Rachford, V. G. Harris, and C. Vittoria, "Tunable negative index metamaterial using yttrium iron garnet," J. Magn. Magn. Mater. **313**, 187-191 (2007).

4. J. B. Pendry, A. J. Holden, D. J. Robbins, and W. J. Stewart, "Magnetism from conductors and enhanced nonlinear phenomena," IEEE Trans. Microw. Theory Tech. **47**, 2075-2084 (1999).

5. H. J. Zhao, J. Zhou, L. Kang, and Q. Zhao, "Tunable two-dimensional left-handed material consisting of ferrite rods and metallic wires," Opt. Express **17**, 13373-13380 (2009).

6. C. Saha, J. Y. Siddiqui, and Y. M. M. Antar, "Square split ring resonator backed coplanar waveguide for filter applications," 2011 XXXth URSI General Assembly and Scientific Symposium, 4 pp.-4 pp. (2011).

7. J. M. L. Beaujour, A. D. Kent, D. W. Abraham, and J. Z. Sun, "Ferromagnetic resonance study of polycrystalline $Fe_{1-x}V_x$ alloy thin films," J. Appl. Phys. **103**, 07B519-511 (2008).

8. G. B. G. Stenning, "X-ray and microwave studies of strongly exchange coupled magnetic multilayers," PhD at *School of Physics and Astronomy* (University of Southampton, Southampton, 2013).

9. A. G. Gurevich, and G. A. Melkov, *Magnetization Oscillations and Waves* (CRC Press, 1996).

10. L. R. Walker, "Resonant modes of ferromagnetic spheroids," J. Appl. Phys. **29**, 318–323 (1958).

11. J. F. Dillon, "Magnetostatic modes in disks and rods," J. Appl. Phys. **31**, 10 (1960).

12. R. W. Damon, and J. R. Eshbach, "Magnetostatic modes of a ferromagnet slab," J. Phys. Chem. Solids. **19**, 2 (1960).

13. P. He, J. Gao, C. T. Marinis, P. V. Parimi, C. Vittoria, and V. G. Harris, "A microstrip tunable negative refractive index metamaterial and phase shifter," Appl. Phys. Lett. **93**, 3 (2008).

14. D. R. Smith, D. C. Vier, T. Koschny, and C. M. Soukoulis, "Electromagnetic parameter retrieval from inhomogeneous metamaterials," Phys. Rev. E **71**, 11 (2005).

15. J. N. Gollub, J. Y. Chin, T. J. Cui, and D. R. Smith, "Hybrid resonant phenomena in a SRR/YIG metamaterial structure," Opt. Express **17**, 2122-2131 (2009).

16. T. Koschny, M. Kafesaki, E. N. Economou, and C. M. Soukoulis, "Effective medium theory of left-handed materials," Phys. Rev. Lett. **93**, 4 (2004).

17. L. Kang, Q. Zhao, H. J. Zhao, and J. Zhou, "Magnetically tunable negative permeability metamaterial composed by split ring resonators and ferrite rods," Opt. Express **16**, 8825-8834 (2008).

C. APPENDIX C
LIST OF PUBLICATIONS

C.1. PUBLICATIONS FROM RESULTS REPORTED IN THIS THESIS

The following publications describe results achieved from experiments described in this thesis.

C.1.1. JOURNAL ARTICLES

- A. Sposito, G.B.G. Stenning, S.A. Gregory, P.A.J. de Groot, R.W. Eason, "Compositional tuning of YIG film properties by multi-beam pulsed laser deposition," Thin Solid Films (in review).
- A. Sposito, S.A. Gregory, P.A.J. de Groot, R.W. Eason, "Combinatorial pulsed laser deposition of doped YIG films on YAG," J. Appl. Phys. **115**, 053102 (2014).
- R.W. Eason, T.C. May-Smith, K.A. Sloyan, R. Gazia, M.S.B. Darby, A. Sposito, T.L. Parsonage, "Multi-beam pulsed laser deposition for advanced thin film optical waveguides," J. Phys. D: Appl. Phys. **47**, 034007 (2014)
- A. Sposito, T.C. May-Smith, G.B.G. Stenning, P.A.J. de Groot, R.W. Eason, "Pulsed laser deposition of high-quality µm-thick YIG films on YAG," Opt. Mater. Express **3**, 624-632 (2013).
- G.B.G. Stenning, G.J. Bowden, L.C. Maple, S.A. Gregory, A. Sposito, R.W. Eason, N.I. Zheludev, P.A.J. de Groot, "Magnetic control of a meta-molecule," Opt. Express **21**, 1456-1464 (2013).
- C.L. Sones, M. Feinäugle, A. Sposito, B. Gholipour, R.W. Eason, "Laser-induced forward transfer-printing of focused ion beam pre-machined crystalline magneto-optic yttrium iron garnet micro-discs," Opt. Express **20**, 15171-15179 (2012).

C.1.2. CONFERENCE PAPERS

- S.A. Gregory, G.B.G. Stenning, A. Sposito, G.J. Bowden, T. Hesjedal, R.W. Eason, N.I. Zheludev, P.A.J. de Groot, "Magnetic Hybrid Metamaterials," META 2014 Conference, Singapore, May 2014
- A. Sposito, G.B.G. Stenning, S.A. Gregory, O. Muskens, P.A.J. de Groot, R.W. Eason, "Multi-beam PLD of magneto-optic garnets," COLA (Conference On Laser Ablation) 2013, Ischia (Italy), Oct. 2013.
- A. Sposito, G.B.G. Stenning, S.A. Gregory, K.A. Sloyan, T.L. Parsonage, O. Muskens, P.A.J. de Groot, R.W. Eason, "Tailoring of YIG film properties via compositional tuning by multi-beam pulsed laser deposition," 2013 IPC (IEEE Photonics Conference), Bellevue (WA, USA), Sep. 2013.
- C.L. Sones, M. Feinäugle, B. Gholipour, A. Sposito, R.W. Eason, "Laser-induced forward transfer-printing of focused ion beam pre-machined crystalline magneto-optic garnet discs," EMRS (European Materials Research Society) 2012 Spring Meeting, Strasbourg (France), May 2012.
- C.L. Sones, M. Feinäugle, B. Gholipour, A. Sposito, R.W. Eason, "Laser-induced forward transfer-printing of pre-machined crystalline magneto-optic garnet discs," CLEO/QELS (Conference on Laser and Electro-Optics / Quantum Electronics and Laser Science conference) 2012 San Jose (CA, USA) May 2012.

C.1.3. INVITED TALKS (PRESENTER)

- A. Sposito, T.C. May-Smith, K.A. Sloyan, R.W. Eason, "Pulsed laser deposition of YIG and Ti:sapphire," Università degli Studi di Palermo, Palermo (Italy), 11 Apr. 2012
- A. Sposito, T.C. May-Smith, K.A. Sloyan, R.W. Eason, "Pulsed laser deposition of YIG and Ti:sapphire," KTH (Royal Institute of Technology), Stockholm (Sweden), 30 Mar. 2012
- A. Sposito, T.C. May-Smith, K.A. Sloyan, R.W. Eason, "PLD physics and photonics in service of future," Università degli Studi di Palermo, Palermo (Italy), 27 Apr. 2011

C.2. OTHER PUBLICATIONS FROM THE PULSED LASER DEPOSITION RESEARCH GROUP

The following publications contain work carried out during my time as a PhD student in the "Pulsed Laser Deposition" research group of the Optoelectronics Research Centre at the University of Southampton, but are not described in detail in this thesis.

C.2.1. INVITED TALKS

- K. Sloyan, T.C .May-Smith, A. Sposito, R.W. Eason, "Multi-beam pulsed laser deposition: Advanced structures and future directions," *Physics with new coherent radiation sorces* (seminar series), University of Hamburg (Germany), 15 Feb 2011.
- T.C. May-Smith, K.A. Sloyan, A. Sposito, R.W. Eason, "Multi-beam pulsed laser deposition: Important techniques and overcoming limitations," *Physics with new coherent radiation sorces* (seminar series), University of Hamburg (Germany), 15 Feb 2011.

C.2.2. BOOK CHAPTERS

- R.W. Eason, T.C. May-Smith, K.A. Sloyan, R. Gazia, M. Darby, A. Sposito, "Emerging pulsed laser deposition techniques" in *Laser growth and processing of photonic devices*, edited by N. Vainos, (Woodhead, UK), Jul. 2012.